

## DISSERTATION

# BASELINE DESIGN OF THE CRYOGENIC SYSTEM FOR EURECA

ausgeführt zum Zwecke der Erlangung des akademischen Grades eines  
Doktors der Technischen Wissenschaften  
unter der Leitung von

**Univ.Prof. Dr.phil. Dr.h.c. Harald W. Weber**

*Atominstitut (E141)*

*Technische Universität Wien*

eingereicht an der Technischen Universität Wien  
Fakultät für Physik

von

**Dipl.-Ing. Gerhard Burghart**

*Matrikelnummer: 9525847*

*20, Rue des Deux-Ponts*

*CH - 1205 Genf*

*Diese Arbeit wurde unterstützt von CERN und vom  
Bundesministerium für Wissenschaft und Forschung, Wien*

Wien, am 27.04.2010

# Gutachter

Diese Dissertation haben begutachtet:

Univ. Prof. Dr. phil. Dr.h.c Harald Weber

Technische Universität Wien, Atominstitut (E141)

Univ.Prof. Dipl.-Ing. Dr.techn. Christian Fabjan

Technische Universität Wien, Atominstitut (E141)

# Kurzfassung

Die Materie im Universum scheint zum überwiegenden Teil aus unbekannter Dunkler Materie zu bestehen. EURECA (EUropean Rare Event Calorimeter Array) ist eine europäische Kooperation, die gegründet wurde, um Weakly Interacting Massive Particles (WIMPs), die Hauptkandidaten für nicht-baryonische Dunkle Materie, zu entdecken und direkt zu erforschen. Dafür muss eine Masse von einigen Tonnen, bestehend aus dem Detektor Material und der Haltestruktur, mit Hilfe eines  $^3\text{He}/^4\text{He}$  Verdünnungskryostaten auf 10 mK gekühlt werden. Die hohen Anforderungen an eine extrem geringe Radioaktivität untersagen die Benutzung von Wärmeübertragern aus gesintertem Silber, welche bisher das einzige Material waren um derartig hohe Kühlleistungen bei diesen tiefen Temperaturen zu erreichen.

Designstudien von kritischen Komponenten des kryogenischen Systems, wie die Abschirmung gegen Hintergrundstrahlung, ein System zum schnellen Austausch von Detektor Material und das angrenzende Kühlsystem, wurden durchgeführt und die am besten angepassten Lösungen bestimmt. Für eine verlässliche Vorhersage der notwendigen Kühlleistung für EURECA wurden die verbleibenden Wärmelasten studiert und analysiert. Die Technik, feine Kupferpulver zu sintern wurde optimiert und die Ergebnisse experimentell charakterisiert und analysiert.

Im Rahmen dieser Doktorarbeit wurde ein Baseline Design des kryogenen Systems des Dunklen Materie Detektors von EURECA entwickelt. Basierend auf den durchgeführten Messungen ist der optimierte Wärmeübertrager aus feinem Kupferpulver dazu in der Lage die notwendige Kühlleistung bei tiefsten Temperaturen zu erbringen, die für das beschriebene Kryostaten Design bestimmt wurde.

# Abstract

Dark Matter appears to dominate the matter in the Universe. EURECA (EUropean Rare Event Calorimeter Array), a large European collaboration, was set up to discover and study directly Weakly Interacting Massive Particles (WIMPs), which are the main candidates for non-baryonic Dark Matter. Therefore, a large mass of several tons, consisting of the detector and the support structure needs to be cooled by a dilution refrigerator to a temperature of 10 mK. The requirement for an ultra-low radioactivity prohibits the use of a heat exchanger made of sintered silver, which so far is the only material to achieve the required very high cooling power at very low temperature.

Design studies of several critical components of the cryogenic system, such as the main shielding, the fast exchange of detector material and the proximity cryogenics, have been accomplished and the most suitable solutions were determined to meet the scientific requirements. For a reliable prediction of the required cooling power of the large detector array of EURECA, the residual heat load was experimentally studied and analysed. The techniques for sintering very fine copper powder have been optimized and the results are experimentally characterized and analysed.

Within the frame of this thesis project, a baseline design of the cryogenic system of the EURECA Dark Matter detector array has been developed. Based on the measurements, the optimised heat exchanger made of fine copper powder was found capable to achieve the required cooling power at the lowest temperature, which has been determined for the described design of the dilution refrigerator.

# Acknowledgements

This thesis would not have been possible without the constant advice of my supervisors Dr. Tapio Niinikoski of CERN and Prof. H. Weber of the Atominstitut of the Technical University of Vienna. Also I am grateful to Prof. Christian Fabjan for providing a reviewer's report and to Johann Bremer for his support.

I am indebted to my colleagues of the Cryolab, Mrs. Leatitia Dufay, Mr. Laurent LeMao, Mr. Sebastian Prunet and Mr. Jean Louis Servals for providing technical advice and for their help in upgrading and maintaining the cryostat. The update of the CCDR electronics, described in Chapter 3, would not have been possible without the cooperation of Ana Sofia Torrento Coello. I would like to thank Gurjun Jesse of the Civil Engineering Research Association who provided the Scanning Electron Microscope image of the copper powders and sintered structures free of charge.

It is an honor for me to thank my colleagues and friends Patrick Wikus and Stefan Rossegger who reviewed my work on short notice. Patrick brought me to cryogenics and in not often long working hours and at weekends, we together learned the practical operation of a dilution refrigerator. Stefan thought me the basics of several software programs inevitable for the evaluation of the data presented in the chapters 4 and 5 and I enjoyed the countless discussions with him.

I owe my deepest gratitude to my family, to my wife Anca for her infinite support and constant encouragement, and to Noel for distracting my mind from the thesis at home and for encouraging me to do some physical activity.



# Contents

Kurzfassung / Abstract . . . . .	iii
Acknowledgements . . . . .	v
<b>1 Introduction</b>	<b>1</b>
1.1 Dark Matter . . . . .	2
1.2 The EURECA Collaboration and Experiment . . . . .	9
1.3 The CERN Cryolab Dilution Refrigerator (CCDR) . . . . .	14
1.4 Kapitza Resistance and Sintered Heat Exchangers . . . . .	17
<b>2 Baseline Design of the EURECA Dark Matter Detector Array</b>	<b>22</b>
2.1 Requirements for the Dilution Refrigerator . . . . .	22
2.2 Design Options for the EURECA DR . . . . .	24
2.3 The Shielding against Background Radiation . . . . .	26
2.4 The “Submarine” versus the “Pool” Design . . . . .	31
2.5 The Exchange of Parts of the Detector Array . . . . .	35
2.6 The Load Lock System . . . . .	36
2.7 A Fast Cycling Dilution Refrigerator . . . . .	42
2.8 The Baseline Design . . . . .	43
2.9 The Detector Unit . . . . .	46
2.10 The Cryogenic Transfer Line . . . . .	51
2.11 The Layout of the Proximity Cryogenics . . . . .	52
2.12 Conclusions . . . . .	55

<b>3</b>	<b>The CCDR Instrumentation and Control System</b>	<b>57</b>
3.1	Electromagnetic Compatibility and Immunity . . . . .	58
3.2	The Electronic Racks . . . . .	59
3.3	The Patch Panels . . . . .	64
3.4	The Cabling . . . . .	69
3.5	Thermometry . . . . .	73
3.6	The Automatic Systems of the CCDR . . . . .	77
3.7	Conclusions . . . . .	83
<b>4</b>	<b>Experimental Study of Residual Heat Loads</b>	<b>84</b>
4.1	Maximum Cooling Power and Optimum Flow . . . . .	84
4.2	Time Constants . . . . .	86
4.3	Measurement of the Maximum Cooling Power and Optimum Flow . . . . .	89
4.4	Experimental Residual Heat Load . . . . .	94
4.5	Time-Independent Sources of Residual Heat Load . . . . .	99
4.6	Time-Dependant Sources of Residual Heat Load . . . . .	104
4.7	Conclusions . . . . .	109
<b>5</b>	<b>Characterization of Sintered 1 <math>\mu\text{m}</math> Copper Powder</b>	<b>112</b>
5.1	Heat Transfer at Very Low Temperatures . . . . .	113
5.2	Heat Exchangers in a Dilution Refrigerator . . . . .	116
5.3	Experimental Study of the 1 $\mu\text{m}$ Copper Powder . . . . .	133
5.4	Conclusions . . . . .	151
<b>6</b>	<b>Conclusions and Outlook</b>	<b>153</b>
<b>A</b>	<b>Measurements of the Thermal Boundary Resistance</b>	<b>155</b>
	<b>Bibliography</b>	<b>157</b>
	List of Figures / List of Tables . . . . .	167
	Nomenclature . . . . .	171

# Chapter 1

## Introduction

The research presented in this thesis was carried out in the framework of EURECA<sup>1</sup>, a large European collaboration. It has been set up with the goal to discover and study directly the Dark Matter (DM), which seems to dominate the visible matter of our Galaxy, and even all matter in the Universe. In Section 1.1 of this introduction the indirect astrophysical evidence for such matter, whose origin remains speculative today, is reviewed. We shall also discuss the properties of the putative Dark Matter particles predicted by the Standard Model (SM) of Big Bang Cosmology (BBC), and by the extensions of the Standard model of particle physics. In Section 1.2, the EURECA collaboration and its planned experiment are described. Section 1.3 contains a brief review of the equipment that was already constructed at CERN for this work. The core of this equipment is a large Dilution Refrigerator (DR) and its instrumentation capable of cooling large heat loads at millikelvin temperatures. Because the leading problem in the cooling power is the thermal boundary resistance<sup>2</sup> between liquid helium and solids, we shall then review the Kapitza resistance and the sintered heat exchanger techniques in Section 1.4.

For the search of Dark Matter, EURECA requires a large calorimeter array for which we develop the Baseline Design in Chapter 2. Chapter 3 is devoted to the upgrades of the instrumentation and control systems of the dilution refrigerator used in this work, made in cooperation with members of the CERN Central Cryogenic Laboratory (Cryolab). In Chapter 4 the residual heat load to the dilution refrigerator is experimentally studied and analysed, in view of reliably predicting the heat

---

<sup>1</sup>EURECA stands for EUropean Rare Event Calorimeter Array

<sup>2</sup>Kapitza resistance

load to the very massive detector system of EURECA. Chapter 5, finally, contains the techniques for sintering very fine copper powders. The results are experimentally characterized and analysed. Heat exchangers sintered from such fine powders are essential for the cooling of several tons of detectors and structural materials at 10 mK temperature.

## 1.1 Dark Matter

Most of the matter in the Universe appears to be Dark Matter (DM) of which a large part is non-baryonic [24]. Observations that give evidence for the existence of DM are given below:

**1. The rotation curves of galaxies** show that there are significant discrepancies between the visible mass and the conventional dynamical mass of galaxies. The circulation velocity calculated assuming Newtonian dynamics is given by

$$v(r) = \sqrt{\frac{G m(r)}{r}}, \quad (1.1)$$

where  $G$  is Newton's constant and  $m(r)$  is the accumulated mass up to the radius  $r$ . The mass of the galaxy can be estimated from the measured luminosity and an assumed mass-to-light ratio. Beyond the optical galactic disc, where  $m(r)$  should remain approximately constant (without DM) with increasing  $r$ , the velocity should drop as  $\sqrt{\frac{1}{r}}$ . However, this is not observed by the extended rotational curves of the cold gas in the outer regions of galaxies which are measured by the redshift of the 21-cm line of neutral hydrogen. In Figure 1.1 the calculated and measured curves of the rotational velocity from stars and gas are shown [22] as a function of their distance from the galactic center. The measured rotation curve features a flat behavior at large distances, beyond the stars which account for the major part of the mass. This cannot be explained by normal newtonian dynamics and gives evidence of a dominant amount of DM in the dark halos around galaxies.

**2. The interaction of galaxy clusters.** Recent indirect detection of DM has been achieved by gravitational lensing, see e.g. Clowe et al. [31]. The gravitational potential in galaxies consists of the stellar components (1 % of the total mass content [6]), the plasma (4 % of the total mass content) and an assumed DM component (25 % of the total mass content) [24]. Under normal conditions they share the same gravitational potential. During the merge of two clusters, the mostly unaffected stellar components are partly separated from the plasma, which experiences back pressure during

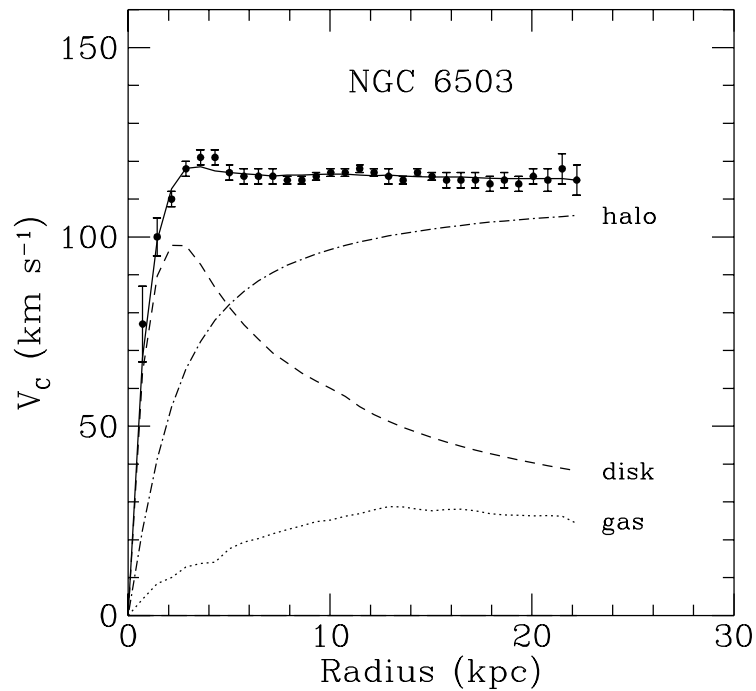


**Figure 1.1:** The observed extended rotation curve of the spiral galaxy DGC 6503 [22]. The dotted, dashed and dash-dotted lines are the contributions of the gas, the visible components and the Dark Matter, respectively.

the collision. In the absence of DM the gravitational potential should stay with the plasma. If Dark Matter existed, it would remain uninfluenced and the gravitational potential would follow the stellar component.

The map of the gravitational potential (green lines in Figure 1.2) is determined with weak gravitational lensing which uses the deflection of the light by gravitation (the light of objects behind is deflected favorably perpendicular to the center of gravity). The mass distribution of the plasma and the stellar component has been determined from X-ray and optical images. It was thus possible to prove that the gravitational potential traces the mostly unaffected stellar components and not the plasma which represents the much larger part of the visible matter. This is another piece of evidence for the existence of Dark Matter.

**3. The uniformity of the Cosmic Microwave Background (CMB) radiation.** The Standard Model of Cosmology has been confirmed by important observations, such as the expansion of the Universe, the abundance of light elements synthesized during the first minutes, and the Cosmic Microwave Background, an intense thermal radiation field created around 300 000 years after the Big Bang when neutral atoms formed. The abundance of helium ( $^3\text{He}$  and  $^4\text{He}$ ), lithium and deuterium,

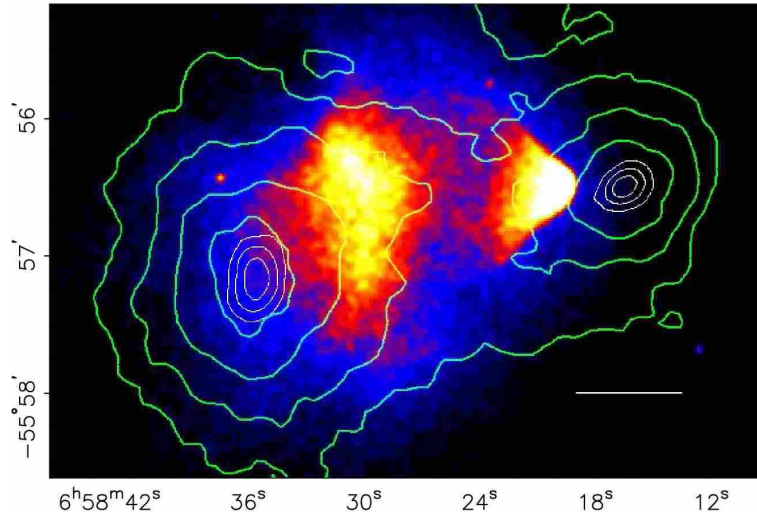


**Figure 1.2:** The interaction of galaxy clusters [31]: The green lines represent the area of same gravitational potential, the colors show the X-ray emitting plasma, which represents the biggest part of the seen matter. The gravitational potential traces the collisionless stellar component, and not the dominant baryonic matter, the X-ray emitting plasma. This gives clear evidence of Dark matter.

predicted by the Big Bang Nucleosynthesis (BBN), agrees remarkably with the observations. Furthermore, the BBN sets stringent constraints on the baryonic energy density of the Universe [113] of

$$0.018 \leq \Omega_b h^2 \leq 0.023 , \quad (1.2)$$

where  $\Omega_b$  is the baryonic energy density  $\varrho_b$  given as a fraction of the critical energy density  $\varrho_c$

$$\Omega_b = \frac{\varrho_b}{\varrho_c} . \quad (1.3)$$

The critical energy density is the necessary energy density for a flat Universe

$$\varrho_c = \frac{3 H^2}{8 \pi G_N} , \quad (1.4)$$

where  $G_N$  is Newton's gravitation constant. The Hubble parameter  $H$  describes the proportionality between the distance  $D$  and the recession velocity  $v$  of a galaxy

$$v(t) = H(t) D(t) . \quad (1.5)$$

According to recent observations [95], the Hubble constant  $H_0$ , where the subscript 0 describes the present day value, amounts to

$$H_0 = 3.2 \cdot 10^{-18} h s^{-1} , \quad (1.6)$$

where  $h$  takes into account the measurement uncertainties of  $H_0$  and amounts to  $0.65 \pm 0.15$ . The cosmological models that fit the isotropy of the CMB predict  $\Omega_0=1$ . The total energy density of the Universe  $\rho_{tot}$  is made up of

$$\rho_{tot} = \rho_m + \rho_r + \rho_\lambda , \quad (1.7)$$

where  $\rho_m$ ,  $\rho_r$  and  $\rho_\lambda$  are the contributions from matter, radiation and perhaps from vacuum energy (cosmological constant, dark energy). The matter density consists of

$$\rho_m = \rho_b + \rho_{DM} , \quad (1.8)$$

where  $\rho_B$  and  $\rho_{DM}$  are the baryonic and the DM energy density.

The CMB spectrum and its almost isotropic distribution enable to evaluate the contributions of the baryonic matter, dark (non-baryonic) matter and dark energy to the total energy density in the Universe. From analysis of very exact measurements of the CMB (WMAP [128], COBE [99]), the following values were found for baryons and matter in the Universe

$$\Omega_b h^2 = 0.024 \pm 0.001 , \quad (1.9)$$

and

$$\Omega_M h^2 = 0.14 \pm 0.02 . \quad (1.10)$$

This is consistent with the predictions of BBN given by equation (1.2)

One contribution to non-baryonic matter are neutrinos. With a mass of  $0.1 \text{ eV}/c^2$  [49], neutrinos could contribute as much to the total mass density of the Universe as the visible stars do. However, this is not enough to account for the whole DM alone. Also, simulations based on the Big Bang Cosmology (BBC) with neutrinos as DM do not correspond with the actual formation of the Universe. Because neutrinos are very light, they were relativistic at the time when structures started to form. Therefore, neutrinos account for hot Dark Matter (HDM). HDM would lead to a top-down formation of the Universe, where large structures break into smaller. Such behavior is not supported by observations, and therefore neutrinos can contribute only a small part to  $\Omega_M$ .

Weakly Interacting Massive Particles (WIMPs) are the main candidates for non-baryonic DM. Due to the massiveness, WIMPs would have been non-relativistic at the time of decoupling and therefore would now behave as cold Dark Matter (CDM), which agrees with the hierarchical formation of the Universe. The supersymmetric extension of the Standard Model provides the main WIMP candidate, the lightest supersymmetric particle (LSP) which is usually the lightest neutralino  $\chi$ . The

conserved quantum number and the R-parity (required to prevent the decay of protons), renders the LSP stable. In the Minimal Supersymmetric Standard Model (MSSM) the LSP is a mixture of the supersymmetric partners of the photon, the Z and the Higgs bosons .

To determine the contribution of neutralinos to  $\Omega_M$ , one has to calculate the time when they decoupled from the baryonic matter. In the early era of the Universe the different particles were in thermal equilibrium. To maintain this equilibrium, the interactions had to be frequent enough. The rate of interaction per particle  $\Gamma$  is given by

$$\Gamma = n_\chi \sigma v , \quad (1.11)$$

where  $n_\chi$  is the number density of  $\chi$  particles,  $\sigma$  is the cross section and  $v$  is the velocity. In an expanding Universe the critical time scale is set by the Hubble parameter  $H$ . Because the particles are weakly interacting, chemical decoupling<sup>3</sup> of these particles occurs when the interaction rate equals the Hubble expansion rate  $H$

$$\Gamma = n_\chi \langle \sigma_A v \rangle \sim H \quad (1.12)$$

where  $\sigma_A$  is the annihilation cross section,  $v$  is the velocity and the brackets denote thermal equilibrium. The approximate contribution from a massive particle  $\chi$  to  $\Omega_M$  is given by [60, 123]

$$\Omega_\chi h^2 \approx \frac{3 \cdot 10^{-27} \text{ cm}^3 \text{ s}^{-1}}{\langle \sigma_A v \rangle} . \quad (1.13)$$

Hence,  $\Omega_\chi$  depends mainly on the particle's annihilation cross section and not on its mass (to logarithmic accuracy). When interaction of the particles is weak, the annihilation cross section is

$$\langle \sigma_A v \rangle \sim \frac{g^2}{m_W^2} , \quad (1.14)$$

where  $g$  is the coupling strength and  $m_W$  is the weak scale. With typical numbers of  $g \sim 0.01$  and  $m_W \sim 100 \text{ GeV}$ , one derives a value for  $\langle \sigma_A v \rangle \sim 10^{-25} \text{ cm}^3 \text{ s}^{-1}$ . Therefore, a stable weakly interacting massive particle which was in thermal equilibrium in the early Universe will have an interesting present day density  $\Omega_\chi$  of

$$\Omega_\chi = \frac{\rho_\chi}{\rho_c} \cong 1 \quad (1.15)$$

Different WIMP candidates can also be found in various other models, for example the Non-minimal Supersymmetric Standard Model. This model provides gravitinos and axions in addition to neutralinos as possible WIMPs.

---

<sup>3</sup>also referred to “freeze-out”

An alternative theory, not requiring DM, tries to explain the astrophysical observations by modifications of the gravitational force law [23, 30] (e.g.: MOdified Newtonian Dynamics - MOND) or the particles response to it [106]. However, recent indirect detection of DM during the merge of galaxy clusters, discussed above, makes an alteration of Newtonian gravitation doubtful. The observations cannot be explained by a modification of the law of gravitation and prove the existence of DM with a much larger mass than the visible one, as was described above.

The discovery of WIMPs can be attempted by the following 3 main classes of methods:

- Direct detection
- Indirect detection
- Production in collider experiments

The rate for direct detection of galactic neutralinos, integrated over deposited energy assuming no energy threshold, is given by

$$R = N_A n_\chi \langle \sigma_{A\chi} v \rangle \quad (1.16)$$

where  $N_A$  is the number of nuclei in the detector,  $n_\chi$  is the local galactic neutralino number density,  $\sigma_{A\chi}$  is the neutralino-nucleus elastic cross section, and the angular brackets denote an average over  $v$ , the neutralino speed relative to the detector [24].

The direct detection can be accomplished via the elastic scattering by detector nuclei. The interaction between WIMP and nucleus can be either spin-independent (scalar) or spin-dependent (axial-vector). Most current (and planned future) experiments use heavy targets (Na, Cs, Ge, I or Xe) for which spin-independent coupling dominates [62] due to the enhancement caused by the coherence of the wavelets scattered off all nucleons in the target nucleus.

The spin-independent elastic neutralino-nucleus differential cross section depends quadratically on the number of neutrons in the target nucleons and is given by [41]

$$\sigma_{A\chi} = \frac{4 m_{A\chi}^2}{\pi} [Z f_p + (A - Z) f_n]^2, \quad (1.17)$$

where  $Z$  is the number of protons,  $A$  is the number of nucleons and  $m_{A\chi}$  is the reduced neutralino mass given by

$$m_{A\chi} = \frac{m_\chi m_A}{m_\chi + m_A}, \quad (1.18)$$

where  $m_A$  is the mass of a detector nucleus and  $m_\chi$  that of the neutralino. The factors  $f_p$  and  $f_n$  take into account model specific parameters. Further information is given in [42].  $\sigma_{A\chi}$  depends by  $A^2$  on the mass number of the target material, which makes the use of heavy target nuclei advantageous.

The differential scattering rate per unit time and unit recoil energy  $E_R$  is given by

$$\frac{dR}{dE_R} = N_A n_\chi \int d^3v f(\vec{v}) v \frac{d\sigma_{A\chi}}{dE_R}(v, E_R), \quad (1.19)$$

where  $E_R$  is the recoil energy of the target nucleus. From the kinematics the minimum speed  $v_{min}$  that can cause a nuclear recoil energy  $E_R$  is given by

$$v_{min} = \sqrt{\frac{E_R(m_A + m_\chi)^2}{m_A m_\chi^2}}. \quad (1.20)$$

$E_R$  is given by

$$E_R = \frac{m_{A\chi}^2 v^2 (1 - \cos \theta^*)}{m_A}, \quad (1.21)$$

where  $\theta^*$  is the scattering angle in the center of mass frame. The recoil energy spectrum depends on the detector material and on the mass of the neutrino. The differential rate for different target materials with  $m_\chi=100 \text{ GeV}/c^2$  is shown in Figure 1.3. For a low mass  $m_\chi$  the spectrum is steeply falling with  $E_R$ , whereas a high mass  $m_\chi$  results in a flat decline. The actual event rate in a detector is derived by multiplying equation (1.19) by the detector mass and the exposure time. With a neutrino-nucleon cross section  $m_{i\chi} < 10^{-7} \text{ pb}$ , the expected event rates are  $< 1 \text{ event}/100 \text{ kg/day}$ .

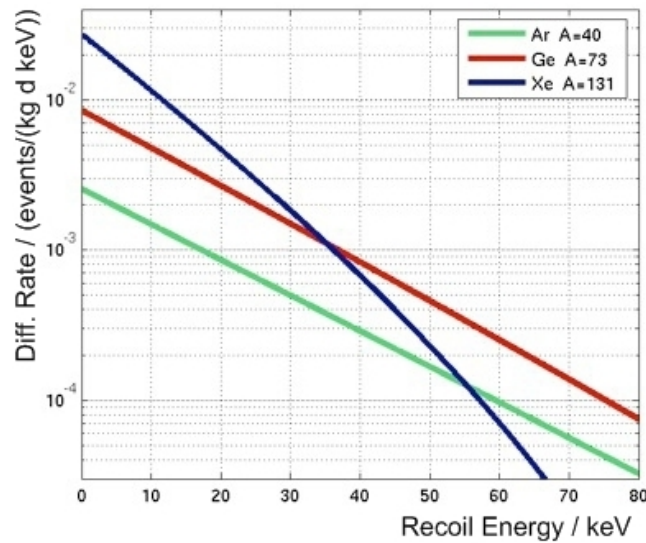


**Figure 1.3:** The differential rate for various target materials with the mass  $m_\chi=100 \text{ GeV}/c^2$  [17].

Indirect WIMP detection can be achieved via detecting annihilation products, e.g. gamma-rays, positrons, anti-protons or neutrinos, discussed in the review by Jungmann, Kamionkowski & Griest [79]. WIMPs with very low velocity are gravitationally captured by the earth or the sun. They then annihilate and produce energetic neutrinos, which escape and can be detected using neutrino telescopes. Also, gamma-rays can be observed in the galactic center, in substructures within the halo and in the diffuse emission. Anti-matter could give evidence of the “local” DM distribution, at a distance of roughly 1 kpc ( $\simeq 3.1 \cdot 10^{16}$  km).

Finally, the accelerator-search for WIMPs can be performed in colliders, e.g. the LHC [44]. Because WIMPs are weakly interacting, they stream out without being seen by the detectors. Therefore, the generic signal would be a missing energy and momentum, transverse to the beam direction. As the possible events are difficult to distinguish from background, one looks in addition for jets in excess to what is expected from the SM [14]. In SUSY models, decays of gluinos and squarks produce invisible WIMPs and energetic quark and lepton jets. Although the production and detection of WIMP-like particles in colliders would be very exciting, it would not prove that the produced particles have a lifetime greater than the age of the Universe and that they dominate the DM.

## 1.2 The EURECA Collaboration and Experiment

EURECA stands for European Underground Rare Event Calorimeter Array. The EURECA collaboration is composed of the members of the CRESST [11], EDELWEISS [125, 126] and ROSEBUD collaborations and individuals at CERN and in a few European institutes. The aim of the collaboration is to design, build and operate a cryogenic detector array with a target mass of several 100 kg at an European underground laboratory to search for Dark Matter particles in the Galactic halo.

The EURECA experiment is aiming at directly detecting WIMPs and to study their properties, or to set considerably stricter exclusion limits. The sensitivity should be improved by two orders of magnitude over the current systems in operation, as shown by Figure 1.4, which use cryogenic and noble liquid targets. EURECA intends to explore a region of the elastic nucleon scattering cross section of  $10^{-9}$  pb in the beginning and of  $10^{-10}$  pb [86] with further improvements. Although it is optimized for finding the WIMP, it will also be capable to detect other types of DM particles.

As a site for EURECA, the Laboratoire Souterrain de Modane (LSM) has been chosen. The LSM lies under the 2900 m high Frejus peak at the border between Italy and France, in the deepest labora-

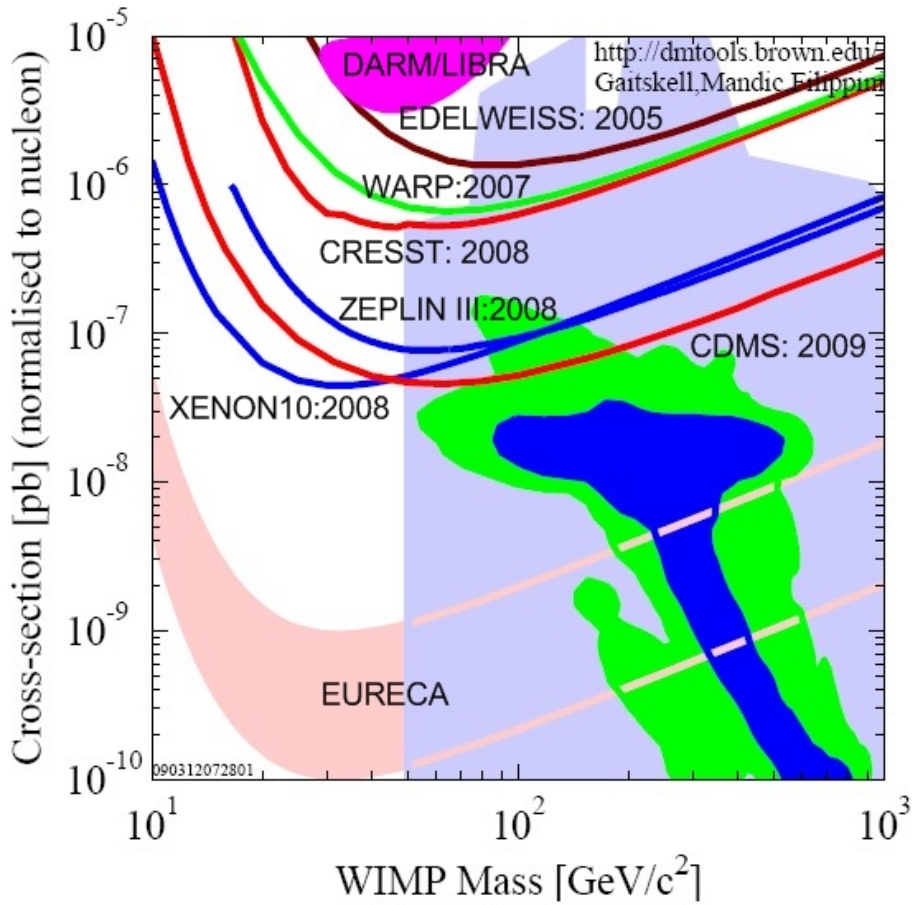


**Figure 1.4:** Exclusion plot showing the targeted sensitivity of EURECA.

tory of Europe and the second deepest of the world. The site has been chosen for its central location in Europe, with an independent, horizontal access and for having more than 20 years experience in running such a facility [53]. The Italo-French intergovernmental agreement of 2006 to build a safety gallery parallel to the existing road tunnel enables the collaboration to integrate the construction of a specially designed site for the needs of EURECA in connection to the LSM laboratories at a moderate cost of 15 million Euros [53]. Two additional caverns, MEGATON and ULISSE (Underground Large Infrastructure for Super Shielded Experiments) will be excavated. The latter one is being designed in close co-operation with the EURECA collaboration in view of implementing the highly radio-pure shielding from the beginning. Radio-pure refers to a materials purity of radioactive components both from radioactive contaminations and from radioactive isotopes of the same material.

The recoil energy of elastic WIMP-nucleus scattering is below a few tens of keV [86] as shown in Figure 1.3. Also, given the low WIMP cross section of equation (1.17), the event rate in one ton of active detector material is expected to be a few events per year only [86], based on equa-

tion (1.19). Therefore, the background rate has to be of the same order or smaller than that, about 1 event/ton/year. This requires ultra-low background from radioactivity, as well as superior shielding and discrimination from cosmic radiation and spallation neutrons due to interactions of muons with nuclei in the rock.

EURECA is aiming to achieve a reduction in the background by 2 orders of magnitude over the phase II experiments of EDELWEISS and CRESST (details are given in Table 1.1). The underground laboratory offers the lowest possible muon-induced background with a depth of 4800 mwe (meters of water equivalent). The ultimately lowest possible level of background radiation will be determined by the radio-purity of the materials inside the shielding and close to the detector. A baseline design for the cryostat layout has been developed, which will be described in chapter 2, with tight control of every material and its quantity.

**Table 1.1:** Achieved and targeted event rates in European cryogenic DM experiments ([126], [125] and [11]). The goal of EURECA is an improvement of a factor of 100 in sensitivity [52]

<i>Experiment</i>	<i>Background</i>			<i>limit of WIMP-nucleus cross section (pb)</i>
	instrumental events at $E_R > 30$ keV ( $\text{kg}^{-1} \text{d}^{-1}$ )	simulated neutron events ( $\text{kg}^{-1} \text{d}^{-1}$ )	expected event rate at $E_R > 20$ keV ( $\text{kg}^{-1} \text{d}^{-1}$ )	
EDW I, CRESST I (current)	0.1	0.03	0.3	$1.5 \cdot 10^{-6}$
EDELWEISS II (targeted)	$< 0.002$	$< 0.002$	0.004	$2 \cdot 10^{-8}$
CRESST II (current)	-	0.083	0.063	$4.8 \cdot 10^{-7}$
EURECA (targeted)	$< 0.00001$	$< 0.00001$	0.00002 $\approx 7 \text{ events}/(\text{ty})$	$10^{-10}$

EURECA will use cryogenic calorimetric detectors that are able to discriminate between electron and nuclear recoil events down to below 10 keV. The detectors have a very low energy threshold because of the low excitation energy of phonons compared to that of charge carriers, which reduces

the relative statistical fluctuations in the number of excitations. EDELWEISS and CREST have also demonstrated in the expected range of recoil energy a background rejection of  $10^{-5}$  based on the capability of discrimination between electron and nuclear recoils. The cryogenic temperatures significantly decrease the heat capacity of the detector material, resulting in a measurable temperature increase for a heat input of only a few keV by a scattered particle. Moreover, the thermal noise of the detector and of the cold electronics may decrease. Both lead to a higher signal to noise ratio.

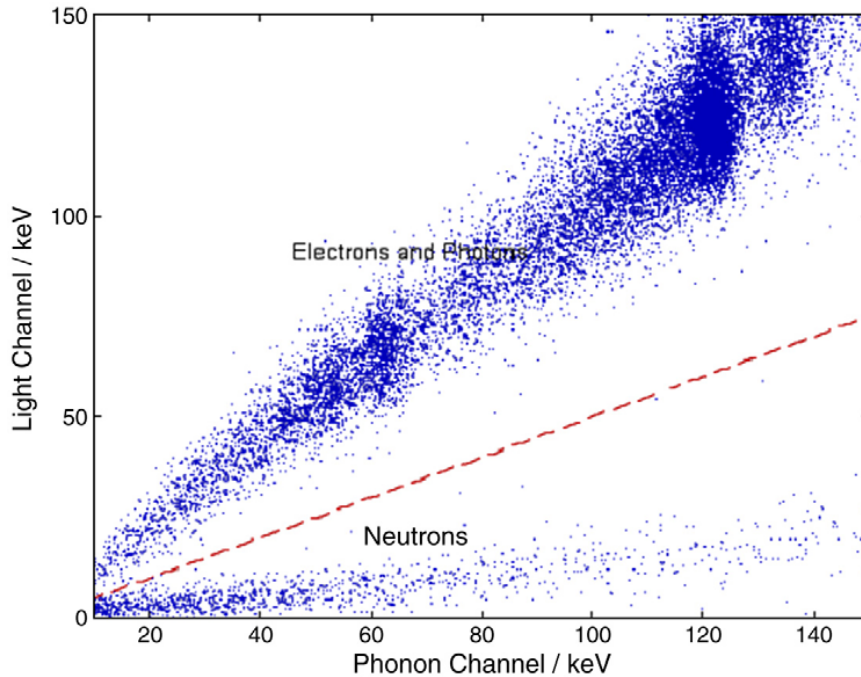


**Figure 1.5:** The experimental data of a CRESST prototype detector [78] that was irradiated by electrons and neutrons. The amount of light is plotted versus the energy of the phonon. The difference in scintillation efficiency between electron recoils and nuclear recoils can be used for the discrimination between WIMP-nucleus events and background events due to gammas and charged particles..

Given the expertise of EDELWEISS and CRESST, which are currently running independent DM search experiments, the detector material will most likely be germanium and calcium tungstate ( $\text{CaWO}_4$ ) in the beginning. In both, the temperature is monitored to determine the total energy deposition in the detector. To discriminate between nuclear and electron recoils, the germanium detectors simultaneously record the charge signal [125], while the  $\text{CaWO}_4$  detectors measure the scintillation light [10]. The ratio of charge or light to the phonon signal provides an efficient discrimination method. Figure 1.5 shows the experimental data of a CRESST prototype detector [78] that was irradiated by electrons and neutrons, which are scattered by nuclei very similarly to WIMP's.

Other target materials are also studied [36, 104, 105] and are foreseen to be used. The use of different target materials is an important feature of EURECA, as this will help to determine the mass and the weak interaction parameters of the WIMP [87].

Figure 1.6 shows the various techniques proposed for the direct detection of the WIMPs in the halo of the Galaxy. In addition to the cryogenic solid detectors discussed above, several collaborations are operating detectors based on liquefied noble gases, where the discrimination between electron and nuclear recoils is based on the ionization and light signals in a strong electric field.

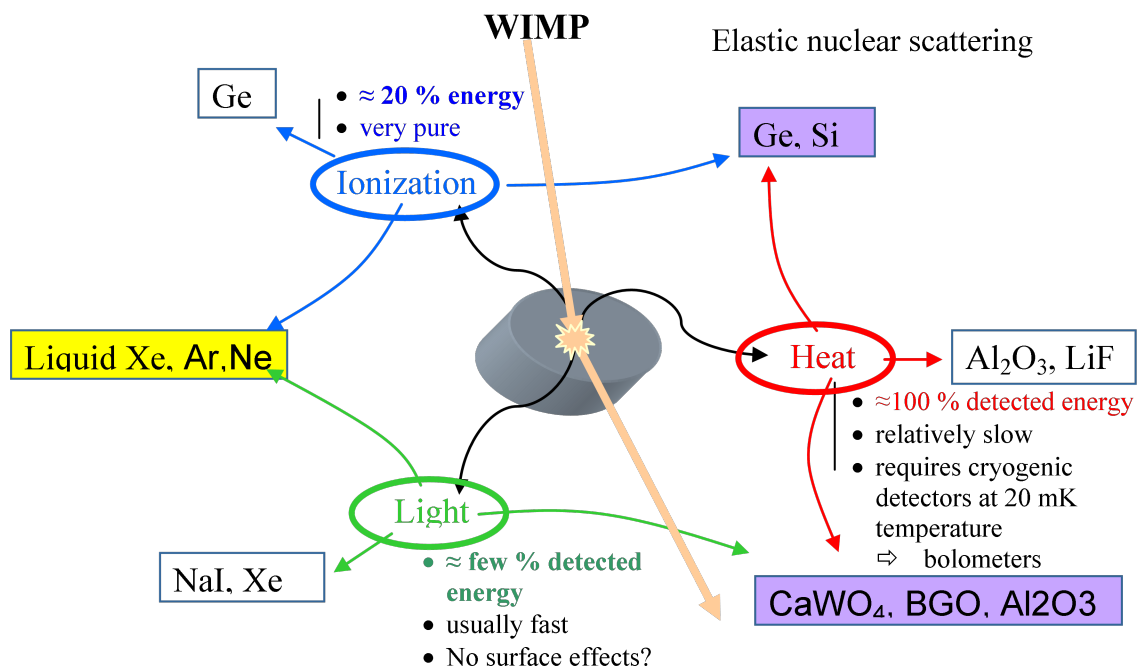


**Figure 1.6:** Direct detection of WIMPs is possible by combined monitoring of two of the following three parameters: temperature, ionization and light.

The detector material will be modularly arranged in arrays of small units. Currently EDELWEISS uses germanium detectors with a mass of 320 g, which would require more than 3000 detector modules for the targeted 1 t detector mass projected for EURECA. Therefore, larger modules (1 kg to 3 kg) with a different geometry are favored, as this could improve the sensitivity substantially [87]. Yet the detector mass will consist of several hundred single detectors. In addition to the modularity, this arrangement provides self-shielding of the detector. It allows the discrimination of a nucleon recoil by residual neutrons from that by a WIMP. Neutrons passing through several detector modules will produce several coincident recoils, whereas a WIMP will induce only a single recoil event. For this reason it is necessary to pack the detectors closely, so that a neutron cannot hit exclusively one

single detector element.

Each of the detector modules will be equipped with a number of sensors. For temperature measurement either superconducting Transition Edge Sensors (TES) or high-impedance thermistors, e.g. Neutron Transmutation Doped thermistors (NTDs) will be used. Both are optimized to achieve a high sensitivity in a narrow temperature region. Because of the large number and the demanding production process of the detectors, the fabrication has to be planned well in advance. For example the NTD sensors require 2 years of “cooling” after the neutron radiation. Moreover, the size of the NTD sensors has to be optimized for the planned operating temperature, in view of the size dependence of the field effect and of the electron-phonon thermal resistance. Also, the production of a single  $\text{CaWO}_4$  detector crystal takes about one week at the current rate. The sequential production of all modules needed for EURECA would take 60 years, obviously raising the need for parallel mass production.

### 1.3 The CERN Cryolab Dilution Refrigerator (CCDR)

A dilution refrigerator will be used to cool EURECA’s detector array to a temperature of 10 mK. This is the only refrigeration technique at such low temperature which can operate continuously. To study important features, such as the scaling of the residual heat loads and the heat transfer at lowest temperatures, the CERN Cryolab Dilution Refrigerator (CCDR) was designed and built at the CERN Central Cryogenic Laboratory.

The mechanical layout of the cryostat with the helium pumps, the  $^3\text{He}$ -rack, the helium tanks and the helium Dewar, as well as the design of the dilution refrigerator has been described elsewhere [142]. Only minor changes were conducted to the mechanical system which will be briefly described below.

The filtering ability of the liquid nitrogen trap was improved. The autonomy of the trap was enhanced by the use of a 36 L nitrogen dewar<sup>4</sup>. The helium counter flow heat exchanger for pre-cooling the  $^3\text{He}$  was also improved. Previously, the  $^4\text{He}$  flow for precooling was throttled by a flow control valve, commanded by a PC. In order to be independent from the limited reliability of the computer, the pre-cooling flow is now controlled by a variable-speed membrane pump<sup>5</sup>. The feedback signal to the compressor is calculated from the signals of the  $^3\text{He}$  and  $^4\text{He}$  flowmeters by

---

<sup>4</sup>BIO 36, Statebourne Cryogenics [35]

<sup>5</sup>KNF Neuenberger

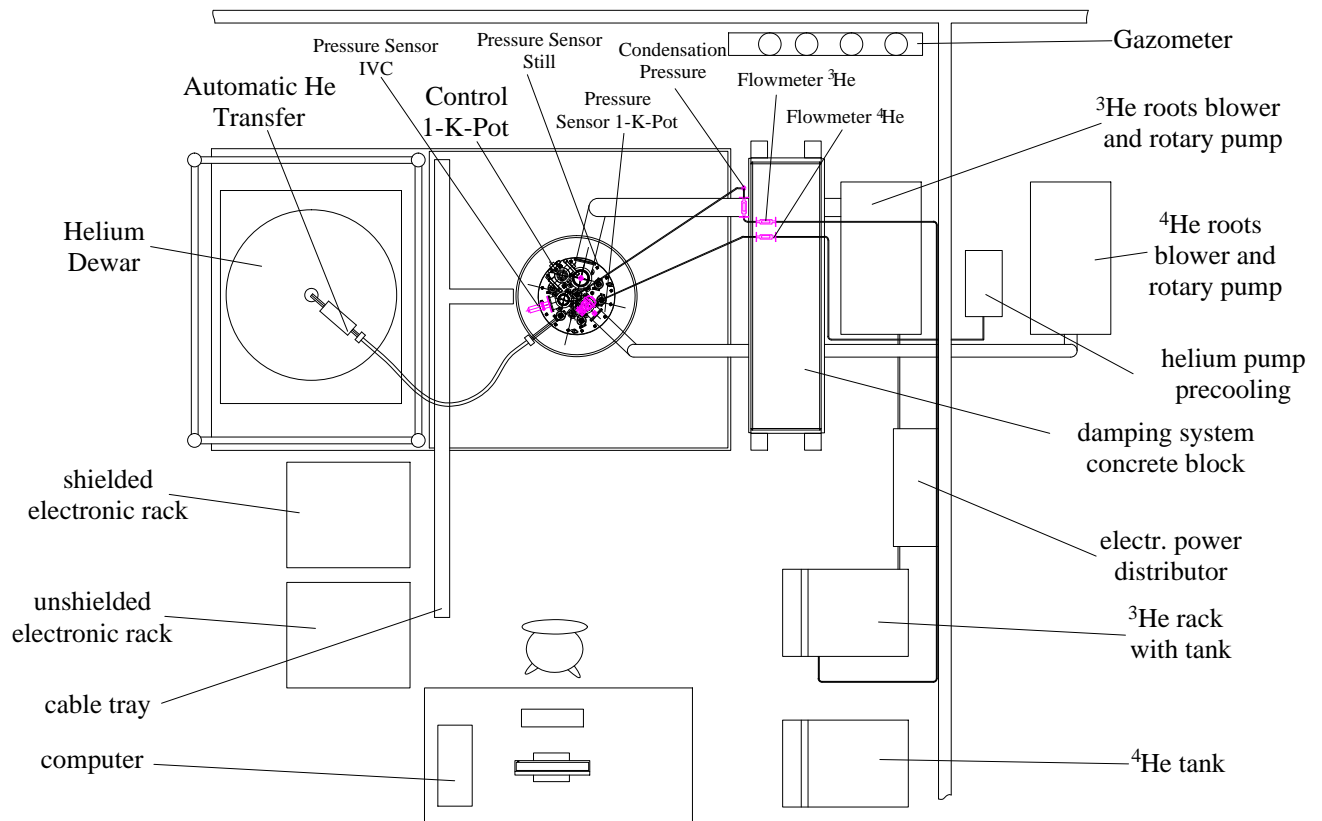


**Figure 1.7:** Layout of the CCDR system.

an analog circuit. The control voltage between 0.5 V and 2.6 V is determined by an analog PID controller<sup>6</sup>, according to the  $^3\text{He}$ -flow with an adjustable offset of 1 mmol/s.

After the primary  $^3\text{He}$  pump broke, it was substituted by a similar hermetically sealed rotary vane pump<sup>7</sup>. It features an internal oil pump for pressure lubricated bearings and a comparable volume flow rate of 65 m<sup>3</sup>/h.

The position of the operator was chosen to ensure optimum control over the system at all times. While working on the computer it is now possible to have a good sight of the analogue pressure gauges of the  $^3\text{He}$  rack on the left hand side and of the electronic racks on the right hand side. The dilution refrigerator located in the back is easily accessible for occasional maintenance work.

The electronic setup was redone completely and will be described in chapter 3. The measurement of ultra low temperatures is very often as difficult as attaining the temperature itself [115]. The electromagnetic environment in laboratories is often heavily polluted with frequencies from 50 Hz to 2.5 GHz by digital devices found in almost all products. At high frequencies even conductors of very

<sup>6</sup>Signal Calculator PR-electronics, Type:2289

<sup>7</sup>Leybold Vacuum Triviatic B, D 65 B

short length can be major sources of ElectroMagnetic Compatibility (EMC) problems. A conductor (wire, open cable shield) with the length of  $\lambda/4$  is an efficient antenna at its resonant frequencies [12]. It converts the signals it carries at these frequencies into an electric field, which is then radiated. Also, it picks up electric fields and the electric field components of electromagnetic fields. Both lead to a loss in the Signal Integrity (SI) and to emission and immunity problems. Ideally, a shielded room should be used to avoid ElectroMagnetic Interferences (EMI). As this is not available, strict EMI control design rules were applied to reduce the self-heating of the thermometers and to reach the required sensitivity for the temperature measurement well below 10 mK. The applied underlying design principles and guidelines are discussed below.

The EMC design techniques for metal conductor interconnections are concentrated on controlling the differential-mode (DM) and common-mode (CM) current paths. Desired signals are always DM, they flow along the send conductor, and flow back along the return conductor. CM currents flow out at the same time on the send and return conductors. They return via another route, often the protective (safety) earth structure and/or the electrical power distribution network. CM currents and voltages are associated with the accidental 'leakage' of DM signals due to stray capacitance/inductance and from interfering with external fields. The conversion of DM into CM and the reverse process, the conversion of CM to DM currents and voltages always happens in any real-life circuit. In most applications it is responsible for most EMC emission/immunity problems above about 1 MHz.

The rate of DM-CM conversion (and CM-DM) can be reduced by using a dedicated conductor for the sent and returned current and route them together as a twisted pair. With a twist-pitch much less than one-tenth of a wavelength at the highest frequency of concern, the effects of stray capacitances and inductances tend to cancel out. However, unavoidable imbalances in the physical realizations of cables cause CM noise voltages and currents to arise.

Due to the existence of DM and CM signals and noises, it is necessary to apply filtering to both of them. Below 1 MHz, filtering DM signals and noise is the main concern. At higher frequencies filtering of DM is applied in order to reduce the amounts of RF present in conductors. This also reduces the amount of CM noise currents and voltages created by their imbalances. CM filtering can be used to reduce the residual CM noise.

The return-current, associated with a given signal power sent in a conductor, takes always the path of least impedance. At frequencies below a few kHz the impedance is dominated by resistance, whilst at higher frequencies it is dominated by inductance. At low frequencies the return-currents will

tend to flow mostly in the RF reference plane. The higher the frequencies, the more they will flow in the return conductors that are physically closest to their send-conductors. This behavior results in the best crosstalk and best EMC that is possible given a particular conductor structure. To achieve this, it is necessary to provide lower-impedance return paths.

Shielding is used to attenuate unwanted frequencies traveling through the air and is characterized by attenuation versus frequency curves. A shield puts an impedance discontinuity in the path of a propagating radiated EM wave, reflecting it and/or absorbing it. Depending on the impedance of the shield structure, a portion is reflected. The remainder continues inside the shield as a transmitted wave, being absorbed by the resistivity of the material and thereby converted into heat.

## 1.4 Kapitza Resistance and Sintered Heat Exchangers

Heat exchangers are critical in a dilution refrigerator, both for maximizing the cooling power of the DR, and for the heat transfer from the thermal load to the helium in the Mixing Chamber (MC). The cooling power of a DR in continuous mode depends upon the  $^3\text{He}$  flow rate  $\dot{n}_3$  and the enthalpies  $H_D(T_m)$  and  $H_C(T_0)$  of the saturated dilute phase at the temperature  $T_m$  and of the concentrated stream at the outlet temperature  $T_0$  of the heat exchanger, and is given by

$$\dot{Q}(T_m, T_0) = \dot{n}_3 [H_D(T_m) - H_C(T_0)] . \quad (1.22)$$

The concentrated  $^3\text{He}$  is precooled by means of a sintered heat exchanger and therefore the cooling power is critically dependent on an efficient heat transfer.

For very small  $\dot{n}_3$ ,  $T_0$  will be very near to  $T_m$ . When increasing the flow rate a little while holding  $T_m$  constant, the cooling power will increase linearly with  $\dot{n}_3$ , assuming constant inlet temperature into the heat exchanger  $T_s$  and  $^4\text{He}$  mole fraction  $X_4$  in the concentrated stream. Increasing the flow rate further will decrease the enthalpy difference because  $T_0$  will rise. This is due to a larger necessary temperature difference in the heat exchanger to transfer the larger quantity of heat. At even higher flow rates a maximum  $Q_m$  will be reached, after which the heat exchanger cannot transfer the heat efficiently anymore and the cooling powder will decrease. The maximum of  $Q_m$  is calculated by  $d\dot{Q}_m/d\dot{n}_3|_{T_m, T_s, X_4} = 0$ , solving for  $\dot{n}_3$  one derives

$$\dot{n}_3 = \frac{H_D(T_m) - H_C(T_0)}{C_c(T_0)(dT_0/d\dot{n}_3)|_{T_m, T_s, X_4}} . \quad (1.23)$$

Considering the characteristics of a continuous heat exchanger, Niinikoski [134] derived

$$C_c(T_0)(dT_0/d\dot{n}_3)|_{T_m, T_s, X_4} = \frac{\sigma \alpha(T_0)}{\dot{n}_3^2}, \quad (1.24)$$

where  $\alpha(T_0)$  is the heat transfer parameter between the dilute and the concentrated stream. Substituting equation (1.24) in the equations (1.22) and (1.23), one obtains the important results for the optimum flow rate and the maximal cooling power [134]

$$\text{opt}\{\dot{n}_3\} = \frac{\sigma \alpha(T_0)}{H_l(T_m) - H_c(T_0)} \quad (1.25)$$

and

$$\max\{\dot{Q}_m(T_m)\} = \sigma \alpha(T_0). \quad (1.26)$$

The above equations (1.25) and (1.26) show that the maximum cooling power of the DR scales directly with the thermal conduction between the warm and cold streams of the main heat exchanger. Because this conduction is dominated by the product of the reduced thermal boundary conductance  $\alpha(T_0)$  and the total surface area of the boundary  $\sigma$  in the concentrated stream, we have developed in this work new methods to extend the heat exchanger surface area and to improve the thermal boundary conductivity.

When transferring heat from an external thermal load at a temperature  $T_{hl}$  to the helium in the MC, for a given heat load  $\dot{Q}$  a heat exchanger reduces the temperature difference  $\Delta T = T_{hl} - T_m$

$$\Delta T = \dot{Q} R \cong \dot{Q} \frac{1}{\sigma}, \quad (1.27)$$

where  $R$  is the thermal resistance which is depending on the heat exchanger. For a required  $T_{hl}$ ,  $T_m$  is higher, which increases the cooling power of a dilution refrigerator as described by equation (1.22). With an increased thermal resistance the DR has to achieve the cooling power at a lower temperature  $T_{He}$ .

Heat exchangers made of sintered metal powder are necessary to overcome the very large Kapitza resistance. At low temperatures, there is a high thermal boundary resistance, which was first discovered and explained by Kapitza [80] as an acoustic mismatching between liquid helium and a solid. The acoustic mismatch theory has later been formulated by Khalatnikov [102] and Little [100].

At the boundary between liquid helium and a metal the heat transfer is dominated by phonons. The sound waves of acoustic phonons obey the rules for reflection and transmission at the boundary. The critical angle, at which phonons from the liquid helium enter the solid is

$$\alpha_l^c = \arcsin\left(\frac{v_l}{v_s}\right), \quad (1.28)$$

where  $v_l$  and  $v_s$  are the velocities of sound in the liquid and the solid. With numerical values for liquid  $^3\text{He}$  ( $v_l = 238$  m/s) and  $^4\text{He}$  ( $v_l = 183$  m/s) and a typical value for a solid ( $v_s = 5000$  m/s),  $\alpha_l^c$  is found to be  $< 3^\circ$ . Thus, the fraction  $f$  of phonons entering the solid is

$$f = \pi \sin^2 \alpha_l^c / 2\pi = \frac{1}{2} \left( \frac{v_l}{v_s} \right)^2. \quad (1.29)$$

With numerical values, one finds  $f < 10^{-3}$ . The actual number is even further reduced and depends upon the transmission coefficient  $t$ . With the acoustic impedances  $Z_l = \rho_l v_l$  and  $Z_s = \rho_s v_s$ ,  $t$  is calculated for a perpendicular incidence by

$$t = \frac{4 Z_l Z_s}{Z_l + Z_s} \cong \frac{4 Z_l}{Z_s} = \frac{4 \rho_l v_l}{\rho_s v_s}. \quad (1.30)$$

With the density of copper  $\rho_s = 9$  g/cm<sup>3</sup> and  $\rho_l = 0.145$  g/cm<sup>3</sup> for liquid  $^4\text{He}$  and  $0.082$  g/cm<sup>3</sup> for liquid  $^3\text{He}$ ,  $t \cong 2 \cdot 10^{-3}$  for  $\alpha_l < \alpha_l^c$ . Therefore, with equation (1.29) and (1.30), the fraction of phonons actually entering the solid is  $tf < 10^{-5}$ .

The energy density of all longitudinal phonons in the liquid is

$$\frac{E}{V} = \frac{4 \pi^5 k^4 T^4}{15 h^3 v_l^3}. \quad (1.31)$$

The heat transfer rate from the helium to the solid via a surface area  $\sigma$  is

$$\dot{Q}_1 = \frac{1}{2} f t \left( \frac{E}{V} \right) v_l \sigma = \frac{4 \pi^5 k^4 \rho_l v_l}{15 h^3 \rho_s v_s^3} \sigma T^4. \quad (1.32)$$

In thermal equilibrium this also corresponds to the energy transferred back to the helium. With the solid and the liquid helium at different temperatures  $T_1$  and  $T_2$ , the net flow of energy is given by

$$\dot{Q} = \dot{Q}_2 - \dot{Q}_1 = \frac{4 \pi^5 k_B^4 \rho_l v_l}{15 h^3 \rho_s v_s^3} \sigma (T_2^4 - T_1^4) = S \sigma (T_2^4 - T_1^4), \quad (1.33)$$

where  $S$  is the Kapitza conductance given by

$$S = \frac{4 \pi^5 k^4 \rho_l v_l}{15 h^3 \rho_s v_s^3}. \quad (1.34)$$

For a small temperature difference  $T_2 - T_1 = \Delta T \ll T_l$  the energy flow is

$$\dot{Q} = \frac{\delta \dot{Q}_1}{\delta T} \Delta T = \frac{16 \pi^5 k^4 \rho_l v_l}{15 h^3 \rho_s v_s^3} \sigma T^3 \Delta T \quad (1.35)$$

The Kapitza resistance is therefore given by

$$R_K = \frac{\sigma \Delta T}{\dot{Q}} = \frac{15 h^3 \rho_s v_s^3}{16 \pi^5 k^4 \rho_l v_l T^3} \quad (1.36)$$

and follows a  $T^3$  law. In principle, the theory is also applicable to an interface between two solids, if at least one is dielectric. However, the impedance for a solid is  $\rho v \sim 10^7 \text{ kgm}^{-2}\text{s}^{-1}$  and for liquid helium  $\rho v \sim 2 \cdot 10^4 \text{ kgm}^{-2}\text{s}^{-1}$ . Therefore, reflection is large and transmissivity is low between helium and solids. Consequently acoustic mismatching is then largest. It is usually the main resistance for heat transfer between bulk solids and liquid helium at temperatures below 1 K.

It has been found in several experiments that  $R_K T^3$  is approximately constant below 100 mK for an interface of copper and liquid helium as predicted by equation (1.36). It drops rapidly between 100 mK and 700 mK, to again be approximately constant above the latter value. The resistance is about the same (within a factor of three) for liquid  $^3\text{He}$ ,  $^4\text{He}$  and mixtures, as well as for different solids [101].

The basic theory described above does not correspond well with measurements around 1 K. Between 20 mK and 200 mK there is usually good agreement for annealed and most ideally prepared (polished) surfaces, both in the temperature dependence and in the absolute value. However, the Kapitza resistance is very sensitive to surface damage. Gentle wiping can decrease  $R_K$  by 30 %. A damaged surface decreases the Kapitza resistance by more than an order of magnitude. Also alloying copper (e.g with 0.6 % of chromium or 30 % of nickel) reduces the resistance by an order of magnitude. However, an oxide or sulfide layer does not change  $R_K$  significantly below 50 mK [101].

Below 20 mK agreement is lacking again, at these low temperatures usually very fine sintered structures are used, which show an unexpectedly low resistance and a temperature dependence of  $T^{-1}$  between metal and  $^3\text{He}$ , and  $T^{-3}$  between metal and dilute  $^3\text{He}$  in  $^4\text{He}$ . The reason for this discrepancy could be that the theory for bulk solids and bulk liquids is not applicable, because at low temperatures the excitations in metals and helium have wavelengths and mean free paths much larger than the dimension of the particles respectively pores. The heat transfer between fine sintered structures and a liquid He mixture is discussed in section 5.1.

Sintered pure copper or silver powder is commonly used in dilution refrigerators as heat exchanger because of their good thermal conductivity and the large surface area. Details are given in Table 1.2. For the highest cooling power at ultra-low temperatures, silver powder proved to be the best choice due to its availability in small grain sizes, as small as 100 nm in diameter. The surface area is inversely proportional upon the particle size and can be derived from the equation for the equivalent diameter [136]. The surface area  $\sigma$  per volume of the sinter  $V_{total}$ , depending upon the equivalent surface-to-volume diameter for mono-sized grains  $d'_K$ , and the fractional density  $V_S$  given

**Table 1.2:** Typical examples of sintered heat exchangers produced with powders of different metals [115].

<i>Material</i>	<i>Particle size</i> ( $\mu\text{m}$ )	<i>Fractional density</i> (1)	<i>Surface area</i> ( $\text{m}^2/\text{cm}^3$ )
Copper	20	0.5	1.3
Silver	0.3	0.45	19
Platinum	0.01	0.3	570

by equation (1.38) is

$$\frac{\sigma}{V_{total}} = \frac{6 V_S}{d'_K}, \quad (1.37)$$

The fractional density or filling factor is the ratio of grain volume  $V_{grain}$  and the total volume  $V_{total}$  of the sinter. It is given by the equation:

$$V_S = \frac{V_{grain}}{V_{total}} = \frac{\rho_{total}}{\rho_b}, \quad (1.38)$$

where  $\rho_b$  is the density of the bulk, void free material and  $\rho_{total}$  is the density of the sintered structure.

Platinum powder is available in even finer powder and accordingly a larger surface area is achievable. However, the author is not aware of any application of platinum in a DR due to the high material costs and its relatively low thermal conductivity compared to copper and silver.

As it would be difficult to transfer the large heat load of the EURECA detector array through long distances, the mixing chamber and the massive heat exchangers have to be placed close to the detector. Therefore, they also must meet the strict requirement of ultra low radioactivity. This makes the use of silver powder impossible<sup>8</sup>. Pure copper, on the contrary, satisfies the radio-purity requirements. Copper powder with a mesh size 325 ( $d < 44 \mu\text{m}$ ) has been used from the beginning of the development of dilution refrigerators and is still common today for high cooling power at higher temperatures ( $T > 20 \text{ mK}$ ). However, with the powders used so far it is impractical for transferring the necessary power at a sufficiently low temperature difference. Therefore, a large portion of the current work focused on optimizing the sintering parameters of a very fine copper powder and on investigating the thermal properties. The results of these studies are discussed in chapter 5.

---

<sup>8</sup>Silver is not available in radio-pure form, because it always contains some radioactive Ag isotopes generated by the neutrons of natural background radiation.

## Chapter 2

# Baseline Design of the EURECA Dark Matter Detector Array

In the frame of this work, a baseline design for the EURECA Dark Matter detector was developed, in accordance with the scientific requirements. The design will be discussed below. Sintered heat exchangers made of radio-pure copper powder are key components of this design. Therefore, a heat exchanger made of fine copper powder was characterized during this work and the results obtained are presented in chapter 5. Also, the reduction of the heat load at the lowest temperature is crucial for the design. For this reason, the residual heat load at temperatures down to 10 mK was studied. The experimental results are presented in chapter 4. The measurements were performed in the CCDR. To enable the necessary sensitivity at lowest temperatures, the electronic system had to be redone from scratch, implementing strict EMC design guidelines. The electronic setup is described in the next chapter.

### 2.1 Requirements for the Dilution Refrigerator

The mixing chamber has to deliver an estimated cooling power of 20  $\mu\text{W}$  [142]. Depending on the heat transfer coefficient, this cooling power has to be provided at a temperature considerably below that of the detector array, namely approximately 7 mK. The mass to be cooled to the lowest temperature consists of 1 t of detector material, as well as of the support structure for the detector array, the mixing chamber and the innermost heat shield. At intermediate temperatures, thermalizations for the

**Table 2.1:** Cryogenic requirements for the EURECA experiment.

<i>Requirement of temperature and cooling</i>	<i>Value</i>
Temperature of the detector crystals	10 mK
Temperature stability of the detector crystals	$\ll 1 \mu\text{K}$
Total cooling power	20 $\mu\text{W}$ at 7 mK
Temperature distribution of the detector towers	$< 1 \text{ mK}$

front end electronic are necessary, in order to enable low noise and high sensitivity measurements.

Each individual detector element is equipped with 6 to 10 sensors and several cables, depending upon the final detector design. The resulting constant heat leak leads to a temperature distribution within the array, which depends on the accumulated heat load and on the thermal conductivity of the support structure. For an efficient mass production of the several hundred to a few thousand detector modules, identical sensors and electronic modules should be used. Therefore, a narrow temperature distribution for all detector modules in the array is required, making a superior heat transfer of the cooling power crucial. The temperature of the mixing chamber has to be controlled precisely because the sensitive region of the temperature sensors is extremely narrow. A temperature variation of less than 1 mK is required. The cryogenic requirements are summarized in Table 2.1

The general requirements can be found in Table 2.2. The experiment is projected for a period of 10 years because the event rate is very low. The cryogenic system has to work reliably during this time. Although innovations are necessary to meet the requirements, the layout of the whole system should involve minimal design risks. All components such as pumps, compressors, cold boxes, etc. have to be chosen for low maintenance and high reliability. A high packing density of the detector elements is required to achieve self shielding. A fast neutron can be discriminated from a WIMP event by its multiple recoils along its trajectory. Therefore, a particle must not be able to hit exclusively one detector element only, apart from those on the outer shell. In order to use different detector materials, as well as the latest detector technology, it is desirable to exchange detector material. A rapid procedure is necessary to minimize the interruption time. Different possibilities were investigated in this work.

**Table 2.2:** General requirements for the EURECA cryogenic and cooling system.

<i>General Requirement</i>	<i>Impact on the design</i>
Projected experiment duration of approximately 10 years	- Reliable, low maintenance system - Remote, automatic control of the cryogenic system - Redundancy in case of failures of the cooling system
Total detector mass of 1000 kg	Offer space and mechanical support
Use of different types of detectors	- Flexible cooling interface - Rapid exchange of part of the detector material
Self-shielding of the detectors	Compact arrangement
Ultra low radioactivity of the immediate environment, reduction by a factor of 100 over current ULR-experiments	- Shielding - Use of radio-pure materials - Development of a suitable detector design
Short cabling for electronics	Shielded or radio-pure electronics
Cold front-end electronics	Thermalizations at intermediate temperatures
Compatibility of operation in a confined underground cave (safety and air conditioning)	- only helium as cryogenic fluids, no nitrogen - reduced amount of cryogenic fluids - availability of cooling, water and electrical power supply
Possibility to test detectors	Test cryostat required

## 2.2 Design Options for the EURECA Dilution Refrigerator

The influence of different cryostat designs on the detector arrangement is shown in Figure 2.1. The dimensions are derived from a single detector module with 320 g of germanium, similar to the one used for EDELWEISS, and have been scaled up to 1 t of detector mass. One module consists of the detector crystal itself and the copper support. A possible arrangement is to pile up the modules to columns. Seven columns are then arranged together to form one tower. Figure 2.1 shows three possible arrangements of the detector towers:

- 7 detector towers with a height of 1600 mm, arranged in a closest packed array inside a single large cryostat (on the left).

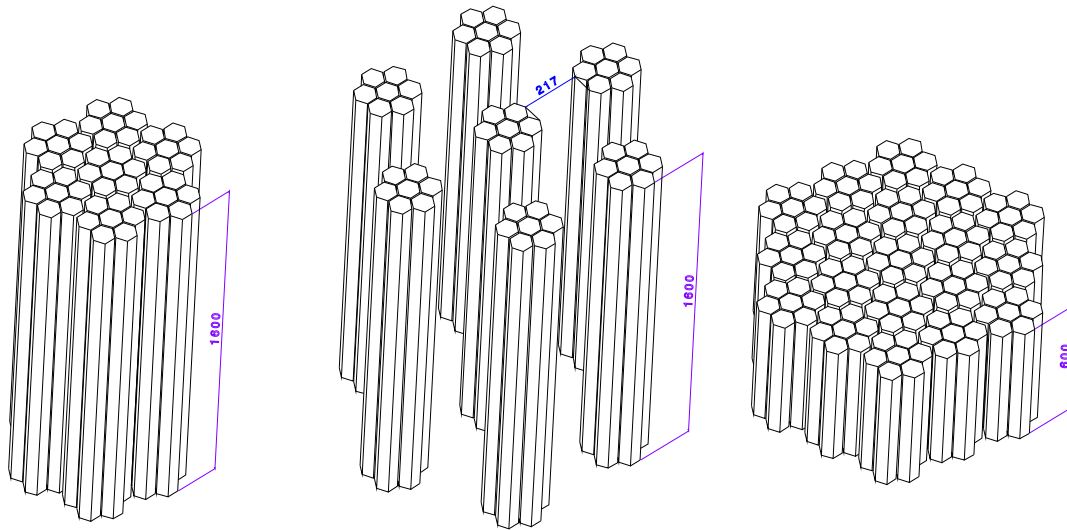


**Figure 2.1:** Comparison of detector arrangements. On the left are 7 detector towers with a height of 1600 mm, arranged in a close package like in a single large cryostat. In the middle, the package consisting of the 7 towers is shown when the single towers are mounted in 7 cryostats. On the right the arrangement of 19 detector towers with a height of 600 mm is shown.

- 7 detector towers, each using a separate smaller cryostat (in the middle).
- 19 detector towers with a height of just 600 mm (on the right).

The second option, of separate cryostats cooling one tower each, are shown in Figure 2.2. This design holds the advantage of distributing the heat load over a number of dilution refrigerators. Therefore, the cooling power would be achievable with state of the art cryostats using conventional technology. Regarding the use of different detector material, a standard design with integrated MC, still and 1 K pot would be the most flexible. Also the exchange of a part of the detector material would be feasible with basically no interference with the remaining detectors. The relatively small cryostats are easy to manufacture and economical to build as they present a large number of equal parts. It is simple to start measurements with a limited number of units, gain further experience and gradually increase the detector mass to the targeted 1 t.

A disadvantage is the detector arrangement, which obviously compromises self-shielding. It offers a multitude of paths for particles to interact with only one detector, decreasing the efficiency of the detector element. The great number of tubes connected to the cryostats would compromise any shielding around the detector array. The integrated still and 1 K pot are close to the detector inside the water shield, requiring a large number of different materials and connections. Meeting the

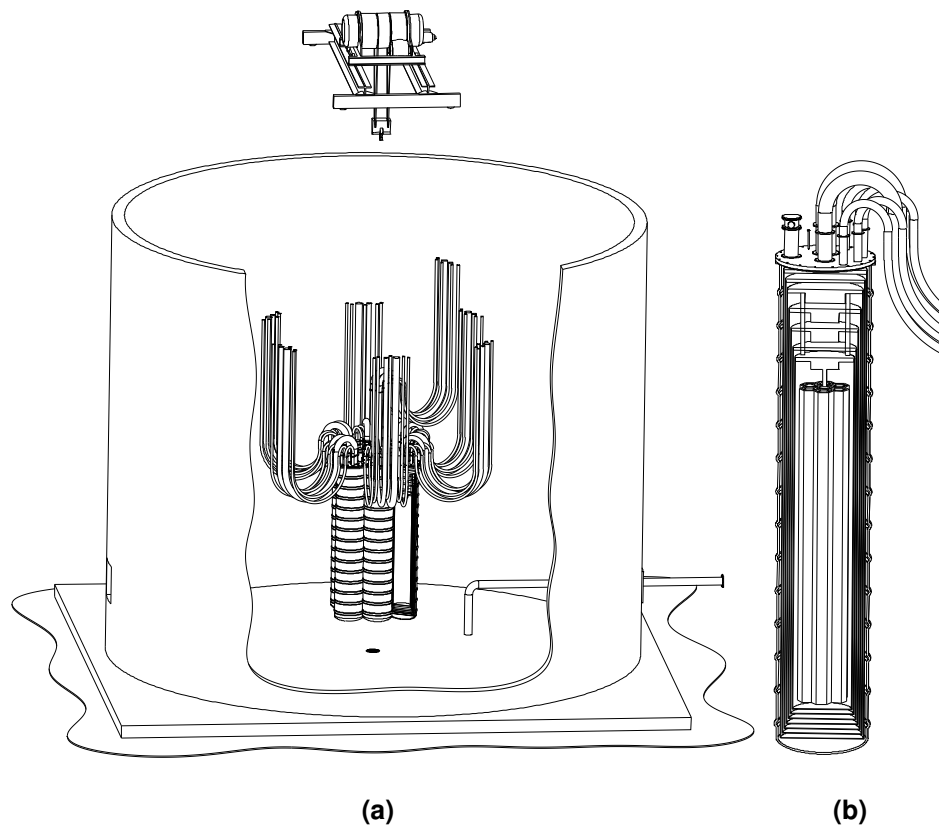


**Figure 2.2:** Design option with 7 independent dilution refrigerators immersed in the “Pool” for shielding (a). One single dilution refrigerator unit (b).

requirements of low radioactivity would be difficult if possible at all, and would increase the cost for R&D and radio-pure materials. A summary of the design features is given in Table 2.3.

For the reasons above, a design with a large cryostat is desirable, allowing self-shielding. Simple consideration of the surface area as a fraction of volume show that the 19 small towers offer the best self shielding of the 3 layouts.

## 2.3 The Shielding against Background Radiation

The background is mainly due to natural radioactivity and cosmic rays. The radioactive contamination is usually expressed either [92]:

- by the concentration of the nuclide of uranium or thorium or potassium in parts per billion by weight (1 ppb =  $10^{-9}$  g U/g) or
- by the decay rate per kilogram Bq/kg, where 1 Bq equals one disintegration per second.

**Table 2.3:** Design features of 7 separate dilution refrigerators with advantages and disadvantages

<i>Design features</i>	<i>Advantages</i>	<i>Disadvantages</i>
7 independent chambers for isolating vacuum	minimal interferences while exchanging a part of detector array; economic production due to the use of identical parts, and common spare parts	large distance between detector towers renders a substantial part of modules poorly self-shielded
Mixing chamber, still and 1 K pot integrated in the cryostat	conventional dilution refrigerator design; reasonable cooling power per dilution refrigerator	large number of tubes traversing the water shield; difficult to add shielding other than water given the large number of tubes; inner Pb shield required between DR and detector

The characteristics of naturally occurring isotopes are given in Table 2.5. The  $\alpha$  and  $\beta$  particles emitted by radionuclides are very short ranging with radiation absorption lengths of a few  $\mu\text{m}$  for  $\alpha$  and a few mm for  $\beta$ . Their direct effects on the detector is important only if the decay occurs in the target itself or very close to it. Against these radiations, shielding is not possible. High purity of the detector as well as of the material in its proximity is necessary to reduce this background.

The  $\gamma$ -rays and neutrons in particular, are capable of penetrating through significant thickness of shielding [92]. On the one hand, the  $\gamma$ -ray yield (number of  $\gamma$  per gram of material) is directly proportional to the concentration of the radioactive isotopes uranium, thorium, potassium. The  $\gamma$ -

**Table 2.4:** Conversion from the specific activity, in Bq/kg, to the atomic fraction of uranium, thorium and potassium, in ppb. [92]

<i>Isotope</i>	<i>Conversion</i>
$^{238}\text{U}$	1 Bq/kg $\equiv$ 81 ppb of $^{238}\text{U}$
$^{232}\text{Th}$	1 Bq/kg $\equiv$ 246 ppb of $^{232}\text{Th}$
$^{40}\text{K}$	1 Bq/kg $\equiv$ 32.3 ppm of K (natural)

**Table 2.5:** Characteristics of naturally occurring isotopes [92] that are likely to dominate in the background radiation of the EURECA detector array.

<i>Isotope</i>	<i>Characteristics</i>
Uranium: $^{238}\text{U}$ (99%), $^{235}\text{U}$ (1%)	<ul style="list-style-type: none"> <li>- <math>^{238}\text{U}</math> half-life = <math>4.47 \cdot 10^9</math> years</li> <li>- <math>\alpha</math>-decay (<math>\alpha</math> are produced)</li> <li>- also spontaneous fission with neutron production (only about 3% probability but may be a large contribution to the neutron flux).</li> <li>- the decay produces another radioactive isotope that also decays.</li> <li>- approximately 8 <math>\alpha</math>, 6 <math>\beta</math> and 2.2 <math>\gamma</math> until the stable isotope <math>^{206}\text{Pb}</math> is produced;</li> </ul>
Thorium $^{232}\text{Th}$	<ul style="list-style-type: none"> <li>- half-life = <math>1.41 \cdot 10^{10}</math> years</li> <li>- <math>\alpha</math>-decay only, spontaneous fission is negligible</li> <li>- chain of decays: on average approximately 6 <math>\alpha</math>, 4 <math>\beta</math>, 2.7 <math>\gamma</math></li> </ul>
$^{40}\text{K}$ (0.0117% in natural potassium)	<ul style="list-style-type: none"> <li>- half-life = <math>1.28 \cdot 10^9</math> years</li> <li>- <math>\beta</math>-decay - 0.89 <math>\beta</math> (electron) per parent decay</li> <li>- also <math>\gamma</math> (1.46 MeV) - 0.11 <math>\gamma</math>-rays per parent decays</li> </ul>
$^{60}\text{Co}$	<ul style="list-style-type: none"> <li>- half-life = 5.271 years</li> <li>- <math>\beta</math>-decay-<math>E_{max}</math>=318 keV, 2 photons per decay: 1.173 MeV and 1.333 MeV</li> </ul>
$^{137}\text{Cs}$	<ul style="list-style-type: none"> <li>- half-life = 30.07 years</li> <li>- <math>\beta</math>-decay - <math>E_{max}</math> = 514 keV, 1 photon per decay: 0.662 MeV</li> </ul>

ray flux out of the material depends upon the materials composition (copper, steel, rock, etc.). To minimize the  $\gamma$ - ray background, materials with high purity and with a favorable composition will be used.

The neutron yield from spontaneous fission is proportional to the  $^{238}\text{U}$  concentration. But spontaneous fission is not the only and sometimes not the main source of neutrons. Neutrons are also produced in ( $\alpha$ ,n) reactions, whose yield and spectrum depend upon the concentration of uranium and thorium as well as on the composition of the material [92].

Extremely low radioactivity levels in stainless steel were found in the measurements carried out for GERDA [93] and XENON100 [92]. The results show roughly one order of magnitude lower concentrations of primordial radionuclides than in previous experiments [93]. Details on the results

**Table 2.6:** Radioactive contaminations in stainless steel, copper and acrylics of different manufacturers [92, 93]

Material	Manufacturer	Contamination of the isotope				
		<sup>238</sup> U (mBq/kg)	<sup>232</sup> Th (mBq/kg)	<sup>40</sup> K (mBq/kg)	Co (mBq/kg)	<sup>226</sup> Ra (μBq/kg)
SS old meas.	-	6	4	16	10	-
SS 1.4571-316Ti	-	1	1	1	10	-
Copper	Norddeutsche Affinerie	-	< 0.023	< 0.088	0.01	< 0.02
Acrylic	Double Chooz	-	< 0.007	< 0.05	-	< 0.002
Acrylic (Perspex)	Harris Spur Ltd	< 0.12	< 0.04	< 1.5	-	-
Acrylic (Polycast)	UVT 450	< 14.8	< 4.9	10.2±0.3	-	-

and on other materials are given in Table 2.6.

Copper is very pure, with the lowest contaminations of uranium, thorium, potassium and <sup>60</sup>Co. Therefore it is probably one of the best structural materials. The uranium and thorium concentrations in copper are 0.01 ppb compared to 1 ppb for stainless steel. In addition, the neutron yield of copper is lower than that of stainless steel for a particular uranium/thorium concentration level. The neutron yield of copper is therefore more than two orders of magnitude lower than that of stainless steel. For this reason stainless steel should be avoided as far as possible in the cryostat design [91]. The best radio-pure copper is produced by the manufacturer Norddeutsche Affinerie [93].

Acrylic (Perspex, PMMA) samples of different suppliers have been tested and show very low contaminations of uranium, thorium and potassium. Samples from the supplier of the Double Chooz experiment [61] were measured by P. Loaiza [93] with gamma ray spectrometry; Perspex from Harris Spur Ltd was measured by Charles Evans from Cascade Scientific using Inductively Coupled Plasma-Mass Spectrometry (ICP-MS); Polycast from the supplier UVT 450 was measured by ICI Tracerco with the neutron activation analysis test method [21]. Acrylic could be used as construction material and also, as a good alternative to CH<sub>2</sub>, as a neutron shield, requiring a twice thicker layer compared

**Table 2.7:** Aimed reduction in the background of EURECA’s integrated multi shielded ELB (Experimental Low Background) facility, in comparison to current underground laboratories [53].

<i>Background rate</i>	<i>Surface</i>	<i>Current underground labs</i>	<i>Goal for EURECA</i>
muons	1	$10^{-6}$	$10^{-10}$
neutrons (fast)	1	$\approx 10^{-4}$	$10^{-8}$
radon	1	$10^{-1}$	$10^{-4}$
$\gamma$ activity up to 2,6 MeV	1	$\approx 0.3$	$10^{-4}$

to  $\text{CH}_2$ . The radioactive contaminations in stainless steel, copper and acrylics are given in Table 2.6. Other possible materials are ultra-pure nickel, which has been reported to be used by SNO [91]. CuNi (70% Cu, 30% Ni) must be used in the thermally isolating pipework.

Shielding against the cosmic rays is accomplished by placing the detector array in the deepest laboratory in Europe, at the Laboratoire Souterrain de Modane, with a water-equivalent depth of 4800 m. Muons and neutrinos are the only cosmic ray components that can reach this large depth. Residual muons deposit energy in the detector, but can be actively vetoed. Scintillating detectors surround the detector array. Signals that occur in coincidence with signals from the scintillators can be rejected. Also, muons produce fast spallation neutrons in the rock and in the shielding material. This production happens either by colliding with nuclei, by being captured by nuclei (negative muons at very low energies only), or by producing secondary particles (hadrons, photons) that collide with nuclei producing neutrons [92]. This is especially dangerous as muons can easily pass shields and produce neutrons in the proximity of the target. Neutrinos have only a very low contribution to the background [108].

The targeted background reduction for EURECA, in comparison to the current underground laboratories, is shown in Figure 2.7. To achieve the goal, an additional shield of purified water will be used as a muon veto detector, and also as  $\gamma$  absorber and neutron moderator. The attenuation of  $\gamma$ -rays by water varies for different energies and, hence, for different radioactive sources (U, Th,  $^{40}\text{K}$ ) [94]. The attenuation of 2 m water for  $\gamma$  at energies of 2 MeV is 1000, and greater than 1000 for energies higher than 2 MeV [53].

Two possible designs using water as the main shield were studied [18, 19, 92, 94]. These designs are: A large clean room inside the water shield, called the “Submarine Design”, and the “Pool Design”, which immerses only the detector array in a water reservoir. The two designs will be discussed below.

## 2.4 The “Submarine” versus the “Pool” Design

The “Submarine” design features a room made of low activity stainless steel that is completely shielded with 2 m pure water all around (hence the name), and is equipped with scintillating detectors. The layout is shown in Figure 2.3. All components inside the shield have to be carefully selected, radio-pure materials matching the required low residual  $\gamma$ -activity after the water-shield [53]. Cleanest conditions inside the “Submarine” are necessary, including the supply of radon free air (10 mBq/m<sup>3</sup> [53]). The accessibility to the detector array is very good, which facilitates the construction and maintenance work.

The “Pool” design shown in Figure 2.4 immerses only the detector array in the water shield. Therefore, the radioactivity of devices outside the vessel is less critical. To gain access to the detector, the water has to be removed first. In comparison to the “Submarine” design, the tube between the mixing chamber and the still is shorter, having the same water shield thickness.

To compare the two designs, the shielding efficiency of both was studied. The detector modules will be mainly able to discriminate  $\beta$  and  $\gamma$  from recoils by neutrons and WIMPs, leaving neutrons as the main background [18]. The simulation for the muon-induced neutron background was done by Michael Bauer [19] using the simulation toolkit GEANT4<sup>1</sup>. As a muon generator, the Frejus spectrum was used [74], shooting from a hemisphere with 50 m radius to the center of the geometry with 15 m smearing. For the simulation the following assumptions were used:

- the detector is in the center of the geometry, directly in the focus of the muon generator,
- the setup is surrounded by 10 m of Frejus rock,
- the detector is a natural germanium cube with 60 cm edge length, segmented into  $3 \times 3 \times 3$  pieces,
- the “Submarine” is modeled as a cube with 13 m edge length, and 2 m of water shielding.

---

<sup>1</sup>GEANT4 Version 9.1.p1QGSP\_BIC\_HP

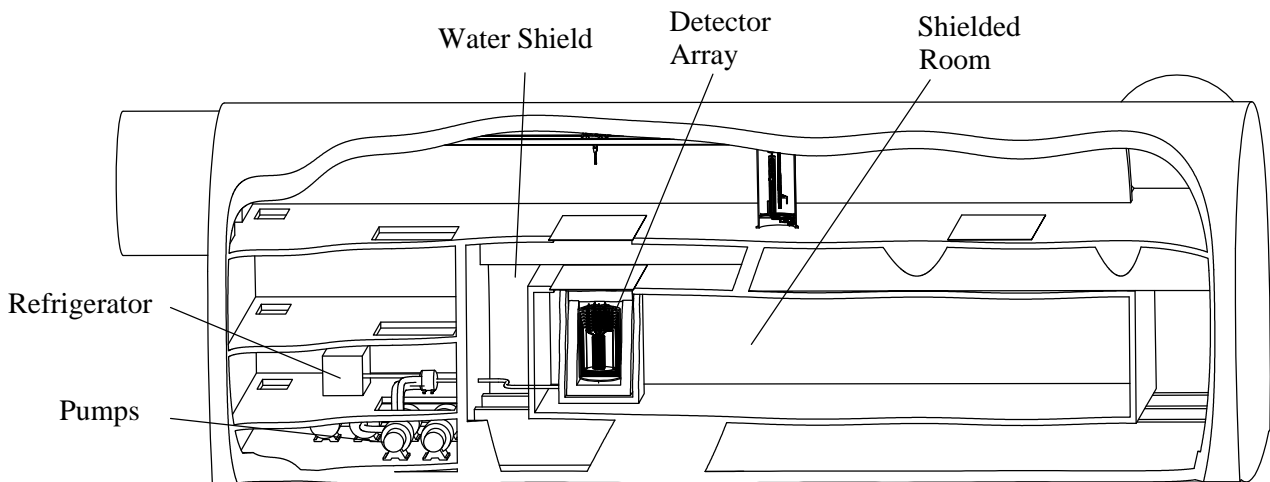


**Figure 2.3:** Implementation of the cryogenics in the “Submarine” design of EURECA.

- the cryostat of the “Pool” design is directly immersed in water.

For both designs the detector was placed inside a simplified cryostat. To study the influence, different parameters were varied. In order to study the influence of the cryostat’s material and mass, the following wall thicknesses were investigated:

- 1 cm copper, 5 cm liquid helium, 1 cm of copper ( $\approx 500$  kg copper) and
- 1 mm of copper, 5 cm liquid helium, 3 mm of copper ( $\approx 100$  kg copper).

Also different veto thresholds, as well as 2 m and 3 m of water shield were used. For the “Submarine” design a thicknesses of the steel wall of 40 cm and 4 cm was studied.

The thickness of the steel wall for the “Submarine” has only a slight influence on the total number of events seen in the detector. However, the number of events not seen in the veto, as well as the number of dangerous “hadronic” events in only one segment are significantly increased with thicker steel walls. “Hadronic” refers to any particles depositing energy that are not an  $e/e+$ ,  $\mu/\mu+$  or  $\gamma$ . Also, the simulation shows that a thicker cryostat presents the advantage to act as a shielding against events from outside, if the background is high. The comparison between the best “Submarine” design (thin steel walls and “thick” cryostat) and the “Pool” design shows that the background from the vicinity of the detector is almost the same for both designs. However, the “Submarine” adds a lot more events from further away [19]. For that reason, in the case of the “Submarine” design it is necessary to rely a lot more on the veto than in the case of the “Pool” design [19]. The results also

show that “dangerous” muons seem to pass mostly close to the detector especially in the “Submarine” design [19].

Simulations of the  $\gamma$  and neutron flux from local radioactivity were performed [94]. For the model, the following assumptions were considered:

- the laboratory size is 30 m  $\times$  10 m  $\times$  10 m with a concrete wall of 30 cm thickness,
- the target is made of 324 germanium crystals packed in 27 floors with 12 crystals on each,
- each crystal has a mass of 320 g and the array weighs 103.68 kg in total,
- the inner copper vessel of the cryostat is 0.5 cm thick with a mass of 139 kg and the outer copper vessel is 0.5 cm thick with a mass of 181 kg,
- the vessel of the “Submarine” is made of 2 cm of stainless steel.

In addition cryostats of different radio-purity were studied. One that is made completely of copper, one including 20 kg, and one including 350 kg of stainless steel, respectively.

For the “Submarine” design the simulation shows that the exact size of the laboratory is not very important. If the laboratory is larger, then the mass of steel is higher but the room’s wall is further away from the detector. Also, the thickness of the water shield (2 m or 3 m) is not crucial in that design, as the electron recoil rate is dominated by  $\gamma$ -rays (about  $8 \cdot 10^5$  events/year at energies between 10 keV to 50 keV) coming from the vessel made of stainless steel. This is much higher than the rate from a cryostat made of copper with about  $7 \cdot 10^3$  events/year, but it is similar to the rate of events from a cryostat with a large amount of stainless steel (350 kg) and from the scintillating detectors. Additional 5 cm of lead would attenuate this flux by more than a factor of 10. However, lead is not radio-pure enough. About 5 cm to 10 cm of ultra-pure copper would be necessary if the discrimination factor of the detector is  $> 10^4$ . For a larger detector mass, more shielding is probably needed.

The nuclear recoil rate is dominated by neutrons from the stainless steel vessel and from the scintillating detectors, with approximately 17 events per year (at energies between 10 keV and 50 keV), under the condition that no “dirty” materials are used in the cryostat’s construction [94].

The “Pool” design presents the advantage of having no stainless steel between the water shield and the cryostat. The electron recoil rate per year in 104 kg of target material is  $10^5$  event/year with a 2 m water-shield due to the uranium, thorium and potassium concentration in the concrete. An

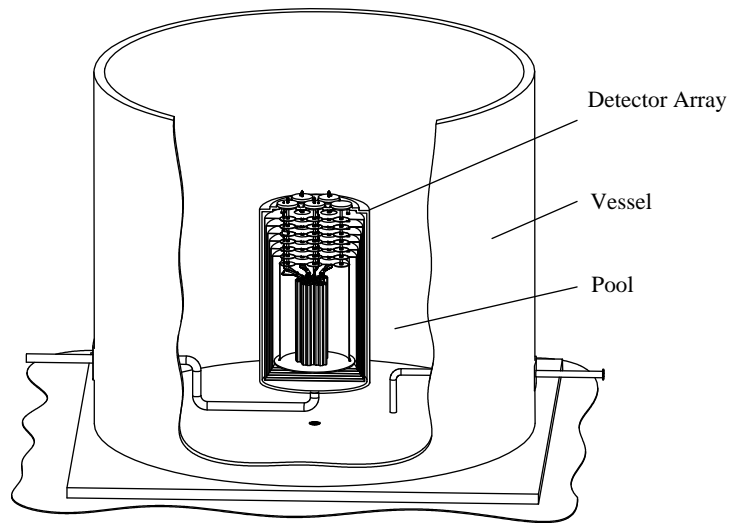


**Figure 2.4:** Implementation of the cryogenics in the “Pool” design of EURECA.

additional inner shield of 5 cm to 10 cm of ultra-pure copper would attenuate this flux by an order of magnitude. However, the inner shield can be entirely avoided by using a thicker water-shield. 3 m of water decreases the electron recoils to  $1.3 \cdot 10^3$  event/year from concrete and below 100 event/year from the surrounding rock. The neutron and  $\gamma$ -ray flux from the water shield is negligible as it has a very low contamination of less than 0.01 ppb of uranium and thorium [94].

For a cryostat made of copper only, the simulation of  $\gamma$  and neutrons from local radioactivity show a very low electron recoil rate of approximately  $7 \cdot 10^3$  events/year from the copper, and a nuclear recoil rate of much less than 1 event/year. This does not require additional shielding even for a large scale detector [94]. However, if 10 kg of stainless steel are added, with 1 ppb of uranium and thorium, then the rate for  $\gamma$  goes up by a factor of 3 and by a factor of 10 for the neutron induced nuclear recoils. For 350 kg of stainless in the proximity to the detector the  $\gamma$  rate is much higher, with approximately  $4.0 \cdot 10^5$  events/year. These values would be too high and would require inner shielding of the detector. 10 cm of  $\text{CH}_2$  can be used to attenuate the neutron flux originating from the stainless steel in the cryostat but  $\text{CH}_2$  is too contaminated to be put in the proximity of the detector array. Therefore, a 5 cm to 10 cm copper shield has to be placed between the  $\text{CH}_2$ -shield and the target to attenuate the  $\gamma$ -rays [94].

The simulation for muon-induced background shows that with a perfectly efficient veto and a low enough veto threshold, both designs reach similar results. However, it is unlikely that this can be achieved in practice because of the veto inefficiency due to real scintillator coverage for light collection. Therefore, it can be concluded that for muon-induced background the “Pool” design is

the best option [19].

Regarding the  $\gamma$  and neutron background from local radioactivity it can be concluded that both designs give comparable rates of events if contaminated stainless steel is used in the cryostat. Due to the high background of stainless steel, the difference is only a factor of 2 to 3, in favor of the “Pool” design. The background rate (both  $\gamma$  and neutron induced) would be too high for the planned sensitivity. A shield inside the cryostat made of 10 cm of  $\text{CH}_2$  and 5 cm to 10 cm of copper inside the  $\text{CH}_2$ -shield [94] would be necessary.

It can be concluded that the “Pool” design is clearly superior, under the condition that it is possible to avoid dirty materials in the proximity of the detector. The  $\gamma$ -flux induced by the steel room of the “Submarine” design is 8 times higher than the residual flux after the 2 m water shield. The “Pool” design experiences no radioactive radiation from the walls of the vessel. Depending on the obtainable purity of the different materials used in the proximity of the detector inside the water vessel, no inner shielding is necessary for the “Pool” design.

At current knowledge, the EURECA collaboration decided to continue with the “Pool” design. Therefore, a design study was conducted to assess the feasibility of a cryostat with materials of the lowest possible contamination, such as high purity copper and acrylic. Although other materials with low conductivity, high mechanical strength, solder to join parts and indium to seal the mixing chamber will be necessary, the amount should be strictly limited. Materials such as stainless steel should be avoided entirely or limited to well below 1 kg.

## 2.5 The Exchange of Parts of the Detector Array

As discussed in section 2.2, the detector material will be placed in a common large cryostat. To operate the detector with a high coverage, two procedures are studied to rapidly exchange detector material. High coverage is defined as the time during which taking data is possible, as a fraction of total time. The measurement is interrupted during any disturbance of the shield around the detector, such as the manipulation of the water or the loss of its radio-purity. Introducing vibrations to the detector array, or a change in the temperature outside its operating margin also disturbs the measurements. Different strategies to exchange a part of the detector material were studied, for a maximisation of coverage. The aim is a maximum interruption of 150 h for an exchange procedure. The exchange can be performed:

- while the main detector mass remains cold by using a load lock system,
- by means of a fast cycling cryostat, which features fast cooling and warming up.

The decision for either system has a wide impact on many components, including the dimensions of the complete system, which determine the space requirements of the hosting cavern. For the Load-Lock system, as well as for a fast cycling dilution refrigerator research and development have to be done on several subcomponents and on the whole system. To focus the available resources in the best possible way, such as manpower, time as well as capital cost, it is necessary to decide on one baseline design at an early stage of the project.

## 2.6 The Load Lock System

The load lock is a mobile ultra high vacuum chamber that enables the exchange of a part of the detector, while the cryostat and the main detector array remain cold. A possible design is shown in Figure 2.5. It is equipped with a pneumatically operated, ultra high vacuum gate valve<sup>2</sup>. The technical specifications of the valve are given Table 2.9. The gates are specially designed for the use in load lock systems, requiring an easy and fast access. The requirements for the load lock are listed in Table 2.8.

To precool a new detector to a temperature as close as possible to the operating temperature, the load lock is equipped with a pulse-tube cooler. The PT415 from Cryomech offers a cooling power of 40 W at 45 K and 1.5 W at 4 K. The cold head of the cryocooler is supplied only with a high and a low pressure tube and the electrical power. This enables sufficient movement of several tenths of meters. Three remotely controlled heat shields, at temperatures of 4 K, 40 K and 100 K reduce the heat load from radiation. The two innermost shields are directly cooled at the stages of the pulse-tube cooler. The first heat shield is thermalized at the 40 K stage via an thermal resistance, which can be the support structure at the bottom, to achieve an intermediate temperature.

Two cranes inside the vacuum chamber have to be able to manipulate independently the weight of several hundred kilograms in three dimensions. One crane handles the new detector tower and the second crane is necessary to remove a detector tower from the array.

During an exchange process the radon free air atmosphere above the water shield has to be broken,

---

<sup>2</sup>VAT Vakuumentile AG pendulum valve Series 16.2

**Table 2.8:** Requirements of a load lock system for EURECA to exchange parts of the detector array rapidly.

<i>Requirement</i>	<i>Comment</i>
minimal interruption of the measurement	< 150 hours
compliance with the radio-purity requirements	use of radio-pure components that are attached to the detector array during an exchange
use of different detectors	flexible interface
short electronic cables, vibration-free mounted	- integrated electronic or - use of cold connectors
close package of the target material	- suitable handling mechanism that can be operated at ultra low temperatures - fully remotely controlled exchange process

**Table 2.9:** Properties of a suitable vacuum lock valve for a load lock system.

<i>Property</i>	<i>Value</i>
Leak rate body and valve seat	$< 1 \cdot 10^{-9} \text{ mbar} \cdot \text{Ls}^{-1}$
Pressure range	$10^{-8} \text{ mbar}$ to 1.2 bar (absolute pressure)
Cycles until first service	200 000
Actuator types	pneumatic actuator
Sealing materials	Viton

the water shield around the detector unit removed and the load lock system has to be mounted on the thoroughly cleaned detector flange. The area between the load lock and the detector has to be evacuated so that the vacuum locks on both sides can be pneumatically opened. Before inserting the new detector tower, another detector tower has to be removed. The heat shields around the pre-cooled target material have to be removed and the detector lifted from its cooling source. From then on, the detector is warming up and has to be rapidly inserted into the detector unit. The heat shield lids in the cryostat are opened sequentially while the new detector material is lowered, to prevent the cold mass from seeing high temperature surfaces. To achieve the closest detector package, the inserted material has to be moved towards the center by means of a pivoting mechanism. This is necessary

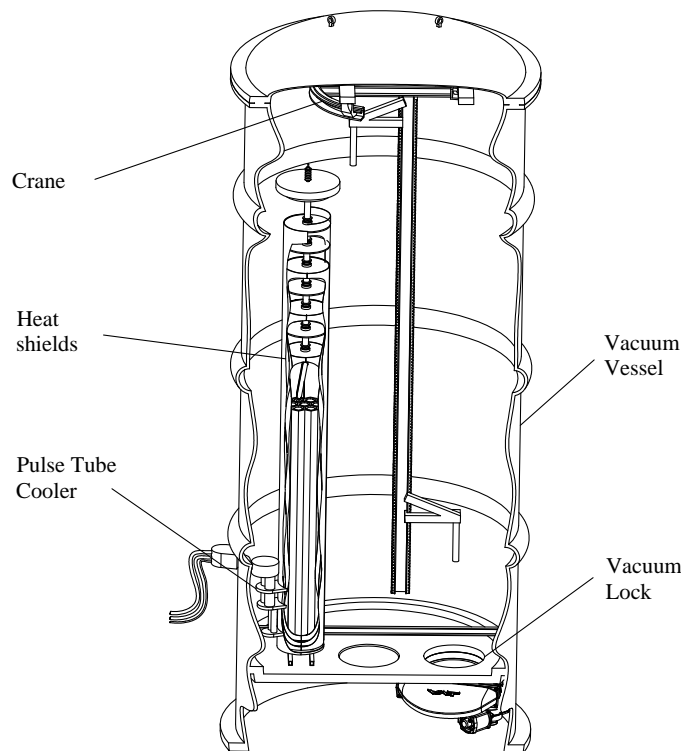


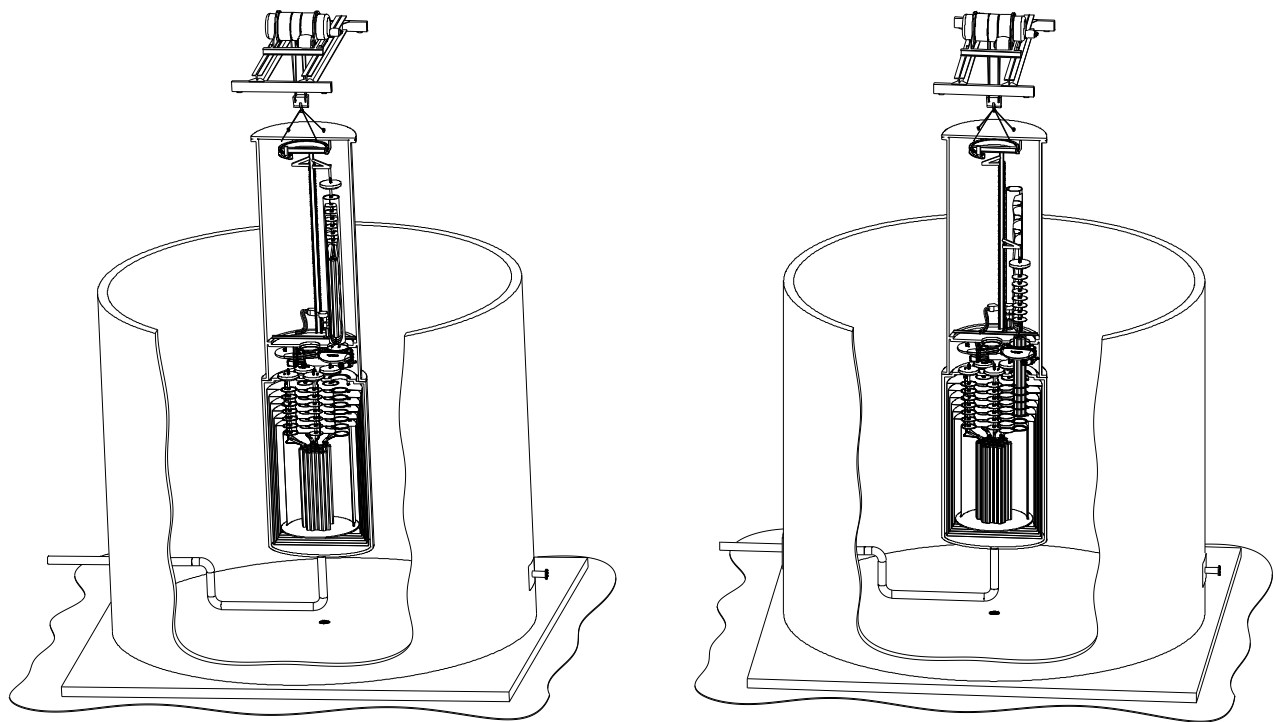
**Figure 2.5:** A possible design of a load lock, with a vacuum chamber with a pneumatic lock, a crane for manipulating the detector in three axis and a pulse tube cryocooler for precooling the detector

because the vacuum gate valves have a larger diameter than the detector towers.

The unloading mechanism has to be able to handle a mass of approximately 300 kg in a precise way and without introducing oscillations, vibrations or an excessive heat load. In addition, to achieve the closest arrangement of the detector, the unloading mechanism also has to be able to move the detector horizontally inside the detector unit.

Research and development for the electronics is still underway and will be discussed below. Therefore, it is not yet decided if it is required to exchange the detector electronics together with the corresponding detector. This may be necessary for flexibility, to adopt the electronics to different detector technologies or in case of a failure. However, this might not be required if the electronics are highly reliable and designed to fit a wide range of detectors. Therefore, the two possibilities, which will be discussed below are:

1. a design with exchangeable electronics,
2. a design with permanent installed electronics.



**(a)** The load lock attached to the detector array and the precooled detector tower is in position

**(b)** The cryocooler and the heat shields are removed and the detector tower is lowered onto the mixing chamber

**Figure 2.6:** Procedure for exchanging a part of the detector material for the 1-ton cryostat.

In the first option, the front-end electronics have to be installed and thermalized at the lids of the heat shield of the unloading mechanism. Therefore, the mechanism has to remain installed during the operation. The available space for the electronics is limited to the diameter of the heat shield lid, which is only slightly larger than the detector tower. Also, the height must remain within reasonable limits, as it directly influences the overall height of the detector unit. Consequently, the cables must also be integrated in the mechanism. The length of the cables is critical for the sensitivity of the electronics. In this design option, the cabling has to be routed along the pivoting arm to the front-end electronics and therefore is relatively long. Design considerations of an unloading mechanism with exchangeable electronics are:

- The exchange mechanism remains in the cryostat  $\Rightarrow$  use of expensive radio-pure materials.
- The heat shield lids and the vacuum lock are integrated in the unloading mechanism.
- The electronics and cabling are integrated in the unloading mechanism and therefore not exchangeable.

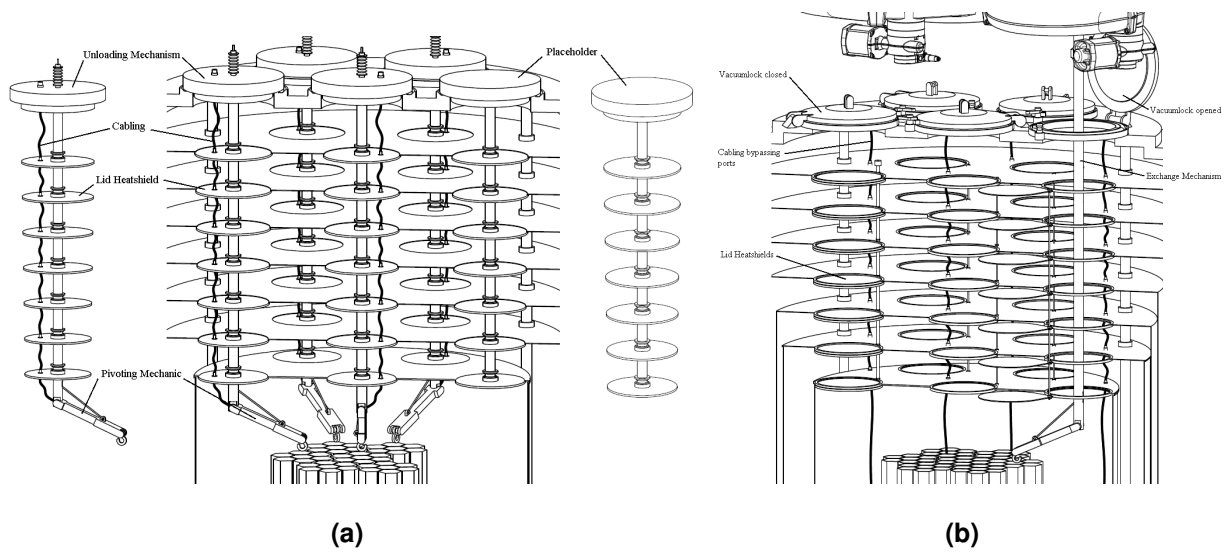


**Figure 2.7:** Unloading mechanism for the one large cryostat design (a) with cables, heat shields and electronics integrated and (b) with the electronics and cabling permanently installed in the cryostat and an exchange mechanism that is removed during normal operation.

- There is limited space available for the electronics.
- The electrical cables are relatively long.
- Additional connections cause an additional heat load.
- The arm of the pivoting mechanism is relatively long, which requires a more rigid support structure.

The support structure has to be optimized to fulfill the conflicting requirements of being mechanically rigid, while transferring minimal heat between the different temperature levels. For a good thermal contact to the cooled heat shields of the cryostats, the lids have to be pressed down by springs. The lids with the electronics have sufficient weight to make good contact.

The distance between the centers of the vacuum locks amounts to 510 mm, because the vacuum lock needs radial space for mechanical reasons. This is significantly larger than the distance of the tower centers in the closest packing of 240 mm. Also, the aperture diameter is considerably larger than would be necessary for the detector alone. Each heat shield lid has to be larger in diameter than the corresponding aperture. To allow for a re-entrant design, the inner lids must be smaller than the warmer, outer lids. The minimum overlap of the aperture and the lid is 5 mm in radius. The clearance between lid and preceding aperture is also 5 mm. Therefore, with 7 heat shield lids and the vacuum

lock, the vacuum aperture has to be 80 mm larger in radius than the detector tower.

For the horizontal movement inside the detector unit the unloading mechanism is equipped with a pivoting arm with several joints for movement and actuation. The length of the arm puts stress on the support structure and requires an even more rigid construction. The joints have to be grease-free, to not degrade the ultra high vacuum. Since the unloading mechanism is permanently installed, all components have to comply with the very strict radio-purity requirements.

If there is no detector in place, the aperture in the heat shield can be closed either by a simplified placeholder as shown in Figure 2.7(a) or by additional lids that are permanently installed in the cryostat, shown in Figure 2.7(b).

In the second design, i.e. the electronics remain permanently installed in the detector unit, a possible design is shown in Figure 2.7 (b). The features of this design with permanently installed electronics are

- A simple design of the pivoting mechanism.
- The heat shield lids are integrated in the cryostat.
- The electronics and the cabling are integrated in the cryostat.
- The electrical conductors can be designed to be very short.
- The pivoting mechanism can be removed during the operation.
- The pivoting can be shorter.
- Cold connectors are required.

The electronics can be placed close to the target material underneath the mixing chamber. Therefore, the cabling is very short, which reduces the noise. The unloading mechanism is much simpler than before, because it does not require heat shield lids. Instead, the lids can be integrated in the detector unit. The requirements for radio-purity and thermal conductivity are highly reduced for the unloading mechanism, as it does not remain in place during operation.

However, this design requires a cold connector between the detector and the readout electronics, with several 100 low noise contacts at the lowest temperature. The use of a standard spring-loaded contact connectors might not be sufficient. Hence, a contactless transmission of signals would have to be developed, which implicates a significant design risk.

## 2.7 A Fast Cycling Dilution Refrigerator

An alternative method for a fast exchange of the detector material is a fast cycling DR, which allows a rapid precooling and a rapid warm up procedure of the whole array. To determine the most efficient heat transfer from the detector to the cooling source, different options were studied. The three possibilities are:

- using an exchange gas to a liquid helium bath,
- cooling by circulating cold gas in the Inner Vacuum Chamber (IVC),
- cooling through a solid-solid interface.

Firstly, cooling with an exchange gas for the heat transfer to a cryogenic bath, is relatively slow. The process relies on natural convection, which is very restricted due to the low thermal conductivity of gas. To cool a 2.3 t cylindrical bar antenna made of Al 5056 to liquid helium temperature takes about one month [50]. Also, a cryogenic bath is not desired for EURECA due to the risks involved in using a large amount of cryogenic liquid in an underground site.

Secondly, the circulation of cold gas considerably improves the heat transfer by applying forced convection [48]. Helium gas is cooled by a refrigerator that also produces the liquid He needed. The cold gas is circulated through the heat exchangers in the IVC, which cool the array for normal operation. By applying this method it was possible to cool a 1.15 t CuAl (6 %) sphere to 1.8 K in 3.5 days [38].

The third possibility, cooling by a solid-solid interface, consists of the heat transfer via a metal body, which is in thermal contact to a cold bath. As metals feature much higher thermal conductivity in comparison to gases, this method can deliver the best performance, as shown below.

The three methods were compared by cooling a 19 kg aluminium body to liquid nitrogen temperature [50]. Cooling by natural convection was clearly the worst, with a cooling time of 200 h. Although the geometry was not in favor of the cooling by solid-solid interface due to a very small cross section of the cold body, this method achieved the same cooling time of 4.5 h as cooling by forced convection. For EURECA the geometry will be much more advantageous for thermal bridging. The support of the detector array, which transfers the heat, has a short length and a large cross section. Also, the additional mass from an inner vacuum chamber, which is required for cooling by

cold gas, is not preferable for EURECA due to background reasons as discussed in section 2.3. For these reasons, thermal bridging is the favored cooling method for EURECA.

**Table 2.10:** Precooling simulation for EURECA depending on the available cooling power of relatively small industrial type helium refrigeration units and the composition of the mass to be cooled. Cool down time 1 considers copper, germanium and stainless steel, 1 t of each. Cool down 2 considers 3 t of copper and 1 t of germanium.

<i>Refrigerator cooling power at 4.5 K</i>	<i>Cool down time 1</i>	<i>Cool down time 2</i>
(W)	(h)	(h)
200	66	90
300	44	60
400	33	45

Simulations of the cooldown time for EURECA, using the solid-solid interface method were undertaken considering standard industrial type helium refrigerators as cooling sources [68]. Small units offer cooling powers of 200 W, 300 W or 400 W at 4.5 K, assuming that heat is only extracted by the turbines of the refrigerator. The mass that was considered to be cooled consists of either 1 t of copper, 1 t of germanium and 1 t of stainless steel (cool down 1), or 3 t of copper and 1 t of germanium (cool down 2). Depending on the material composition of the cryostat and the chosen refrigerator unit<sup>3</sup>, the precooling to 4.5 K takes between 2 and 4 days. The details are listed in Table 2.10.

It can be concluded that cooling by thermal bridging proves to be a reliable method with little design risks. Also, the simulations show that even with relatively small refrigeration units, very short precooling times are achievable. This leaves hardly any space for improvements by a load lock system. Therefore, a fast cycling cryostat with rapid precooling and warming up will be used for EURECA baseline design. The design will be discussed in the following section.

## 2.8 The Baseline Design

For EURECA two identical DRs shall be used. In this way a detector tower can be tested under the same conditions as in the final setup or the two cryostats can be operated alternatingly or simultaneously. Each DR is capable to house a detector mass of 500 kg. The cryostats are placed in separate

<sup>3</sup>Linde Kryotechnik AG, model Lr 70, LR 140, LR 280

water pools and are supplied by independent cryogenic systems. Both DRs are housed in a common large cavern, possibly sharing the space with other experiments. A water purification system for the pool shield is placed close to the experiment and is connected via flexible tubes. An additional storage reservoir is foreseen, with enough capacity to contain the water of at least one detector array.

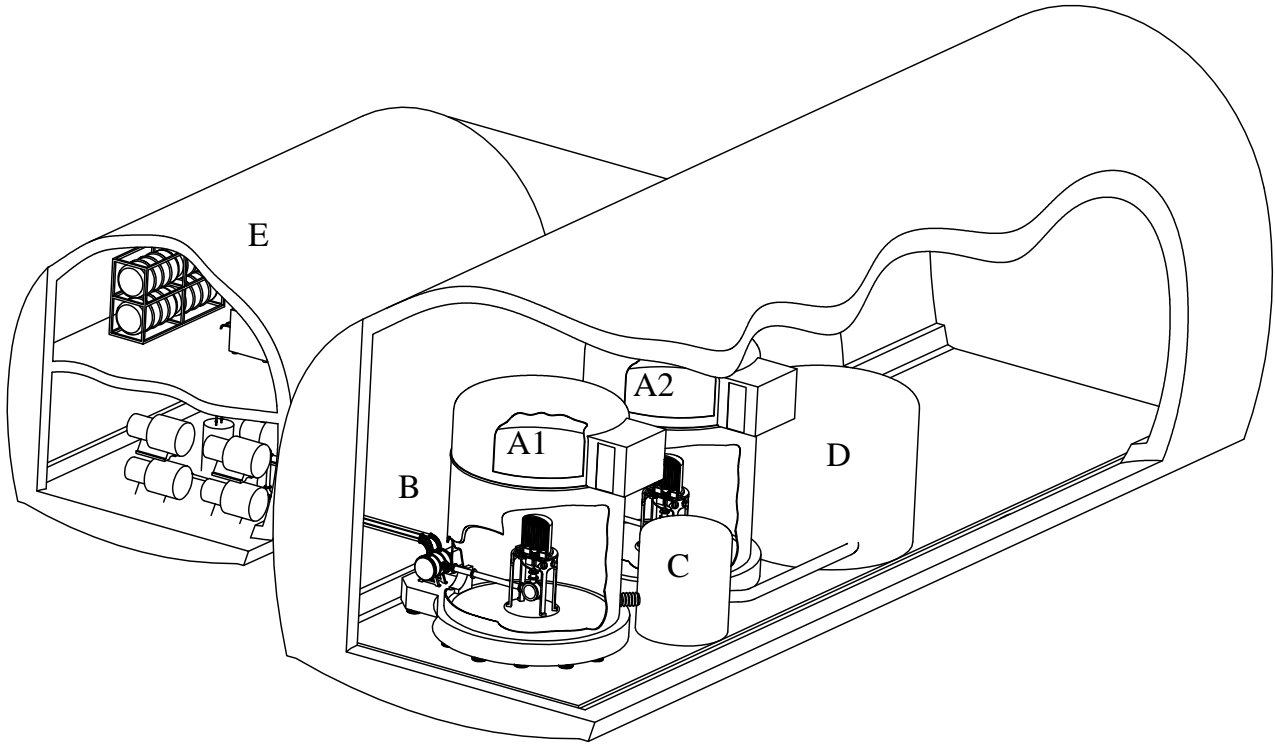


**Figure 2.8:** Baseline Design of the EURECA cooling and cryogenic system within the newly excavated hall in LSM. A1 and A2 are the “Pools” of the detector arrays, B the dilution refrigerator outside the shield, C marks the water purification plant, D marks the storage vessel for the shielding water when access to the detector array is required and E marks the proximity cryogenic.

The vessel of the water shield has a diameter of roughly 8 m and a height of 10 m. Stainless steel is tolerable as a construction material, because the water shield sufficiently filters  $\gamma$ -rays both from the rock and from the vessel wall. The construction has to take place *in situ*, as the transport of the whole vessel is impossible due to its large dimensions.

The vessels are covered by accessible lids that confine the radon-free air or nitrogen above the water shield. The radon level should be approximately  $20 \text{ mBq/m}^3$  [54]. The lids contain a clean room that is entered via an air lock. During maintenance of the array, the lid also facilitates the operation of the pool space as a clean room.

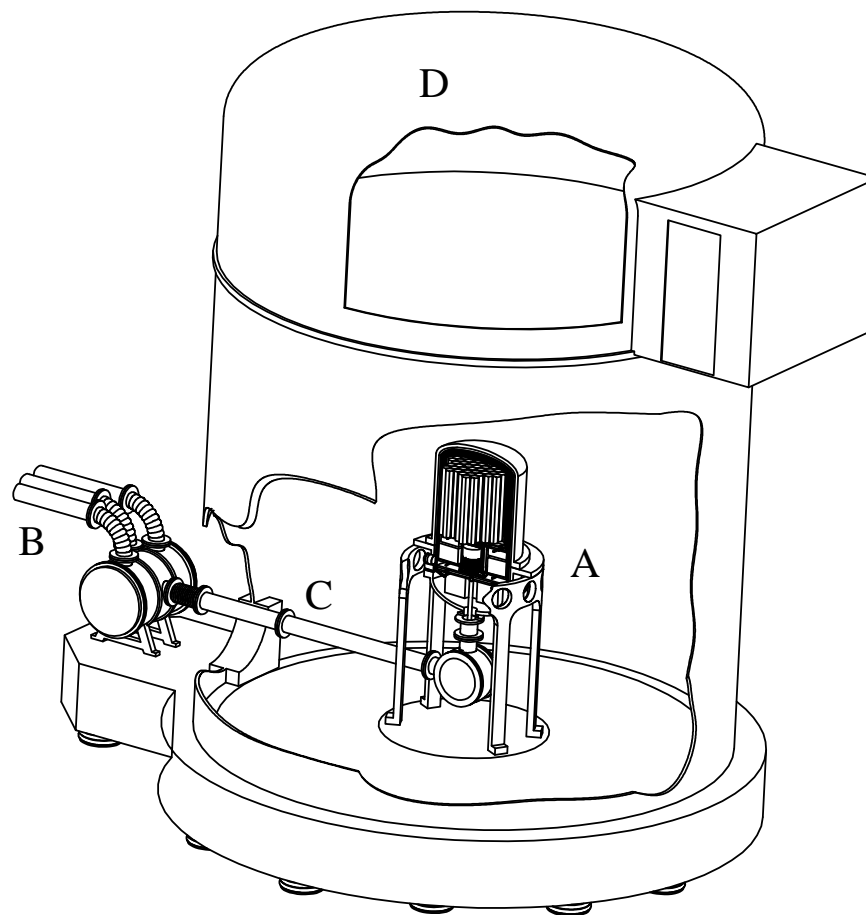


**Figure 2.9:** The layout of the EURECA detector array. *A* is the first vacuum chamber inside the pool housing the detector array, *B* is the second vacuum chamber outside the pool, *C* is the cryoline and *D* is the accessible lids that confine the radon-free air or nitrogen above the water shield.

Figure 2.9 shows the cryogenic parts of the array which are separated into two vacuum chambers and linked by a cryoline. The vacuum chamber for the array is positioned in the middle of the pool, surrounded all around by a 3 m thick water shield. The cryoline with a 90° bend traverses the water shield towards the second vacuum chamber, situated just outside the pool.

This second vacuum chamber shown in Figure 2.10 houses the still of the DR, the precooling heat exchangers and the condenser of the  $^3\text{He}$ . Also, the valves for the fast precooling of the array are situated there. The whole unit has an external diameter of about 100 cm and a total length of 200 cm. The central cylinder carries all feedthroughs, valves and pipe connections, while the bare dome-shaped ends can be dismantled to provide easy access to the inner parts. The whole unit can contain stainless steel as it is located outside the water shield. It is mounted on the same base like the detector array because they are connected by a rigid cryoline.

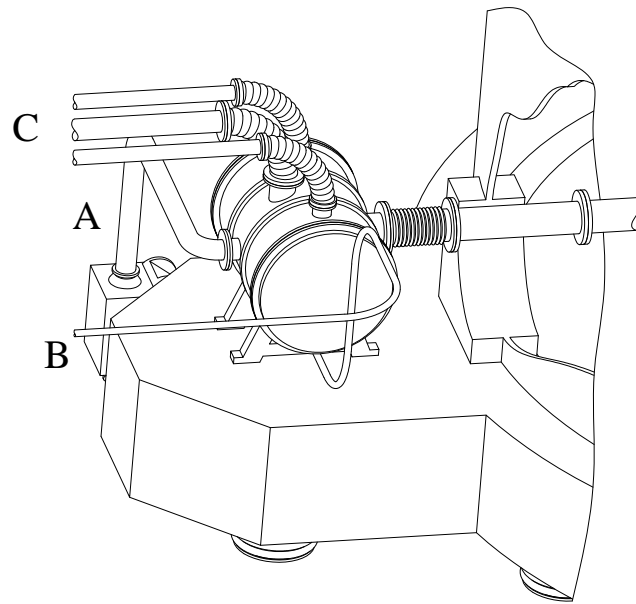


**Figure 2.10:** The dilution refrigerator unit outside the water shield. *A* marks the vacuum system, *B* marks the liquid helium supply from the refrigerator and *C* marks the lines for pumping the  $^4\text{He}$  pot and the still.

## 2.9 The Detector Unit

The detector unit houses the array together with the mixing chamber and the main heat exchanger at a temperature below 50 mK, and 5 concentric heat shields. It can be made almost exclusively of high-purity copper, which has a high thermal conductivity and therefore provides good isothermal shield and support structure. However, the function as thermally isolating support structure is limited by the low elastic limit and by the high thermal conductivity of copper.

The experimental area on top of the mixing chamber offers space for an array of 1 m in diameter and 1 m in height. For the mixing chamber flange that supports the detector, a compromise has to be found between an excellent radial heat transfer and the reduction of the mass in the proximity to the detector for low background. To achieve a sufficient thermal conductivity, the array's support has to be made considerably thick. Therefore, the mounting plate of the array should be made of a 1 cm layer of high-conductivity annealed copper, supported by a 4 cm plate of cold worked high-purity copper with higher elastic limit. If it is found that the creep of the plate produces too high residual heat loads under the weight of the array, parts of it should be made of beryllium copper made of highly radio-pure components. The support structure could also feature an electro-eroded honeycomb structure, if ultimate weight saving is required. Such a structure would also facilitate the

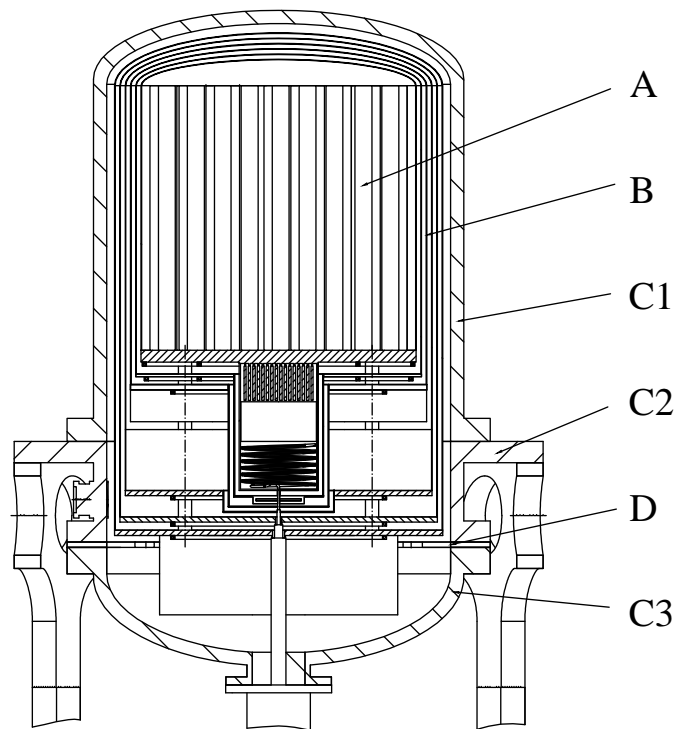


**Figure 2.11:** The vacuum vessel inside the “Pool” housing the detector array. *A* is the detector array, *B* are the heat shields, *C1*, *C2*, *C3* are the three parts of the vacuum vessel made of radio-pure PMMA cast around a hermetic, thin-walled copper structure. *D* is a sub-frame made of titanium alloy.

access to the cabling between the detectors and the front-end electronics.

The total weight of the detector array consists of 500 kg detector material and a substantial amount of support structure. Scaling up the current germanium detectors modules of EDELWEISS II to 600 kg of detector material would occupy a volume of 1.2 m<sup>3</sup>. The total weight of the array would be between 2.5 t and 3 t. The design for EURECA should be more elaborate to make the large array more compact and to reduce the amount of copper. The mass of the holders should amount to no more than 1000 kg, resulting in a total mass of 1500 kg for one array.

A good thermal contact between the liquid helium and the MC lid is ensured by a heat exchanger made of sintered copper powder that offers a large surface area per unit volume. For the 1 μm copper powder studied in this work, a surface area of 5.3 m<sup>2</sup> is required (see section 5.3) to transfer the heat load of EURECA. With an optimal sinter thickness of 1 mm, this requires a substrate area of only 40 cm<sup>2</sup>. The heat exchanger can be placed directly to the lid of the MC, which is in contact with the detector array. The direct contact improves the heat transfer as it avoids thermal resistances of additional interfaces.

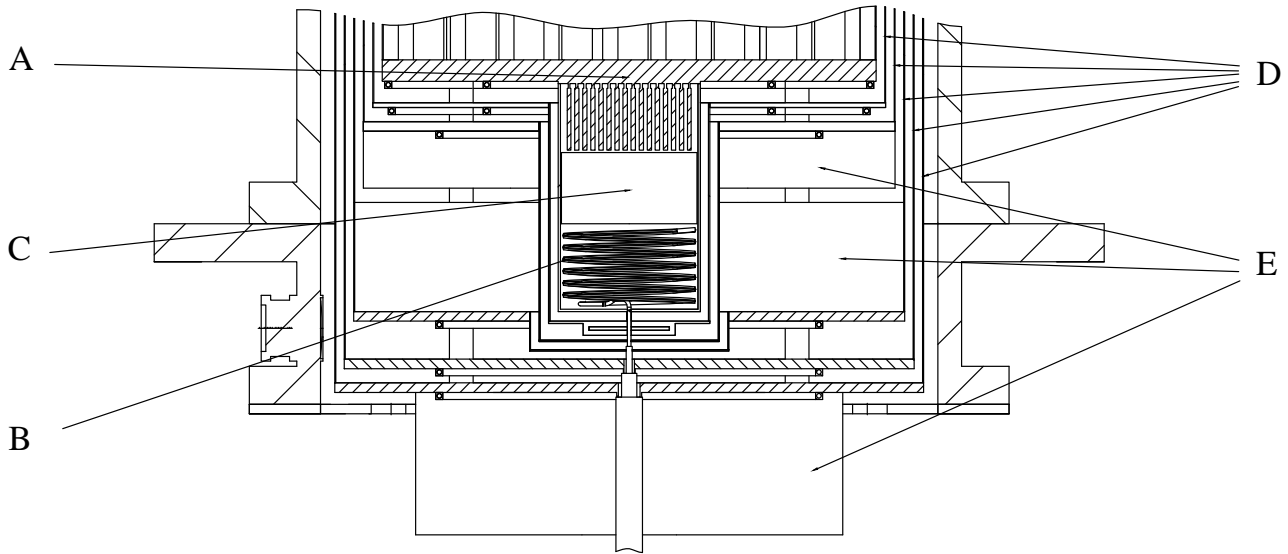


**Figure 2.12:** *A* is the mounting plate of the detector array with the heat exchanger inside the mixing chamber connected to it, *B* is the low temperature part of the DR's main heat exchanger, *C* offers space for an additional heat exchanger, *D* are the heat shields at 50 mK, 1 K, 5 K, 30 K and 100 K. *E* are thermalization regions for the front-end electronics.

The main heat exchanger of the DR and most of its pipe-work can be made of radio-pure copper, with minimal amount of eutectic Pb-Sn alloy for solder joints. The pipe sections between the step heat exchangers, which need to be thermally isolating, can be made of short lengths of thin-wall Cu-Ni alloy, weighing below 1 g. Their radio-purity has to be verified. The heat exchanger sponge will be made partly of standard mesh 325 copper powder and below 30 mK of fine copper powder. The low temperature part of the step heat exchanger is placed directly inside the mixing chamber. The dimensions have to be optimized to minimize the thermal conductivity of the dilute stream inside the mixing chamber at optimum flow. The optimum flow  $\text{opt}\{\dot{n}_3\}$  can be calculated with Niinikoski's theory [134]:

$$\text{opt}\{\dot{n}_3\} = 0.27 \sigma S T_m^2 \left( \frac{\text{K}^2 \text{ mol}}{\text{J}} \right) = 8.3 \frac{\text{mmol}}{\text{s}} \quad (2.1)$$

where  $\sigma$  is the heat exchanger surface area,  $S$  is the Kapitza conductance and  $T_m$  is the temperature of the helium mixture. In case the cooling power should prove insufficient to meet the requirements, more space is foreseen for a third heat exchanger that could feature a novel design.

The five concentric heat shields are cooled to approximately 50 mK, 1 K, 5 K, 30 K and 100 K. The shields are spaced closely with only 20 mm distance. This reduces the overall dimensions of the detector unit, while ensuring no contact between neighboring shields. The shields are made of highly radio-pure copper with thicknesses of around 2 mm, which is probably determined by the integrity

under their own weight during handling, rather than by thermal conductivity. By adding strength to their flanges and by designing appropriate tooling for handling, it may be possible to reduce the wall thickness even below 2 mm.

The cooling of the heat shields is achieved via the flanges. The thermal contact to the shields is mainly obtained by the pressed contact, provided by the shield's own weight. The 50 mK shield is cooled by the dilute stream of the DR and the 1-K shield by a pumped  $^4\text{He}$  bath. This lowers the temperature of the shield close to 1 K, and reduces the radiated heat load to the 50 mK shield. The 3 outer shields are cooled in series by a common flow of supercritical  $^4\text{He}$ . The helium stream enters at low temperature to cool the 5 K shield and increases in temperature while cooling the 30 K and 100 K shield.

For a fast precooling of the detector mass, the mixing chamber flange and the two innermost heat shields are cooled by a separate common tube, containing cold helium gas at a temperature of approximately 5 K. The detector mass will be cooled very efficiently by the mixing chamber flange made of high conductivity copper (RRR 1500) by means of a solid-solid interface, discussed in section 2.7. For good thermal conductivity the flanges of the heat shields and the mixing chamber are relatively massive.

The precooling strategy requires that the detectors are thermally connected to their support in such a way that a sufficient cooldown by conduction is possible at higher temperatures. However, at base temperature the detector has to be thermally weakly linked, to enable a sufficient increase in temperature, as a reaction to an impinging particle. This could be achieved by an optimization of the thermal contraction of the contacts. In case this is not possible, precooling of the detectors has to be performed with helium as an exchange gas. However, this option would require that the 50 mK shield be made a hermetic inner vacuum chamber, which introduces substantial changes in the design of the signal cables.

The thermal isolation support structures are made of radio-pure beryllium copper or suitable radio-pure titanium or vanadium alloys. These are very critical components because all of them include sections possessing buckling failure mode. The support structures between 10 mK and 50 mK are particularly delicate, because they are the nearest to the array and the hardest to shield. A stress already well below the elastic limit may lead to a large heat load that has not been characterized yet.

R&D is still ongoing to find a satisfactory technology for the cold electronics. The aim is to reduce the sensitivity to microphonic pick-up in the high impedance lines, connecting the sensors

on the detectors and the preamplifiers located outside the feedthroughs at room temperature. At the 100 K plate, the 5 K plate and the 1 K plate, spaces are available for thermalizing the front-end electronics. The design is flexible to adapt to the space requirements at different temperatures. Also the temperature of the last shield can be adapted according to the needs of the electronics. The refrigerator can be dimensioned to provide several hundreds of watts of cooling power at 5 K and 100 K, in order to absorb the heat from the front-end electronics.

The residual activity of the cold front-end stages of the preamplifiers should be characterized and minimized. In any case they will be located behind the detector array's support plate, which consists of a substantial amount of copper and will act as a shield. Furthermore, the plates of the thermalizations can be designed as additional shields if necessary.

The vacuum chamber for the array could be made almost entirely of radio-pure copper, whose thickness should be above 3 cm to achieve the required elastic stability. However, a composite construction with radio-pure PMMA, cast around a hermetic, thin-walled copper vacuum chamber, will be used, to reduce the amount of copper. Also, copper would dissolve in the deionized water, which would cause problems in the purifications circuit. PMMA has the disadvantage to be permeable to water. The combination will provide a perfect diffusion barrier and impermeability, with the PMMA providing the necessary strength for handling and resistance against elastic instability.

For good accessibility during assembly and maintenance work, the vacuum vessel is designed in three parts. The feedthroughs for the electrical connections are arranged on the middle part. This permits an easy removal of the top and of the bottom part of the vacuum chamber. The middle flange is made of a relatively soft acrylic-copper composite that cannot sustain directly the heavy load of the cold mass. A sub-frame that supports the cold mass weighing approximately 3 t is mounted to it. It is made of titanium alloy, which is mechanically strong and has a low thermal conductivity.

The cryoline is attached to the bottom of the vacuum vessel and will be discussed below. The whole detector unit should be mounted on a structure of acrylic (PMMA) or fibre reinforced plastic with high radio-purity. Several apertures are available for mounting the vacuum vessel and the connections, as well as for drainage of the water shield.

## 2.10 The Cryogenic Transfer Line

The cryogenic transfer line is a sophisticated connection, carrying the 50 mK to 750 mK part of the main heat exchanger of the DR, as well as the  $^4\text{He}$  tubes for precooling the array and the  $^4\text{He}$  lines for cooling the thermal shields. As shown in Figure 2.9, the cryogenic line bridges the 6 m gap between the detector unit and the still, which is situated inside the second vacuum vessel outside the water shield. The outermost line at ambient temperature acts as a pumping tube for the vacuum vessel of the detector array. The parts at different temperatures are thermally isolated by vacuum. The 100 K and 5 K tubes are thermalized by the outgoing and the returning supercritical helium stream used for cooling the outermost 3 shields. The 1 K shield carries the supply line and the pumping tube for the helium bath in the detector unit, as well as the lines of the fast precooling. The innermost line is the main heat exchanger of the DR. All inner tubes of the cryoline should be made of copper. For the outermost tube and also for the tubes which carry the signal cables through the water shield, a similar design as for the vacuum chamber should be used, made of a Cu/PMMA composite.

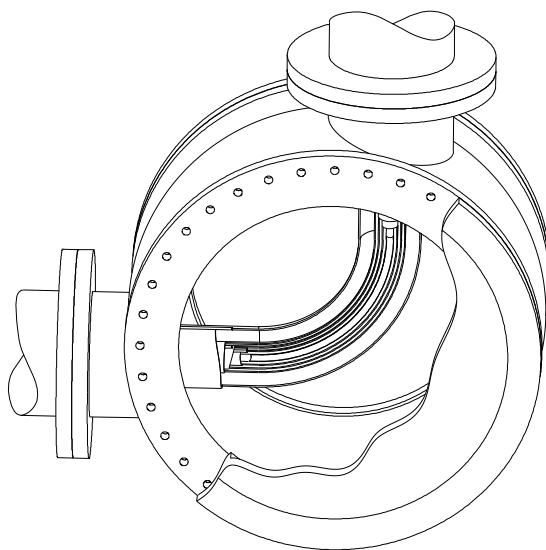


**Figure 2.13:** A cylindrical structure around the 90° bend of the cryoline provides access to the inner lines to enable the assembly.

To avoid guiding fast neutrons through the cryoline traversing the water shield into the detector unit, the line is designed as small as possible in diameter, and it features a 90° bend within the water shield. Simulations were carried out concerning the influence of “holes” in the water shield, created by the cryoline and the tubes for signal and power cables, on the neutron flux [43]. A 2.5 m long straight pipe, with a diameter of 10 cm, followed by a 50 cm elbow suppresses the flux of fast

neutrons by a factor of  $4 \cdot 10^7$ . This attenuation corresponds roughly to 1 m of water. The flux is not much influenced by the pipe material and thickness, nor by its diameter. An increase in diameter from 10 cm to 20 cm worsens the suppression only by a factor of 2. On the contrary, increasing the radius of the  $90^\circ$  bend from 30 cm to 100 cm improves the suppression by roughly 2 orders of magnitude.

An access area, shown in Figure 2.13, is foreseen at the bend to enable the assembly of the line. This permits sufficient access from 2 sides for assembling the large number of tubes. The heat shields need to be well thermalized and can be screwed for easy access. The main heat exchanger, the cooling and the precooling tubes require absolute leak tightness and therefore should preferably be welded or soldered. A screwing connection would simplify the installation but would likely raise a reliability issue in the long term.

The signal lines can also pass through the cryoline, which would enable to move the vacuum feedthroughs outside the water shield. If they follow independent paths, it is mandatory that they have  $90^\circ$  bends inside the water shield.

## 2.11 The Layout of the Proximity Cryogenics

For EURECA, industrial type helium refrigerators will be used. The Gifford McMahon and the Pulse Tubes refrigerators, or other small scale cryocoolers are not suitable for the main cryogenics cycle. The large scale detector array of EURECA requires a well designed, powerful and flexible cryogenic system. Cryocoolers are limited in their performance to approximately 1 W to 2 W at 4.2 K. Therefore, approximately 50 or more cryocoolers would be required to replace one large helium refrigerator. The cooling power, the liquefaction capacities and the dimensions of the available systems<sup>4</sup> are given in Table 2.11. As an option, built-in purifier systems, with online treatment of impurities, can be integrated. Also, cryocoolers have a lower efficiency by more than an order of magnitude in comparison to a cold box with two or more turbine expanders. Accordingly, the installed electrical power and the cooling of dissipated electrical power would be higher by more than a factor of 10. Furthermore, cryocoolers do not permit a priori to circulate the helium fluid flow for precooling or for baseline operation as it is possible in the case of refrigerators. This circulation system would have to be specifically designed, which would cause additional complications [68].

---

<sup>4</sup>Linde Kryotechnik AG, model L(R) 70, L(R) 140, L(R) 280

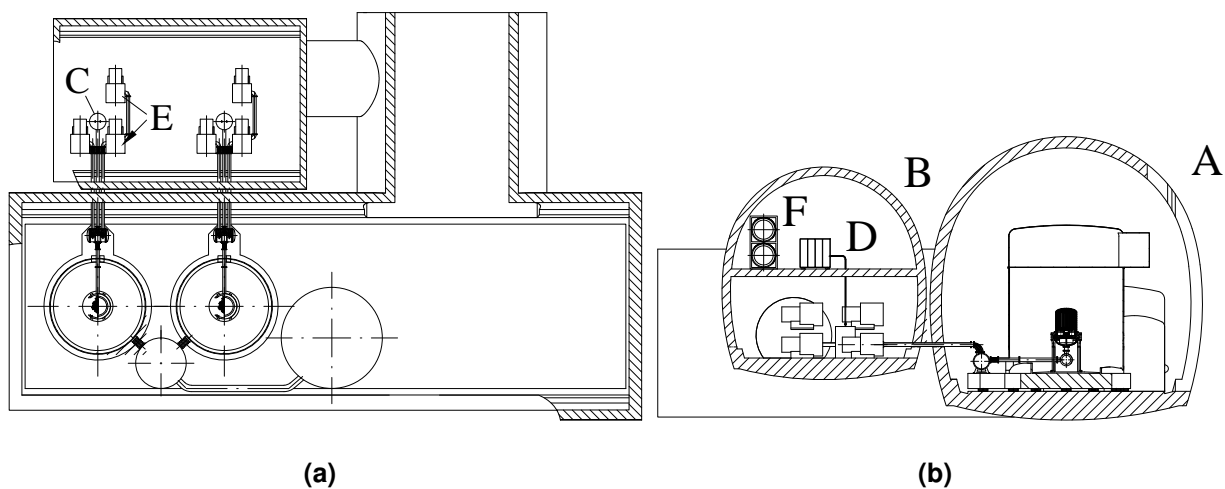


**Figure 2.14:** Layout of the proximity cryogenics. A is the main cavern, B is the side cavern, C is the helium refrigerator, D is the compressor, E are the pumps and F are the pressurized helium vessels.

**Table 2.11:** Dimensions, liquefaction capacities and further properties for industrial type helium liquefiers.

Liquefaction capacity (L/h)	44	56	67
Cooling power at 4 K (W)	100	200	400
Noise level (dB)	> 70		
Outer diameter (m)	1.3		
Min. height to remove internals (m)	4.8		
Weight (kg)	2000		

For placing the compressor of the refrigerator, two options were studied:

1. outside the tunnel at large distance with pneumatic links to the refrigerator and,
2. close to the refrigerator and the experiment.

The compressor of a refrigeration unit is very noisy and requires 125 kW electrical power and the equivalent cooling water flow. The noise level is approximate 73 dB. The available cooling options of sample compressors are either water cooling (5.6 m<sup>3</sup>/h to 8.1 m<sup>3</sup>/h) or air cooling (13 000 m<sup>3</sup>/h to 14 000 m<sup>3</sup>/h). The electrical power demand, the dimensions and the mass of sample compressor

units<sup>5</sup> are given in Table 2.12. For these reasons, the first option would be interesting, because cooling and electrical power is easily available at the surface. Also, the great distance from the experiment would facilitate the vibration control. The gaseous helium reservoir, which presents a potential safety risk underground, could also be removed from the cavern. However, a distance of 6 km would have to be bridged with high and low pressure lines. This represents disadvantages of high costs and safety risks due to the pressure lines running through the tunnel. This setup would also complicate the start up of the system with a delayed pressure signal due to the large distances and volumes. Furthermore, commissioning and trouble shooting in case of a leak could prove to be difficult [68].

**Table 2.12:** Examples of average compressor properties.

<i>Electr. Power</i> (kW)	<i>Dimensions</i> (m)	<i>Mass</i> (kg)
90	1.95 x 1.285 x 2.1	2050
110	2.23 x 1.96 x 1.89	3300
132	2.23 x 1.96 x 1.89	3400

Secondly, option number 2 will be presented. Given the disadvantages of the first one, the latter option was chosen for the baseline design. Placing the compressor in the proximity of the refrigerator will clearly minimize the cost for infrastructure and commissioning of the system. Therefore, this option is more efficient than the other due to its compactness. However, the pressurized helium vessel has to be placed inside the cavern, requiring additional safety precautions. For damping the vibrations, suitable solutions are available and are discussed below.

The two DRs will be supplied by two independent helium refrigerator cryoplants that feature facilities for fast precooling and warm-up of the arrays. The pumps of the DR and the cold boxes of the helium cryostats are housed in a side cavern. The liquifier is less noisy, but its vibration spectrum features strong components at the frequencies of the turbines and their harmonics, which fall into the spectrum of phonon signals of the detectors. The compressor and the gas handling system for the liquifier are located in another room in the side cavern, with easy access from the safety tunnel. This facilitates the vibration isolation, maintenance and access for electrical power and cooling.

Vibrations are a source of heat load and microphonic parasitic signals, and therefore these have to be minimized in a cryogenic system. Vibrations are mainly excited by the pumps and the com-

<sup>5</sup>KAESER KOMPRESSOREN, model DSD 172, DSD 202 and DSD 238

pressors. The signal lines inside the detector unit must be designed to provide immunity against microphonic pick-up and to damp vibrations.

The vibrations from the pumps and compressors are transferred via the tubes but also via the basement. The detector-unit inside the pool and the cryogenic-unit are placed on a common platform shown in Figure 2.9, constructed of 1 m concrete as they are connected via the rigid cryoline. The whole mass is supported by air springs that must sustain the mass of approximately 700 t. Suitable dampers are available from seismologic protection systems for buildings<sup>6</sup> that can support an axial force of up to 6000 kN. A possible strategy could be offered by a semi-active system [131] or an active feed-forward vibration isolation system [4, 132]. Seismometric measurements can determine the level of vibration and piezo-electric actuators could then compensate the movements [91].

The lines to the <sup>3</sup>He and <sup>4</sup>He pumps, as well as the liquid helium transfer line pass through the wall between the main cavern and the side cavern, which is acoustically decoupled from the main hall. The cryogenic unit is decoupled from vibration by flexible sections and damping structures that are optimized for the spectrum of the vibration of the pumps and the helium liquifier. These flexible sections also allow the necessary movement of the platforms of several centimeters when emptying the water vessel.

## 2.12 Conclusions

As was suggested in Section 2.4, the EURECA Collaboration has already chosen the Pool design of the water shield as Baseline solution. Based on this and the design studies conducted in this work, the EURECA collaboration adopted a fast cycling dilution refrigerator in the Baseline design. Two dilution refrigerators will be used, able to cool 500 kg of detector material each; this will permit to run continuously one half of the array while exchanging parts of the other half. The fast precooling of the DR allows a rapid exchange of detector material. The alternative method for rapidly exchanging part of the detector material, the load lock system, was studied and discussed in this chapter. The system is technically feasible but not favourable due to its mechanical complications and necessity to use materials whose radio-purity is questionable. The R&D of the load lock design is still ongoing within the EURECA collaboration (in the Néel Laboratory of CNRS Grenoble), and it could be still used for one of the detector units. The comparison of the two shielding concepts using water as

---

<sup>6</sup>MAURER SÖHNE, seismic viscous dampers MHD and MHD-R

shielding material, the pool and the submarine design, showed clearly the superiority of the former under the condition of a detector unit with ultra low radioactivity. The design of such a DR was discussed in this work using almost exclusively radio-pure materials, like copper and PMMA. The feasibility of producing a heat exchanger made of copper will be discussed in Chapter 5.

## Chapter 3

# The CDR Instrumentation and Control System

The CDR is a dilution refrigerator that was designed and built at the CERN Central Cryogenic Laboratory and which is used for measurements at temperatures down to 10 mK. To enable highly sensitive temperature measurements at very low temperatures, the electrical setup was completely redesigned. Thermometers and heaters are excited with very low currents, often with a few pA only, due to the small cooling power and the low thermal conductivity at low temperatures. Not only is the integrity of these very small signals easily corrupted by interferences at radio frequencies, but the unwanted pickup signals dissipate power in resistance thermometers, which is seen as a parasitic heating of the thermometer above the temperature of its heatsink.

Until a few years ago, most of the Electro Magnetic Compatibility (EMC) problems concerned external cables that were long enough to act as 'accidental antenna' at the frequencies being employed by the electronic technologies of the time, generally at Radio Frequencies (RF). The design techniques used then were developed to save money. However, techniques such as single-point grounding and terminating cable shields at one end only, are not sufficient anymore for today's electromagnetic environment. Nowadays, electromagnetic signals are present at frequencies between 50 Hz and 2.5 GHz. Therefore, the implementation of strict EMC techniques is essential to avoid the parasitic coupling of these signals to the electronic setup.

### 3.1 Electromagnetic Compatibility and Immunity

All cables and conductors of the circuitry have to use EMC design. They carry both Differential Mode (DM) and Common Mode (CM) signal and noise, caused by digital and analogue high-speed electronic devices. A conductor with a length of only 10 mm is an excellent antenna at 30 GHz and it is only a little less good antenna at a frequency of around 70 MHz, where its antenna gain is -40 dB. For sensitive applications even this can cause interference problems at frequencies as low as 7 MHz [12]. Wire loops emit and pick up magnetic fields and the magnetic components of electromagnetic fields. The characteristic dimension corresponding to the half wave length is the length of a straight conductor or the radius of a circular loop, or half the loop's longest diagonal dimension.

Filters are used to attenuate unwanted frequencies traveling along conductors and are also characterized by attenuation versus frequency curves. By creating an intentional discontinuity in the characteristic impedance of a current path, RF energy is either reflected away from a protected circuit or dissipated by the filter.

Therefore, shielding and filtering techniques have to be applied. For shielding to work well, especially at frequencies above 100 MHz, it needs to be uninterrupted. Cable shields have to be connected with the shield bond 360 ° at both ends to components that are shielded themselves.

The RF reference, often referred to as “earth” or “ground”, is important for shieldings and filters to control CM currents. For ground installation of buildings the main consideration is safety against electrical power system faults and transients due to lightning, with typical currents being 10 kA. They utilize long conductors to connect to the main safety ground terminal. Depending upon the material and the cross section, the inductive impedance of a wire of 10 m length exceeds its resistive impedance above a few kHz. Even worse, at about 75 kHz it significantly starts to behave as an antenna, which renders it useless at such frequencies.

The only effective RF reference is a local one. In order to be useful for EMC, a low impedance earth or ground structure in an installation should be closer to the device to be grounded than one-tenth of a wavelength at the highest frequency of concern. Such a structure is called RF reference structure. To work well as RF reference up to highest frequencies, a structure should be made of a large metal sheet or of a meshed common bonding network<sup>1</sup> as described by the International

---

<sup>1</sup>MESH-CBN

Electrotechnical Commission in IEC 61000-5-2 [51].

The electronics layout provides metallic structures working as an effective RF reference with a low impedance at frequencies as high as possible. The reference plane is established by the metallic cryostat around the DR and by the electronic racks and boxes, which are connected by a mesh of several copper braids. The cryostat with its metal sheet provides an almost ideal grounding structure with a low impedance up to several hundred MHz [12]. The electronic racks are constructed as closed metallic boxes and will be discussed below. The connections made by a large number of copper braid shields around the cables connecting the cryostat and the electronic rack, form a low-impedance mesh up to tens of MHz.

## 3.2 The Electronic Racks

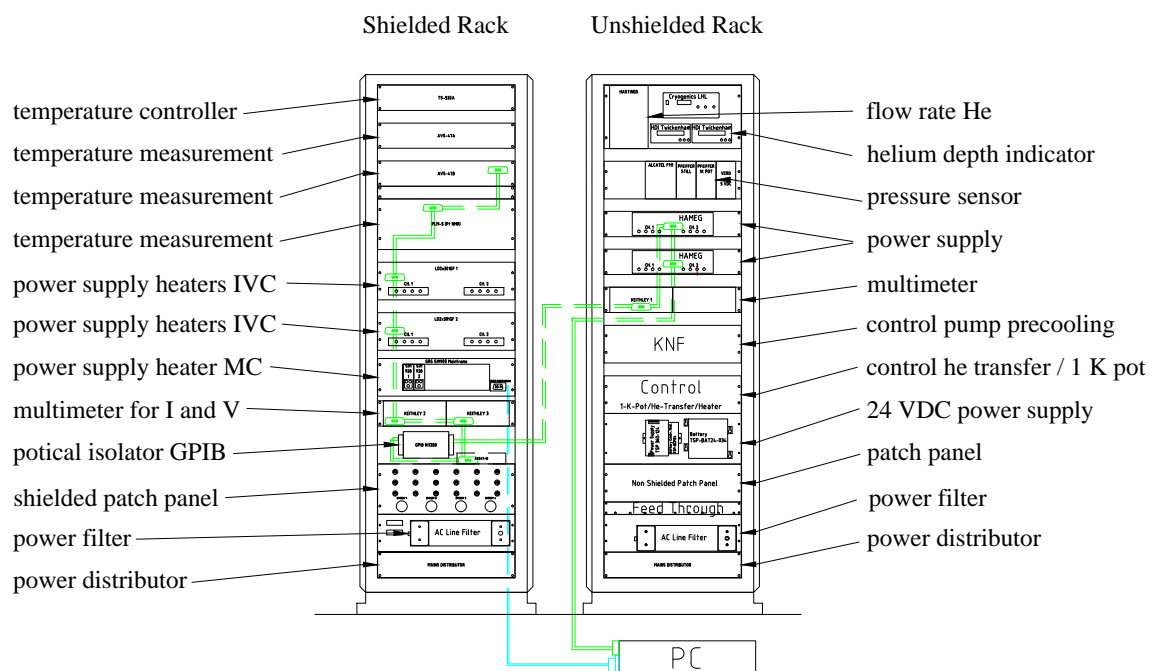


**Figure 3.1:** The devices in the shielded and in the unshielded electronic rack, with the connection scheme of the GPIB and the serial bus system.

The electronics at room temperature are segregated into two racks. The noisy and less sensitive components are placed in one rack called the “unshielded” rack, whereas the very sensitive ones are situated in a second rack called the “shielded” rack. The signals of the devices placed in the unshielded rack are less sensitive. Therefore, shielding from external sources is less important. Instead, the aim is to reduce emissions, in order not to interfere with the devices of the sensitive electronic

rack. However, shielding in the near-field of a source proves very difficult, because the shield's efficiency is strongly corrupted by apertures. Even through very small holes, very significant amounts of leakage can occur, especially at low frequencies [5]. The approximate estimations on the far field (see below) are mostly not applicable and therefore, the leakage is difficult to predict. Thus, the segregation of devices with different sensitivities is a more suitable approach for this application.

**Table 3.1:** List of devices used in the shielded electronic rack with their EMC relevant description.

<i>Device</i>	<i>Manufacturer</i>	<i>EMC comment</i>
Temperature controller	Picowatt TS-530A	-
Thermometer	Picowatt AVS-47A	-
Thermometer	Picowatt AVS-47B	-
Thermometer	Picowatt PML-5	-
Power supply	Zentro-Electric LD2x301GF	Emission: EN50081-1, Immunity: EN50082-2
Isolated voltage source	Stanford Research Systems Sim 928	Battery powered ultra-clean voltage source
Mainframe for SIMs	Stanford Research Systems Sim 900	-
Patch panel	Elma Electronics AG	superior level, given in Table 3.4
GPIB optical isolator	National Instruments	Emission: EN 61326-1:2006, immunity: EN 61326-1:2006
RS-232 fiber optic modem	B&B Electronics Mfg. Co. 9PFLST	EN 55022, EN 61000-6-1, EN 61000-4 (-2 to -6, -8, -11)
Power distributor	MPS 2972	Metallic enclosure

The devices in the shielded rack are used for sensitive signals entering the cryostat, such as the thermometry and the power supply of the heaters inside the Inner Vacuum Chamber (IVC). A complete list of all devices is given in Table 3.1.

In the “unshielded” electronic rack, the noisier, less sensitive devices are placed whose signals are not entering the cryostat, such as the readout electronics for the sensors at ambient temperature.

**Table 3.2:** List of devices used in the unshielded electronic rack with their EMC properties.

<i>Device</i>	<i>Manufacturer</i>	<i>EMC comment</i>
<sup>3</sup> He Flow-Meter (< 10 mmol)	Hastings	-
<sup>3</sup> He Flow-Meter (< 3 mmol)	Bronkhorst	-
Helium depth indicator	Twickenham	-
Pressure IVC	Alcatel F111	-
Pressure still / 1 K pot	Pfeiffer	Emission: EN 61000-6-3, immunity: EN 61000-6-2
Condensation pressure	WIKA	EN 61326
Multimeter	Keithley	89/336/EEC, EN61326-1.
Patch panel	CERN store	Metallic enclosure with improved contacts
Control precooling pump	PR Electronics 2289	EN 61326
Control helium transfer/1 K pot	Cryolab	Relays, noisy switching devices
Power supply	Hameg	Switching
24 VDC power supply	Traco Power TSP 360-124	Emissions: EN 61000-6-3, EN 61204-3 Immunity: EN 55011 class B, EN 55022 class B
Battery controller module UPS	Traco Power TSP-BCM24	EN 61000-6-3, EN 61204-3
Battery	Panasonic LC-R123R4P	-
Power distributor	MPS 2972	Metallic enclosure

The indicators of the pressure gages, the helium depth indicators and the flow meters are located there. Their analogue signals are routed to the readout electronics. Also, the control electronics for the automatic helium transfer and the control of the 1 K pot, which will be described in section 3.6, are placed in this rack. Moreover this rack contains the DC power supplies for 5 VDC and 24 VDC.

The 24 VDC Ultra safe Power Supply (UPS) feeds critical systems, such as the helium transfer, to ensure the fail safe control of the cryostat in case of a electrical power cut. The complete list of components in the unshielded electronic rack can be found in Table 3.2.

The very noisy electrical power relays and other such devices are completely removed from both racks. The noisy control of the  $^3\text{He}$  and  $^4\text{He}$  pumps was placed in the electrical power distributor, remote from the electronic racks.

Both electronic racks are constructed as closed metallic boxes, to provide a low impedance RF reference plane. The doors are pressed with a spring-loaded mechanism to achieve electric contact, while allowing fast access. At the front, the electronic devices are screwed extensively to the metallic chassis, forming a low impedance connection. For good thermal stability inside the closed racks, the devices are mounted with spacings. Those gaps are closed with 3 mm thick aluminium panels.

Sufficient cooling of the devices in the racks is provided by fans installed on top of the racks, with a volume flow rate of 100 L/s. The maximal power dissipation from the single devices is shown in Table 3.3. As never all devices are operated at their maximal power at the same time, a value of 500 W per rack shall be estimated for the following very simplified calculations. Assuming that all this power  $P$  is removed only by the air, the maximal increase in the air temperature  $\Delta T$  can be calculated by

$$\Delta T = \frac{P}{c_{P,air} \rho_{air} \dot{V}}, \quad (3.1)$$

where  $c_{P,air}$  and  $\rho_{air}$  are the specific enthalpy and the density of air at ambient temperature.  $\dot{V}$  is the volume flow rate of the fan. With the values  $\rho_{air} = 1,293 \text{ kg/m}^3$  and  $c_{P,air} = 1.005 \text{ kJ/kg K}$ ,  $\Delta T$  amounts to less than 4 K.

The ventilation aperture for the fan is screened from EM interference with a fine perforated metal grid with round holes (diameter 8 mm, pitch distance 12 mm, thickness 2 mm) that restricts the airflow in a small measure. For EMC round mesh shapes are preferred over rectangular or slot apertures with the same area, because they have a smaller characteristic dimension.

The ventilation system needs regular cleaning from the dust that is carried by the air-passing through. Therefore, an air filter at the bottom of the electronic rack would be a recommended improvement in the future. Although it would lead to a minimal increase of the flow restriction, an air-filter would reduce the maintenance significantly.

The communication between the readout electronics of both electronic racks and the computer is

**Table 3.3:** The power dissipation of the components located in the electronic racks.

<i>Shielded rack</i>				<i>Unshielded rack</i>			
<i>Device</i>	<i>Qt.</i>	<i>Power/device</i> (W)	<i>Power</i> (W)	<i>Device</i>	<i>Qt.</i>	<i>Power/Device</i> (W)	<i>Power</i> (W)
Sim 928	2	10	20	Twickenham	3	100	300
Keithley	2	22	44	Keithley	1	22	22
TS-530A	1	24	24	Hastings	1	15	15
AVS-47A	1	24	24	Pfeiffer	2	15	30
AVS-47B	1	11.5	11.5	Alcatel F111	1	15	15
Sim 900	1	150	150	Hameg	2	150	300
LD2x301GF	2	60	120	KNF	1	72	72
Total power		392.5		max. 814			

performed by a combination of GPIB<sup>2</sup> and a serial bus system. The latter is used by the SIM 900 mainframe to communicate with the isolated power supply module<sup>3</sup>. As an opto-isolation, a fiber-optic modem<sup>4</sup> is used. The unit is port powered by the RS-232 transmit data and handshake lines, which avoids a coupling via galvanic connection. Fibre-optics is the best medium for communication when considering EMC because metal conductors and their typical problems are avoided. Metal-free fibre-optic cables can pass right through the walls of shielded enclosures, without compromising the enclosure shielding. Another advantage is the automatic achievement of galvanic isolation of very high voltages.

The GPIB bus system connects in series all the readout electronics of the sensitive rack, the devices from the unshielded electronic rack and the computer. An optical isolator<sup>5</sup> separates the shielded rack electrically at the interconnection to the unshielded one, in order to control induced common-mode noise. Double-shielded GPIB cables reduce the emissions inside the shielded rack and improve the immunity. The connection scheme is shown in Figure 3.1.

<sup>2</sup>General Purpose Interface Bus

<sup>3</sup>Stanford Research Systems SIM928

<sup>4</sup>B&B Electronics, type 9PFLST

<sup>5</sup>National Instruments, NI GPIB-120B

### 3.3 The Patch Panels

The patch panel of the shielded rack is a central part of the electronic system. It distributes the cabling for the heaters in the inner vacuum chamber (IVC) and of the AVS-46 thermometer. The latter was upgraded by the newer AVS-47B thermometer, which was directly connected to the sensors. The patch panel<sup>6</sup>, is constructed as a shielded enclosure, often called a 'Faraday Cage'. It fits in the 19 inch electronic rack and has a height of 4 inches. The frame is made of electrically conductive aluminium extrusions, the side/front/back panels being 2 mm aluminium and the bottom/top panels being unperforated 1.5 mm aluminium.

Having thicknesses of 1.5 mm and 2 mm, the aluminium panels achieve several skin-depths of absorption above frequencies of a few 10 kHz. In combination with the high conductivity of aluminium, they are good at shielding any kind of fields. The shielding efficiency figures of the shielded patch panel given in Table 3.4 show an attenuation that is fairly good above 10 kHz and excellent above 10 MHz.

**Table 3.4:** Attenuation of the patch panel of the shielded electronic rack.

<i>Attenuation</i>	<i>Value</i> (dB)	<i>Frequency Range</i>
Magnetic-field	≈ 40 to 70	from 10 kHz to 30 MHz
Electric-field	> 60	from 10 MHz to 1 GHz

All devices in the sensitive electronic rack were chosen for their low emissions, therefore no excessive electric or magnetic emissions are evident in the proximity. Accordingly, the patch panel has to shield from electromagnetic fields originating from sources further away. These far-field electromagnetic waves have an impedance of propagation in air of approximately  $377 \Omega$  [12]. Therefore, good shielding efficiency depends upon the surface conductivity and the thickness of the shield.

The necessary thickness depends upon the skin depth. When a radiated wave impinges upon a conductive material it generates surface currents in the material. As the transmitted wave penetrates a shield it gives rise to eddy currents inside the material of the shield. The finite conductivity of the material causes these eddy currents to lose energy as heat, governing the absorption rate of the

---

<sup>6</sup>Elma Electronics EMC subrack type 12

transmitted wave. The rate depends upon the frequency, the conductivity and permeability of the shield material. This decline in current density with depth is called the 'skin effect'. The skin depth  $\delta$  is the depth in the shield material at which the current density has decreased to  $1/e$ . It can be calculated from [26]

$$\delta = \frac{1}{\sqrt{\pi f \mu_0 \mu_R \sigma}}, \quad (3.2)$$

where  $f$  is the frequency,  $\mu_0$  is the permeability of free space,  $\mu_R$  is the relative permeability and  $\sigma$  is the electrical conductivity,

The external surface currents created by the interaction of the shield with its external EM environment are CM currents. The internal surface currents are created by the CM currents leaking from the DM signals or RF noise in the send/return conductor in a twisted pair. For good immunity/low emissions the current density in the shield material has to be very low by the time it reaches the inner/outer surface of the shield. Therefore, the shield should provide several skin depths. Using the values for aluminium, of which the shielded patch panel is made of, equation (3.2) yields for the skin depth to

$$\delta = 66 \text{ mm} / \sqrt{f/\text{Hz}}. \quad (3.3)$$

For example at a frequency of 160 MHz one skin-depth for aluminium is 0.005 mm.

However, problems at higher frequencies are mostly caused by apertures and by penetrations of unfiltered cables. The currents flowing at the surface of a shield, originating from interaction with a field, are diverted around apertures. This creates a magnetic field oriented to pass straight through the aperture. The voltage difference originating from the currents flowing in the inductance generates an electric field. The penetration of both magnetic and electric fields reduces the shielding efficiency.

Therefore, the control of apertures is essential to achieve and maintain the good EMC level specified by the data-sheet of the patch panel installed in the shielded rack. In practice, apertures are the single dominant factor at higher frequencies (above 100 kHz) and more important than the material and the thickness of the shield [12].

The shielding efficiency  $SE$  of a single aperture in the far field, below its first resonance, decreases approximately by 20 dB per decade. The lowest resonance is the frequency, at which the largest dimension  $g$  of an aperture equals  $\lambda/2$ , half the wavelength. The dimension  $g$  can be the diameter or the longest diagonal [12]. The efficiency varies as

$$SE \simeq 20 \log_{10}(\lambda/2g) \text{ dB}. \quad (3.4)$$

A single aperture of  $\lambda/100$  gives a shielding efficiency of 34 dB. To achieve a shielding efficiency of 40 dB at 1 GHz the largest aperture should be less than 1.5 mm.

Apertures with a characteristic dimension  $d$  larger than  $\lambda/2$  act like perfect antennas. The shape makes little difference and gaps of the width of a coat of paint or the film of oxide is sufficient to ruin the shielding efficiency. For that reason, all spaces between fixes, where good electrical contact cannot be assured or might degrade in time, have to be treated as large apertures.

The effect of  $N$  apertures in the far field with a separation distance of less than  $\lambda/6$  is assumed to add in-phase. The shielding efficiency of the shielded enclosure will be reduced by

$$\Delta SE \simeq 20 \log_{10}(N) \text{ dB.} \quad (3.5)$$

Two identical apertures will reduce the shielding efficiency by 6 dB and every doubling of the number of apertures will reduce the efficiency by further 6 dB [12]. Placing the apertures at distances larger than  $\lambda/6$  from each other, will partly result in phase-canceling of the leakage. The improvement is dependent on the frequency and on the location of the apertures in the enclosure.

Although the simplified equations (3.4) and (3.5) derive a different result, in practice many small holes have a better shielding efficiency than a single hole with the same surface area [12]. For evaluating the effect on the shielding efficiency when replacing a large square aperture by a large number of small apertures, a suitable equation is

$$SE \simeq 20 \log_{10} \left[ \left( \frac{p^2 l}{f^3} \right) + 27 \left( \frac{d}{l} \right) + 0.8 \right] \text{ dB,} \quad (3.6)$$

where  $d$  and  $l$  are the length of the side of the original and of the small square holes,  $p$  is the pitch of the smaller holes and  $f$  is the thickness of the shield material. The equation is valid for  $l < \lambda/6$ . The shielding efficiency of a single square hole with a dimension of 100 mm amounts to 11 dB at 300 MHz according to equation (3.4). Replacing it by hundred 10 mm square holes with 11 mm pitch in a metal with a wall thickness of 1 mm, improves the shielding efficiency by about 25 dB.

To reduce aperture leakages in the patch panel, unnecessary holes were eliminated. Unperforated covers were used and the holes in the side panels, available for different mounting options, were closed using electrically conducting tape. The size of apertures was reduced in order to raise their resonant frequencies above the highest frequency of concern. Flexible conductive gaskets, called EMC gaskets, were used to reduce the aperture size of removable covers. It is not possible to rely on a good electrical contact between the screwed connections. Necessary apertures for connectors were broken up into smaller ones, by the use of several small connectors instead of a few large ones.

To prevent shield degradation from conductor penetrations, all cables have to be shielded or filtered at the point of penetration. The cables that are connected to the patch panel use shielded twisted pairs. Their shields are only used for interference control but not for carrying signals or power return currents. This ensures the best EMC performance for both immunity and emission. The cable shields have to be 360 ° metal-to-metal bond to the enclosure's wall at the point of penetration.

A list of the EMC compatible connectors is given in Table 3.5. They enable a good electrical contact between cable shield and connector, between two mating connectors, and between connector and patch panel. A large number of cables are necessary that penetrate the shield of the patch panel in order to supply the various heaters in the cryostat and to determine their heating power. 15 audio connectors<sup>7</sup> on the front of the patch panel are used to connect several power supplies, an ampere- and a voltmeter. The signals are rerouted inside the patch panel and exit again at the front by means of two 37-pin connectors<sup>8</sup>, to the cryostat. The first connector is dedicated to the heaters in the MC and the second one to the heaters in the IVC. A third 37-pin connector was used for the AVS-46 thermometer, which was replaced later. At the back of the patch panel, 4 EMC Sub-D connectors (DB9) are foreseen for thermometers used during the precooling of the cryostat, one EMC Sub-D connector (DB937) for the previously used thermometer AVS-46 and a 4-pin<sup>9</sup> connector for supplying the temperature controller.

To achieve the best shielding up to high frequencies, the shield has to be connected on both ends. In Figure 3.2 the metallic boxes are shown that were used where the connector of a device did not offer the possibility of connecting the shield properly. The shield is connected to the metallic box, with a 360 ° bond. The box covers the connector and is electrically connected to the plank panels of the electronic rack. Consequently, a low impedance path for the common mode currents of the cable shield is provided.

The cabling inside the patch panel was done with unshielded twisted pairs. To maximize the EMC performance of the cables, a dedicated conductor for the send- and the return-signal was used in each twisted pair. The effects of stray capacitances and inductances tend to cancel out for frequencies with wavelengths much larger than 10 times the twist-pitch, which reduces the rate of DM-CM (and CM-DM) conversion. Shielded twisted pairs would be even better, but they are difficult to handle in the necessary large number inside a small box. The EMC connectors maintain close proximity

---

<sup>7</sup>5-pin DIN PrehKeyTec

<sup>8</sup>Burndy, type 37-pin

<sup>9</sup>Burndy, type 4-pin

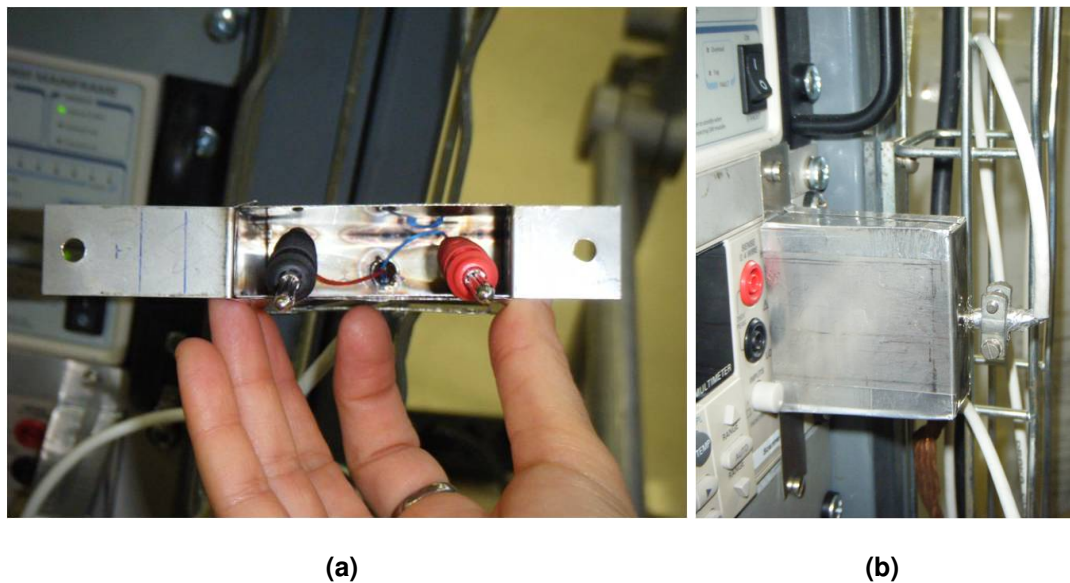


**Figure 3.2:** Metallic box for connecting the cable shield with a 360 ° bond to devices with banana connectors.

between their send- and return-pins.

The cables are routed close to the metallic chassis of the patch panel to control the CM currents and voltages. The conductive chassis acts as the CM return path and minimizes the CM current's send-/return-loop, which reduces the emissions and improves the immunity.

To reduce crosstalk, signal cables were segregated from power cables and were routed with as much as possible space between them. When cables of different sensitivity had to cross each other, this was preferably done at 90°, because in this way the negative impact is reduced.

The “unshielded” patch panel routes the signals from the sensors to the readout electronics and distributes the 24 VDC and the 5 VDC power supply. This patch panel uses the same design rules described above for the “shielded” patch panel. However, instead of purchasing a dedicated shielded enclosure, a standard 19 inch sub-rack casing was used and adapted for EMC. It features metallic covers all around that are bolted in short distances to reduce the effective aperture size. Having a maximal distance of 100 mm between reliable electric bonds, an improvement of the immunity against external interferences is expected at least at lower frequencies. All conductors that enter the patch panel use shielded twisted pairs, with their shield 360° bonded to EMC connectors. The unshielded cables of the DC power supply are filtered at the point of penetration.

Real-life filter performance is strongly dependent upon filter installation, especially upon the impedance of the RF reference and of the bond between the filter and the RF reference. The

**Table 3.5:** The EMC connectors used in the patch panel.

<i>Supplier</i>	<i>Connector</i>	<i>Description</i>	<i>EMC</i>
PrehKeyTec	Audio 5-pin DIN	4-wire signal routed to instruments	qualified for very low-level audio signals
CERN store	EMC Sub-D connectors (DB9, 25, 37)	miscellaneous	improved cable shield termination and EMI/RFI shielding, EMC notches, metal backshell.
Burndy	37-pin	for heaters in cryostat	connector with metallic shell
Burndy	4-pin	for power supply	connector with metallic shell

impedance should be much lower than that of the shunt capacitors in the filter, in order to allow the internal and external CM surface currents to find their optimum return paths. To specify a filter, it is necessary to know the spectrum of the wanted signals, so that the filter lets them pass whilst impeding unwanted noises. The performance of shielded enclosures can easily be degraded by RF noise that 'leaks' out along the cables that enter and exit the enclosure.

As filters, 'bulkhead'-mounted single line 5 VDC/24 VDC direct current line units<sup>10</sup> are used, with a power rating of 1 A and 10 A, respectively. The filters are mounted on the front wall of the shielded enclosure, with the metal cases of the filters electrically bonded to the shielding surface of the wall. They are situated inside the shielded box, with only the filter's input penetrating the enclosure. This reduces considerably the stray coupling between the filter's input and output. The filters offer attenuations of 100 dB above 50 kHz and above 200 kHz respectively, which remain constant up to 10 GHz.

### 3.4 The Cabling

Outside shielded enclosures, all cables use shielded twisted pairs. Inside the electronic racks, the cables were separated according to their sensitivity and to the noisiness of the signals they carry. The more noisy (although filtered) electrical power cables were routed on one side of the rack, whereas

<sup>10</sup>Modern Precision Engineers Limited, model DS23540 and DS23489

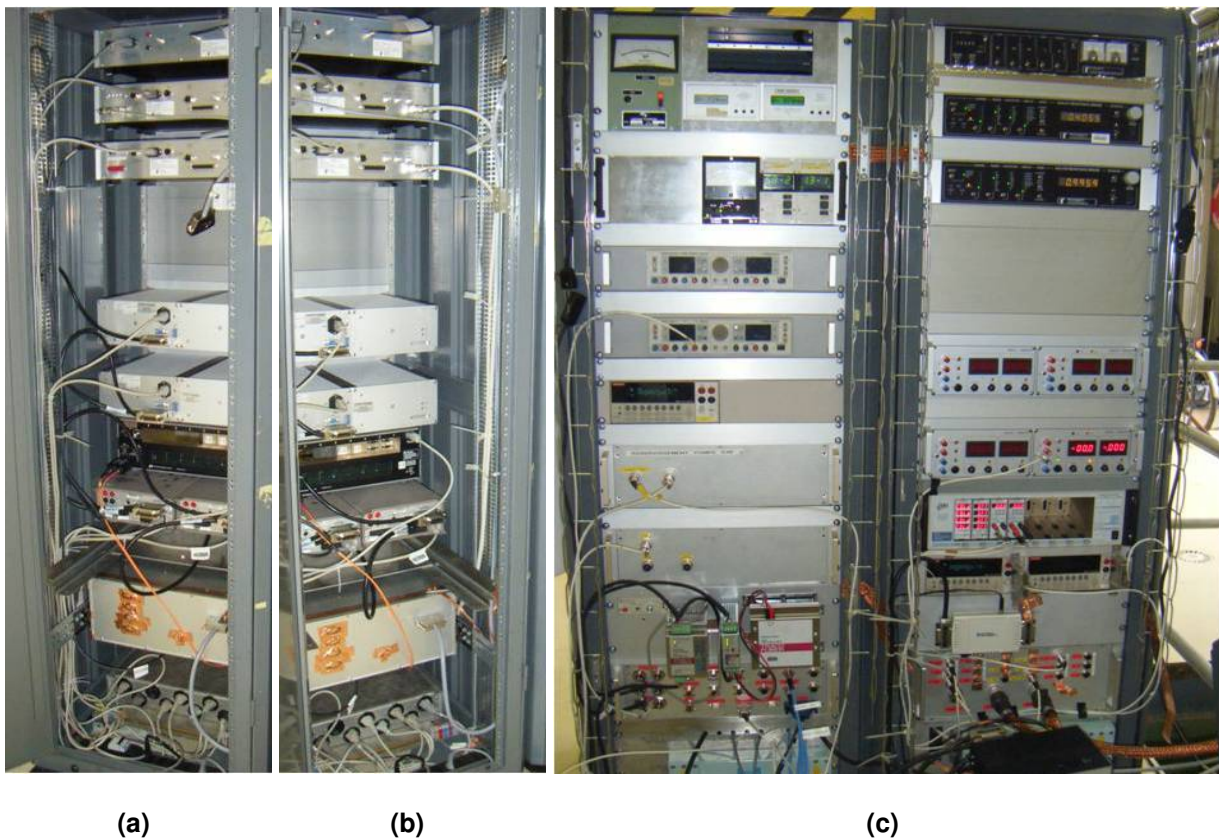


**Figure 3.3:** Segregation and grounding of the power cables left (a) from the signal cables on the right side (b) at the back of the sensitive electronic rack and at the front of both electronic racks (c). All cables are routed closely to a conductive path to minimize the CM send and return current loop.

the sensitive signals were run on the opposite side, as shown in Figure 3.3(a) and (b). All cables run side-by-side inside metallic cable trays along their whole length, to ensure the closest proximity to the reference ground. The trays are connected to the electronic rack (the RF plane) and offer a low impedance current loop for the CM currents.

The shielding of the shielded twisted-pair cables together with the EMC-connectors already provide a very high-performance (low-impedance) common mode return path for the “leakage” from the send/return pair of conductors. However, it is beneficial for EMC to route cables close to a low impedance structure (RF reference) in order to reduce surface currents on the outside.

The electrical power for the electronic racks is fed by a cable, shielded by a copper braid, from the power distributor. The electrical power is split inside a closed metallic box among the electrical power filters of both electronic racks. 360° metal to metal bonds are used between the braid, the

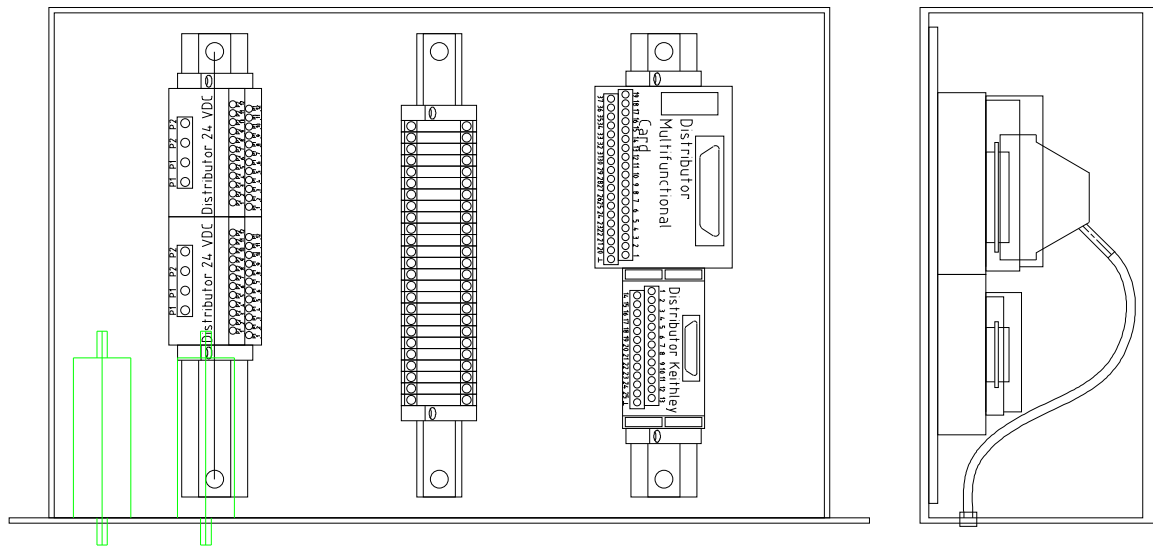


**Figure 3.4:** The patch panel of the not shielded electronic rack.

power distributor and the filters. Multi-line AC line filters<sup>11</sup> with a current rating of 10 A at 250 VAC are used as electrical power filters. It features a seamless metallic enclosure for good shielding performance. For the best performance up to the highest frequencies, the filter's metalwork is screwed directly to a blank panel of the electronic rack, forming a low impedance bond to the RF reference plane. The specification of the electrical filter is not extremely critical as the interferences are at a much higher frequency than the desired 50 Hz sine wave. The power filters use multiple filter-stages to provide high impedance discontinuity and thus high attenuation of 100 dB between frequencies of 100 kHz and 1 GHz. Due to the filter's construction, the device retains full performance even for different source and load impedances. In the real application this helps to achieve the specifications of the data-sheet.

Radio frequency stray coupling between the conductors of the unfiltered and filtered sides can easily degrade filter attenuation. At higher frequencies the impedances of the stray capacitances decrease whereas those of the stray mutual inductances increases. Therefore the amount of stray coupling bypassing the filter increases. To control this effect, the screw terminals are located in separate boxes, far from each other, on opposite sides of the device. The apertures for accessing the screw terminals on the input and output sides are closed with metallic lids using EMC gaskets to ensure a good electrical contact. The filtered side exits the filter directly into the rack's shield.

The structure of the cryostat with gapless metal sheets is an ideal shield. The shielding efficiency

<sup>11</sup>Modern Precision Engineers Limited , model DS23794

is mainly corrupted by metallic conductors penetrating the shield. To control the interferences caused by penetrating conductors, filters were placed at all four electrical connectors that were used during the operation of the cryostat.

The filters<sup>12</sup> are mounted directly at the connectors of the cryostat. They are  $\pi$ -filters with capacitances from 6000 pF to 12000 pF. To ensure that no gain occurs at any frequency of interest, extensive tests were performed on the electronic system with good results [135]. The very low base temperature that was measured by resistance thermometry, proves the efficiency of the filters and the whole electronic setup.

**Table 3.6:** The attenuation of the filters of the cabling entering the cryostat defined per MIL-STD 220 at 25 °, with no applied voltage or current, in a 50  $\Omega$  system.

<i>Frequency</i> (MHz)	1	3	10	30	100	300	1000
<i>Attenuation</i> (dB)	2	7	18	35	55	60	60

The cabling inside the dewar between 300 K and 4.2 K was achieved by 4 ribbon cables, one for every connector of the cryostat. They conduct the signals to the feed-through of the inner vacuum chamber (IVC). To optimize the EMC performance, the corresponding signal and return conductors were paired next to each other in the cables, as well as in the feed-throughs.

All thermometers and heaters inside the MC use 4-wire measurement technique. The cabling inside the IVC was done by two superconducting NbTi wire ribbon cables<sup>13</sup>, each consisting of 12 twisted pair wires. One ribbon cable was used for the thermometers, the other one for the heaters. The thermalization of the cables, from 4.2 K down to the MC temperature was performed at different temperature levels of 1.5 K, 700 mK and 50 mK, by wrapping the cables several times around copper bars of approximately 60 mm length and 10 mm in diameter and fixing them by means of Kapton adhesive tape. This ensures a negligible heat load to the MC by the wires via thermal conduction. Inside the MC, manganin wires with a diameter of 0.09 mm were used. The heaters and thermometers outside the mixing chamber use CuNi conductors for the current supply and manganin wires for the voltage measurement.

<sup>12</sup>Souriau 8AF51 M 26 pins

<sup>13</sup>Oxford instruments, loom 8, ref. A8-313

### 3.5 Thermometry

Inside the MC, a NTD<sup>14</sup> Ge temperature sensor<sup>15</sup>, which shall be called REF in the following, was used as the reference thermometer, calibrated in the range from 40 K down to 40 mK. A Chebychev polynomial type fit was provided to the calibration data for the temperatures between 44 mK and 853 mK

$$T = \sum_{i=0}^{10} A_i \cos \left[ i \arccos \left( \frac{(\log_{10}(R) - Z_L) - (Z_U - \log_{10}(R))}{Z_U - Z_L} \right) \right] \quad (3.7)$$

where  $T$  is the temperature,  $R$  is the sensor resistance,  $Z_U = 4.86487284241$  and  $Z_L = 3.63499992268$  are the upper and lower limits of  $\log_{10}(R)$  used in computing the Chebychev coefficients  $A_n$  given in Table 3.7.

**Table 3.7:** Chebychev coefficients of the calibration curve for the Lakeshore thermometer.

$A_0$	$A_1$	$A_2$	$A_3$	$A_4$	$A_5$
0.294701	-0.386296	0.201307	-0.095691	0.042883	0.018858
	$A_6$	$A_7$	$A_8$	$A_9$	$A_{10}$
	0.008535	0.003647	0.001454	0.000541	0.000108

A carbon composite<sup>16</sup> resistor and an off-the-shelf RuO<sub>2</sub><sup>17</sup> thick film resistor, called REF 1 and REF 2, were placed close to thermometer REF. These were used as reference thermometers below 44 mK due to their better resistance characteristics. Resistors of the same type as REF 2, called MC 1 to MC 3, were placed on samples inside the MC to measure their temperatures. The measurements inside the cryostat were performed in two cool downs. The names, types and mounting positions of the sensors inside the mixing chamber used for the cold runs 1 and 2 are given in Table 3.8.

The resistance thermometers at the lowest temperatures were read by 2 resistance bridges<sup>18</sup> with 8 multiplexed 4-wire input channels. These devices feature an external preamplifier that was placed at approximately 30 cm from the feedthroughs of the cryostat to reduce EMI parasitics on the sensitive lines. The connection to the cryostat is made via a double-shielded multiple-twisted pair cable. The shields have 360° bonds to the EMC connectors on both ends. The preamplifiers are mounted inside

<sup>14</sup>Neutron Transmutation Doped

<sup>15</sup>Lakeshore type RX-202A-AA-0.05B

<sup>16</sup>Speer 100 Ω 1/2 W grade 1002

<sup>17</sup>NIC components Corp., type 1206±1, 1 kΩ at 300 K

<sup>18</sup>Picowatt AVS-47A and AVS-47B

**Table 3.8:** Temperature sensors inside the mixing chamber.

<i>Mounting position</i>	<i>Sensor type</i>	<i>Name in cold run 1</i>	<i>Name in cold run 2</i>
Liquid He	NTD Ge	REF	REF
Liquid He	Carbon composite	REF 1.1	REF 1.2
Liquid He	RuO <sub>2</sub>	REF 2.1	REF 2.2
Sample 1	RuO <sub>2</sub>	MC 1.1	MC 1.2
Sample 2	RuO <sub>2</sub>	MC 2.1	MC 2.2
Sample 3	RuO <sub>2</sub>	-	MC 3.2

metallic boxes that are connected by their metallic support structures to the cryostat; this establishes a low impedance connection. The amplified signal is transferred via a shielded cable directly to the main electronics and display units of the bridges, without passing through the patch panel.

The communication with the computer is made via a secondary computer interface unit<sup>19</sup> via GPIB (IEEE-488). These units were placed outside the electronic rack, therefore providing an additional physical distance to the noisy PC. While the AVS-47 with the option “A” uses a metallic conductor between the resistance bridge and its computer interface, the option “B” uses optical fibre lines, called “Picoline”. This eliminates the EMC complications of a metallic conductor. The latter resistance bridge was used exclusively for the sensors inside the mixing chamber. One additional thermometer inside the mixing chamber was connected to the former resistance bride and was used as a reference thermometer at the lowest temperatures in order to enable a fast calibration of all thermometers in the mixing chamber.

For the calibration of the thermometers the temperature was continuously monitored with two thermometers connected to different resistance bridges. The MC temperature was slowly varied by means of the MC heater. The measurements were performed while increasing and decreasing the temperature in order to avoid systematical errors due to different time constants of the thermometers.

The thermometer REF 2 was calibrated against the thermometer REF with a large number of data points over a wide temperature range between 44 mK and 630 mK. It was used as reference thermometer below 44 mK by extrapolating the fitting function to lower temperatures. REF 1 was then calibrated against the REF 2 thermometer to obtain a second possibility to measure the MC

<sup>19</sup>Picowatt AVS47-IB

**Table 3.9:** Fitting of the thermometers in the mixing chamber for cold runs 5 and 6. For the ruthenium oxide and the carbon resistor thermometers the fitting function given in equation (3.9) and (3.8) were used.

<i>Calibration cold run 1</i>						
<i>Sensor calibrated</i>	<i>Reference thermometer</i>	<i>Data points</i>	<i>Calibrated temp. region (mK)</i>	<i>Coefficients</i>		
				<i>A</i>	<i>B</i>	<i>C</i>
REF 1.1	REF	40	43 to 350	0.0512	-0.8120	5.2862
MC 1.1	REF 1.1	67	10 to 300	$1.0426 \cdot 10^{-21}$	$2.1656 \cdot 10^{177}$	0.0098
MC 2.1	REF 1.1	69	10 to 300	0.0715	$1.8646 \cdot 10^{20}$	0.0492

<i>Calibration cold run 2</i>						
<i>Sensor calibrated</i>	<i>Reference thermometer</i>	<i>Data points</i>	<i>Calibrated temp. region (mK)</i>	<i>Coefficients</i>		
				<i>A</i>	<i>B</i>	<i>C</i>
REF 2.2	REF	38271	44 to 630	27.5602	645680.9027	0.1057
REF 1.2	REF 2.2	42522	9 to 70	0.1202	-0.4325	5.7928
MC 1.2	REF 2.2	22708	9.5 to 114	981.0380	0.8991	0.2606
MC 2.2	REF 2.2	21644	9.4 to 39	344.6530	25.4691	0.1798
MC 3.2	REF 2.2	9437	9.1 to 41	257.4070	69.8230	0.1670

temperature. The thermometers MC 1, MC 2 and MC 3 were calibrated against the REF 2 in a slightly widened temperature region than required for the measurements in order to obtain a good interpolation.

The characteristic of the carbon resistor can be described by [112]

$$R = e^{A(\ln T)^2 + B \ln T + C}, \quad (3.8)$$

where  $R$  is the resistance,  $T$  is the temperature and  $A$ ,  $B$  and  $C$  are constants. The low temperature  $R$ - $T$  characteristic of RuO<sub>2</sub>-based thick film resistors is described by

$$R(T) = A \cdot e^{\left(\frac{B}{T}\right)^C}, \quad (3.9)$$

where  $A$ ,  $B$  and  $C$  are fit parameters. The function adequately describes the physical mechanisms of the RuO<sub>2</sub> resistors, which was studied in various publications [16, 98, 110, 139, 143] and was suc-

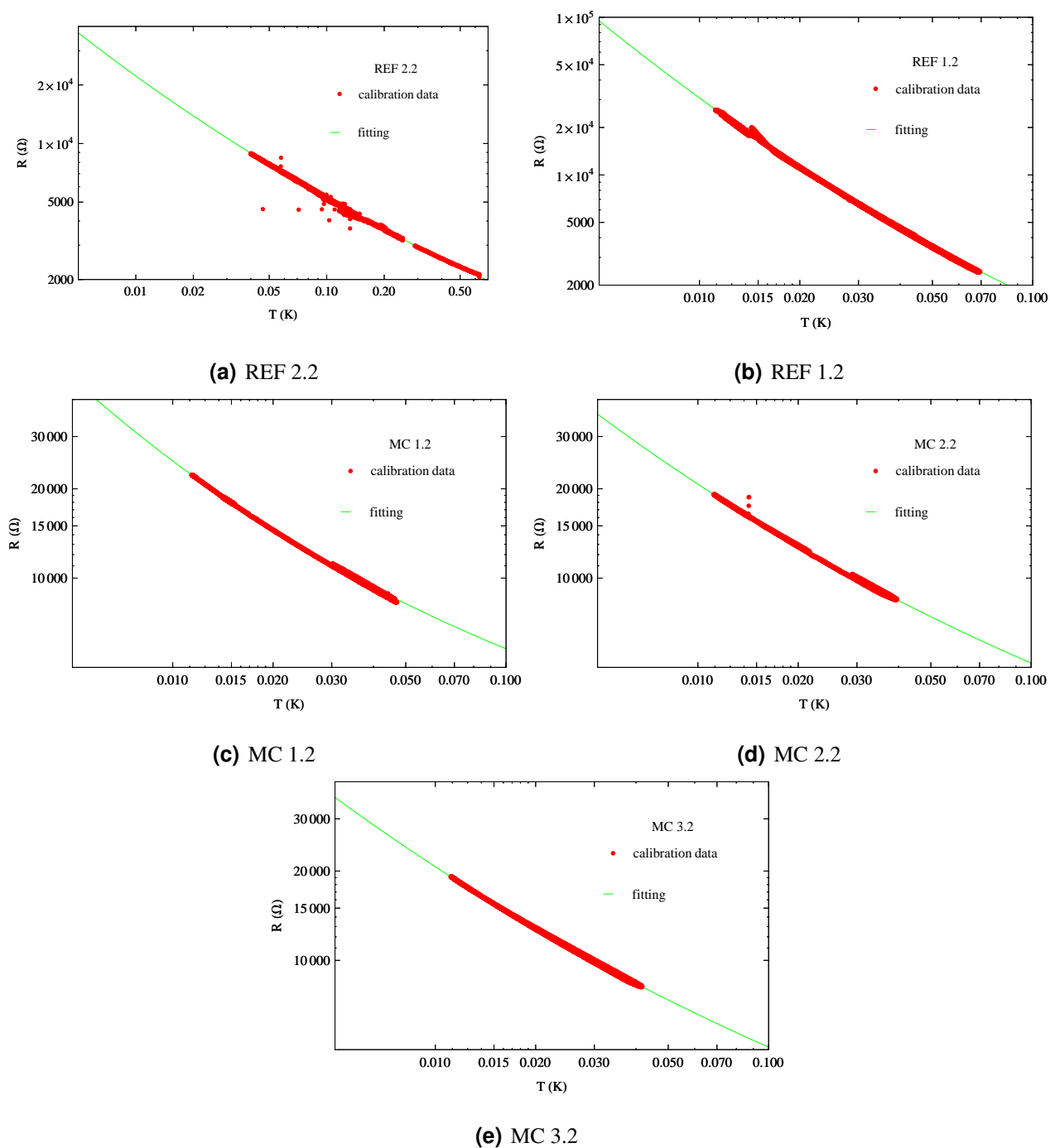


**Figure 3.5:** Details of the calibration of the temperature sensors inside the mixing chamber for the cold run 2. The REF 2.2 was calibrated against the REF (a) , whereas MC 1.2 (c), MC 1.2 (d) and MC 1.2 (e) were calibrated against REF 2.2 with the fitting function given by equation (3.9). The REF 1.2 thermometer (b) was fitted against the REF 2.2 using the equation (3.8).

cessfully used in many ultra low temperature applications [16, 143]. The coefficients were calculated

using a computational software program<sup>20</sup>. The fits are depicted in Figure 3.5 and the coefficients of the fit, the number of data points and the temperature range of the calibration of the cold runs 1 and 2 are given in Table 3.9.

### 3.6 The Automatic Systems of the CCCR

For operating a complicated apparatus such as a DR over several weeks, the use of automatic systems is important. They are required for improving the reliability as well as the autonomy to operate without human intervention. Therefore, an automatic He transfer to the DR main helium bath and a control of the 1 K pot were implemented.

**Table 3.10:** The components of the automatic level control of the helium bath.

<i>Device</i>	<i>Description</i>
Linear motor	Hansen type H2001006
Level gauge	Twickenham
HDI	Twickenham HDI-ASC
Relay 24 VDC	ERNI REL 50-C5
Pressure valve	-

The first automatic system is the level control of the main helium bath. The level control reduces the helium consumption because a low He level can be adjusted and ensures a reliable operation of the cryostat. While a too high level of the bath in the cryostat increases the consumption, a too low level increases the heat-load on the 1 K pot. The transfer is accomplished exclusively analogically, using a Helium Depth Indicator (HDI)<sup>21</sup>. The HDI is equipped with a relay with 2 adjustable thresholds that can be set from the front-panel of the device. The relay is closed when the lower limit is passed and opens when the upper threshold is exceeded. This relay switches a voltage and controls a second relay that is connected that way, to start a helium transfer when its coil is powered. Otherwise the relay reverses the polarity to the motor and stops the transfer. The HDI and the transfer motor are powered by a 24 VDC uninterruptible power supply (UPS) system, to secure the system against failures of the electrical network. This allows a normal helium transfer and most importantly, to stop

<sup>20</sup>Wolfram Mathematica 7.01.0

<sup>21</sup>Twickenham Scientific Instruments HDI-A

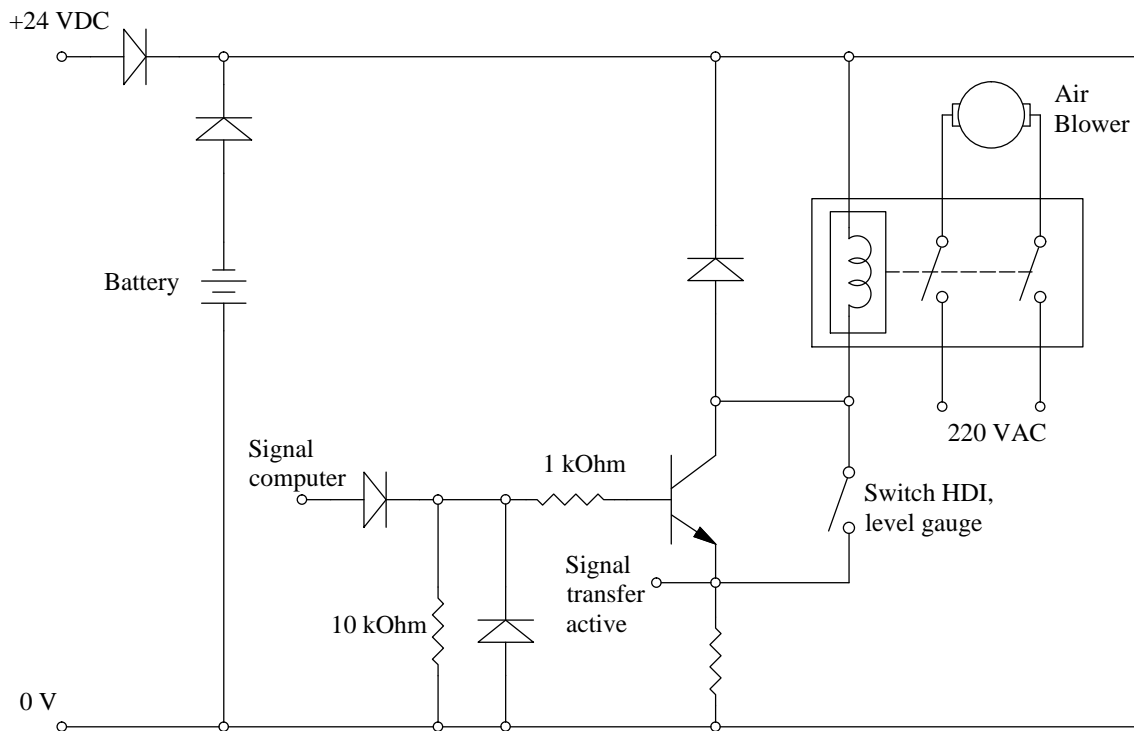


**Figure 3.6:** Analog control circuit for the automatic helium transfer.

the transfer in case of an electrical power outage.

The cryostat and the dewar are connected to a recovery volume (gasometer) that is kept at 40 mbar above ambient pressure to avoid contamination by accidental leakage. To enable a transfer, the pressure in the helium dewar is increased by 100 mbar by a mechanical valve in the recovery line. At higher pressures the transfer speed is too high forcing a 2-phase flow, which carries liquid helium droplets with the boil-off gas to the recovery line. This results in a large helium consumption during the transfer and can even inhibit refilling. When the helium dewar is 1/3 emptied, the pressurized gaseous helium volume in the transfer dewar is sufficient to transfer approximately 25 L (from a helium level of 1250 mm to 1400 mm) liquid helium to the cryostat. The heat leak to the liquid helium between two transfers is sufficient for self pressurizing the dewar. Otherwise, the pressure is supplied by means of a helium gas cylinder.

Figure 3.7 shows the motor for the automatic transfer unit, mounted directly on the transfer line. The linear movement of the transfer line is accomplished by a pivoting arm with a slotted hole. The motor was mounted on the dewar's transfer line, after experiencing thermo-acoustic oscillations when it was placed at the cryostat's transfer line.

The second automatic system controls the level of the 1 K pot. This is necessary both for a good



**Figure 3.7:** Motor He-transfer.

economy and for a safe operation of the cryostat. A too high helium level (e.g. up in the pumping tube) results in excessive helium boil-off and in a too high temperature due to a large heat-leak to the 1 K pot. Furthermore, a too low level results in insufficient cooling of the condenser. Therefore, the  $^3\text{He}$  condensation pressure will rise, which could lead to a loss of expensive  $^3\text{He}$  without intervention.

**Table 3.11:** The components of the 1 K pot control system.

<i>Device</i>	<i>Manufacturer</i>
Motor	Faulhaber brushless DC-servomotor series 2444 S 024 B
Primary transmission	Faulhaber planetary gearhead Series 23/1, 66:1
Secondary transmission	Gear belt and gearwheels with 10 and 30 teeth
Motion control	Faulhaber series MCBL2805
Angle sensor	Novotechnik WAL305 hollow-shaft potentiometric sensor

The mechanical design of the 1 K pot control shown in Figure 3.8 features a compact layout with easy implementation. It can be mounted on a standard KF<sup>22</sup> clamp and hence can be used to upgrade an existing system without any changes. The helium flow into the 1 K pot is adjusted by means of a needle valve. The manipulation of the valve is possible via a long, thin walled tube (Figure 3.8, detail 4). A brass piece (Figure 3.8, detail 6) is soldered to the fragile tube to allow manipulation. To decouple the rotational and the axial movement of the control tube, the pin in the brass piece

<sup>22</sup>Klein Flange

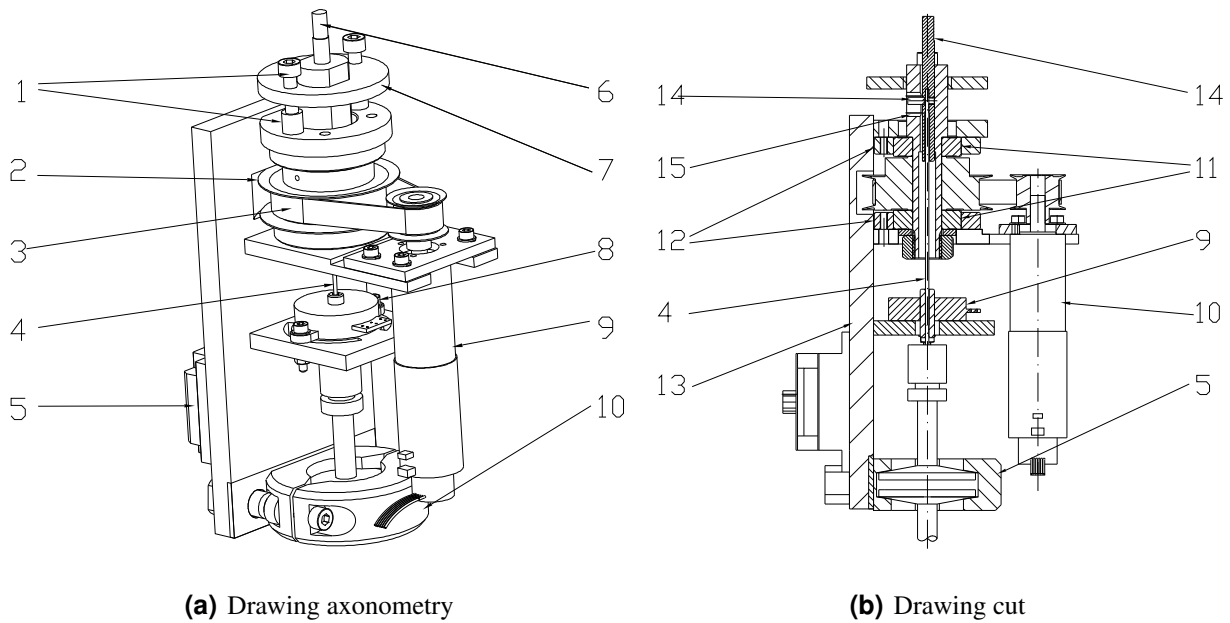


**Figure 3.8:** Design of the 1 K pot control hardware, *1*: limit stopper, *2*: gearwheels, *3*: belt, *4*: control tube, *5*: motion control, *6*: brass piece soldered to control tube, *7*: limit traveler, *8*: hollow-shaft potentiometer, *9*: motor, *10*: clamp, *11*: bearings, *12*: adjustment bearing, *13*: mounting plate, *14*: connecting pin, *15*: slot hole and *16*: external rotary piece.

(Figure 3.8, detail *14*) can slide axially in a slotted hole (Figure 3.8, detail *15*) of the external rotary piece. To enable manual manipulation, the control tube can be quickly mechanically decoupled from the motor by removing the pin.

Once the support is installed, both bearings (Figure 3.8, detail *11*) allow individual adjustment to achieve a good axial arrangement. An additional hollow-shaft potentiometric sensor (Figure 3.8, detail *9*) is installed at the lower end so that the absolute angle can be measured. This proved to be useful for determining the optimal motor settings. To prevent the motor from turning beyond the valve's range of operation, electrical end stops were implemented at the maximal and minimal limits (Figure 3.8, detail *1*). A little bit further, mechanical boundaries ensure a stoppage in case of an electronics failure. Closing the valve beyond its design limit can damage the control tube, which would require a time-consuming repair. The motor and the control tube are connected with a belt (Figure 3.8, detail *3*), ensuring smooth operation. The transmission ratio between the motor and the control tube is given by the gearwheel ratio (Figure 3.8, detail *2*) of  $\frac{1}{3}$  and by the planetary transmission ratio of the motor of  $\frac{1}{66}$ .

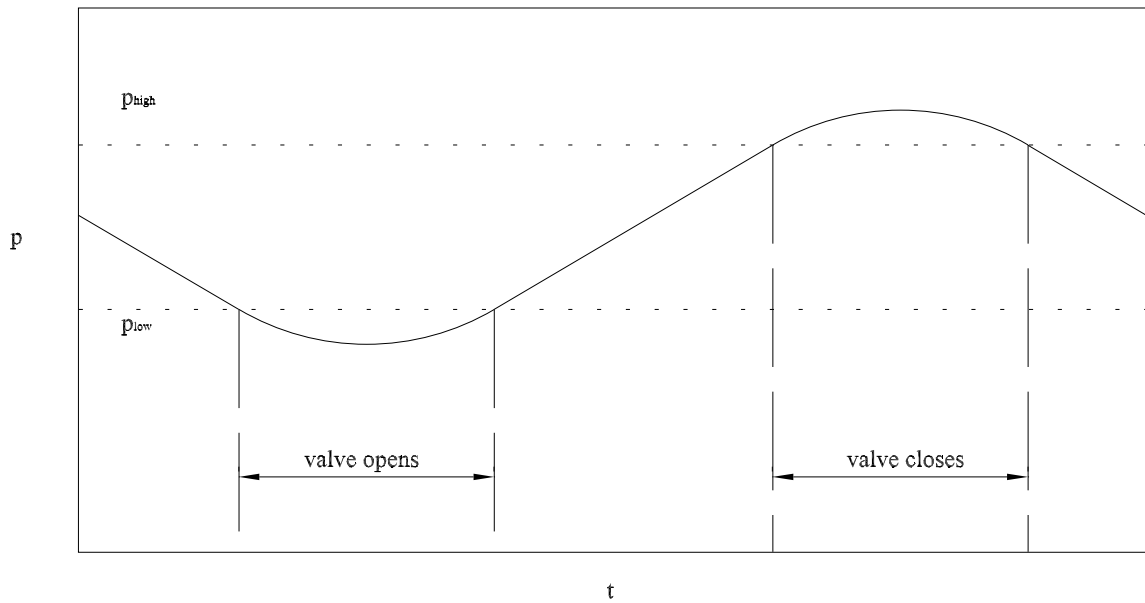


**Figure 3.9:** 2-point control strategy of the 1 K pot pressure to reduce the wear of the needle valve. The valve is closed when the upper threshold is exceeded and opened when the pressure falls below the lower limit.

The motor is controlled by a motion controller<sup>23</sup>, which can be programmed with the motor settings for speed, acceleration, etc., via a serial connection to the computer. The information is saved on the onboard memory of the device and remains available after a power cut. In order to turn the motor clockwise or counterclockwise, the analogue control input of 10 V to the motion controller must be reversed. The motion control also offers the possibility to implement two electrical limit stops.

The 1 K pot pressure was used as the control variable. A PID controller was abandoned to avoid permanent movement of the needle valve, resulting in excessive wear. Instead a two-point control was realized, which is shown in Figure 3.9. When exceeding the upper pressure, the valve closes; when the lower pressure is passed, the valve opens. Due to the delayed reaction of the pressure, a low valve velocity was required. A speed of  $\frac{1}{8} \frac{\text{rev}}{\text{min}}$  of the needle valve results in a sufficiently fast reaction for this application, without experiencing overshooting. The pressure limits have to be chosen carefully. The flow rate  $\dot{n}_4$  from the 1 K bath is the sum of superfluid film flow, flash evaporation and boil-off, which depends on the heat load. The boiling pressure  $p_4$  of the bath depends upon this and the

<sup>23</sup>Faulhaber Motion Controller, series MCBL2805

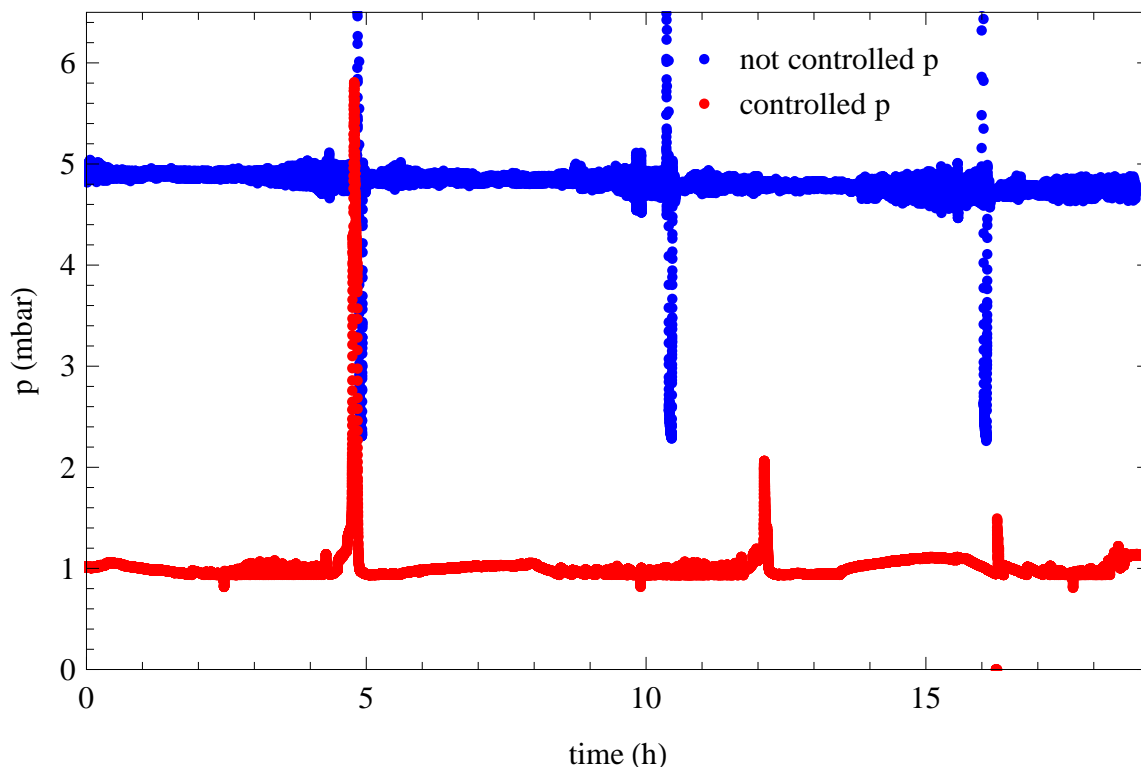


**Figure 3.10:** Experimental data from the 1 K pot pressure control. The refilling of helium is evident by the characteristic peak in the pressure. For the controlled pressure the increased time between helium refillings and the lower possible pressure are obvious compared to the uncontrolled pressure, as well as a modest improved in pressure stability.

volume speed  $\dot{V}_4$  of the pumping system:

$$p_4 = \frac{\dot{n}_4 k_B T}{\dot{V}_4}, \quad (3.10)$$

where  $T$  is the gas temperature at the pump and  $k_B$  is the Boltzmann constant.

Alternatively, the bath level could have been used as a controlling variable. However, the measurement of the level in the superfluid helium bath was not implemented. Controlling the 1 K pot pressure presents also the advantage of stabilizing the condenser's temperature and thus improving the stability of the MC temperature.

Pressure thresholds of 0.8 mbar and 1.2 mbar proved to work reliably over several weeks of operation. Compared to the constant needle valve setting used without 1 K pot controller, the much lower achievable controlled pressure improved the helium boil-off considerably. The helium refilling intervals of the main He bath increased by one third, from 6 h to 8 h. In addition to the cost savings, the enhanced time for undisturbed measurement was a valuable improvement. In Figure 3.10 the refilling of the main helium bath is evident by large peaks in the 1 K pot pressure. The third pressure

peak of the pressure curve with controlled needle valve is however not triggered by a transfer but some other disturbance.

## 3.7 Conclusions

In this chapter, the basic techniques for efficient EMC were briefly reviewed. The techniques are mainly segregation, filtering, shielding and establishing of a RF reference, which is efficient up to the highest frequency of concern for the specific application. In cooperation with members of the CERN Cryolab, the measures were implemented to the electrical system of the CCDR. The practical implementation was discussed as an example where the excellent results proved the soundness of these principles.

Avoiding EMI is of utmost importance for a reliable thermometry at lowest temperatures. The standard approach would be to operate the DR in a shielded room. In the previous electrical setup of the CCDR [142], large temperature instabilities were experienced below 50 mK. To read lower temperatures, all electrical connections except those of the thermometry had to be disconnected, which obviously limited the possible measurements. The implementation of the EMC techniques discussed in this chapter, enabled measurements at the lowest temperatures accessible with the CCDR and the studies presented in the following chapters. Stable temperature measurements were conducted at temperatures as low as 4 mK. To the knowledge of the author this is the first time that temperatures below 10 mK were measured with resistance thermometers outside a shielded room.

The calibration of the RuO<sub>2</sub> and carbon composite resistance thermometers was described. Both types of thermometer are known for their suitability at lowest temperatures and reference is given to successful ultra low temperature applications. The good agreement of the measurements with theory, which will be presented in Chapter 4, not only shows the effectiveness of the EMC measurements taken but provides further proof for the correctness of the thermometry based on the extrapolation of the scale established using a commercially calibrated device.

The automatic systems for controlling the level of the helium bath and the pressure of the 1 K pot were described above. Both were indispensable for operating the CCDR autonomically for a sufficient period. The systems enabled the automatised without intervention measurement programs for 24 h a day, which were necessary for the time consuming measurements at the lowest temperatures.

# Chapter 4

## Experimental Study of Residual Heat Loads

In this Chapter, dealing much with the performance characterization of dilution refrigerators, we shall first discuss the techniques used for the measurement of the maximum cooling power and optimum flow of  $^3\text{He}$  in the dilution refrigerator of the Cryolab. We shall show that the time constants involved in the approach of dynamic equilibrium are rather long if the flow rate is not stabilized, which suggests to determine the highest cooling power points from the scans of applied power at constant flow rates. The measurement of these points is then described, before determining the residual heat load from this data and from the one-shot cooling power. The residual heat loads are finally discussed theoretically, evaluated, and compared with our experimental results.

### 4.1 Maximum Cooling Power and Optimum Flow

In Section 1.4 we briefly reviewed the cooling power available in the mixing chamber of a dilution refrigerator. By optimizing the flow of  $^3\text{He}$  at a given heat load applied to the mixing chamber, one can minimize its temperature. The sum of this heat load and the residual heat losses is then the maximum cooling power at the minimized temperature. The maximum cooling power and the optimum flow depend on the performance of the heat exchanger, which is mainly limited by the Kapitza thermal boundary resistance. The theoretical expressions of these maxima and optima are [134]

$$\max\{\dot{Q}_m\} = \left(\frac{a}{2b}\right)^2 \sigma S T_m^4, \quad (4.1)$$

$$\text{opt}\{\dot{n}_3\} = \frac{a}{2b^2} \sigma S T_m^2, \quad (4.2)$$

These expressions are valid below roughly  $T_m = 50$  mK, where the enthalpies approach their asymptotic temperature dependence. Here  $a$  is the coefficient in the asymptotic expression  $H_l(T_m) = a T_m^2$  of the enthalpy of the dilute solution along the solubility line, and  $b$  is that of the fluid circulated in the concentrated stream,  $H_c(T_c) = b T_c^2$ . The latter takes into account that the concentrated stream also has a small component of the dilute fluid.

In practice the optimum flow and maximum cooling power are more easily determined by keeping the flow constant while stepping the applied power around the optimum point. This is because the thermal transients involved in the change of the flow speed are more complex and slower than those where the flow speed is kept constant. A step in the flow rate is obtained by applying more power into the still, whose temperature and therefore vapour pressure are increased. The increase of the still temperature is almost instantaneous, increasing during several seconds the osmotic pressure of the dilute fluid there. This reverses the flow in the dilute stream for a few seconds, which causes the temperature of the mixing chamber to increase first for a while. After the osmotic pressure has reached a new equilibrium in the dilute stream, the flow in it is increased so that it corresponds to the higher heating power applied to the still. As the pressure in the condenser line cannot increase very rapidly because of the dead volumes in the pumps and the pipework, the flow in the concentrated stream stays at its initial value for some ten minutes, which entails unbalanced flow in the heat exchanger. The unbalance is favourable for the cooling power, and the mixing chamber therefore cools now to a temperature that is usually below its equilibrium value.

Once the flow speed on both sides of the exchanger has reached a common equilibrium value, which may take some hours at very low temperatures, one still has to wait for the mixing chamber to reach the new steady state. This also takes hours at low temperatures.

If the flow is kept constant, the transients in the still and heat exchanger are very short, as the flow in the two sides stays balanced. The remaining transients only involve those of the heat capacities of the fluid in the MC and of some possible magnetic materials used for its construction. These may also require hours for reaching the new steady state, and therefore the measurements are made with upward and downward stepped power ramps. The hysteresis of these ramps depends on the relation between the leading time constant and the step duration, and an averaging process can help in finding the equilibrium value without waiting hours to reach it at each step. The hysteresis also lets us estimate the size of the error made in this process.

## 4.2 Time Constants

The Cryolab dilution refrigerator has a batch-filled helium bath to which liquid helium is transferred with about 6 h intervals. The filling involves a large flow of cold helium gas from the phase separator following the transfer line. This cold gas cools the inlet line of  $^3\text{He}$ , which drops the pressure in it and reduces for a while the flow in the concentrated stream of the heat exchanger. The operation at base temperature is substantially influenced by this transient. Therefore it is necessary to evaluate the time constants involved in the measurements of the cooling power, so as to find a method to take data so that the effects of these spurious transient are minimized.

In the following we shall estimate the time constants for approaching steady state dynamic equilibrium in the mixing chamber.

Let us consider a dilution refrigerator running in a steady state in the continuous mode. All parts of the cooling cycle are then in dynamic equilibrium, which implies that the temperatures of all points are constant, and the mass flow and composition of the circulated helium are constant at any point of the cycle. From these it follows that the amount of  $^3\text{He}$ -rich mixture in the pumps and pump lines, precooling heat exchangers and condenser is constant. A small step up is now made in the power applied to the heater of the mixing chamber. The temperature in the mixing chamber will respond to this by a slow evolution towards the new equilibrium value  $T_{eq}$  so that at time  $t$  the difference is

$$\Delta T_m(t) = T_m(t) - T_{m,eq} . \quad (4.3)$$

The cooling power at constant flow is given by equation (4.1) only at the optimum point, and is lower than optimum at all other points. Our results show that, to a good approximation, the temperature dependence at constant flow is rather given by

$$\dot{Q}_m(T_m)|_{\dot{n}_3=const} = A(\dot{n}_3) T_m^2 - B(\dot{n}_3) . \quad (4.4)$$

It should be noted that in this purely empirical expression the constants  $A$  and  $B$  are different for each flow rate, and that  $B$  is a parameter that has nothing to do with the residual heat load.

With these definitions, the time evolution of the temperature in the mixing chamber will now follow the equation

$$C_m \frac{d}{dt}(\Delta T_m) n = \dot{Q}_m(T_m) - \dot{Q}_m(T_{m,eq}) = \frac{d\dot{Q}_m(T_m)}{d(T_m)} \Delta T_m , \quad (4.5)$$

when the steps in temperature and power are small. This gives a simple exponential approach of equilibrium with the time constant

$$\tau_m = \frac{\Delta T_m}{\frac{d}{dt}(\Delta T_m)} = \frac{C_m(T_m) n}{\frac{d\dot{Q}_m(T_m)}{d(T_m)}} = \frac{C_m(T_m) n}{2 A (\dot{n}_3) T_m}. \quad (4.6)$$

Knowing that the heat capacity  $C_m$  is proportional to  $T_m$ , the time constant  $\tau_m$  of the MC fluid is same for all power steps at a particular flow rate.

The specific heat capacity below 40 mK is given for the dilute phase by

$$C_{m,l}(T_m) = 2 a T_m \quad (4.7)$$

and for the concentrated phase by

$$C_{m,c}(T_m) = 2 b T_m. \quad (4.8)$$

The magnetic materials in contact with the fluid in the MC may also relax slowly towards the new equilibrium; this will slow down further the time evolution. In our case such materials include the stainless steel AISI 316 L chamber walls, and the manganin<sup>1</sup> wire of the MC heater. Both of these are in direct contact with the helium fluid, with contact surface  $\sigma_i$  and mass  $m_i$ , with  $i = c, h$  for the chamber and heater, respectively. Their thermal relaxation time constant for a small temperature difference is simply

$$\tau_i = R_{K,i} C_i m_i. \quad (4.9)$$

Using equation (1.36) we can express this in terms of the surface boundary conductances  $S_i$ :

$$\tau_i = \frac{C_i m_i}{4 S_i \sigma_i T_m^3}. \quad (4.10)$$

The temperature dependences of  $C_i$  in zero external field are given by [72]

$$C_h(T_m) = A_h T + B_h T^{-2} + C_h T^3, \quad (4.11)$$

and by [115]

$$C_c(T_m) = A_c T + B_c T^{-2}. \quad (4.12)$$

The constants  $a$  and  $b$  amount to 95 J/(mol K<sup>2</sup>) [63] and 11 J/(mol K<sup>2</sup>) [115], respectively. The amount of <sup>3</sup>He in the CCDR was determined in the single-shot mode, by monitoring the pressure of the helium in the recovery reservoirs while recording the mixing chamber temperature. A rise in

---

<sup>1</sup>87% Cu, 13% Mn [115]

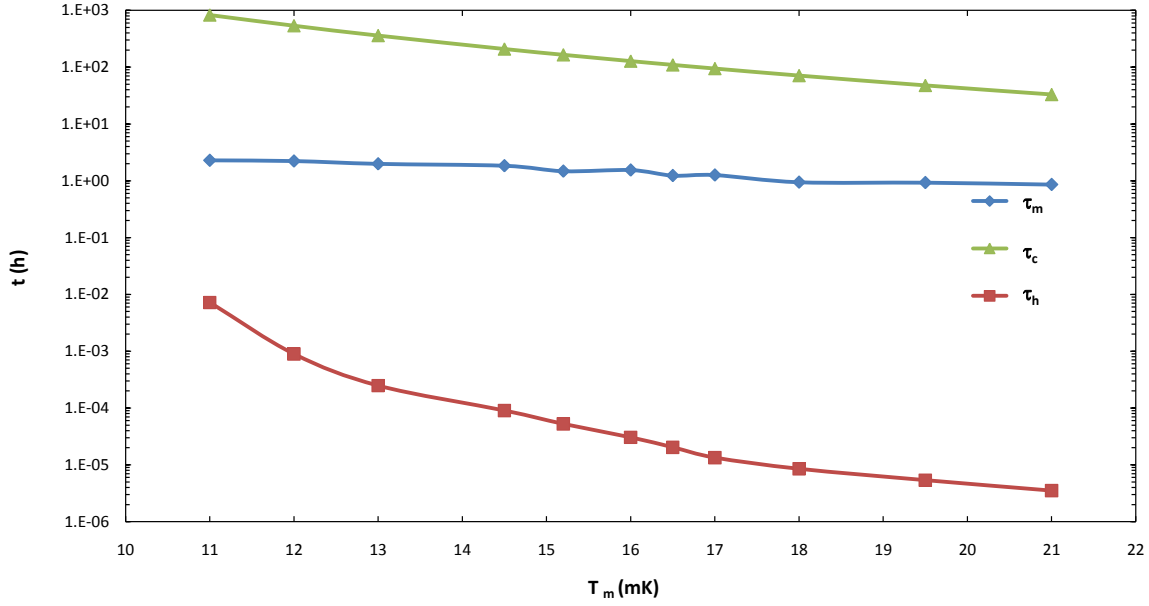


**Figure 4.1:** Comparison of the time constants of the helium mixture  $\tau_m$ , the heater  $\tau_h$  and the MC  $\tau_c$ .

temperature indicated the depletion of the  $^3\text{He}$ -rich phase in the mixing chamber. The  $^3\text{He}$  amounts to  $79.5 L_{STP} \pm 0.8 L_{STP}$  and the  $^4\text{He}$  to  $350 L_{STP}$ . This is equal to 3.5 mol and 0.42 mol of  $^3\text{He}$  in the concentrated phase  $n_c$  and in the dilute phase  $n_l$ . The value of the coefficient  $A$  in equation (4.4) is given in Table 4.1 for different flow rates. With equation (4.6) one calculates the time constant for the helium mixture

$$\tau_m = \frac{156.0 \text{ J/K}^2}{2 A}. \quad (4.13)$$

For interfaces between the dilute solution and copper a value for the Kapitza conductance  $S = 2.5 \cdot 10^{-3} \frac{\text{W}}{\text{cm}^2 \cdot \text{K}^4}$  is given in the literature [115]. The Kapitza conductance does not change significantly for different metals, therefore, this should be a good approximation for manganin. The heater has a length of 30 m, a diameter of 0.09 mm, and thus the surface area  $\sigma_h = 160 \text{ cm}^2$  and the mass  $m_h = 1.6 \text{ g}$ . The constants in equation (4.11) amount to [72]  $A_h = 0.0595 \text{ mJ/g K}^2$ ,  $B_h = 0.0115 \text{ mJ K/g}$  and  $C_h = 0.00294 \text{ mJ/g K}^4$ . From equation (4.10) one derives the time constant of the heater

$$\tau_h = \frac{0.0952 \text{ mJ/K}^2 T_m + 0.0184 \text{ mJ K} T_m^{-2} + 0.00470 \text{ mJ/K}^4 T_m^3}{1600 \text{ mW/K}^4 T_h^3}. \quad (4.14)$$

The heater temperature  $T_h$  is significantly higher than  $T_m$  and can be calculated with equation (1.34).

The MC was made of AISI 316 L, but no data on the specific heat was available for this material. The specific heat of 304 stainless steel was measured [65] between 70 mK and 600 mK, which should at least give the right order of magnitude. The constants in equation (4.12) amount to

$A_c = 465 \mu\text{J/g K}^2$  and  $B_c = 0.56 \mu\text{J K/g}$ . The chamber has a mass  $m_c = 1890 \text{ g}$  and a surface area  $\sigma_c = 220 \text{ cm}^2$  of the pot in contact with the helium. The time constant of the chamber amounts to

$$\tau_c = \frac{878.85 \text{ mJ K}^{-2} T_m + 1.0584 \text{ mJ K } T_m^{-2}}{2200 \text{ mW K}^{-4} T_m^3}. \quad (4.15)$$

It is now possible to compare the temperature dependences of the three time constants at various flow rates. They are plotted in Figure 4.1 as a function of  $T_m$ ; for  $\tau_m$  we assumed the flow rate close to its optimum value. For  $\tau_h$ ,  $T_h$  was calculated using the heating power  $Q_{appl}$  from Table 4.2. We conclude that it is advisable to take data with intervals shorter than any of these time constants and shorter than the 6 h filling interval of the helium bath. As such data does not represent the full steady state equilibrium, the scans of applied power must be made with a sequence of ascending steps followed by a sequence of descending steps. A procedure can then be applied to average the data in these sequences, which also enables to evaluate the systematic error made by applying this procedure.

For EURECA the heat capacity at the lowest temperature should be minimized, in order to optimize the precooling time and the temperature control during operation at base temperature. It is strongly recommended to reduce the amount of  $^3\text{He}$  inside the mixing chamber, because liquid  $^3\text{He}$  has a large heat capacity at low temperatures. Stainless steel dominates by far the heat capacity in the CCDR and should be totally eliminated from any DR operating below 20 mK.

### 4.3 Measurement of the Maximum Cooling Power and Optimum Flow

The cooling power of the CCDR was measured in this work below 30 mK as a complement to previous measurements at higher temperatures [142]. The cooling power was measured at different constant  $^3\text{He}$  flow rates between  $60 \mu\text{mol/s}$  and  $300 \mu\text{mol/s}$  while varying the heating power to the mixing chamber. For the measurements, constant 30 min step durations were used and very small heating power steps were applied. To reduce the systematic errors, the measurements were performed for ascending and descending heating power. The voltage steps were performed automatically by the Labview program. The power to the heater was supplied by an ultra-low-noise isolated voltage source <sup>2</sup> in voltage steps of 1 mV, from 1 mV to 100 mV. The voltage drop at the heater was

<sup>2</sup>Stanford Research Systems, type SIM928

determined by a 4-wire measurement. The current was measured with a high performance digital multimeter <sup>3</sup> in series with the power supply. The heating power steps range from 606.06 pW to 120.6 nW, the maximum power applied amounts to 10  $\mu$ W. The temperature was determined at a frequency of 1 Hz and for the measurements the average of 30 s before a voltage step were taken.

In order to stabilize the flow rate the still heater was controlled by a PI controller which was integrated in the data acquisition. The P and I control parameters were optimized for a minimal offset during normal operation. As an input the average value of 10 flow measurements was used. At flow rates below 160  $\mu$ mol/s the Film Burner (FB) of the still was solely used for controlling the flow rate in order to reduce the superfluid <sup>4</sup>He-film. Above that flow rate, the optimum temperature of the film burner of 3.5 K would have been exceeded. Therefore, the power to the FB heater was kept constant and the still heater was used for flow control.

**Table 4.1:** Coefficient  $A$  and  $B$  of the fitting function given in equation (4.4) for the measured cooling power of the CCDR. The measurements were performed at temperatures below 30 mK at constant flow rates between 60  $\frac{\mu\text{mol}}{\text{s}}$  and 300  $\frac{\mu\text{mol}}{\text{s}}$ , in steps of 20  $\frac{\mu\text{mol}}{\text{s}}$ .

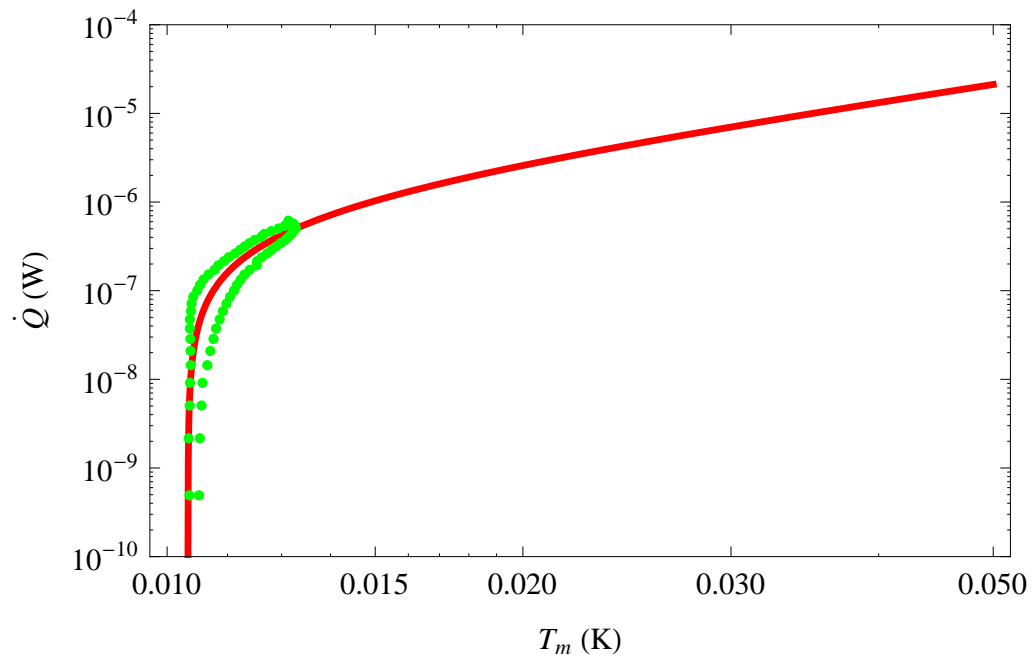
<sup>3</sup> He flow ( $\mu\text{mol/s}$ )	$A$ (W/K <sup>2</sup> )	$B$ (K)	<sup>3</sup> He flow ( $\mu\text{mol/s}$ )	$A$ (W/K <sup>2</sup> )	$B$ (K)
80	0.00946	$8.75 \cdot 10^{-7}$	200	0.03754	$6.37 \cdot 10^{-6}$
100	0.00974	$8.81 \cdot 10^{-7}$	220	0.01717	$2.25 \cdot 10^{-6}$
120	0.01091	$1.08 \cdot 10^{-6}$	260	0.02295	$3.80 \cdot 10^{-6}$
140	0.01178	$1.12 \cdot 10^{-6}$	280	0.02333	$4.02 \cdot 10^{-6}$
180	0.01403	$1.62 \cdot 10^{-6}$	300	0.02522	$4.63 \cdot 10^{-6}$

The measured temperature dependence of the cooling power at constant flow rates was fitted to equation (4.4). The coefficients were determined by a computational software program<sup>4</sup> by finding the least-squares fit to the measured data. The fitting parameters  $A$  and  $B$  of the different flow rates are listed in Table 4.1. The measured data and the fits are exemplarily given in Figure 4.2 for flow rates of 80 $\mu$ mol/s and 300 $\mu$ mol/s. At higher flow rates, the hysteresis is minimal. At lower circulation the difference increases, due to the larger time constant at lower flow rates.

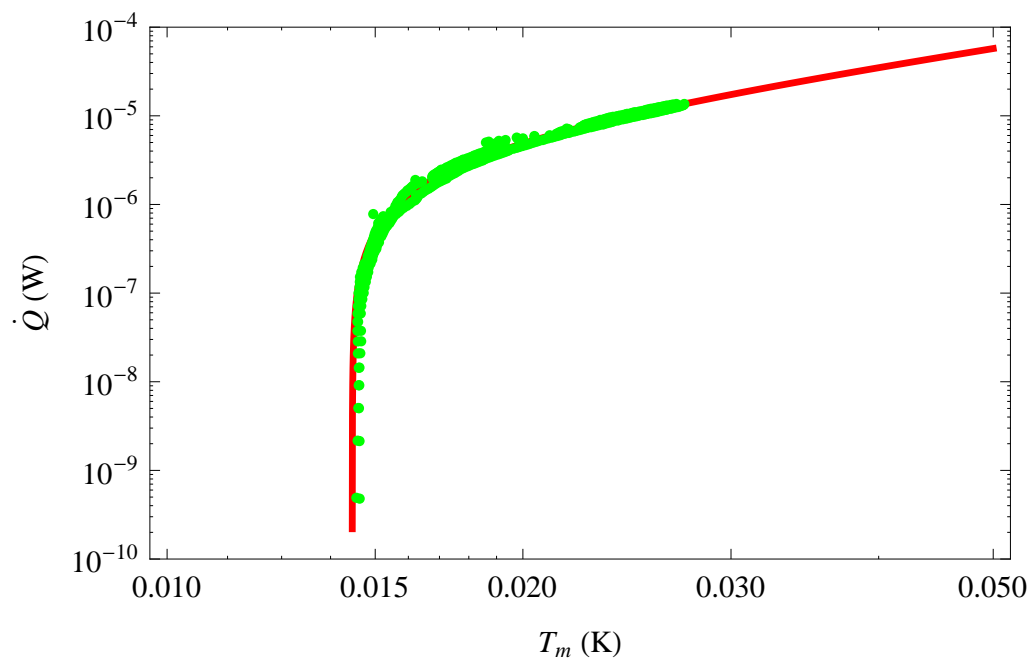
Starting from an equilibrium temperature, the measured temperature  $T_m(t)$  for ascending/de-

<sup>3</sup>Keithley, model 2000 6-1/2-Digit DMM

<sup>4</sup>Wolfram Mathematica 7.01.0



(a)



(b)

**Figure 4.2:** Fitting of the cooling power measurements at constant flow rates of (a)  $80 \mu\text{mol/s}$  and (b)  $300 \mu\text{mol/s}$ .

scending power is always lower/higher than the equilibrium temperature  $T_{m,eq}$  due to the long time constants involved. The fits use all the data and should roughly average the error. The hysteresis lets us estimate the size of the error made in this process. The maximal hysteresis is found at low temperatures and low flow rates as the time constants involved are largest there. At a flow rate of  $80 \mu\text{mol/s}$  the maximal temperature difference is  $880 \text{ nK}$  at  $11 \text{ mK}$  at a heating power of  $193 \text{ nW}$ , which gives a relative systematical error in temperature of  $\pm 4\%$ .

On each cooling power curve at  $\dot{n}_3$ , a point of maximal cooling power  $\max\{\dot{Q}_{appl}\}$  exists for which the minimal temperature of the dilution refrigerator is reached and the flow is optimal  $\text{opt}\{\dot{n}\}$ . The points of optimum flow can be easily selected upon visual judgement and are given in Table 4.2.

**Table 4.2:** Points of optimal  $^3\text{He}$  flow rate  $\text{opt}\{\dot{n}\}$  of the CCDR at different applied heat loads  $\dot{Q}_{appl}$ .

$\text{opt}\{\dot{n}\}$ ( $\mu\text{mol/s}$ )	$T_{MC}$ (mK)	$\dot{Q}_{appl}$ (nW)	$\text{opt}\{\dot{n}\}$ ( $\mu\text{mol/s}$ )	$T_{MC}$ (mK)	$\dot{Q}_{appl}$ (nW)
80	9.56	0	180	16.0	1665.7
80	11.0	135.3	220	17.0	2309.3
100	12.0	344.5	260	18.0	3090.7
120	13.0	645.3	280	19.5	4308.5
140	14.5	1152.3	300	21.0	5885.2

Equations (4.1) and (4.2) give the theoretical maximum cooling power available in the mixing chamber, and the optimum flow at which this power is reached. Using the first of these, the external power applied to the mixing chamber can be expressed as

$$\max\{\dot{Q}_{appl}\} = \gamma T_m^4 - \dot{Q}_{res}, \quad (4.16)$$

where  $\dot{Q}_{res}$  includes all residual thermal loads from internal sources of heat; these will be discussed in detail in the following Sections.

Figure 4.3 shows the experimental maximum cooling power points as a function of MC temperature, together with the curve fit to equation (4.16). The fit yields the free parameters

$$\gamma = 31.8 \frac{\text{W}}{\text{K}^4} \quad (4.17)$$

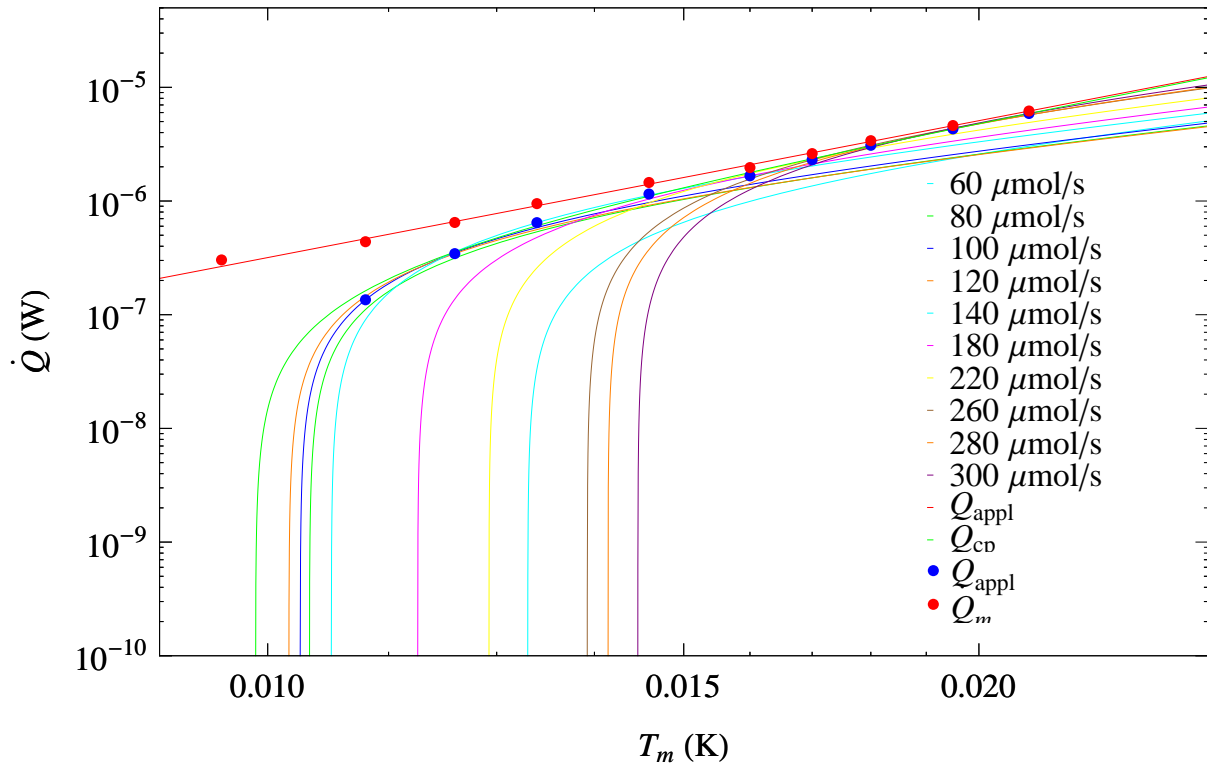


**Figure 4.3:** Cooling power curves from  $60 \frac{\mu\text{mol}}{\text{s}}$  to  $300 \frac{\mu\text{mol}}{\text{s}}$  (thin lines), the fitted cooling power curve (thick blue line) and the maximal cooling power minus the fitted residual heat load given by equation (4.16) (thick red line).

$$\dot{Q}_{res} = 303 \text{ nW} . \quad (4.18)$$

In Chapter 5 we shall compare this experimental value of  $\gamma$  with that calculated directly from the measured surface area  $\sigma$  and the Kapitza conductivity  $S$  of the copper powder used in the heat exchanger.

Figure 4.4 shows the optimum flow rates as a function of MC temperature, together with the curve representing the fit of equation (4.2)

$$\text{opt} \{ \dot{n}_3 \} = g T_m^2 , \quad (4.19)$$

to the data points of Table 4.2. The fit yields the free parameter

$$g = 0.722 \frac{\text{mol}}{\text{s K}^2} , \quad (4.20)$$

By dividing the equation (4.1) by equation (4.2), we get

$$\frac{\max \{ \dot{Q}_m \}}{\text{opt} \{ \dot{n}_3 \}} = \frac{a}{2} T_m^2 = 47.5 \frac{\text{J}}{\text{mol K}^2} T_m^2 , \quad (4.21)$$

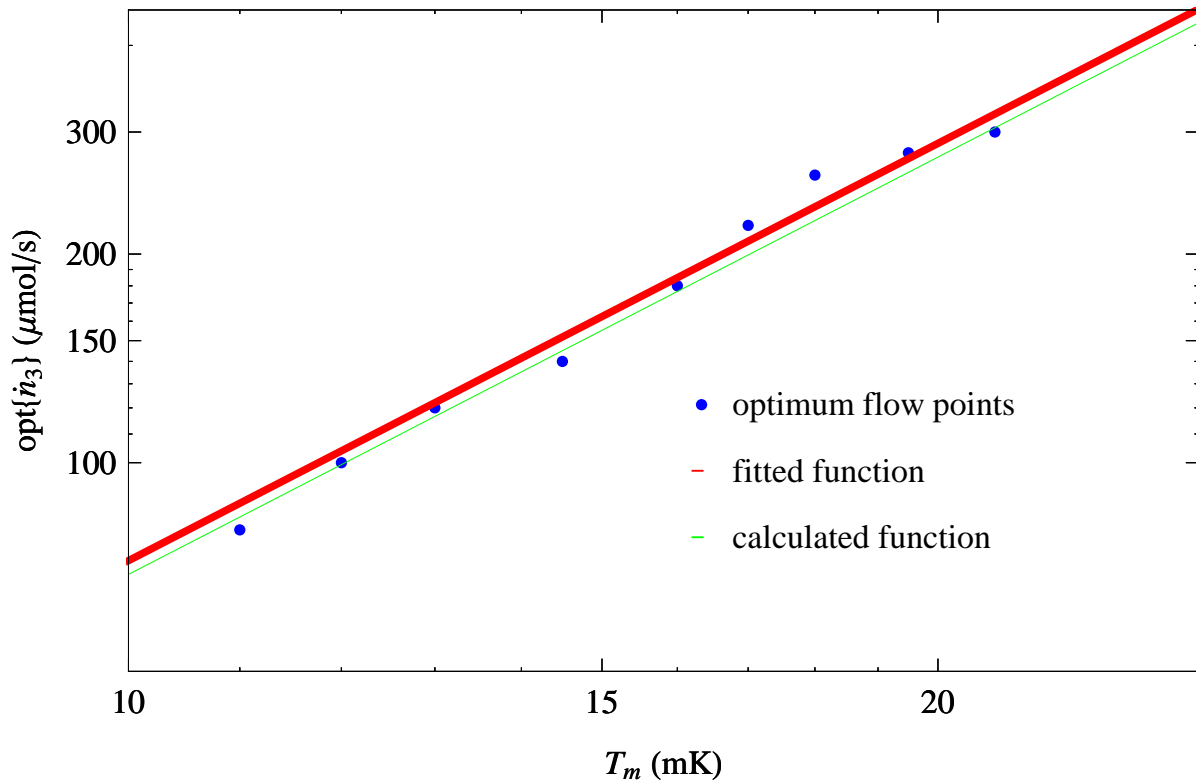


**Figure 4.4:** Optimum flow points.

which can be compared with our experimental values given in the equations (4.17) and (4.20)

$$\frac{\max\{\dot{Q}_m\}}{\text{opt}\{\dot{n}_3\}} = \frac{\gamma}{g} T_m^2 = 44.0 \frac{\text{J}}{\text{mol K}^2} T_m^2, \quad (4.22)$$

We see that the experimental  $\gamma/g$  is in very good agreement with its theoretically expected value  $a/2$ . This shows that the data is internally consistent. Moreover, this agreement and the fairly good power law agreement of both fits indicate that all thermometers are well calibrated over the entire range of temperatures covered by these measurements, and that spurious phenomena do not disturb thermometry. These effects may include notably self heating and heating by EMI-induced parasitic signals. Furthermore, the absence of these tells that the efforts described in Chapter 3 were highly successful.

## 4.4 Experimental Residual Heat Load

The value of  $\dot{Q}_{res}$  yielded by the fit above can be regarded as an experimental residual heat load averaged over the period during which the data was taken. This period covers 24 weeks, and includes

one warm-up to about 30 K. The above experimental value of  $\gamma$ , on the other hand, can be used for determining the time evolution of  $\dot{Q}_{res}(t)$  at all points  $t$  when the machine has been running over a substantial period of time with no applied heat load, in steady state, and at a flow close to the optimum. We then have simply

$$\dot{Q}_{res}(t) = \gamma T_{m,min}^4(t), \quad (4.23)$$

which enables us to get some idea about the time evolution of the time-dependent residual heat loads.

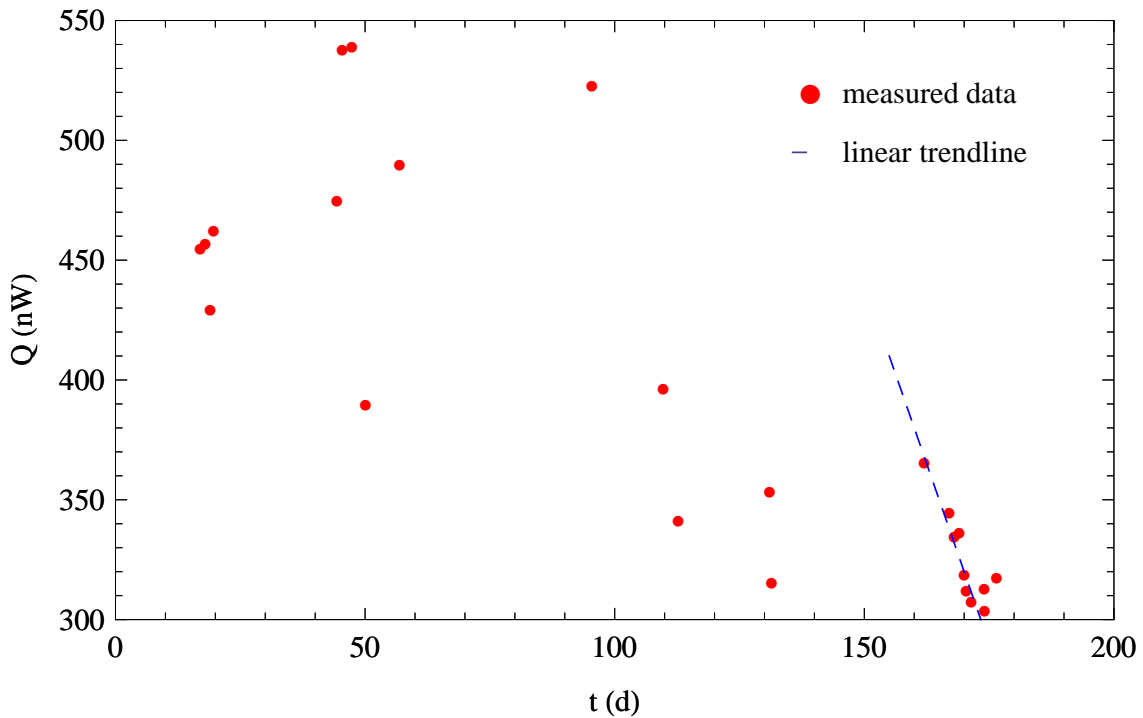


**Figure 4.5:** The points show the time development of the residual heat load, determined by the measured base temperatures at that time and by equation (4.23). The dashed line is a trend line assuming an exponential decline of the residual heat loads.

Figure 4.5 shows this evolution over the period in which the data was taken. A failure of the  $^3\text{He}$  backup pump at day 50 forced an interruption of the operation for approximately 1 month. During this time the cryostat was slowly warming up to approximately 30 K. The large scattering of the heat load is very likely due to the large heat capacity of the stainless steel MC. The time constant of stainless steel is much shorter at higher temperature and the chamber will thermalize much faster at higher temperature. When cooling down, the chamber will remain for a long period at a considerable higher temperature than the helium mixture. Therefore, the heat load from the chamber depends on the previous history of the measurement program.

The heat load from the chamber can be calculated by

$$\dot{Q}_c = \sigma S (T_c^4 - T_m^4). \quad (4.24)$$

With the time-independent residual heat load of 303 nW determined above, the maximal heat load from the chamber material amounts to 240 nW at day 47. With  $T_m$  at approximately 10 mK,  $T_c$  amounts to 26 mK, a very reasonable value which has been exceeded regularly during the measurements.

The measured time constant of the chamber shall now be compared to the one calculated above. The former is best monitored from day 162 and the following, where the DR was almost permanently at base temperature for a period of 2 weeks. The change in heat load is presumably originating from the chamber. At base temperature,  $T_m$  is almost constant. The change in the heat load is therefore given by

$$\frac{d\dot{Q}_c}{dt} = \sigma S T_c^4 \frac{dT_c}{dt}, \quad (4.25)$$

where

$$\frac{dT_c}{dt} = \frac{T_c}{\tau(T_c)}. \quad (4.26)$$

$\frac{d\dot{Q}_c}{dt}$  is derived from the measurements. A linear fit of the data is shown in Figure 4.5 as the dashed line and yields  $\frac{d\dot{Q}_c}{dt} = 6$  nW/d. The chamber temperature at day 162 is calculated from the heat load of approximately 70 nW and amounts to  $T_{c,162} = 19.2$  mK. Equation (4.25) yields the time constant of the chamber

$$\tau(T_{c,162}) = 352 \text{ h}. \quad (4.27)$$

The time constant of the chamber calculated from equation (4.15)  $\tau(T_{c,162}) = 54$  h is in reasonable agreement with this measured time constant given the uncertainties in the specific heat of stainless steel 316 L, in the effective inner surface area and the Kapitza resistance of the MC, which can vary by an order of magnitude depending on the surface treatment.

A second value for the residual heat load can be experimentally derived by the base temperature in single-shot. Instead of resupplying  $^3\text{He}$ , it is not recirculated and stored in the helium reservoirs. The advantage of this method is the simplicity of calculating the cooling power. The heat exchanger efficiency has no influence. The cooling power in single-shot operating mode  $\dot{Q}_{single-shot}$  is calculated as a function of temperature by

$$\dot{Q}_{single-shot} = \dot{n}_3 (H_d(T) - H_c(T)), \quad (4.28)$$

where  $\dot{n}_3$  is the flow rate,  $H_d(T) = aT^2$  and  $H_c(T) = bT^2$  are the enthalpies of the dilute and of the concentrated phase respectively. With the numerical values of the enthalpies, equation (4.28) yields:

$$\dot{Q}_{one-shot} = (a - b) \dot{n}_3 T^2 = 84 \frac{\text{J}}{\text{mol K}^2} \dot{n}_3 T^2 . \quad (4.29)$$

Provided sufficient  $^3\text{He}$  is in the mixing chamber to reach the minimum temperature, the cooling power equals the residual heat load:

$$\dot{Q}_{one-shot} = \dot{Q}_{res} . \quad (4.30)$$

At the beginning of the measurements, the cryostat was operated at base temperature in continuous operation. The flow rate was controlled at  $80 \mu\text{mol/s}$  and the vacuum baffles were closed. The single-shot mode was started at a temperature of  $T = 9.4 \text{ mK}$  measured by the carbon thermometer.

The flow rate in the one-shot mode can not be measured directly as the flow meter is placed in the condensation line which is not used. Instead, the heating power to the still was kept constant and the flow rate was verified by monitoring the helium pressure in the reservoir volume which did confirm a constant flow of  $80 \mu\text{mol/s}$ .

A minimum temperature of  $3.64 \text{ mK}$  and  $5.47 \text{ mK}$  was measured by the carbon composite and the ruthenium oxide thermometers. The difference in temperature can be explained by self-heating of the latter thermometer at lowest temperatures. It was connected to the older AVS-47-A which required a higher excitation in order to avoid saturation of this resistance bridge. This proved to be uncritical at temperatures above  $10 \text{ mK}$ , where the agreement between the two thermometers was very good, but can have a significant effect at the very lowest temperatures. With equation (4.29) and the temperature measured by the carbon composite thermometer one derives a residual heat load of  $89.7 \text{ nW}$ .

However, at low flow rates it is not possible to operate the still film burner sufficiently and a significant amount of  $^4\text{He}$  could contaminate the  $^3\text{He}$  flow. The  $^4\text{He}$  contamination can be estimated from the enthalpy balance of the still.

$$\dot{n}_3 L_3(T_{st}, x_{d,st}) = \dot{n}_3 [H_3(T_{cond}) - H(T_{st})] + \dot{Q}_{st}, \quad (4.31)$$

where  $H_3(T_{cond})$  and  $H(T_{st})$  are the enthalpies of the concentrated  $^3\text{He}$  at the condenser and still temperature. At a flow rate  $\dot{n}_3 = 80 \mu\text{mol/s}$ , a heating power  $\dot{Q}_{st} = 1.07 \text{ mW}$  is applied to the still heater, and the product  $\dot{n}_3 [H_3(T_{cond}) - H(T_{st})]$  amounts to  $1.31 \text{ mW}$ . For the calculated heat of

vaporization of the liquid in the still  $L_3(T_{st}, x_{d,st}) = 30 \text{ J/mol}$  and neglecting the film flow, the vapor concentration  $x_{d,st} = 0.79$  at the still temperature  $T_{st} = 0.75 \text{ K}$  can be derived [120]. In the one-shot mode the cooling power is reduced proportional to the  $^4\text{He}$  contamination. Thus, using the derived  $X_{d,st}$ , the residual heat load amounts to 71 nW.

The heat load from the chamber in the single-shot mode depends on the chamber temperature. For an ideal thermalization of the stainless steel  $T_c = 10 \text{ mK}$  before starting the single-shot mode. Equation (4.24) yields a heat load of 5.4 nW. Otherwise the chamber is at an elevated temperature,  $T_c$  of 13 mK, 16 mK and 19 mK yield a heat load of 15.6 nW, 35.9 nW and 71.6 nW.

**Table 4.3:** The measured residual heat load determined by the cooling power in continuous and in one-shot mode.

<i>Method</i>	<i>Residual heat load</i> (nW)
Cooling power measurements	303
One-shot mode	71

It is clear that there is a fairly substantial disagreement between all residual heat load values determined from the cooling power in continuous mode operation, and from the base temperatures obtained in the single-shot mode. We therefore attempted to understand if any of the sources of the residual heat loads could be influenced by the operating mode. An obvious reason could stem from the coldest thermal screen surrounding the mixing chamber. This screen is cooled by the dilute stream via a sintered heat exchanger brazed on the intermediate cold plate between the still and the mixing chamber. Its temperature is at 55 mK in continuous mode [142], while in single-shot mode it may be much colder at approximately 25 mK. The support rods of the mixing chamber are also attached to this plate. At least the following sources are therefore influenced by the operating mode:

- Thermal radiation between the innermost shield and the MC.
- Thermal conduction along the support rods and the cables for the instrumentation of the MC
- Thermal conduction by a thermalized residual gas
- Life time and temperature of the hot molecules leaking inside the innermost shield

While the first and second are relatively easy to evaluate numerically, we have no reliable method to evaluate the two last ones theoretically. Thermal radiation is known to be negligible in both modes, and thermal conduction by a thermalized residual gas is certainly much lower than the heat leak due to hot molecules. The various sources of residual heat loads will be discussed in more detail in the following sections.

## 4.5 Time-Independent Sources of Residual Heat Load

Various contributions to the residual heat load of very low temperature systems in general and the CCDR in particular have been studied in the work of Wikus [142]. The findings will be summarized briefly. Experimental studies on theoretically less well supported residual heat loads were conducted in this work, which will be discussed below.

### Radiated Heat

The radiated heat is calculated by

$$\dot{Q} = \varphi_{12} A_2 \varepsilon_1 \varepsilon_2 \sigma (T_2^4 - T_1^4), \quad (4.32)$$

where  $\varphi_{12}$  is the viewing factor,  $A_2$  is the surface area at the lower temperature,  $\varepsilon_{1,2}$  is the emissivity of the two bodies,  $\sigma$  is the Stefan-Boltzmann constant and  $T_{1,2}$  are the temperatures of the surfaces. The surface of the MC and the last heat shield amount to  $0.03 \text{ m}^2$  and  $0.3 \text{ m}^2$ . The temperature of the last heat shield  $T_2$  amount to  $55 \text{ mK}$  and  $25 \text{ mK}$  in continuous and in single-shot mode. Even for  $\varphi_{12} = 1$  and assuming black body radiation, the heat loads to the MC are very small and amount to  $16 \text{ fW}$  and  $0.6 \text{ fW}$ , respectively.

### Cosmic Rays

The heat load caused by cosmic rays depends upon the particle flux, the spectral distribution of the cosmic rays and the interacting material. For the CCDR this has been estimated to be  $36 \text{ pW}$  [142]. For an underground experiment the particle flux is hugely reduced and thus the heat load negligible.

## Decay of Radioactive Nuclei

Decay of radioactive nuclei gives rise to a practically time independent heat leak due to the long half-life of the nuclei. In the CCDR the heat load has been estimated to be 1.3 nW [142]. In a low background experiment with extremely high requirements of radio-purity, this heat load is expected to be insignificant.

## Thermal Conduction

Thermal conduction to the MC can occur in the support structure, in electrical wiring and in condensed gases. Conduction along the superconducting NbTi wires and by condensed gases were found to be negligible [142]. The support of the CCDR is accomplished by three stainless steel tubes with a length  $l$  of 235 mm and a cross section  $A$  of 7.1 mm<sup>2</sup> each. For a structure with constant cross section, the heat load is calculated by:

$$\dot{Q} = \frac{A}{l} \int_{T_1}^{T_2} \lambda(T) \delta T, \quad (4.33)$$

where  $\lambda$  is the thermal conductivity, and  $T_1$  and  $T_2$  are the temperatures at the ends of the structure. At low temperatures the thermal conductivity  $\lambda$  of stainless steel can be fitted to the function

$$\lambda(T) = AT^B, \quad (4.34)$$

where  $T$  is the structures' local temperature and  $A$  and  $B$  are fit parameters. The coefficients  $A = 0.145 \text{ W}/(\text{K}^2 \cdot \text{m})$  and  $B = 1$  have been fitted to measurements performed at temperatures above 165 mK [64]. Extrapolating this function to 10 mK derives a heat load to the MC at base temperature, in continuous mode with the intermediate flange at 55 mK, of 19.2 nW. In the one-shot mode one derives a heat load of 3.5 nW with a temperature of the last heat shield of 25 mK,.

To evaluate the validity of extrapolating the above fit to lower temperatures, the thermal conductivity of the support structure was measured at temperatures below 100 mK in this work. An equivalent stainless steel tube like the one used as support structure in the CCDR was thermally anchored to the mixing chamber. In a distance of 20 mm two copper pieces were attached to the tube and equipped with a temperature sensor each. A heater was placed on a third copper piece, placed furthest away from the mixing chamber. Equation (4.34) was used to fit the data and yield parameters  $A = 0.008285 \text{ W}/(\text{K}^2 \cdot \text{m})$  and  $B = 0.313$ . A comparison of the current fit with a previous one [64]

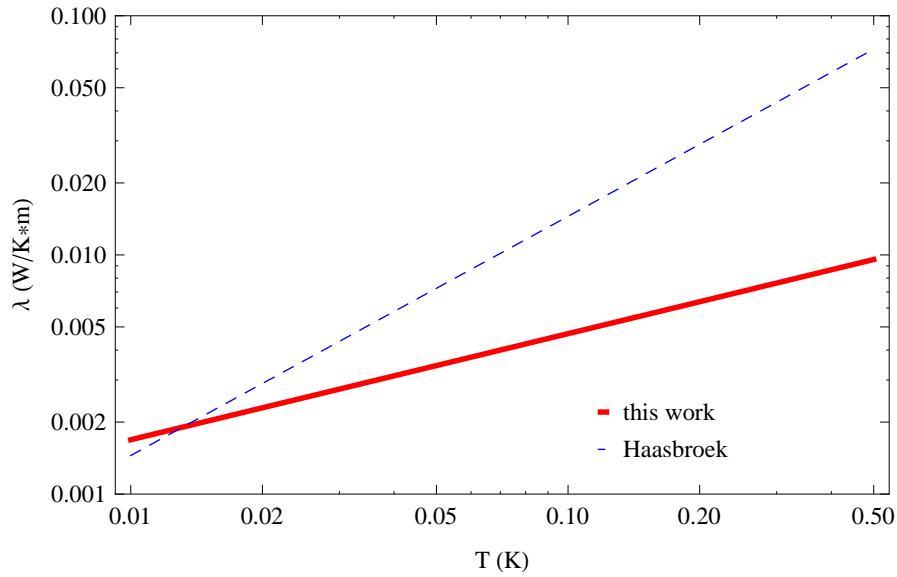


**Figure 4.6:** Measurement of the thermal conductivity of a stainless steel tube between 15 mK and 140 mK in comparison to an extrapolation of the fits to measurements performed at temperatures as low as 100 mK [64].

is presented in Figure 4.6 and shows a different temperature dependence. Using the thermal conductivity measured in this work, heat loads of 12.2 nW and 3.4 nW were determined in continuous and in single-shot mode, which is in good agreement with the value derived above.

## Vibrations

Three mechanisms have been found to potentially convert vibrations into heat [142]. First, eddy currents induced in a conductor are dissipated by converting into heat by the finite conductivity. In a dilution refrigerator the conductor is vibrating in the time constant magnetic field determined by the earth magnetic field. The eddy current heating can be estimated from a very simplified model of a bar moving in a constant magnetic field:

$$\dot{Q} = \frac{B^2 \bar{w}^2 V}{\rho}, \quad (4.35)$$

where  $B$  is the magnetic field,  $\bar{w}$  is the mean velocity,  $V$  is the conductor volume and  $\rho$  is the conductor's resistance. The heat dissipation in the CCDR has been calculated to be 7.3 aW/g [142]. This amounts to an absolute value of 138 pW for the mixing chamber of the CCDR. While this is a major heat source in the case of demagnetization cryostats with strongly time dependent fields, it is insignificant for a dilution refrigerator.

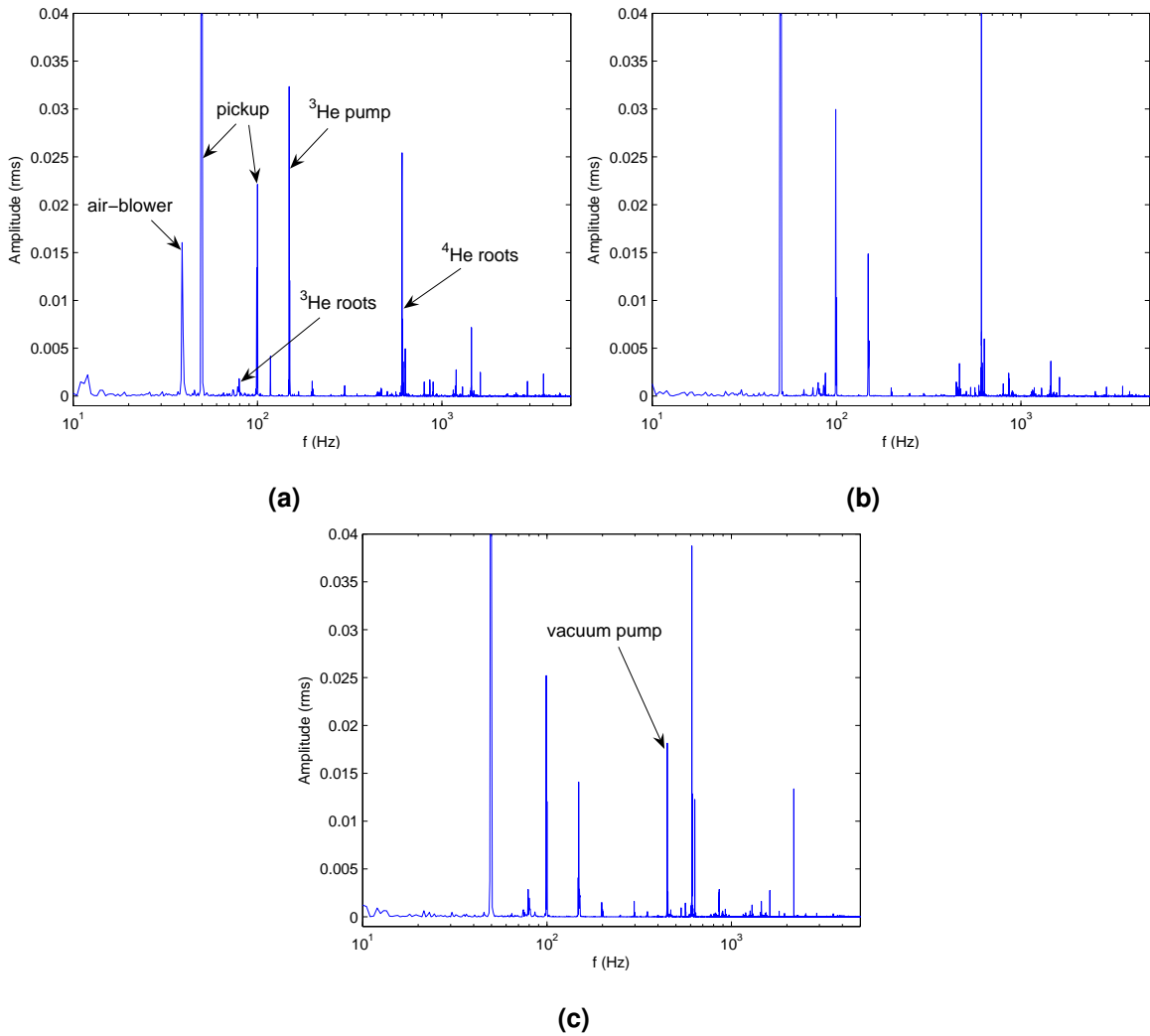


**Figure 4.7:** Vibrations of the top-flange of the CCDR (a) in normal operational configuration, (b) without the air-blower and with (c) a vacuum pump in contact with the CCDR to introduce additional vibrations.

Secondly, the heat load on the CCDR due to structural damping of vibrations has been calculated [142] with

$$\dot{Q} = \int_0^{\infty} P(f) W(f) df, \quad (4.36)$$

where  $P(f)$  is a characteristic function for every structure, yielded from FEM simulations.  $W(f)$  is the PSD function measured on the top flange of the CCDR. The heat load amounts to  $1.25 \cdot 10^{-22}$  W [142] and is thus negligible.

The third vibration induced heat load is viscous dissipation in liquids. Due to the high viscosity of  $^3\text{He}$ , movement of the liquids may produce considerable heating. It was suggested that this heat load was much larger than that due to structural damping. Due to the difficulty of simulating the motion

of the fluids, only an upper limit of 16 nW/g could be given [142]. By deducting the calculated heat loads above from the measured residual heat load in the one-shot mode, reported in section 4.4, a value of 64.2 nW for the CCDR is found in this work. Attributing all of this heat load to vibrations, a threshold for viscous heating of 16.4 nW/g of  $^3\text{He}$  at base temperature can be given in this work.

To further investigate this heat load source, the vibrations at the CCDR were deliberately varied, both reduced and increased. The vibrations of the DR were determined at the top flange with an accelerometer <sup>5</sup>, able to detect accelerations as high as 5 g from 3 Hz to 500 Hz. The acceleration was then recorded and treated according to a previous description [142]. The frequency spectrum of the CCDR during normal operation is shown in Figure 4.7 (a). An air-blower was used to avoid condensing water on the top flange. Removing the pipe directing the warm air to the top-flange reduced the vibrations at 40 Hz, compare Figure 4.7 (b). In Figure 4.7 (c) the additional vibrations at approximately 450 Hz, induced by means of a vacuum pump brought into contact with the cryostat, are shown.

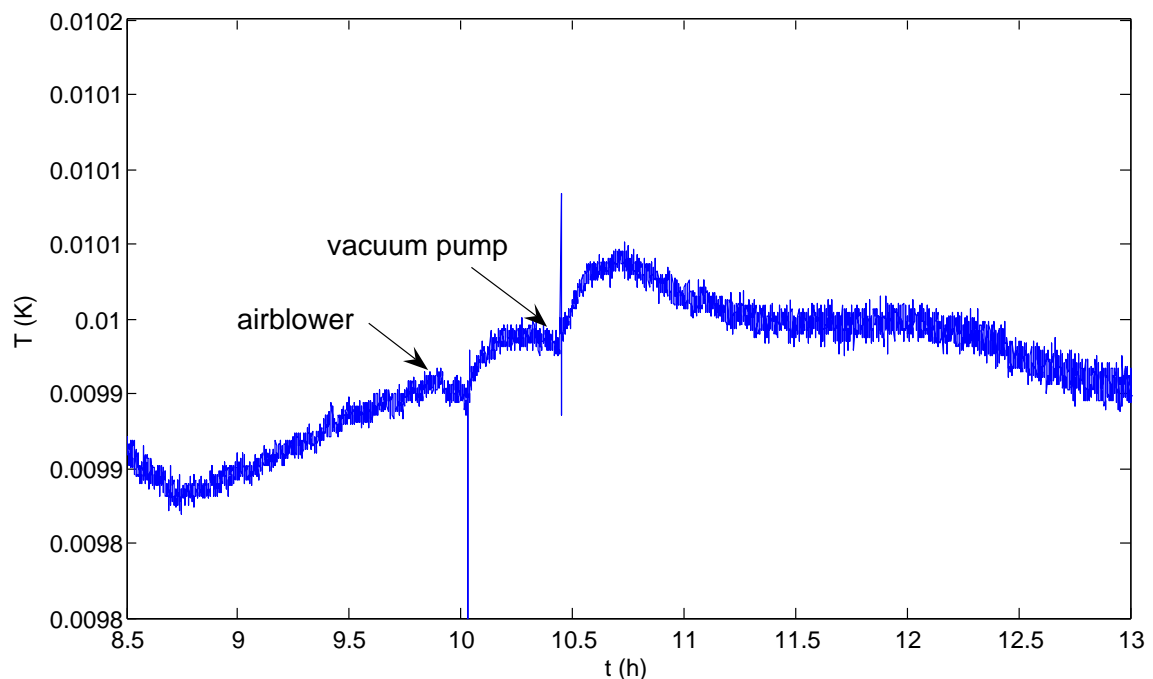


**Figure 4.8:** Influence of vibrations on the temperature of the CCDR. At 9.5 hours the vibrations have been reduced by switching off an air-blower. At 10.5 hours vibrations have been increased by turning on a vacuum pump.

The temperature development is shown in Figure 4.8. The vibrations were reduced at 9.8 hours.

<sup>5</sup>Honeywell PA (Ag714)

A decline in temperature is evident until approximately 10.05 hours, where a sharp rise occurs. This is probably due to vibrations accidentally introduced while installing the vacuum pump. At 10.5 hours additional vibrations were introduced. A sharp rise in temperature is evident. An estimation of the heat load is difficult due to the steady temperature variation within an amplitude of approximately 200  $\mu\text{K}$ . However, it is evident that the variation of vibrations does have an influence on the temperature, at least a transient one. A possible source could be the variation of the amount of superfluid  $^4\text{He}$  accumulated locally in the heat exchanger. Therefore, the observed temperature variations are more likely attributed to transient changes in the flow rate.

## 4.6 Time-Dependant Sources of Residual Heat Load

### Ortho-Para Conversion of $\text{H}_2$

The ortho-para conversion of  $\text{H}_2$  causes a heat load that depends upon the contamination of the material. The hydrogen contamination of the stainless steel used for the CCDR was previously measured by Bach et al. [13] and an upper limit of 0.9  $\mu\text{g/g}$  determined. The total amount of hydrogen in the MC at the CCDR therefore amounts to 0.83 mmol. As determined in a previous work [142], the time dependence of the heat load for the CCDR is described by the equation

$$\dot{Q} = \frac{3.5}{(1 + 0.01425t)^2} \mu\text{W}, \quad (4.37)$$

where  $t$  is the time in hours. This gives rise to a heat load of 15 nW after 6 weeks, which declines to 1 nW after 24 weeks.

### Tunneling Effects in Amorphous Solids

Tunneling effects in amorphous solids depend upon the quantity of material used. In the CCDR amorphous materials are used as cable feed-throughs to the mixing chamber and as a support for the mixing chamber heater. This gives rise to a time dependent heat load determined previously [142] of

$$\dot{Q} = 17.3 \text{ nW h} \frac{1}{t}. \quad (4.38)$$

This amounts to 17 pW after 6 weeks and to 1 pW after 24 weeks. Also in a future large detector array, this heat load should be of minor importance as the mass of amorphous material is not expected to be significant.

### Tunneling Effects in Crystalline Material

The steel body of the mixing chamber is the source of a heat load due to tunneling effects in the crystalline material. With a mass of 1856 g, the time dependence can be described by [142]

$$\dot{Q} = 1220 \text{ nW h } \frac{1}{t}. \quad (4.39)$$

After 6 weeks the heat load amounts to 1.2 nW and drops to 303 pW after 24 weeks.

### Structural Relaxation and Thermoelastic Stress

Structural relaxation and thermoelastic stress lead to a time dependent heat load for the CCDR given by [142]

$$\dot{Q} = 2914 \text{ nW } e^{-\frac{t}{100}}, \quad (4.40)$$

where  $t$  is the time in hours. This amounts to a heat load of 122 pW after 6 weeks and to 9 fW after 24 weeks. The heat load due to creep is expected to be negligible, as the stress in the support structure is low.

### Residual Gases

The heat load from residual gas originates from

- Conduction of thermalized gas
- Hot molecules leaking inside the innermost shield

The heat load due to conduction of thermalized residual gas can be calculated by the equation given by Kennard [81]

$$\dot{Q} = A_2 \alpha_0 \frac{\kappa + 1}{\kappa - 1} \sqrt{\frac{R}{8 M \pi}} \frac{p}{\sqrt{T_g}} (T_1 - T_2), \quad (4.41)$$

which describes the free-molecule heat conduction between two surfaces of comparable size.  $R$  is the ideal gas constant,  $\kappa$  is the ratio of specific heats,  $M$  is the molecular weight,  $T_1$  and  $T_2$  are the temperatures of the surfaces  $A_1$  and  $A_2$ .  $\alpha_0$  is calculated from the accommodation coefficients  $\alpha_1$  and  $\alpha_2$  at the corresponding surfaces by

$$\alpha_0 = \frac{\alpha_1 \alpha_2}{\alpha_2 + \alpha_1 (1 - \alpha_2) A_1 / A_2}. \quad (4.42)$$

$p$  and  $T_g$  are the local effective pressure and the temperature of the gas. The accommodation coefficients  $\alpha_1$  and  $\alpha_2$  are defined as the energy transferred in average by an impinging particle, as the fraction of the maximal energy transferable by the particle. As the gas is not in thermal equilibrium with neither of the surfaces,  $T_g$  has a value intermediate between  $T_1$  and  $T_2$  but is not the average [34]. The local gas temperature and pressure do not have to be known, however, because  $p$  and  $T_g$  are associated in equation (4.41). Under free-molecule heat conduction conditions the local pressure varies with the local temperature, due to the thermal transpiration effect, by

$$\frac{p}{\sqrt{T}} = \text{constant} . \quad (4.43)$$

The pressure can be determined at a known gas temperature, usually at room temperature, as long as the free mean path in the gas  $L$  is much larger than the width of the passage  $D$  connecting the gauge and the vacuum space. Considering the geometry of the cryostat, it has been suggested to multiply equation (4.41) with the same viewing factor  $\varphi_{12}$ , used for thermal radiation [138].

By removing two heat shields and directly exposing the mixing chamber to the 1 K shield at a temperature of 1.6 K, an additional heat load of 430 nW was experienced. Assuming that the entire heat load originated from conduction in residual gas, an upper threshold for  $p/\sqrt{T}$  in equation (4.41) of  $7.3 \cdot 10^{-7} \text{ Pa K}^{-0.5}$  was derived [142]. This shows that the value  $p/\sqrt{T} = 5.8 \cdot 10^{-6} \text{ Pa K}^{-0.5}$  calculated from the measured pressure at room temperature would overestimate the actual pressure considerably, the condition  $L \gg D$  is obviously not fulfilled.

The CCDR is equipped with apertures at all heat shield, which allow efficient pumping of the isolation vacuum. At 4 K, at 1.6 K and at 700 mK, vacuum baffles can be closed remotely to reduce the heat load during normal operation. With the baffles closed, a heat load to the MC by conduction in residual gas of 1.9 nW is calculated from equation (4.41) in the continuous mode, with the last heat shield at 55 mK. In the one-shot mode, the last heat shield is at a considerably lower temperature  $T = 25 \text{ mK}$ , which causes a heat load of 0.7 nW.

With opened baffles an increased heat load of 10 nW was experienced. After 35 hours at a flow rate of 80 mmol/s the MC reached a stable base temperature with closed vacuum baffles. The vacuum baffles were then opened, which enabled molecules at higher temperatures to impact on the MC. The temperature development of the MC is shown in Figure 4.9. The oscillations with a period of approximately 6 hours were caused by the refilling of the helium bath, leading to flow variations. The arithmetic mean temperature with closed baffles during two of those refilling periods amounts to 9.98 mK. From the increase in temperature by 60  $\mu\text{K}$ , determined at the consecutive period with

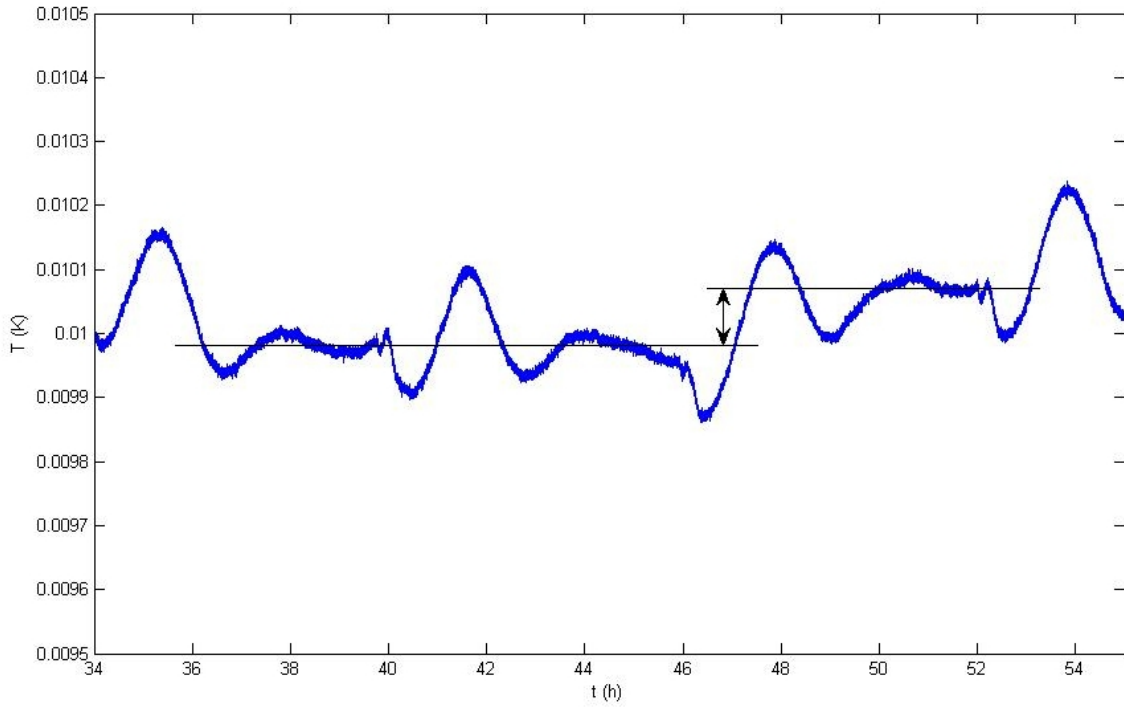


**Figure 4.9:** The temperature development of the CCDR at a flow of  $80 \mu\text{mol/s}$ . The horizontal lines show the arithmetical mean temperatures with closed and with opened vacuum baffles.

opened baffles, the additional heat load was calculated from equation (4.4) using the coefficient for  $80 \mu\text{mol/s}$ , given in Table 4.1.

Friction of the actuation mechanism of the baffles can be excluded, because any occurring heat load would be absorbed at the 700 mK heat sink. An additional heat source could be radiated heat from the 1 K shield at a temperature of approximately 1.6 K. Assuming that the whole additional heat load originated from residual gas, an upper threshold of  $\varphi_{12} = 0.014$  was calculated from equation (4.41). Using this viewing factor in equation (4.32), the heat load radiated from a black body amounts to only 1 pW. Thus, the heat load of 10 nW originated exclusively from residual gas.

The second heat load from residual gas, originating from hot molecules entering the vacuum chamber, is given by

$$\dot{Q}_{hm} = \dot{n} \frac{\bar{E}}{N} \alpha f, \quad (4.44)$$

where  $\dot{n}$  is the flow rate of particles entering the vacuum chamber and  $\alpha$  is the accommodation coefficient like above. The factor  $f$  takes into account that a reduced number of particles actually reach the MC at a lower energy.  $\bar{E}$  is the energy of  $N$  particles given by

$$\bar{E} = N k_B T, \quad (4.45)$$

where  $k_B$  is the Boltzmann constant and  $T$  is the temperature of the gas. The particle flow rate  $\dot{n}$  is calculated by

$$\dot{n} = v A \frac{N}{V}, \quad (4.46)$$

where  $A$  is the cross section of the aperture and  $N$  is the number of particles in the volume  $V$ . The particle density is given by

$$\frac{N}{V} = \frac{p}{k_B T}. \quad (4.47)$$

$v$  is the average speed of a particle, which can be calculated by

$$v = \sqrt{\frac{3 k_B T}{m}}, \quad (4.48)$$

where  $m$  is the mass of the particle. By substituting to equation (4.44), one derives

$$\dot{Q}_{hm} = \sqrt{\frac{3 k_B T}{m}} A p \alpha f. \quad (4.49)$$

The pressure measured at the pumping line of the vacuum chamber at room temperature amounts to  $10^{-7}$  mbar and the cross section of the line is roughly  $30 \text{ cm}^2$ . Considering helium as the main residual gas, the accommodation coefficient amounts to 0.36 and equation (4.49) yields a heat load of 202 nW, assuming  $f = 0.1$ . This heat load is in the right order of magnitude to make up for the residual heat load of the CCDR in the continuous operation mode. The lower temperature of the innermost heat shield in the single-shot mode could reduce the flow of hot molecules to the MC considerably, which would explain the large temperature difference between the two operation modes.

The flow rate of hot molecules is resupplied to the vacuum chamber by the outgassing and leakage through O-rings and feedthroughs. Equation (4.46) yields the particle flow rate  $\dot{n} = 2 \cdot 10^{15} \text{ s}^{-1}$ , which equals a plausible leakage of  $5.6 \cdot 10^{-5} \text{ mbar L/s}$

The time constant can be estimated from the accommodation coefficient, the duration of flight between two surfaces and the sojourn time of a particle. The speed of a helium atom is derived from equation (4.48) and amounts to roughly 160 m/s at 4 K,  $l = 0.1 \text{ m}$  for the CCDR. The sum of the flight duration and the typical sojourn time of particles amounts to roughly 1 ms. This yields a frequency of particle impingements on surfaces of  $1000 \text{ s}^{-1}$ , which should give a duration of a few seconds for a particle to thermalize.

## 4.7 Conclusions

The maximum cooling power  $\max\{\dot{Q}_m\}$  and optimum flow  $\text{opt}\{\dot{n}_3\}$  of the CCDR were experimentally determined from the scans of applied power at constant flow rates. The maximal cooling power yielded an average value for the residual heat load during 24 weeks of measurement of 303 nW. Also, the time evolution of the residual heat load during this period was derived from the maximal cooling power. The residual heat loads are clearly declining with time, but show a large scatter. This can be credibly attributed to the large time constant at low temperatures of the stainless steel MC, which is the source to a time dependent heat load that evolves with the history of the MC temperature.

The fraction of the experimentally derived values of  $\max\{\dot{Q}_m\}$  and  $\text{opt}\{\dot{n}_3\}$  was found to be in very good agreement with the theoretically expected value. This proves the internal consistency of the measured data and the effectiveness of the EMC efforts on the thermometry, described in Chapter 3.

**Table 4.4:** Summary of time-dependent and time-independent residual heat sources.

<i>Time-independent sources of residual HL</i>	<i>Time-dependant sources of residual HL</i>
- Radiated heat	- Ortho-para conversion of H <sub>2</sub>
- Cosmic rays	- Tunneling effects in amorphous solids
- Decay of radioactive nuclei	- Tunneling effects in crystalline material
- Thermal conduction	- Structural relaxation and thermoelastic stress
- Vibrations	- Residual gases
	- Stainless steel chamber

The time-dependent and time-independent residual heat sources were theoretically treated in this chapter and are summarized in Table 4.4. The theoretically well supported time-independent residual heat loads in continuous and in one-shot mode for the CCDR are given in Table 4.5.

The measurement of the residual heat load in the single-shot mode yielded a substantially lower value of 71 nW than in the continuous mode. The different temperatures of the innermost heat shield in the two modes of operation is an obvious reason. Table 4.6 compares the total theoretical residual heat load with the experimentally determined one, after 6 weeks and after 24 weeks in continuous operation and in one-shot mode after 24 weeks. The difference between the theoretical and measured values can only be attributed to a combination of three poorly known sources: vibration, residual

**Table 4.5:** Summary of the theoretical well supported time-independent residual heat loads in continuous mode  $\dot{Q}_{cont}$  and in one-shot mode  $\dot{Q}_{one-shot}$ .

<i>Origin of heat load</i>	$\dot{Q}_{cont}$ (nW)	$\dot{Q}_{one-shot}$ (nW)
Radiated heat	$1.6 \cdot 10^{-5}$	$6 \cdot 10^{-7}$
Thermal conduction	19.2	3.5
Decay of radioactive nuclei	1.3	1.3
Cosmic rays	0.036	0.036
Sum time-independent residual heat load	20.5	4.8

gas (hot molecules) and the large time constant of the stainless steel MC. Among these three, hot molecules are the only ones that can be substantially affected by a temperature variation of the innermost heat shield. Therefore, hot molecules may make up about 200 nW in continuous mode, which could be by far the largest contribution.

To reduce the heat load from hot molecules, it is recommended for EURECA to minimize the leakage rate of gases by using metal gaskets and materials with low outgassing inside the isolation vacuum. The innermost heat shield should be at a temperature as low as possible, preferably close to 20 mK. Stainless steel and other materials with long time constants should be completely abandoned from systems operating at very low temperatures. This applies especially to EURECA because the whole cryostat is brought to ambient temperature during the exchange of detector material. In case SS should be unavoidable, the additional heat load has to be taken into account for determining the DR cooling power. The influence of vibrations on the CCDR showed at least transient effects, which compromised the temperature stability. For this reason alone, an efficient vibration control will be necessary for a large detector array.

**Table 4.6:** Summary of the time-dependent residual heat loads in continuous operation  $\dot{Q}_{cont}$  after 6 weeks and 24 weeks, and of the residual heat loads in one-shot mode  $\dot{Q}_{1-shot}$  after 24 weeks.

<i>Origin of heat load</i>	$\dot{Q}_{cont}$ <i>after 6 weeks</i> (nW)	$\dot{Q}_{cont}$ <i>after 24 weeks</i> (nW)	$\dot{Q}_{one-shot}$ <i>after 24 weeks</i> (nW)
Time-independent residual heat load	20.5	20.5	4.8
Ortho-para conversion of H <sub>2</sub>	15	1	1
Tunneling effects in amorphous solids	0.017	0.001	0.001
Tunneling effects in crystalline material	1.2	0.303	0.303
Structural relaxation and thermoelastic stress	0.122	$9 \cdot 10^{-6}$	$9 \cdot 10^{-6}$
Residual gases (thermalized)	1.9	1.9	0.7
Total theoretical heat load	38.8	23.7	6.8
Total experimental heat load	329	303	71
Vibrations, residual gases (hot molecules), stainless steel chamber	290.2	276.3	64.2

## Chapter 5

# Characterization of Sintered 1 $\mu\text{m}$ Copper Powder

In the DR for EURECA, the use of sintered silver heat exchangers is not possible in the proximity of the detectors due to the relatively high background from radioactive of Ag isotopes generated by the neutrons of natural background radiation [116]. For example,  $^{108}_{47}\text{Ag(m)}$  has a decay time of 127 y, while  $^{110}_{47}\text{Ag(m)}$  has a decay time of 250 d. While the latter could enable one to store silver deep underground so long that its activity becomes sufficiently low, the former is clearly inconvenient unless a method of cleaning can be developed.

Copper, in contrast, can be made extremely radio-pure by chemical purification and is probably the best material to use, as discussed in section 2.3. However, conventional 325 mesh copper powder is not adequate for the application at lowest temperatures because of its insufficient surface area per unit volume. This powder has a surface-to-volume grain diameter of 22.8  $\mu\text{m}$ .

For the required cooling power of approximately 20  $\mu\text{W}$  at a temperature of 7 mK specified for EURECA, given in section 2.1, very fine copper powder<sup>1</sup> of 1  $\mu\text{m}$  particle diameter was investigated. Extensive studies were performed to evaluate the optimal sintering parameters, geared towards obtaining a large surface per unit volume. The thermal properties of the produced sintered heat exchanger were then tested at ultra-low temperatures between 10 mK and 40 mK.

---

<sup>1</sup>Ferro Electronic Material Systems Cu 10K-1

## 5.1 Heat Transfer at Very Low Temperatures

In pure  $^3\text{He}$  below 100 mK, quasiparticle excitations dominate the specific heat as well as most other thermal and transport properties. In this temperature region, longitudinal and transverse zero sound [96] are evident as thermally excited density excitations in  $^3\text{He}$ . However, the energy density of the zero-sound modes is insignificant compared to that of the quasiparticle excitations. Only at elevated temperatures, ordinary sound waves (first sound) contribute significantly to the specific heat.

**Table 5.1:** The specific heat  $C$  ([1]), the thermal conductivity  $S$  ([2]), the mean free path  $L$  of quasiparticles ([7] and [20]) and the viscosity  $\eta$  ([140]) of liquid pure  $^3\text{He}$ , and of  $^3\text{He}/^4\text{He}$  mixtures with 5 %  $^3\text{He}$  in  $^4\text{He}$  and 1.3 %  $^3\text{He}$  in  $^4\text{He}$ .

Property	pure $^3\text{He}$	5 % $^3\text{He}$ in $^4\text{He}$	1.3 % $^3\text{He}$ in $^4\text{He}$
$C$	$6.5 \cdot 10^5 T \text{ Jm}^{-3}\text{K}^{-2}$ for $T < 30 \text{ mK}$ )	$2.2 \cdot 10^5 T \text{ Jm}^{-3}\text{K}^{-2}$ for $T < 50 \text{ mK}$	$1.3 \cdot 10^5 T \text{ Jm}^{-3}\text{K}^{-2}$ for $T < 20 \text{ mK}$
$S$	$3.3 \cdot 10^{-4} T^{-2} \text{ Wm}^{-1}\text{K}^{-1}$	$2.4 \cdot 10^{-4} T^{-2} \text{ Wm}^{-1}\text{K}^{-1}$ for $T < 10 \text{ mK}$	$1.1 \cdot 10^{-4} T^{-2} \text{ Wm}^{-1}\text{K}^{-1}$ for $T < 10 \text{ mK}$
$l$	$2.5 \cdot 10^{-11} T^{-2} \text{ mK}^2$	$5 \cdot 10^{-10} T^{-2} \text{ mK}^2$	$1.1 \cdot 10^{-4} T^{-2} \text{ mK}^2$
$\eta$	$2 \cdot 10^{-6} T^{-2} \text{ gK}^2\text{cm}^{-1}\text{s}^{-1}$	$5 \cdot 10^{-7} T^{-2} \text{ gK}^2\text{cm}^{-1}\text{s}^{-1}$	-

In dilute  $^3\text{He}$  in  $^4\text{He}$ , the main excitation of the mixture is the single quasiparticle excitation of  $^3\text{He}$ . The properties of  $^3\text{He}$ , and of mixtures of 5.0 % and of 1.3 % of  $^3\text{He}$  in  $^4\text{He}$  are given in Table 5.1. The specific heat of the longitudinal phonons in  $^4\text{He}$  is only  $C = 3.0 \cdot 10^3 T^3 \text{ Jm}^{-3} \text{ K}^{-4}$ . Although the influence on the specific heat of the mixture is negligible, the heat conduction above 20 mK is dominated by these acoustic phonons of the  $^4\text{He}$  background-liquid for dimensions larger than 1 mm because of the very short mean free path of the  $^3\text{He}$  quasiparticles. Below 10 mK, however, the heat is transported mainly by the quasiparticles. In dilute mixtures zero sound excitations do not exist.

For pure metals, the heat capacity and the thermal conductivity below 100 mK are dominated by the single-particle excitations of the electron gas, only at very much higher temperatures the acoustic phonons gain importance. The conduction electrons form a Pauli paramagnet and magnetic

impurities provide magnetic moments that interact with the electrons. This can provide a significant energy density between 1mK and 100 mK. In the presence of a magnetic field also nuclear moments add to the heat capacity.

To cool bulk copper by means of a DR, it is necessary to transfer energy from the quasiparticles of  $^3\text{He}$ , which dominate the properties of the mixture, to the electrons in the metal. The main energy transport mechanism is from the quasiparticles in  $^3\text{He}$  via a phonon-quasiparticle interaction to the acoustic phonons in  $^4\text{He}$ , then to the phonons of the metal, and eventually to the electrons. The energy transfer between the phonons in  $^4\text{He}$  and in the metal is described by the acoustic mismatch theory, discussed in section 1.4. Direct heat flow from the  $^3\text{He}$  quasiparticles to the acoustic phonons in the metal and to the electrons is very small in diluted  $^3\text{He}$  because there is a layer of  $^4\text{He}$  on the solid [141]. Also, the coupling of the quasiparticle spins directly to the electron spins via the dipole-dipole interaction should be negligible, with the exception of very pure  $^3\text{He}$  in contact with paramagnetic dielectrics such as cerium magnesium nitrate. The dipole-dipole interaction is only short-ranged and there is a layer of  $^4\text{He}$  on the solid separating the bulk  $^3\text{He}$  [25, 45, 66].

The resistances of the main heat transfer path are in series and add up to the complete thermal resistance between the bulk metal and the  $^3\text{He}/^4\text{He}$  mixture. The individual components are:

1. Heat transfer between the  $^3\text{He}$  quasiparticles and the acoustic phonons in the mixture:

Wheatley et al. [141] analyzed the heat transfer from  $^3\text{He}$  quasiparticles to  $^4\text{He}$  acoustic phonons, based on the loss of energy of the acoustic phonons by scattering of quasiparticles that are carried along, with other quasiparticles. According to this, the conductivity in a mixture of 5 % and 1.3 % of  $^3\text{He}$  in  $^4\text{He}$  is given by  $RV T^5 \sim 10^{-11} \text{ K}^6 \text{ m}^3 \text{ W}^{-1}$ , respectively,  $RV T^5 \sim 6 \cdot 10^{-11} \text{ K}^6 \text{ m}^3 \text{ W}^{-1}$ .

2. The heat transfer between the acoustic phonons in the metal and the acoustic phonons in the mixture was discussed in section 1.4

3. Heat transfer between the acoustic phonons and the electrons in metals:

The electrons can interact with the transverse and longitudinal phonons in a metal. A theoretical analysis was first made by Little [100], who observed that below a certain particle size, this resistance would dominate over the resistance due to the acoustic mismatch. At 1 mK this would be 10  $\mu\text{m}$  for a copper-helium interface with a resistivity of  $R\sigma T^3 = 0.1 \text{ m}^2 \text{ K}^4 \text{ W}^{-1}$ . Little's theory was extended by Anderson and Peterson [8], who calcu-

lated for the thermal resistance due to the attenuation of longitudinal phonons a value of  $RV T^4 = 3.5 \cdot 10^{-9} \text{ m}^3 \text{ K}^5 \text{ W}^{-1}$  and for the transverse phonons  $RV T^3 = 8 \cdot 10^{-8} \text{ m}^3 \text{ K}^4 \text{ W}^{-1}$ . According to these results, the first is dominant above 50 mK and the latter below that value. Measurements to validate this model failed though with a discrepancy by an order of magnitude [8] and an empirical value of  $RV T^3 = 10^{-8} \text{ m}^3 \text{ K}^4 \text{ W}^{-1}$  proved useful.

Further complications arise when fine powder is used for heat exchangers. The  $^4\text{He}$  atoms are preferentially attracted to a solid surface [25, 45, 66] and a layer of 1 nm - 2 nm free of  $^3\text{He}$  atoms will form on a heat exchanger. This layer behaves much like solid  $^4\text{He}$ . Therefore, even on the concentrated  $^3\text{He}$ -rich side of a phase separated  $^3\text{He}/^4\text{He}$  mixture, a direct coupling between single quasiparticles of  $^3\text{He}$  to the metal is unlikely. In addition, solids are covered by a layer of about 50 nm of superfluid dilute phase due to Van der Waals forces [67]. Firstly, this will prevent the direct energy transfer from the acoustic phonons in the solid to  $^3\text{He}$ . Secondly, in a heat exchanger made of very small particles, the smallest pores will be filled with dilute  $^4\text{He}$  rich mixture, even in the concentrated  $^3\text{He}$  rich side.

In the small particles of sintered heat exchanger sponges, the thermal conductivity is reduced compared to the bulk metal. The electron mean free path is limited by the boundaries instead of the impurities. For pure copper ( $\text{RRR} = 100$ ) the mean free path is  $5 \mu\text{m}$  at low temperatures. For particles smaller than that, the resistance will increase. Smaller coordination number and smaller neck size will enlarge the resistivity even further.

The situation is similar for the liquid helium in the pores of a sintered sponge. The quasiparticle mean free path has a  $T^{-2}$  temperature dependence [67] and amounts to  $0.3 \mu\text{m}$  for pure  $^3\text{He}$ ,  $3 \mu\text{m}$  for 1 %  $^3\text{He}$  in  $^4\text{He}$  and  $9 \mu\text{m}$  for 5 %  $^3\text{He}$  in  $^4\text{He}$  at 10 mK. When the pore diameter  $D$  is smaller than the mean free path of the quasiparticle  $L_{qp}$ , the conductivity of the helium  $\kappa$  is given by

$$\kappa = \kappa_{bulk} \frac{D}{L_{qp}} . \quad (5.1)$$

To summarize, it should be noted that all of the above mechanisms tend to reduce the heat transfer between the liquid and solids. It is well known, however, that heat exchangers made of submicrometer size powders work well below 10 mK [137], which was the motivation to test these fine Cu powders.

## 5.2 Heat Exchangers in a Dilution Refrigerator

Sintering is a thermal treatment for bonding particles into a coherent, predominantly solid structure via mass transport events that often occur on the atomic scale [57]. The bonding leads to improved strength and to a lower system energy. The sintering temperature depends on the material and on the particle size, and is usually approximately 0.5 to 0.8 times the absolute melting temperature. As materials melt over a wide range, sintering is performed over an equally wide range of temperatures. A pile of ice cubes in the freezer give an example of sintering at low temperatures. After a few days, they form bonds and turn into a single piece of ice. On the other side, most metals sinter at several hundred  $^{\circ}\text{C}$  only. Mass transport takes place by evaporation - condensation, surface diffusion, volume diffusion, grain boundary diffusion, viscous flow, dislocation flow and plastic flow.

### Sintering Parameters

Some combinations of independent parameters prove useful to describe the properties of sintered structures. First some important vocabulary shall be defined:

- Neck:

The neck is the contact region between two particles.

- “Green” state:

The initial structure is termed the “green” state, reflecting the unfired condition of the powder [57].

- Compact:

The shaped, but unsintered powder is often termed a compact, to reflect the pressed condition. Most compacts are prepared by applying pressure to the powder to increase the density and invoke shape to the powder, common examples are vitamin pills and aspirin [57].

For a heat exchanger the natural characterisation criterion is the surface area. In addition, the fractional density is of interest to estimate the penetration of the liquid helium. Important parameters are:

- The equivalent mono-sized spherical particle diameter  $d_s$  of a sinter is given by

$$d_s = \frac{V_{bulk} \sum_i A_i}{\sum_i V_i^2} = \frac{6 V_{bulk}}{\sigma} \quad (5.2)$$

where  $V_i$  is the volume and  $A_i$  is the surface area of the  $i$ th particle,  $V_{bulk}$  is the volume of the bulk material and  $\sigma$  is the surface area of the sintered sponge.

- The coordination number  $N_C$ :

Gives the average number of contacts for a particle with its neighbour particles.

- The fractional density of the sinter or filling factor  $V_S$ , and the fractional porosity  $V_P$ :

The fractional density  $V_S$  has been given in equation (1.38). Alternatively, the fractional porosity  $V_P$ , the fractional void space in the sinter, is defined by

$$V_P = 1 - V_S, \quad (5.3)$$

In sintering both terms are widely used because they are independent of the materials and make sintering of different material comparable.

- The shrinkage  $S_L$ :

The shrinkage is the change in one dimension divided by the original dimension  $L_0$ :

$$S_L = \frac{\Delta L}{L_0}. \quad (5.4)$$

Due to density variations of the compact, shrinkage can be anisotropic (as will be discussed in section 5.2) and the result depends on the measured dimension. Assuming isotropic shrinkage the relation between volumetric and linear shrinkage is:

$$\frac{\Delta V}{V_0} = 1 - \left(1 - \frac{\Delta L}{L_0}\right)^3 \approx \frac{3 \Delta L}{L_0}, \quad (5.5)$$

where  $\Delta V$  is the change in volume and  $V_0$  is the initial volume of the compact. The latter expression in equation (5.5) is an approximation for small shrinkages only.

- The densification parameter  $\psi$ :

It gives the actual densification during sintering as a fraction of the theoretically possible shrinkage:

$$\psi = \frac{V_S - V_G}{1 - V_G}, \quad (5.6)$$

where  $V_G$  is the original green fractional density and  $V_S$  is the fractional density of the sinter.

- Grain size and shape, pore size and shape:

Pores can be divided in open and closed pores, an open pore structure usually becomes unstable at a fractional density of about 92%, because the pore length becomes large compared to a decreasing pore diameter [57].

- The relative neck size ratio  $R_{NSR}$ :

It is the effective diameter  $X$  of the neck divided by the effective particle diameter  $D$

$$R_{NSR} = \frac{X}{D}, \quad (5.7)$$

shown in Figure 5.1. The neck contains a zone of disrupted atomic bonds, forming the grain boundary. The neck size ratio is an important parameter for the mechanical and physical properties such as the strength and the thermal and electrical conductivities.

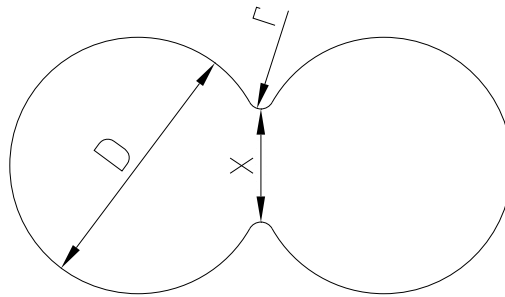


**Figure 5.1:** The neck size ratio is the fraction of the diameter of the particle contact  $X$  and of the particle diameter  $D$ . The neck is rounded by the radius  $r$ .

## Sintering Techniques

Sintering processes can be classified as pressureless and pressure-assisted sintering. The latter is a more recent technique and is useful when sintering to a low residual porosity level is desired. This technique is also applicable for sintering materials that are otherwise unresponsive to traditional sintering cycles, such as composites and high temperature intermetallics. Low pressure is used for densification control, whereas high pressure leads to a rapid densification, if the stress exceeds the yield strength of the material [57]. Pressure is usually applied hydrostatically or uniaxially only.

The pressureless sintering techniques can be classified as solid-state and liquid-phase sintering [55]. Pressureless single-phase sintering is applicable to pure substances such as nickel, alumina and copper and is the theoretically best understood sintering process. The technique can produce a

large surface area and consequently has great importance for heat exchangers for ultra low temperature (ULT) application. Therefore, single-phase sintering will be discussed below.

### Sintering Stages

In the following the sintering stages of pressureless single-phase sintering shall be summarized. The contact area of the loose powder particles before sintering can range from point contacts to highly deformed areas. It depends on the preparation of the compact, which can range from gentle tapping to arrange the particles, to isostatic or uniaxial compression with high pressure.

The initial stage is characterized by neck growth that is usually smaller than 30 %, little shrinkage of less than 3 % and an extensive loss in surface area that can be as high as 50 %. In the initial stage of solid-state sintering the relation

$$\frac{\Delta L}{L_0} = - \left( \frac{X}{2D} \right)^2 \quad (5.8)$$

between shrinkage and neck size applies for sintering that is dominated by volume mass transport mechanisms, as will be discussed below. In the initial stage the surface area depends on the neck size ratio and on the particle coordination number [57, 59], as each contact contributes equally to a loss in surface area. Therefore, a low particle coordination number before sintering is preferable for heat exchangers, to achieve a large surface area. The coordination number of the unsintered powder is influenced by the compact preparation as will be discussed below. A sufficient neck size ratio is necessary, however, to ensure mechanical strength and good thermal conduction within the sponge.

In the intermediate stage the pores become rounded, discrete particles become less evident and a significant densification occurs. The pore structure becomes tubular but remains open to the bulk material until very late in this stage, so that gas can still permeate. Also grains and pores increase in size. Materials which should have a porous structure must end sintering in this stage at the latest.

In the final stage the pores become spherical and are no longer connected to the bulk surface. This stage features final densification and extensive grain growth.

Clearly, this classification is rather theoretical and the transition is not clearly defined. In practice, different stages occur simultaneously at different locations in the sinter. During sintering, the particles rearrange to a compound with lower surface energies by rotation, which increases the number of contacts. Those new contacts will start at the initial sintering stage, while the old contacts already have progressed in sintering.

### Sintering Mass Transport Mechanisms

On the microstructural scale, the bonding by sintering is achieved by the neck growth between particles. This is driven by different mass transport mechanisms on the atomic scale, which can be categorized in surface and volume transport mechanisms.

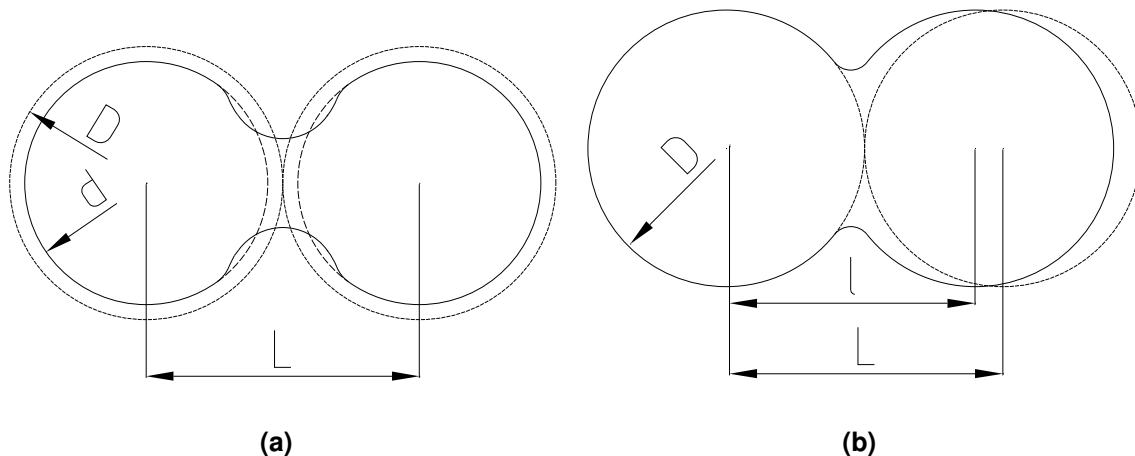


**Figure 5.2:** In sintering due to surface diffusion the material for growing bonds between particles originates from the particle surfaces reducing the particle sizes (a). This is called coarsening. In volume mass transport dominated sintering the particles use internal mass sources to grow interparticle necks. Therefore, the particle centers approach each other (b), which leads to shrinkage.

Surface transport mechanisms are flow over free surfaces and vaporization/condensation [82, 90]. The first one is dominant in the low temperature region during heating, because the necessary activation energy is lower than that for vaporization and condensation. It loses importance at higher temperatures because of the low surface vacancy density at elevated temperatures. The flow over free surfaces is important for almost all materials in the initial stage of sintering. In the latter stages it acts to distribute mass transported to the surface at the grain boundaries by grain boundary diffusion [130]. Vaporization and condensation are most active in low-stability materials such as lead-based compounds [57], for powders with high surface area and with high vapour pressure.

Due to mass flow originating and terminating at the surface, surface transport mechanisms enable neck growth without a change in distance of particle centers, as illustrated in Figure 5.2 (a), and hence without densification. This is called coarsening. There is a reduction in surface area and a growth in grain size and mechanical strength. Also, the thermal conductivity of the sponge increases. This stage is best monitored by the surface area and by pore and grain size parameters. Low temperatures

and low heating rates favor the surface transport mechanisms, while high heating rates have to be applied to avoid surface diffusion when high densification is desired.

Bulk transport mechanisms are volume diffusion, grain boundary diffusion [32], plastic flow and viscous flow. Volume diffusion is the transport of vacancies from the neck to the interparticle grain boundary. This sinter mechanism needs a relatively high activation energy and thus can only dominate at high temperatures. In the final stage of sintering, volume diffusion drives densification of small pores and coarsening of large ones, due to their vacancy distribution gradient.

Grain boundary diffusion is important for crystalline metals and requires intermediate activation energy. During sintering grain boundaries form bonds between particles that are misaligned crystal structures. The importance of grain boundary diffusion for sintering depends on the number of grain boundaries per unit volume and thus on the particle size [85]. After the formation of new grain boundaries by surface diffusion in the initial stage of sintering, the impact of grain boundary diffusion increases.

Plastic flow is usually only important during heating for particles with many dislocations such as in highly compacted powders. It is due to the movement of dislocations, either dislocation climb due to vacancy absorption, or dislocation glide due to surface stress that exceeds the flow stress at the sintering temperature. Both result in an elimination of dislocations and therefore the effect declines with time. Plastic flow is a transient process that is not active during isothermal sintering, it is only important when sintering stress and thermal stress incorporate. Together with a high dislocation density, plastic flow can result in a 10 to 100 times higher sintering rate during the initial phase of sintering [29, 109]. Viscous flow is important for amorphous materials and for metals in the presence of a liquid phase.

Volume transport mechanisms are necessary for densification because material from the bulk is deposited at the neck, which leads to an approach of the particle centers as shown in Figure 5.2 (b). Both surface transport mechanisms and volume transport dominated sintering equally lead to a loss in surface area. While in the former case the particles shrink, in the latter case the particle size remains unchanged but the particles approach each other.

Depending on which atomic transport mechanism dominates during sintering, coarsening or densification is favored, but a loss of surface occurs either way. By choosing the sintering parameters accordingly, the atomic mass transport mechanisms and the sintering result can be influenced. In sintering usually a combination of mass transport mechanisms is evident, leading to a further densifi-

cation of already dense areas and coarsening of less dense regions in the compact [46]. For that reason gradients of the compact density due to improper preparation or unequal particle size distribution in the compact have to be avoided.

### The Driving Force of Sintering

While the sintering transport mechanisms determine the path of the mass flow, the sintering stress is the driving force. Sintering stress aims at minimizing the surface energy (and thus, the surface area), the source of which is disrupted atomic bonding. This can be done either by growing grains and pores or by reducing curvatures, preferably by growing necks between particles, as this area has the largest curvature.

The stress  $\sigma_S$  associated by a curved surface is expressed by

$$\sigma_S = \gamma \left( \frac{1}{R_1} + \frac{1}{R_2} \right), \quad (5.9)$$

where the surface energy is  $\gamma$  and  $R_1$  and  $R_2$  are the main perpendicular radii. A convex radius has a positive value, because it leads to tensile stress, while a concave radius is negative for its compression stress. For a spherical particle  $R_1$  and  $R_2$  are both  $D/2$  and equation (5.9) for a sphere becomes:

$$\sigma_S = \frac{4\gamma}{D}, \quad (5.10)$$

where  $D$  is the diameter of the sphere. The surface tension increases with decreasing particle size and becomes zero when  $D = \infty$ . Therefore, sintering increases the particle size.

For the neck, the contact area of two particles, equation (5.9) becomes

$$\sigma_S = \gamma \left( \frac{2}{X} - \frac{4D}{X^2} \right), \quad (5.11)$$

where  $X$  is the neck size diameter and  $-X^2/(4D)$  is approximately the radius  $r$  between the two particles in Figure 5.1. The minus sign results from  $r$  being concave. The difference between equations (5.10) and (5.11) is the sintering stress in the neck region. It is the driving force for mass transport and is large due to the change of the sign of the stress.

In addition to the sintering stress  $\sigma_S$  which directs the mass flow, a thermal activation is necessary to enable a mass transport. With rising temperature, the atoms move faster and mass flows, driven by the sintering stress. The influence of the temperature on sintering is given by the Arrhenius equation

$$\frac{N}{N_0} = e^{-\frac{E_a}{k_B T}} \quad (5.12)$$

where  $T$  is the absolute temperature,  $E_q$  is the activation energy,  $k_B$  is the Boltzmann constant,  $N$  is the number of activated molecules or available vacant atomic sites and  $N_0$  is the absolute number of molecules.

### Sintering of Small Particles

Particles sinter due to atomic level events that reduce the surface energy. Smaller particles have a higher curvature and a larger surface area per volume, resulting in higher energy per volume and thus featuring faster sintering. This is evident by an increased density when sintering finer powders under the same conditions [39].

**Table 5.2:** For a simplified analysis the parameters  $m$ ,  $n$  and  $B_0$  can be considered approximately constant with the mechanism of mass transport. The sintering time and temperature given by the equations (5.13) and (5.14) show different sensitivities to the particle size, depending on the dominant sintering mass transport mechanism. The symbols of  $B_0$  are described in the text.

<i>sintering mass transport mechanism</i>	$m$	$n$	$B_0$
Viscous flow	1	2	$3\gamma/\eta$
Plastic flow	1	2	$9\pi\gamma b D_v/(kT)$
Evaporation-condensation	2	3	$(3P\gamma/\rho^2)(\pi/2)^{1/2}(M/(kT))^{3/2}$
Volume diffusion	3	5	$80 D_v \gamma \Omega/(kT)$
Grain boundary diffusion	4	6	$10\delta D_b \gamma \Omega/(kT)$
Surface diffusion	4	7	$56 D_S \gamma \Omega^{4/3}/(kT)$

The sintering result can be evaluated by the neck size ratio. The neck size ratio is crucial for the mechanical strength, as well as for the thermal conductivity of a sinter. To achieve the same result when using powders with different particle diameters  $D$ , one has to sinter isothermally for the time  $t$  [70]

$$t_1 = t_2 \left( \frac{D_2}{D_1} \right)^m, \quad (5.13)$$

where the exponent  $m$  depends upon the mass transport mechanism and is given in Table 5.2. Each mechanism shows a different sensitivity to the particle size. For surface diffusion and grain boundary diffusion the influence on grain size is largest, because smaller particles have a larger surface and

a higher interface density per volume, as well as a higher curvature. The values of  $m$  are given in Table 5.2.

For porous structures sintering finishes in the initial stage of sintering. Derived from a simple model, in this initial stage of sintering the neck size ratio  $X/D$  up to a value of 0.3 can be roughly estimated by the equation:

$$\left(\frac{X}{D}\right)^n = \frac{B_0 t}{D^m}, \quad (5.14)$$

where  $t$  is the isothermal sintering time and  $B_0$  is given by an Arrhenius temperature dependence

$$B = B_0 e^{-\frac{E_a}{k_B T}}, \quad (5.15)$$

where  $k_B$  is Boltzmann's constant,  $T$  is the absolute temperature and  $m$ ,  $n$  and  $B_0$  are given in Table 5.2 and depend on the sintering mechanism and on the material properties. The symbols used in the Table are the surface energy  $\gamma$ , the viscosity  $\eta$ , the Burgers vector<sup>2</sup>  $b$ , the theoretical density  $\rho$ , the grain boundary width  $\delta$ , the volume diffusivity  $D_v$ , the surface diffusivity  $D_s$ , the vapour pressure  $P$ , the molecular weight  $M$  and the atomic volume  $\Omega$ .

It can be seen from equation (5.14) and (5.15) that smaller particles result in faster sintering. Also, the sintering depends strongly on the sintering temperature, whereas time has a relatively small impact. Ultra fine metallic powders ( $< 100 \text{ nm}$ ) have very low sintering temperatures ( $T < 400 \text{ }^\circ\text{C}$ ) [9]. This can be the problematic for removing impurities from their surface, because it requires a minimum temperature.

## Sintering Theory

In most sintering models, with a few exceptions [133], the idealizations feature:

- mono-sized spheres,
- in point contacts between the particles,
- very high heating rates,
- sintering under isothermal conditions.

In reality, powder with a range of particle sizes is used. The powder is usually sieved with one certain mesh size and thus consists of a wide particle size distribution, from which only the maximal grain

<sup>2</sup>The Burgers vector is the fundamental quantity defining an arbitrary dislocation

size is known. Also the particle shape typically deviates from spherical. While in pressureless sintering the point contact hypothesis is valid, in pressure-assisted sintering the contact surface between particles can be quite large.

Practical heating rates are limited due to the power rating of the heating elements and the heat capacity of the compact. Also low heating rates are applied on purpose to avoid thermal stress that might damage the sintered piece and to achieve the desired mass transport mechanism. On the contrary, short sintering times are used to reduce the shrinkage.

Also the effects of a sintering atmosphere with an oxidation or reduction reaction, and the surface condition of the powder, which can be affected by organic binders, are difficult to take into account in modeling. Lubricant additives and atmospheric gas films do strongly influence the mass transport mechanism. The same applies to the crystal orientation and the crystal defects like dislocations due to high heating rates and powder preparation. Further discrepancies between reality and theory arise from a difficult structure of the grain boundaries and from a non uniform green compact density, which will be discussed below.

Even the simplest and best understood case of pressureless single-phase sintering is a very complex process. Thus, the simulation results are only in very rare cases in excellent agreement with reality. Therefore, experimental studies are necessary. In the following, practical considerations and techniques about sintering are discussed.

### **Sintering Support**

The support has to be resistant to high temperatures, must not stick to the sinter or contaminate the sample. Suitable materials are molybdenum, silica, graphite or alumina, a complete list with their properties can be found elsewhere [40]. Figure 5.3 (a) shows the support for the sintering the samples for the surface area measurement. Graphite was chosen due to its availability, low cost and ease of manufacturing. A mould made of three parts was used to facilitate an even compact preparation. The powder was filled to the top of the third part and soft tapping was applied, which caused a rearrangement of the particles and therefore, considerable shrinkage. Then the top piece was removed and the excessive powder was wiped off.

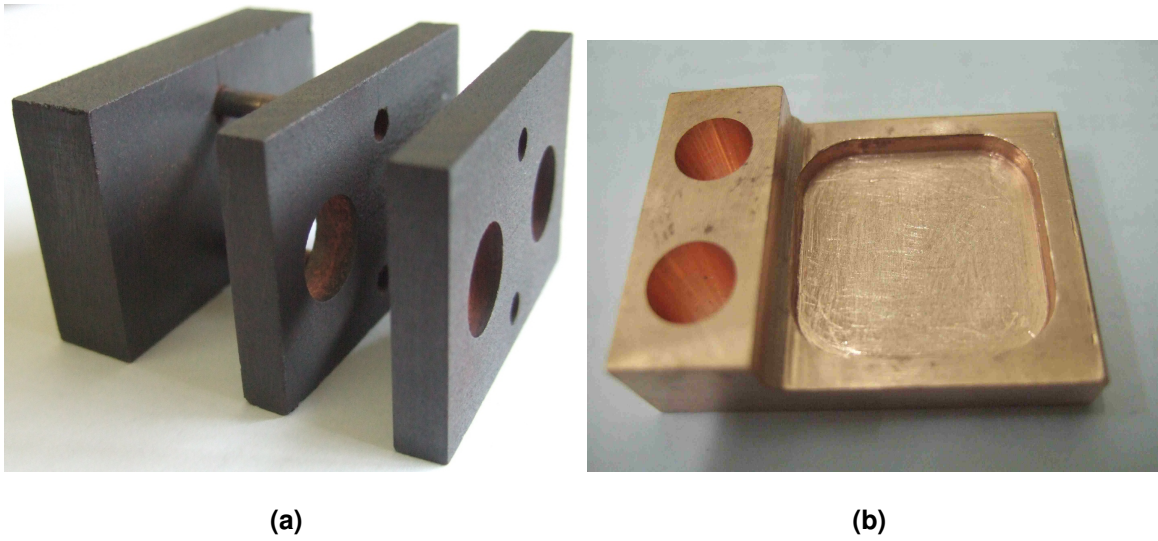


**Figure 5.3:** A mould for sintering 2 cylinders for the measurement of the surface area (a) and the support for measuring the heat exchanger performance in the DR (b).

### Compact Preparation and the Influence on the Sintering Result

Problems that become evident during sintering are often originating from a bad compact preparation. An unequal green density distribution is only evident after sintering, as sintering is more likely to enlarge faults rather than to cure them. Therefore, a careful compact preparation is essential to achieve a good sintered product.

Under pressure the particle rearrangement results in a higher coordination number  $N_C$ . It can range from 7, for a non-treated powder, up to 14 when high pressure is applied [47, 58, 103]. The pore size and the porosity decrease with higher pressure, whereas the density and the size of particle contact areas increase. A higher fractional green density  $V_G$  leads to faster sintering and a higher final density, but also to less shrinking and less dimensional change. Thus, a higher precision of a product's final dimensions is achievable.

To qualify the shaped powder, the packing coordination number  $N_C$ , the initial relative neck size ratio  $X/D$  and the fractional density of the green powder  $V_G$  are suitable parameters. During the densification of a powder with ductile particles, the coordination number and the neck-size ratio will increase. Starting from initially  $X/D \approx 0$  of the loose powder, the neck size ratio can be calculated from [57]

$$\frac{X}{D} = 4 \left[ 1 - \left( \frac{V_G}{V_C} \right)^{\frac{1}{3}} \right]^{\frac{1}{2}}, \quad (5.16)$$

where  $V_G$  and  $V_C$  are the green and the compacted fractional densities of the powder. The coordina-

tion number of mono-sized spherical particles in a regular packing increases almost linearly with the powder compaction, up to a fractional packing density of approximately 0.64 [58]. The assumption of regular packing is only valid for very large particle sizes. For small grains a statistical packing with varying coordination number is applicable. The average coordination number of a statistical packing is always lower than those of a regular packing up to a fractional density of 0.7 [118].

During sintering new contacts are formed due to the densification, entailing the coordination number [57]

$$N_C = 7 + 17.5 (V_S - 0.6) . \quad (5.17)$$

The expression is most accurate for sintered fractional densities between 0.6 and 0.9. As packing and coordination number are correlated, particles with high coordination numbers will densify, while those with few contacts are likely to produce pore coarsening. Thus, a variation of the compact density will result in unequal densification during sintering. Also, for larger compacts, compression by gravitational forces may lead to an unequal shrinkage. The lower powder is vertically more densified and therefore shrinks more in that direction and less horizontally.

Also the ordering of the particle sizes during compact preparation may play a role in anisotropic shrinking. A mono-sized powder gives a uniform green density distribution. On the contrary, a distribution of particle sizes leads to a local densification and coarsening. However, in the initial sintering stage the small particles provide a high sintering activity [56, 114].

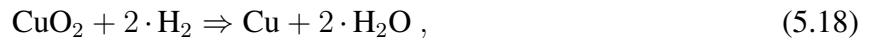
For heat exchangers a wide particle size distribution can be advantageous if used correctly. Under gentle tapping and gravitational drive, the smaller particles are prone to collect at the bottom onto the bulk copper substrate. The preferred occurrence of small, highly active particles at the bottom can form a good mechanical and thermal contact to the bulk copper. On the top a pore structure open toward the liquid helium is achieved by the larger particles.

A disadvantage of an unequal density distribution for a heat exchanger is the potential reduction in surface area. Pores start closing over a wide range of average fractional densities, because locally the critical density can be reached [144]. Depending on the standard deviation of the particle distribution, closed pores already develop at a fairly low fractional density of 0.66. This is a value that can be reached with the investigated 1  $\mu\text{m}$  copper powder.

## The Sintering Atmosphere

The sintering atmosphere is selected for different purposes, depending on the sintered material. Common sintering atmospheres are helium, 6% of hydrogen in argon, 100% of hydrogen or vacuum.

Fine copper powder, which is not stored in an inert gas, reacts with oxygen and sulphur dioxide in the atmosphere ( $\text{CuO}_2$  is red,  $\text{CuS}$  is black). Although copper will also sinter in the presence of an oxide layer [71], it is beneficial to remove the oxide in order to improve bonding of the particles. For this pre-sintering, the compact is heated to an elevated temperature of  $500^\circ\text{C}$  in a deoxidizing atmosphere. Hydrogen deoxidises the copper oxide by the reaction



and is commonly used for presintering copper [33, 97]. The reducing reaction depends on the ratio of the partial pressures of the  $\text{H}_2$  and the  $\text{H}_2\text{O}$ . A high partial pressure of  $\text{H}_2$  leads to reduction, whereas a high partial pressure of  $\text{H}_2\text{O}$  leads to oxidation. The water formed during the presintering changes this ratio. A key measurement of the water impurity is the dew point. It gives the temperature at which water vapour will condense. With a higher  $\text{H}_2\text{O}$  partial pressure, higher temperatures are necessary to achieve a deoxidizing reaction.

To control impurities, it can be advantageous to permanently subject the compact to vacuum until the pre-sintering temperature is reached. In a  $\text{H}_2$  atmosphere, the water vapor produced during the reducing reaction is easily transported by purging the sintering atmosphere.

The sintering atmosphere also has the function to transfer heat to the sinter and within the porous structure. Heat is transferred by radiation, and by conduction and convection by the gas in the furnace. Porous structures have a strongly reduced conductivity compared to the bulk material. The heat transfer can be calculated, depending on the fractional porosity  $V_P$ , the fractional density  $V_S$  and an empirical constant  $\chi$  that was determined to fit a value of 11 best [84], with the equation [3]

$$\frac{\kappa}{\kappa_0} = \frac{V_S}{1 + \chi V_P^2} . \quad (5.19)$$

For a compact with  $V_S = 0.4$  and  $V_P = 0.6$ , this yields a reduction of the thermal conductivity by a factor of 0.081 for the sinter. With normal heating rates, however, the thermal conductance in the compound is not an issue for a highly conductive material such as copper.

More problematic is the heat transfer to the sinter. At higher temperatures the heat  $\dot{Q}$  is effectively transferred by radiation. At low temperatures in particular, the ambient gas has a major impact in

transferring heat from the furnace wall to the compact by conduction and convection. Hydrogen has a very high thermal conductivity  $\kappa \simeq 378 \frac{\text{mW}}{\text{K m}}$  [57]. The heat transfer  $\dot{Q}$  by the sintering atmosphere, depends on the thermal conductivity  $\kappa$  of the gas and on the distance  $y$  between the sample and the furnace wall.

After the presintering process, a thorough evacuation of the hydrogen is important. Any remaining gas could be absorbed during the following sintering and result in a large time dependent heat leak, due to a very slow exothermal ortho-para conversion of hydrogen as was discussed in section 4.6. During sintering, an inert helium atmosphere ensures a good thermal conductivity between the furnace walls and the sample. Helium also features a high thermal conductivity  $\kappa \simeq 304 \frac{\text{mW}}{\text{K m}}$  [57] and protects the sinter against contamination.

## Measurement Techniques

The requirements for a good sintered heat exchanger are:

- 1) A large surface to volume ratio to overcome Kapitza resistance,
- 2) A porous structure with open pores to the liquid to allow access for the helium,
- 3) A good thermal conductivity of the sinter itself and between the sinter and the bulk of the copper substrate.

**Table 5.3:** Possible measurement techniques for important sintering parameters.

<i>Sintering parameter</i>	<i>Measurement technique</i>
Fractional density and porosity	- Dimensions and weight - Archimedes technique
Grain and pore size	- Optical microscopy - Electron microscopy - Mercury porosimetry
Surface area	- Gas adsorption - Mercury porosimetry - Gas permeability

To validate a sintered sample for its suitability as heat exchanger, the surface area has to be verified. This can be done roughly by determining the fractional density. The determination of the fractional density and porosity can be done as simply as by measuring the dimensions and the weight, if the geometry is simple. In more complex cases the Archimedes technique or microscopy and the point counting technique can be applied.

Measurement techniques to determine the surface area are gas adsorption<sup>3</sup>, mercury porosimetry [28, 117], gas permeability and microscopic analysis. The first three methods are suitable for high surface areas and only for open pores. On the contrary, the last method is most useful for small surface areas or for closed pores. Gas permeability measurement only takes into account the pores through the sinter, whereas gas adsorption and mercury porosimetry measures all pores open to the surface. Gas permeability determines the surface area accessible by the helium, which is the important dimension for the heat transfer. The latter two methods can overestimate the surface area effective for the heat transfer. Therefore, gas permeability is more suitable for the application of a heat exchanger. The practical procedure will be discussed in more detail below.

The microstructure, which has an influence on the heat exchange between the sintered structure and the liquid helium, can be studied with optical and electron microscopy to evaluate the grain and pore size and shape. A list of common measurement techniques for validating important sinter parameters is given in Table 5.3.

## The Surface Area

An important parameter for the sintering processes and an essential design feature for a heat exchanger is the surface area  $\sigma$ , available for the heat transfer between liquid helium and the copper grains. It can be expressed either per unit volume or per unit mass, the first being more valuable for the application in a DR.

The determination of the surface area of a porous structure with the gas permeability method is a straightforward and exact technique. A sintered element is streamed through by a gas with reasonable low flow, to achieve laminar flow. The flow velocity and the pressure drop are measured. For very accurate measurements the absorption of the gas on the sinter must be taken into account.

---

<sup>3</sup>often referred to as BET after the developers Brunauer, Emmett and Teller

With the equation by Kozeny and Carman [119] the surface area  $\sigma$  can be calculated from

$$\frac{\sigma}{V} = \left[ \frac{V_P^3}{5\alpha} \right]^{\frac{1}{2}}, \quad (5.20)$$

where  $V$  is the volume of the sinter and  $V_P$  is the fractional porosity. The permeability coefficient  $\alpha$  can be calculated from Darcy's law [57]

$$\alpha = \frac{\omega_0 H \eta}{\Delta P}, \quad (5.21)$$

where  $\Delta P$  is the pressure drop across a sample with height  $H$ , and  $\eta$  is the dynamic viscosity of the gas. The flow velocity through the porous material is given by

$$\omega_0 = \frac{\dot{V}}{A}, \quad (5.22)$$

where  $\dot{V}$  is the volumetric gas flow and  $A$  is the cross-sectional area. Equations (5.20), (5.21) and (5.22) give finally the surface per unit volume

$$\frac{\sigma}{V} = \sqrt{\frac{V_P^3 A \Delta P}{5 \dot{V} H \eta}}, \quad (5.23)$$

An alternative equation to determine the surface area can be derived from the formula of the pressure drop  $\Delta P_{tube}$  in a tube

$$\Delta P_{tube} = \zeta \frac{L}{d} \frac{\rho}{2} \omega_0^2, \quad (5.24)$$

where  $\zeta$  is the coefficient of drag,  $L$  is the length of the tube,  $d$  is the tube diameter,  $\rho$  is the density of the flowing medium and  $\omega$  the flow velocity of the medium. The surface area of a porous material can be calculated with the following changes:

The hydraulic pore diameter  $d'$  in the sinter can be calculated in analogy to a tube with non-circular cross-section by:

$$d' = \frac{4 V_{void}}{\sigma} = \frac{2 V_P}{3(1 - V_P)} d_s, \quad (5.25)$$

where  $V_{void}$  is the void space in the sinter,  $\sigma$  is the surface area,  $V_P$  is the fractional porosity given by equation (5.3) and  $d_s$  is the equivalent particle diameter for mono-sized spherical particles. For particles of non spherical shape,  $d_s$  is given by

$$d_s = \frac{6 V_{bulk}}{\sigma} \quad (5.26)$$

where  $V_{bulk}$  is the volume of the bulk material only. As the gas velocity in the sinter increases with lower fractional porosity  $V_P$ , a characteristic velocity  $\omega$  in the sinter can be defined by

$$\omega = \frac{\omega_0}{V_P}, \quad (5.27)$$

where  $\omega_0$  is the velocity in the empty tube like above. The coefficient of drag for laminar flow is given by

$$\zeta = \frac{64}{Re} . \quad (5.28)$$

The Reynolds number is calculated by

$$Re = \frac{\omega_0 d'}{V_P \nu} , \quad (5.29)$$

where  $\nu$  is the kinematic viscosity of the flowing medium. The extended passage  $l$  through the porous structure is considered by the factor  $\mu$  given by

$$l = \mu H , \quad (5.30)$$

where  $H$  is the height of the sinter in the direction of the flow. For unordered, mono-sized particles, for a porosity between 0.37 and 0.42,  $\mu$  is given by [15, 88]

$$\mu = \frac{2.2}{\zeta} \left( \frac{64}{Re} + \frac{1.8}{Re^{0.1}} \right) . \quad (5.31)$$

With the additional factor  $\left(\frac{0.4}{V_P}\right)^{0.78}$ , equation (5.31) is also valid for sinters with porosities between 0.195 and 0.64 and for a distribution of particle sizes [75, 76, 107, 124], resulting in:

$$\mu = \frac{2.2}{\zeta} \left( \frac{0.4}{V_P} \right)^{0.78} \left( \frac{64}{Re} + \frac{1.8}{Re^{0.1}} \right) \quad (5.32)$$

This gives the general equation for a porous structure

$$\Delta P = \zeta \frac{l}{d'} \frac{\rho}{2} \omega^2 . \quad (5.33)$$

The drag coefficient  $\zeta$  in equation (5.33) is substituted by equation (5.28) with the Reynolds number from equation (5.29). The hydraulic diameter  $d'$  is replaced by equation (5.25). This leads after some transformations to the relation between the surface area  $\sigma$  as a function of the pressure drop, the flow velocity and the properties of the flowing medium,  $\rho$  and  $\nu$ , as well as the parameters of the sinter  $V_P$  and  $V_{void}$

$$\sigma = \sqrt{\frac{\Delta P A V_{void}^3}{2 \mu H \eta \dot{V} V}} . \quad (5.34)$$

Equations (5.23) and (5.34) are equivalent for the simplified assumption in the former equation that  $2\mu = 5$ . The latter equation is applicable for a broader range of fractional densities.

## 5.3 Experimental Study of the 1 $\mu\text{m}$ Copper Powder

In this section the results of the study of two copper powders will be presented. The investigated powders are, firstly, the ESPI<sup>4</sup> powder with a maximal particle size of 44  $\mu\text{m}$  and secondly, the powder from FERRO<sup>5</sup>, with a mean green particle size of 1.15  $\mu\text{m}$ . The first powder was used in the main heat exchanger of the CCDR. The properties determined for this powder will allow to calculate the cooling power of the CCDR and compare the derived value with the cooling power reported in Chapter 4.

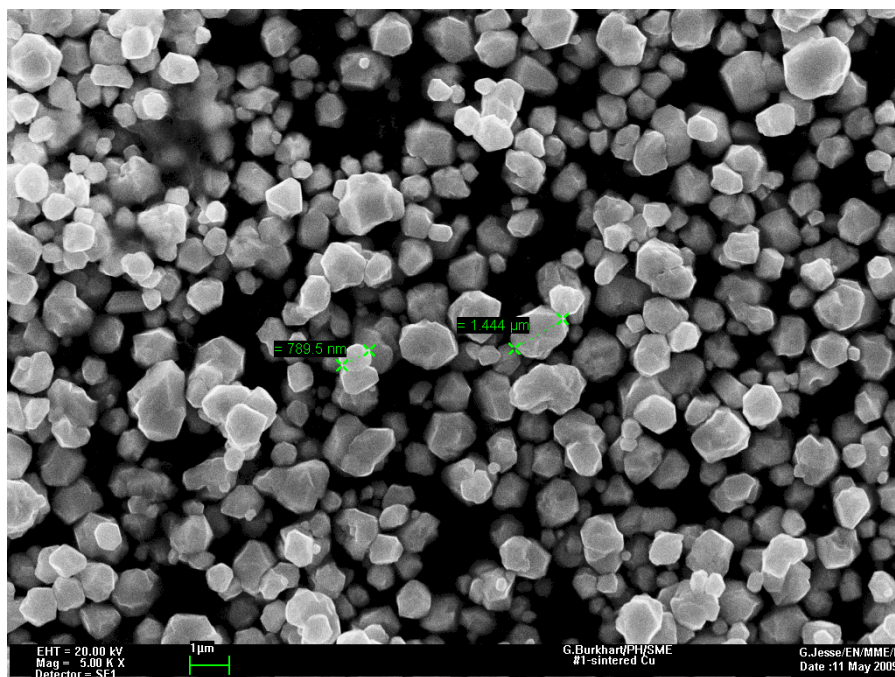


**Figure 5.4:** SEM image of the green FERRO copper powder at a magnification factor of 5000.

The Particle Size Distribution (PSD) of the fine powder has been determined by a laser diffraction analyzer<sup>6</sup> [77]. Figure 5.4, made by a scanning electron microscope<sup>7</sup>, shows the fine crystalline structure of the powder and the minimal and maximal measured particle sizes of 0.7  $\mu\text{m}$  and 1.5  $\mu\text{m}$ . The purity of the powder is approximately 99.19 %, with the dominant impurities being carbon and oxygen. The carbon is not dissolved in copper, and it does not influence the thermal properties of the sintered powder. Also, the purity of the compound after sintering will be better than that because

<sup>4</sup>Electronic Space Products International 325 mesh Cu powder

<sup>5</sup>FERRO Electro Material Systems Cu 10K-1

<sup>6</sup>Leeds & Northrup Microtrac model X100

<sup>7</sup>Leo 430 SEM (Scanning Electron Microscope)

most of the oxygen is removed during presintering. Without the oxygen, the sinter has a purity of approximately 99.55 %. Details of both powders are given in Table 5.4.

**Table 5.4:** The Particle Size Distribution (PSD), the fractional green density  $V_G$ , the specific surface areas and the purity for the green powders FERRO Cu 10K-1 and ESPI 325 mesh.

<i>Powder</i>	<i>PSD</i> ( $\mu\text{m}$ )	$V_G$ ( $\mu\text{m}$ )	$\sigma/V$ ( $\frac{\text{cm}^2}{\text{cm}^3}$ )	<i>Purity</i>
Ferro Cu 10K-1	95 % < 2.44, 90 % < 1.96, 50 % < 1.15, 10 % < 0.76	0.37	29044	$\sim$ 99.19 % [C = 4376 ppm, O = 3571 ppm, Ag = 60 ppm, Ca = 23 ppm, Cr, Si, Zn, Sn, Fe, Na, Al, Mg, Ni and Li < 20 ppm each]
ESPI 325 mesh	< 44	0.39	-	3N (99.9 %)

### Optimisation of the Sinter Parameters

To optimise the sinter parameters, samples of cylindrical shape were sintered in a graphite mould. The mould is depicted in Figure 5.3 (a). The green dimensions of the samples amount to 5 mm in height and 10 mm in diameter. The sintering temperature was varied between  $650^\circ$  and  $850^\circ$  in steps of  $50^\circ$ , and the sintering time from 1 min to 1 h. The sintered structures were evaluated by determining their fractional density, surface area, mechanical resistance and bonding to the bulk copper substrate. The results are outlined below.

As compact preparation, the powder was only gently tapped. This ensures a good particle arrangement but avoids too high a coordination number. As each particle contact is consuming the same amount of surface area during initial sintering, the surface area is inversely proportional to the coordination number, as was discussed in section 5.2. Therefore, a low green density is desirable to achieve a porous heat exchanger with a high surface area. This cautious preparation technique also prevents excessive segregation of particles of different sizes. The green fractional density  $V_G$  was measured to be 0.37 for the 1  $\mu\text{m}$  powder, and 0.39 for the 44  $\mu\text{m}$  powder.

The sintering was carried out in a furnace capable of operating at a maximum temperature of  $1500^\circ\text{C}$  and heating rates of approximately  $10 \frac{^\circ\text{C}}{\text{min}}$ . To enable the sintering in different atmospheres,

the furnace was equipped with a leak tight cylindrical chamber, made of high-temperature steel alloy. The chamber is sealed with a water cooled O-ring. The space available for samples is approximately 200 mm in length and 80 mm in diameter.

The temperature was measured by a K-type<sup>8</sup> thermocouple with the ambient temperature as reference. The temperature was recorded by a chart recorder. A more exact temperature value was determined from the potential of the thermocouple measured with a digital multimeter, using a potential-temperature look-up table.

The 325 mesh powder was sintered according to the recipe of Niinikoski [111]:

1. vacuum pumping with a turbo-molecular pump for 60 min at ambient temperature,
2. heating to the pre-sintering temperature of 500 °C while continuing pumping,
3. 60 min presintering at 500 °C with a deoxidizing atmosphere of a mixture of 6 % hydrogen and 94 % argon at 1100 mbar,
4. pumping the hydrogen-argon mixture while heating to the sintering temperature of 850 °C, which took approximately 50 minutes,
5. isothermal sintering for 20 min with helium at 1100 mbar as sintering atmosphere,
6. slow cool down to ambient temperature, for about 1 h, to avoid thermal stress in the sinter.

For the 1  $\mu\text{m}$  powder, the presintering in the 6 % hydrogen atmosphere proved insufficient due to the much larger surface area. Owing to the large amount of oxide at the particle's surface, the diluted hydrogen atmosphere obviously became saturated by the produced  $\text{H}_2\text{O}$  vapour. The samples did not achieve satisfying results, even when sintered at elevated temperature and for a long time. Therefore, the Ar- $\text{H}_2$  mixture was substituted by pure  $\text{H}_2$ . In addition, the gas was purged three times during the presintering process to remove the water vapour.

A heat exchanger must have a high porosity to allow helium to enter. Therefore a low fractional density is desirable. The fractional density of samples, sintered with different parameters, was determined from the mass of the sample and from the dimensions, which were measured by a caliper rule. With a precision of  $\pm 50 \mu\text{m}$  for the linear measurement and of  $\pm 0.01 \text{ g}$  for the mass measurement,  $V_S$  was determined to an accuracy of better than  $\pm 5\%$ . The evaluated fractional densities are plotted

---

<sup>8</sup>nickel-chrome/nickel-aluminium

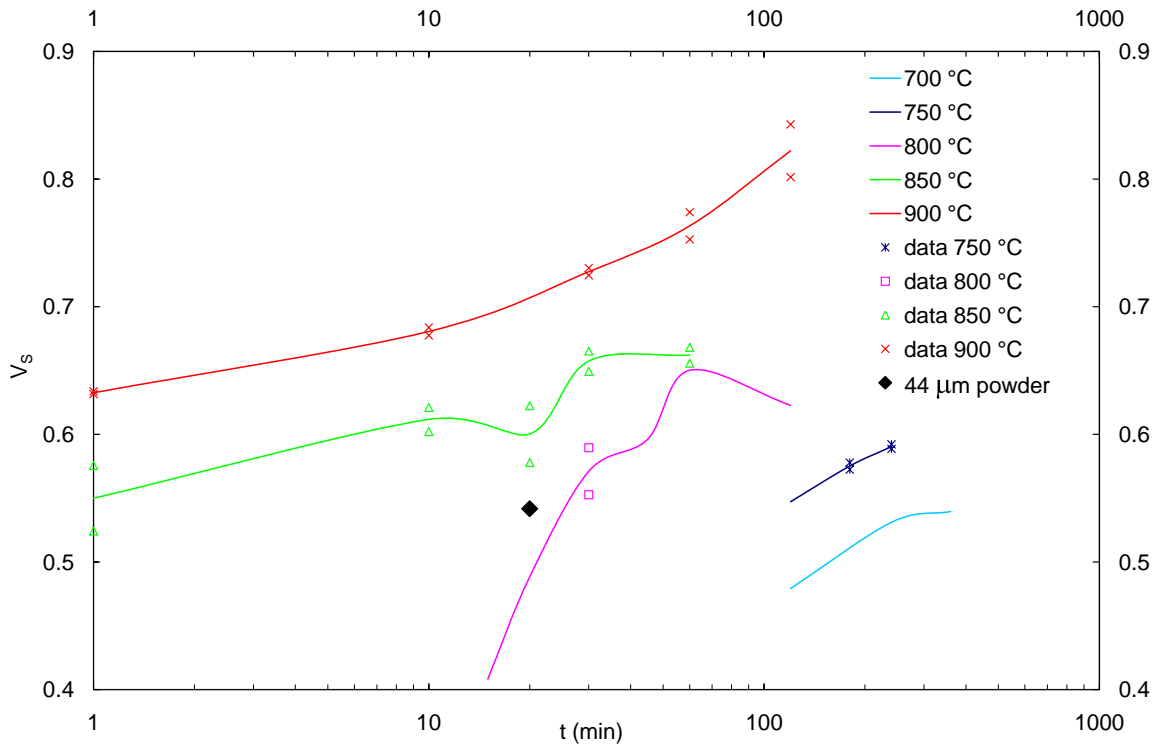


**Figure 5.5:** The fractional density  $V_S$  depending on the isothermally sintered duration  $t$ . The 1  $\mu\text{m}$  powder was sintered at temperatures of 700 °C, 750 °C, 800 °C, 850 °C and 900 °C. The 44  $\mu\text{m}$  powder was sintered for 20 min at 850 °C.

in Figure 5.5 as a function of sintering time and for sintering temperatures ranging from 700 °C to 900 °C, in steps of 50 °C. In the beginning of the 800 °C sintering curve, there is a steep increase, indicating a very active growth of necks at particle interfaces. Later  $V_S$  is relatively stable and the sinter result is fairly independent of the sintering time. For the 850 °C curve this slope is not evident, probably because sintering occurs already during the heating phase. At higher temperatures the fractional density is higher for all isothermal sintering times, indicating too high a sintering temperature. At 750 °C and 700 °C a substantial time for sintering is necessary to get a sufficiently strong sinter. In general, lower isothermal sintering temperatures result in a higher surface area but in a longer sintering time to obtain a mechanically strong sinter.

The surface areas of three samples of the 1  $\mu\text{m}$  powder and for the 44  $\mu\text{m}$  powder were determined by the permeability measurement described above in section 5.2. The fine powder was sintered at temperatures of 750 °C, 800 °C and 850 °C, for the minimum time to achieve a sufficient mechanical strength.

Helium was used as a flow medium for the permeability measurements. The differential pressure

**Table 5.5:** Maximal absolute errors of the gas permeability measurements to determine the surface area.

<i>Dimension</i>	<i>Pressure</i> (Pa)	<i>Time</i> (s)	<i>Length</i> (mm)	<i>Diameter</i> (mm)	<i>Mass</i> (g)
Max. Absolute Deviation	100	0.5	0.05	0.05	0.01

across the sample of 60 mbar was measured by a differential pressure sensor<sup>9</sup>. The very low volume flow was determined by collecting the volume of helium gas permeating the sample in a given time interval. Using the uncertainties of Table 5.5, the relative error in surface area amounts to  $\pm 8.2\%$  when assuming a Gaussian distribution of the deviations. The measured equivalent mono-sized spherical particle diameter  $d_s$  was derived from equation (1.37). The surface area was calculated by equation (5.34), using equation (5.32) to determine  $\mu$ . The results of the measurements are summarized in Table (5.6).

**Table 5.6:** The fractional density  $V_S$ , the surface area  $\sigma$  measured by gas permeability and the equivalent mono-sized spherical particle diameter  $d_s$  for different powders, isothermally sintered for the duration  $t$  at the temperature  $T$ .

<i>Powder</i>	<i>t</i> (min)	<i>T</i> (°C)	$V_S$	$\frac{\sigma}{m}$ ( $\text{cm}^2/\text{cm}^3$ )	$d_s$ ( $\mu\text{m}$ )	<i>Error</i> (%)
ESPI -325 mesh	20	850	0.524	1529	20.6	6.6
Ferro Cu 10K-1	10	750	0.428	13293	1.9	5.7
Ferro Cu 10K-1	10	800	0.481	10852	2.7	6.3
Ferro Cu 10K-1	10	850	0.603	3990	9.1	8.2

The largest surface area of  $1.3293 \text{ m}^2/\text{cm}^3$  for the  $1 \mu\text{m}$  powder was obtained for a sintering time of 10 minutes at  $750 \text{ }^\circ\text{C}$ . In Figure 5.6 a SEM image of a fracture of this sintered structure at a magnification of 1000 is shown. With higher sintering temperatures the surface area declines rapidly and is only  $1/3$  of the highest value at  $850 \text{ }^\circ\text{C}$ . The best sample of the  $1 \mu\text{m}$  powder has a larger surface area by almost 1 order of magnitude than the sample sintered with the  $44 \mu\text{m}$  powder.

For a sintered sponge to efficiently work as a heat exchanger, critical requirements are a sufficient

<sup>9</sup>Siemens SITRANS P 7MF 4420

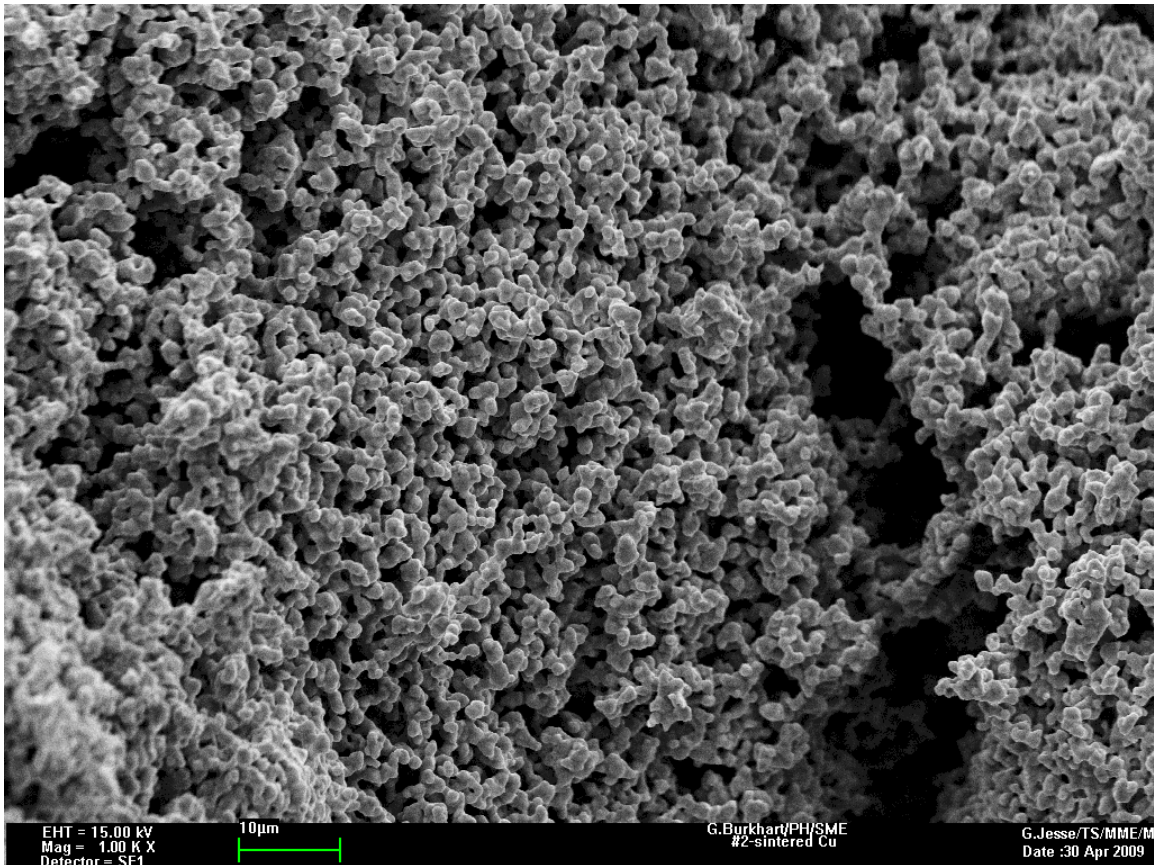


**Figure 5.6:** SEM image of the sintered 1  $\mu\text{m}$  Cu-powder at a magnification of 1000.

mechanical strength, a good intergrain thermal conductivity, and an excellent bond to the bulk copper surface. In a good approximation, the mechanical strength increases with decreasing porosity, as pores reduce the cross section. At low densities, pores concentrate the stress such that the interparticle sinter bond determines the strength. The stress concentration depends on the grain size and on the pore characteristics, such as porosity and pore shape [69, 73]. Also the neck size plays an important role, and different models have been developed [27]. In a simple model the mechanical strength is given by the equation:

$$\sigma = \sigma_0 K V_S^m, \quad (5.35)$$

where  $\sigma_0$  is the strength of the bulk material,  $V_S$  is the fractional density,  $K$  and  $m$  are factors that are dependent on the stress concentration and have to be determined experimentally. Equation (5.35) shows the main dependence of the strength on the fractional density and on the microstructure.

The mechanical properties were tested for the 1  $\mu\text{m}$  powder, using the previously evaluated optimum sintering temperature of 750  $^{\circ}\text{C}$ . The surface of the substrate was carefully prepared to improve the bonding of the sinter. The surface was roughened using fine sand paper to remove the oxide layer

and to increase the coordination number between powder and support, as was discussed in section 5.2. Subsequently the copper substrate was air-cleaned and degreased with ethanol.

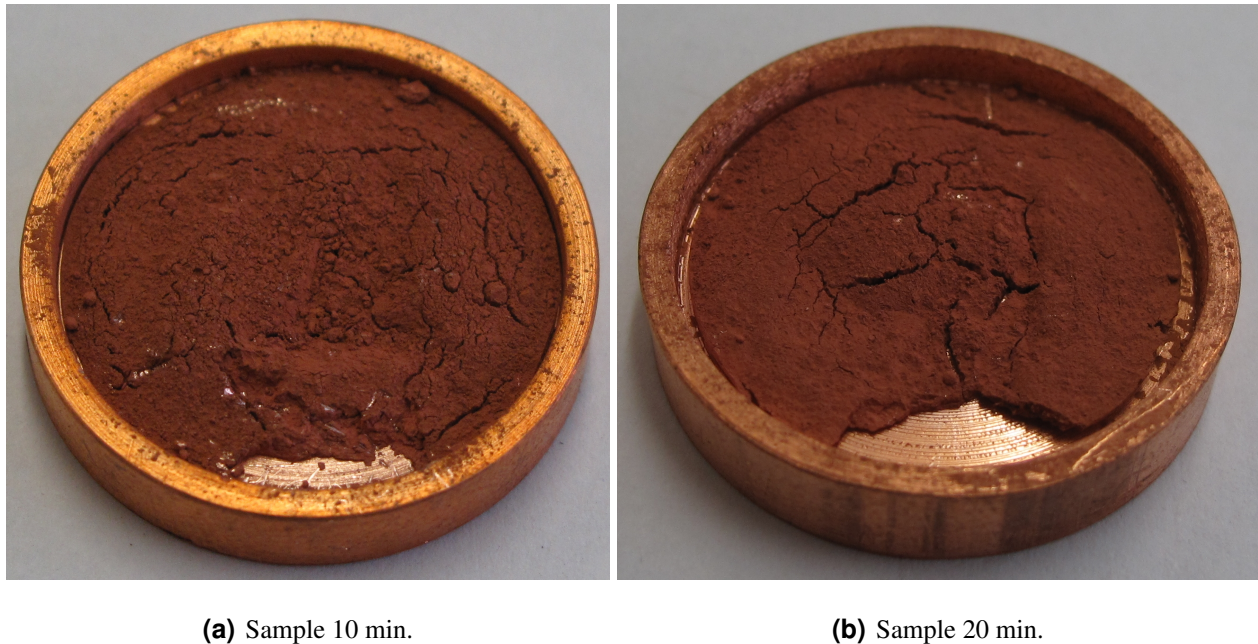


**Figure 5.7:** Samples of the fine powder sintered in simple copper moulds at a temperature of 750 °C for 10 min (a) and for 20 min (b). The shrinkage of the right sample is obvious. Also a larger piece broke loose at sample (b) during the mechanical test.

The sintering parameters are influenced by the sintering mould. While for the surface area measurement moulds of graphite were used, for the thermal characterization copper moulds were used. Sintering durations of 10 min and 20 min were studied. The mechanical strength of the powder, as well as its bonding to a surface, are tested by tearing the sinter off with a sharp tool. Figure 5.7 shows samples sintered for 10 min and 20 min at 750 °C. The sample that was sintered for 20 min showed significant radial shrinkage, indicating an insufficient bond to the support. The sample with 10 min sintering time showed minimal radial shrinkage and the mechanical test confirmed an excellent bond. Therefore, the optimum sintering parameters for the fine powder has been determined to be an isothermal sintering duration of 10 min at a temperature of 750 °C. To determine the thermal properties, samples of both powders with different thicknesses were investigated inside the MC of the CCDR.

### Measurement of the Heat Exchanger Performance

To characterize the thermal behavior of the 1  $\mu\text{m}$  powder at temperatures between 10 mK and 40 mK, specimens were tested in the CCDR. Three heat exchangers made of the 1  $\mu\text{m}$  powder with thicknesses of 0.1 mm, 0.5 mm, and 1.0 mm, and two samples of the 44  $\mu\text{m}$  powder with thicknesses of 0.5 mm and 1.0 mm were tested inside the mixing chamber. The details of the samples are listed in Table 5.7.

**Table 5.7:** The dimensions, the nominal powder thickness  $h$  and the powder mass  $m_p$  of the sintered samples tested in the CCDR. The surface area  $\sigma$  was determined via the measured powder mass and  $\sigma/m$  from Table 5.6.

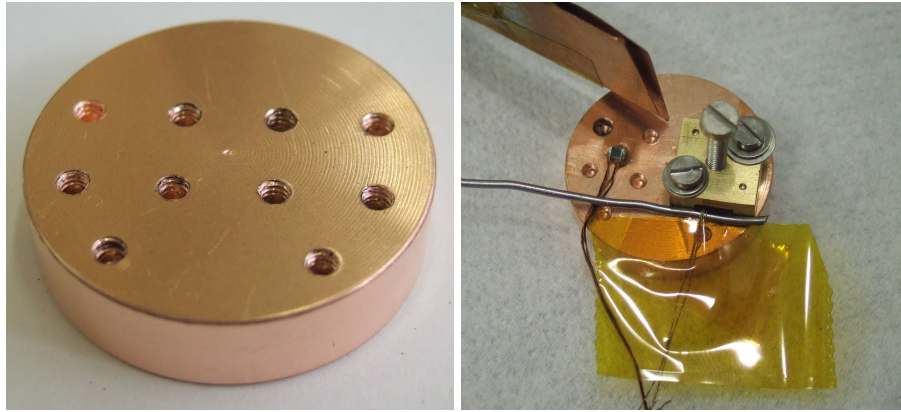
Sample	Dimensions (mm)	$h$ (mm)	$m_p$ (g)	$\sigma$ ( $\text{cm}^2$ )
1.1	$d = 22$	0.5	0.68	222
1.2		1.0	1.36	445
2.1	20 x 20, corner radius	0.1	0.13	453
2.2		1.0	1.17	4074
2.3	$r = 5$	0.5	0.59	2054



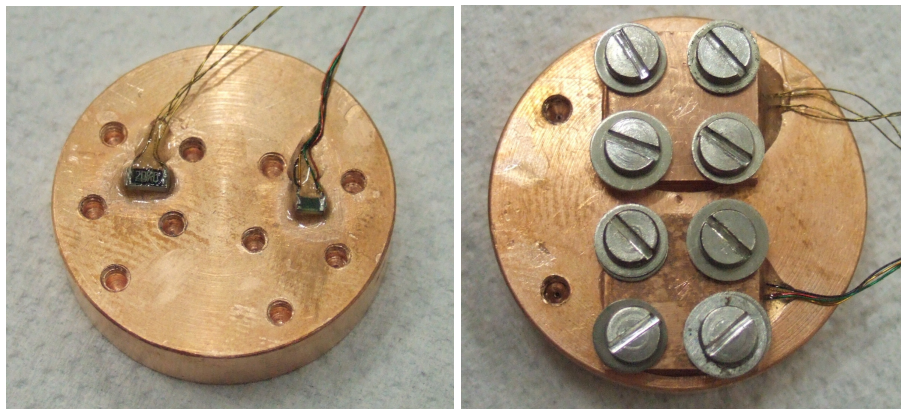
**Figure 5.8:** The sintered samples of the ESPI copper powder.

Figure 5.8 shows the heat exchanger samples of the ESPI powder. The substrates were cylindrical cups with a diameter of 22 mm. In Figure 5.9 the mounting process is illustrated at different steps. In this setup the sensors and the cables on a length of approximately 10 mm, were glued directly onto

the copper support with epoxy. A small tool was used to press the sensors to the surface while the glue was hardening. Finally, the sensors were encapsulated in epoxy and a lid with a suitable recess was mounted on top, secured by four M2 screws.



(a) Backside of the sample with the threaded holes. (b) the heater and thermometer are mounted.



(c) The heater and thermometer glued in place. (d) Final assembly with the lids in place.

**Figure 5.9:** The mounting of the sensors onto the supports of the 44  $\mu\text{m}$  copper powder.

The heat exchangers made of the FERRO powder are shown in Figure 5.10. Figure 5.11 shows the design of the support for the 1  $\mu\text{m}$  samples. The cavity for the heat exchanger is rectangular with a lateral length of 20 mm and a curve of 5 mm radius. The support features two conical holes for mounting the sensors. In this design each sensor was mounted inside a separate copper piece shown on the right in Figure 5.11. Each sensor was demountably attached to the support of the heat exchanger, which allows to reuse the sensors in further measurements. The sensors were pressed onto the inner surface of the copper cones while gluing them, to ensure good thermal contact. The sensors were then encapsulated in epoxy too isolate them from the liquid helium. The conical pieces were then

screwed to the copper support with a M3 screw, to achieve a sufficiently large contact pressing force. The small angle of the cone increases this force and therefore the thermal contact considerably.

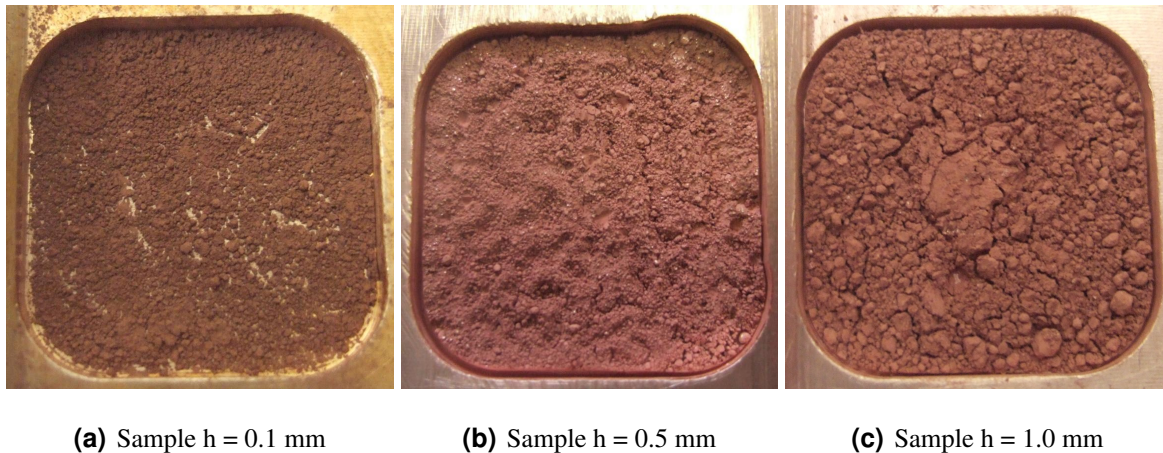


**Figure 5.10:** Sample of the FERRO with different sinter thicknesses.

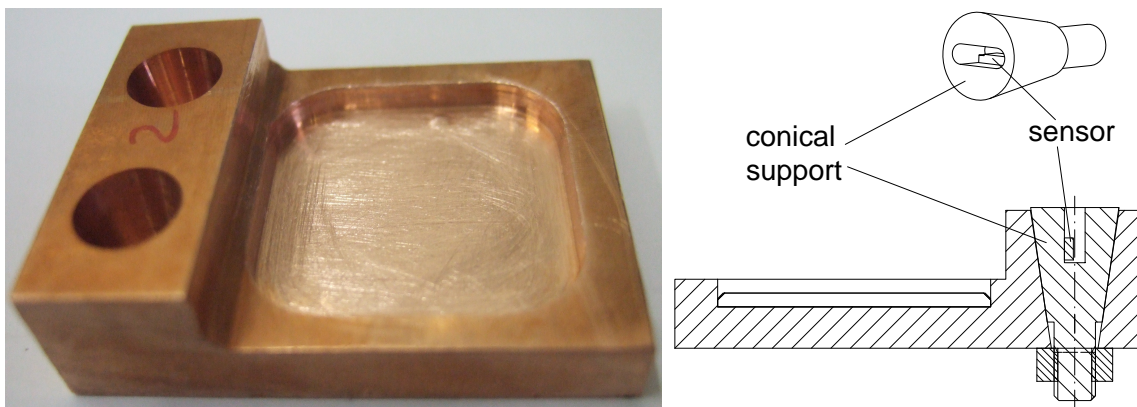


**Figure 5.11:** The copper support for the 1  $\mu\text{m}$  powder sample and the sensors mounted with a conical copper contact. The epoxy potting of the sensor cavity is not shown for clarity.

Figure 5.12 shows the assembly of the 1  $\mu\text{m}$  powder samples mounted inside the MC. The amount of  $^3\text{He}$  was determined in the one-shot mode, described in Section 4.2, to be  $79.5 L_{STP} \pm 0.8 L_{STP}$ . The mixing chamber has a diameter of 96.6 mm and a height of 44.15 mm. The phase boundary in the mixing chamber is located  $18.9 \text{ mm} \pm 0.2 \text{ mm}$  below the lid. The amount of  $^3\text{He}$  in the heat exchanger, in the still and in the pipework and pumps was not taken into account. Hence, the samples were approximately half immersed in the concentrated phase of the helium mixture. This does not influence the measurements, since a layer of  $^4\text{He}$  covers the sinter in both phases, as was described in Section 5.1.

To determine the thermal performance of the heat exchangers, each sample was heated while

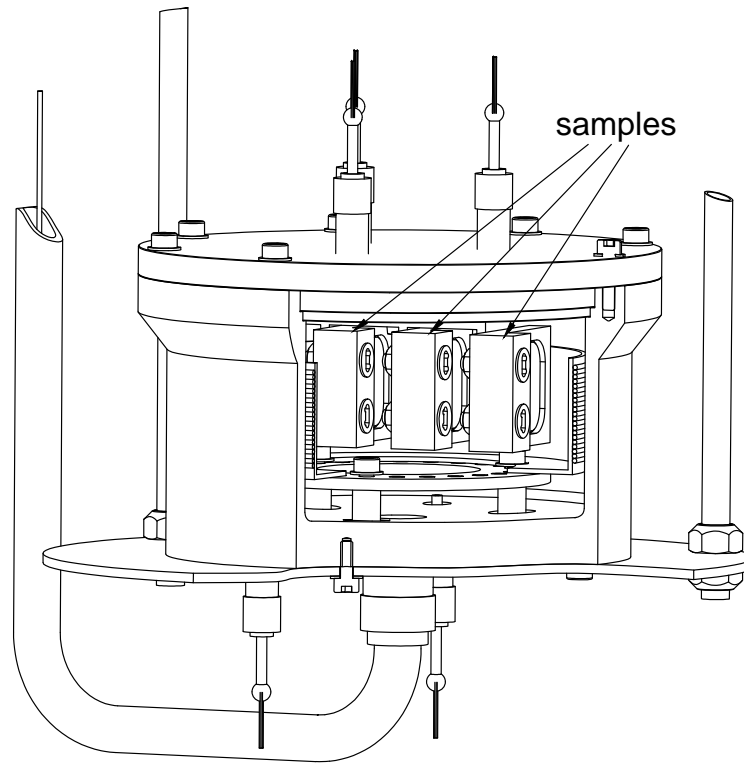


**Figure 5.12:** Three samples with the FERRO powder, mounted in the mixing chamber

the MC temperature was close to the base temperature. The heating power was determined and the temperatures of the sample and of the helium mixture were measured by resistance thermometers. The heater was biased with an ultra-low-noise isolated voltage source and the power changed in small steps corresponding to the measurements described in section 4.3. To reduce systematic errors, each sample was measured with ascending and descending heating power steps.

The time constant of the sintered samples can be determined in analogy to the discussion in section 4.2 by the equations (4.9) and (4.10). The specific heat capacity of copper  $C_c$  is given by

$$C_c = A_c T, \quad (5.36)$$

where  $A_c$  amounts to  $0.691 \text{ mJ}/(\text{mol K}^2)$  [37]. The thermal resistance of screwed copper-copper joints was measured by Suomi et al. [129] at temperatures between 20 mK and 200 mK. The joints were screwed together only “finger tight”. The thermal resistance was found to be inversely linear in temperature and the upper limit for the resistance amounts to

$$R_{\text{Cu-Cu}} = \frac{\Delta T}{\dot{Q}} = 4 \frac{\text{K}^2}{\text{W}} T^{-1}. \quad (5.37)$$

This should be a very conservative figure for the copper-copper connection used in this setup since a maximal torque was used for tightening the screw and the cone increased the pressing force further.

A copper cone for mounting one sensor has the mass  $m_c = 2$  g. The mass of the copper substrate  $m_s$  amounts to 40 g. The time constant for the cone  $\tau_{\text{cone-sub}}$  and the substrate  $\tau_{\text{sub-cone}}$  to thermalize with each other, is temperature independent and given by

$$\tau_{\text{cone-sub}} = 9 \cdot 10^{-5} \text{ s} \quad (5.38)$$

and

$$\tau_{\text{sub-cone}} = 2 \cdot 10^{-3} \text{ s} . \quad (5.39)$$

A typical value of  $S = 2.5 \cdot 10^{-3} \text{ W/cm}^2 \text{ K}^4$  for the Kapitza conductance at an interface between bulk copper and helium will be used for a worst case estimate. The surface area at the interface amounts to  $381 \text{ cm}^2$  at least. The time constant  $\tau_{\text{sub-He}}$  of the substrate to thermalize with the helium bath is given by

$$\tau_{\text{sub-He}} = 10^{-4} \text{ s K}^2 T^{-2} . \quad (5.40)$$

The time constant increases at lower temperatures but is still far less than 1 s at 10 mK.

To estimate the heat leak from a copper cone directly to the helium bath, the ratio of the thermal resistance cone - substrate and cone - liquid helium is important. For a small heat leak the ratio has to be very small. The thermal resistance to the copper cone and the substrate is given by equation (5.37). The heat transfer between bulk copper and a liquid helium mixture was measured between 14 mK and 200 mK [121] and is given by

$$R_K = 50 \frac{\text{cm}^2 \text{ K}^4}{\text{W}} T^{-3} . \quad (5.41)$$

The relation of the resistances is given by

$$\frac{R_{\text{Cu-Cu}}}{R_K} = 0.08 \frac{\text{cm}}{\text{K}^2} T^2 . \quad (5.42)$$

The surface area of the cone exposed to the liquid helium amounts to less than  $1 \text{ cm}^2$ . At 100 mK the thermal resistance from the cone to the helium is more than three orders of magnitude larger than a good copper-copper joint.

For the measurements of the sample with a sinter thickness of 0.1 mm, 0.5 mm and 1.0 mm, constant step durations of 15 min, 20 min and 25 min were used, respectively.

## Results of the Measurements

The heat transfer rate from the sample to the helium mixture is given by

$$\dot{Q} = \sigma S (T_S^4 - T_m^4), \quad (5.43)$$

where  $T_s$  and  $T_m$  are the temperatures of the substrate and of the helium mixture, and  $S$  is the Kapitza conductance given by equation (1.34).

The measured Kapitza conductance of the ESPI powder is given in Figure 5.13 depending on the sample temperature. Values for  $S$  of  $0.0017 \frac{\text{W}}{\text{cm}^2 \text{K}^4}$  and  $0.0010 \frac{\text{W}}{\text{cm}^2 \text{K}^4}$  have been found for sinters with thicknesses of 0.5 mm and 1.0 mm, respectively. The temperature dependence agrees well with the theoretical one given by equation (5.43).

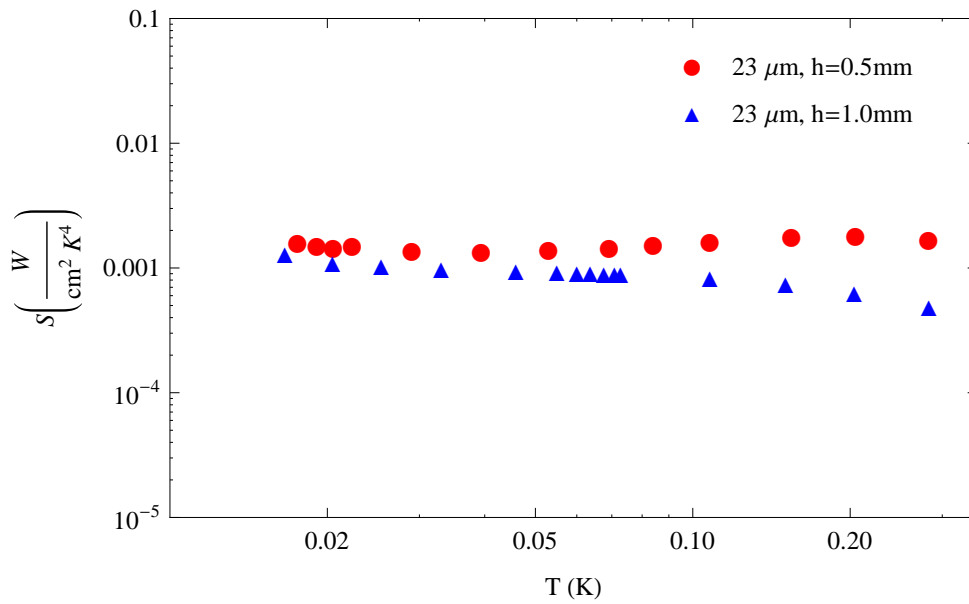


**Figure 5.13:** The measured thermal conductance  $S$  of the 44  $\mu\text{m}$  powder to dilute  $^3\text{He}$  in  $^4\text{He}$ , determined by the equation (5.43) as a function of the sample temperature  $T$ .

With the measured surface area and Kapitza conductance of the ESPI powder, it is now possible to calculate directly  $\gamma$  that was experimentally determined in Section 4.3 to amount to  $31.8 \text{ W/K}^4$ . The surface area  $\sigma$  in the CCDR between the concentrated stream and the heat exchanger was previously calculated by equation (1.37), assuming an equivalent surface-to-volume diameter of  $d_s = 18 \mu\text{m}$  [142]. With the newly measured value of  $d_s = 20.6 \mu\text{m}$ , the surface area amounts to  $\sigma = 1530 \text{ cm}^2$ . The thickness of the sintered layer in the CCDR is approximately 1 mm, therefore the measured value for  $S$  of the 1.0 mm thick heat exchanger was used. From the Equations (4.1) and (4.16) one finds

$$\gamma = \left(\frac{a}{2b}\right)^2 \sigma S = 28.5 \frac{\text{W}}{\text{K}^4}. \quad (5.44)$$

The calculated value for  $\gamma$  is in very good agreement with that (Chapter 4) experimentally determined, which amounts to  $\gamma = 31.8 \frac{\text{W}}{\text{K}^4}$ . This not only shows the quality of the measured data but also of the

thermometry.

The Kapitza conductance of the 1  $\mu\text{m}$  powder is given in the Figure 5.14.  $S$  increases with decreasing temperature due to the temperature dependent penetration depth [89]. The penetration depth increases the, for the heat transfer effective, surface area with decreasing temperature until it equals the depth of the pores. This occurs at a temperature of 25 mK and 20 mK for the 0.5 mm and 1 mm thick sample, respectively. Below these temperatures the full heat exchanger surface areas are effective and  $S$  is constant with maximum values of  $0.05 \frac{\text{W}}{\text{cm}^2 \text{K}^4}$  and  $0.20 \frac{\text{W}}{\text{cm}^2 \text{K}^4}$  for the sinter thicknesses of 0.5 mm and 1 mm, respectively. For the thinnest sample,  $S$  would be expected to be constant in the whole temperature range as the penetration depth is reached at higher temperature. However, it shows a  $T^{-2}$  dependence, the reason for which is unknown.

Historically, the thermal resistance  $R = \sigma \Delta T / \dot{Q}$  was first discovered and studied by P. Kapitza at rather high temperatures above 1 K where the condition  $\Delta T \ll T$  was easy to obtain experimentally. For a very small temperature difference  $\Delta T = T_S - T_{MC} \ll T_{MC}$ , equation (5.43) may be written as

$$\dot{Q} = \sigma S (T_S^4 - T_m^4) = 4 \sigma S T_m^3 \Delta T. \quad (5.45)$$

Therefore in the literature the results are mostly presented in the form

$$\frac{\Delta T}{\dot{Q}} = \frac{1}{4 \sigma S T^3} = R_K \quad (5.46)$$

and the data plotted for the parameter  $R_K \sigma T^3 = \frac{1}{4S}$ , which is constant as long as  $S$  is constant.

The measured  $S$  for the 44  $\mu\text{m}$  powder with thicknesses of 1.0 mm and 0.5 mm, equals Kapitza resistances of  $147 \frac{\text{cm}^2 \text{K}^4}{\text{W}}$  and  $250 \frac{\text{cm}^2 \text{K}^4}{\text{W}}$ . For comparison,  $R_K \sigma T^3$  of the 44  $\mu\text{m}$  samples are shown in Figure 5.15, together with measurements by Radebaugh et al. [122] on the thermal boundary resistance between dilute  $^3\text{He}$  and annealed bulk copper, and between dilute  $^3\text{He}$  and sintered 16  $\mu\text{m}$  copper powder. The original graphs are given in Figure A.1. The measurements in this work agree very well in magnitude and in temperature dependence with the previous measurements.

For the 1  $\mu\text{m}$  powder minimal values for  $R_K \sigma T^3$  of  $5 \frac{\text{cm}^2 \text{K}^4}{\text{W}}$  and  $1.25 \frac{\text{cm}^2 \text{K}^4}{\text{W}}$  were found in this work for the 0.5 mm and the 1.0 mm thick samples. The temperature dependences of the three samples are given in Figure 5.16, together with measurements again by Radebaugh et al. [122] and by Siegwarth et al. [127] on the thermal boundary resistance between dilute  $^3\text{He}$  and

- annealed bulk copper,

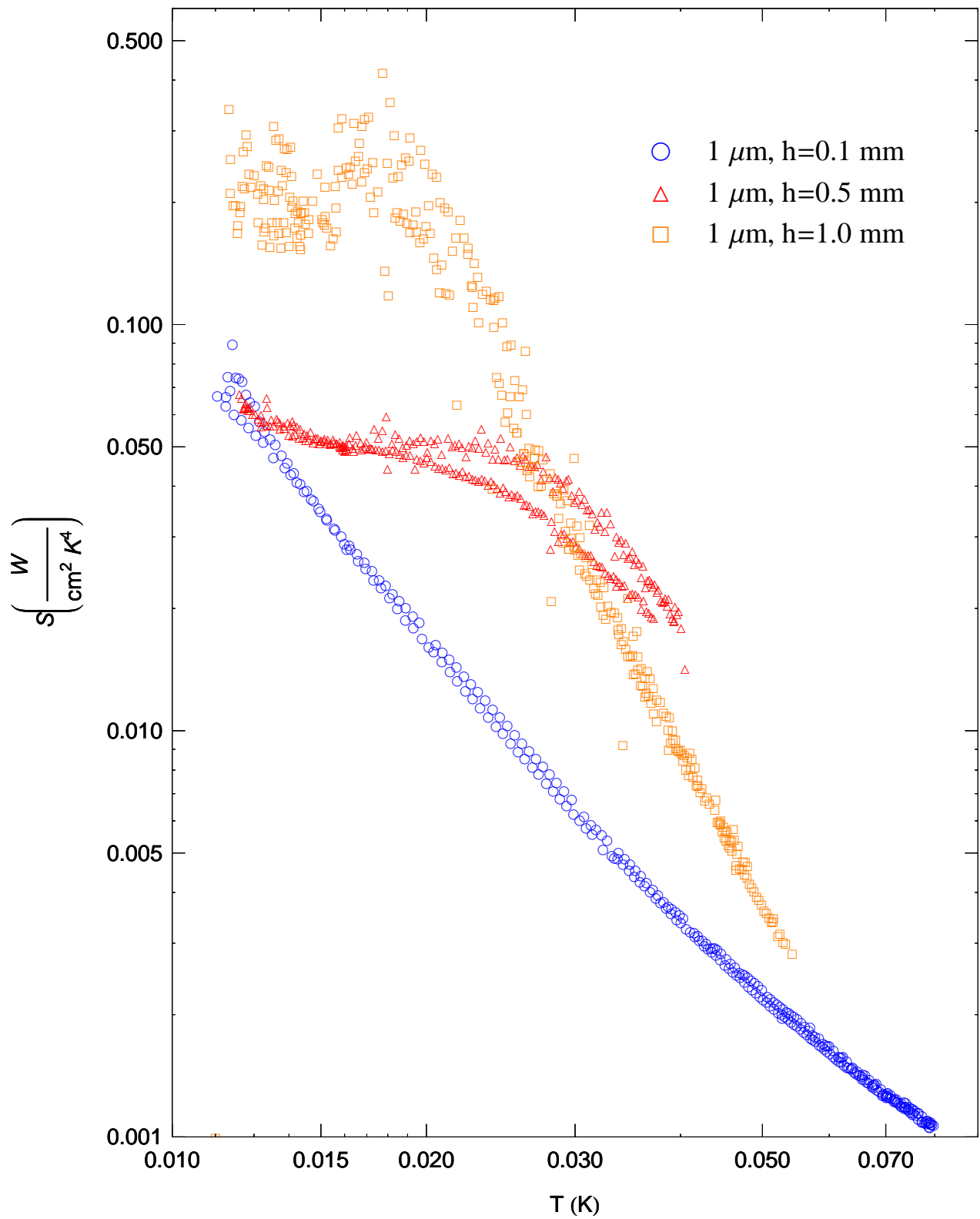


**Figure 5.14:** The measured thermal conductance  $S$  of 1  $\mu\text{m}$  powder to dilute  $^3\text{He}$  in  $^4\text{He}$ , determined by the equation (5.43) as a function of the sample temperature  $T$ .

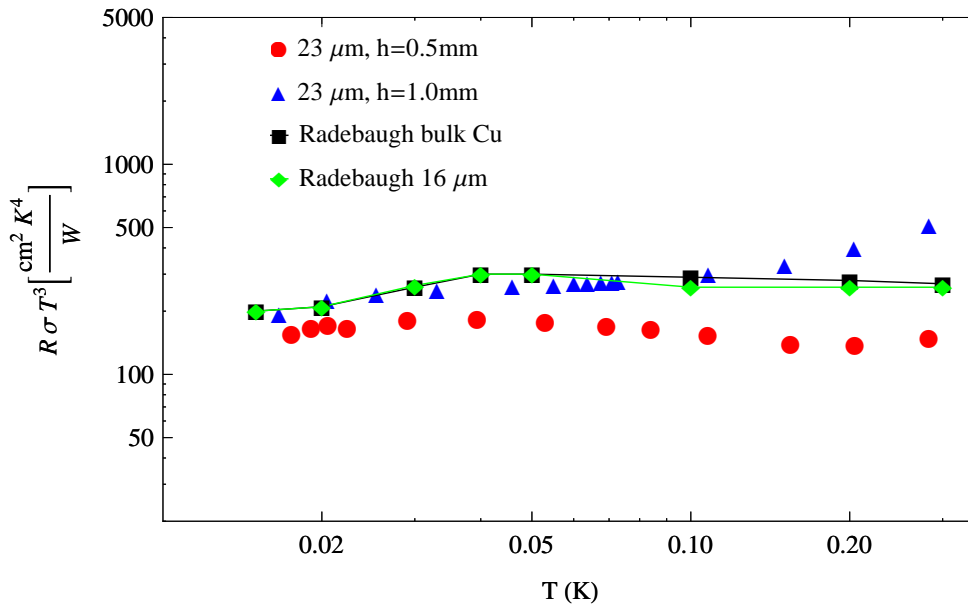


**Figure 5.15:** Experimental boundary resistivity of the ESPI copper powder, with  $d_s = 23 \mu\text{m}$ , as a function of the sample temperature  $T$ . It is compared to a  $16 \mu\text{m}$  copper powder and with an annealed bulk copper surface [122].

- sintered  $1.8 \mu\text{m}$  copper powder with thicknesses of  $0.17 \text{ mm}$  and  $0.67 \text{ mm}$ ,
- heat treated  $\text{Cu}(\text{Cr})$ , with  $0.6 \text{ wt. } \%$  chromium in OFHC copper.

The results of the original papers are depicted in the figures A.1 and A.2.

The temperature dependence of  $R_K \sigma T^3$  of the  $1.0 \text{ mm}$  and the  $0.5 \text{ mm}$  sample found in this work agrees very well with the measurements of Radebaugh on the fine copper powder.  $R_K \sigma T^3$  of both samples are decreasing with decreasing temperature until the penetration depth is reached and are constant underneath that temperature. The thinner sinters show a boundary resistance that is higher by a factor of 3 compared to the thicker samples.

The measurements in this work on the thermal conductance of the  $1 \mu\text{m}$  powder yield lower values by 2 orders of magnitude than previous measurements. A possible reason for this are impurities in the copper powder. The  $1 \mu\text{m}$  powder has a purity of  $99.19\%$  with various impurities given in Table 5.4. It is well known that the Kapitza resistance is sensitive to the surface treatment, the amount of dislocations and the impurities. The Kapitza resistance of heat treated copper alloy  $\text{Cu}(\text{Cr})$  is given in Figure 5.16. It shows a reduced  $R_K \sigma T^3$  by an order of magnitude compared to annealed OFHC copper.

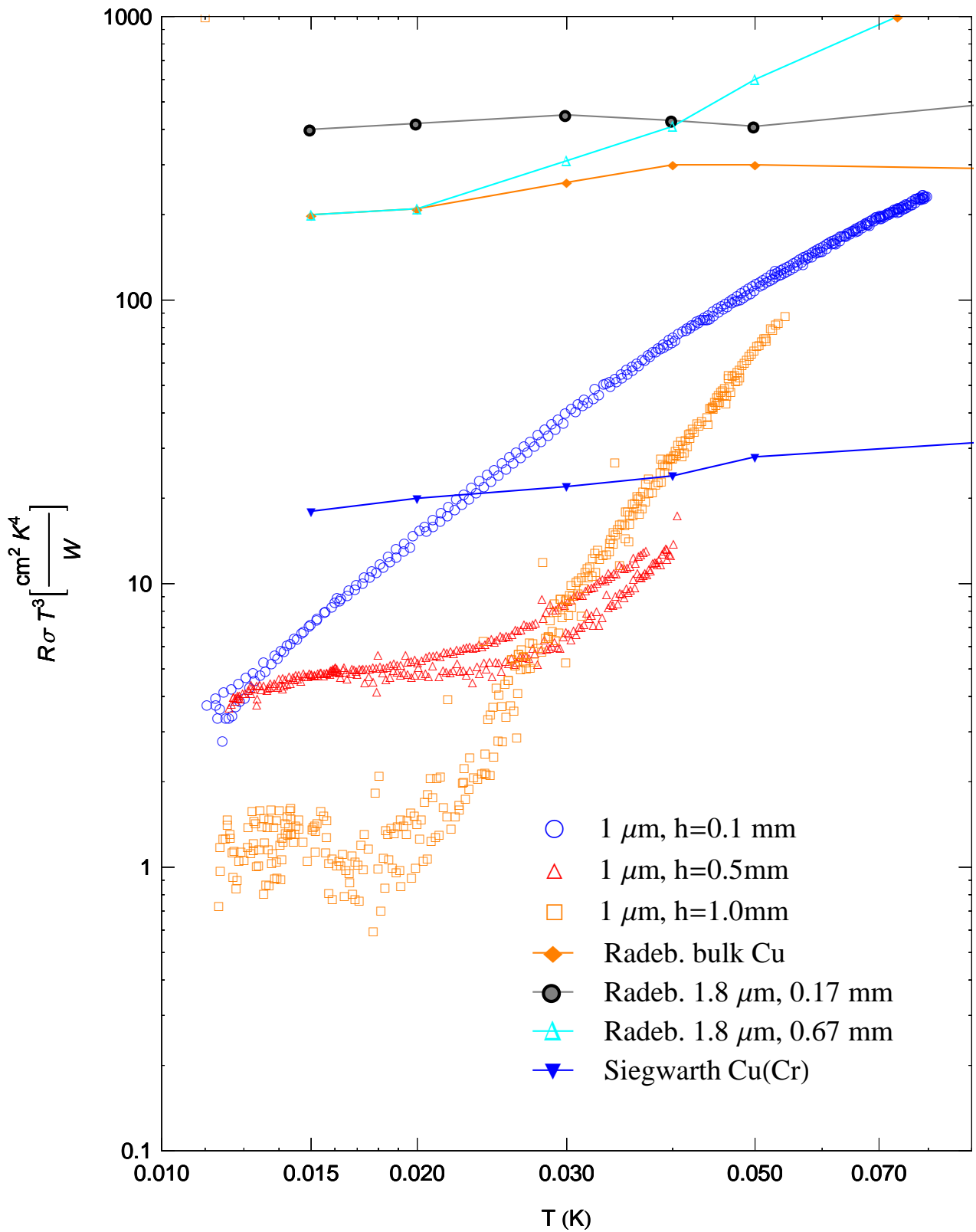


**Figure 5.16:** Experimental boundary resistivity of the 1  $\mu\text{m}$  copper powder determined by equation (5.43) as a function of the sample temperature  $T$ , compared with 1  $\mu\text{m}$  copper powders of different thicknesses and with an annealed bulk copper surface [122].

Errors of the measurement that were considered are:

- Error in the surface area measurement
- Heat leak from the sensors to the helium mixture

The surface area of the fine powder may be underestimated due to pores not penetrating the sponge which are not measured by the gas permeability method but which are efficient in the heat transfer. From the surface area determined from the measured particle size of the green powder, the error in surface area cannot exceed a factor of two. This would reduce the thermal boundary conductance by a factor of two. Heat leaks due the cabling of the sensors can be excluded, taking into account the good agreement of the measurements of the 44  $\mu\text{m}$  powder with previous measurements on similar sinters. The only difference in the sample preparation was the mounting of the sensors, which was detachable for the setup of the 1  $\mu\text{m}$  powder. The heat leak from a heater support directly to the helium bath is given in equation (5.42) and found to be very small. A badly mounted cone would result in a higher heat leak and apparently improve the heat exchanger performance. However, the mounting of the cones was investigated after the measurements and found to be still well joined. Also a different thermal contraction during cooling can be excluded because the cone and the substrate are made of identical material.

For EURECA a heat exchanger made of sintered copper powder will be used for a good thermal contact between the helium mixture at the temperature  $T_m = 7$  mK and the detector array at approximately  $T_d = 10$  mK. The necessary surface area  $\sigma$  to transfer the heat load  $\dot{Q}$  can be calculated by

$$\sigma = \frac{\dot{Q}}{S(T_d^4 - T_m^4)}. \quad (5.47)$$

The ESPI powder requires a surface area of 263  $\text{m}^2$ , with a mass of 3.4 kg and a volume of 1720  $\text{cm}^3$  to transfer the 20  $\mu\text{W}$  predicted for EURECA [142]. For the 1  $\mu\text{m}$  copper powder, using the more conservative value of  $S = 0.05 \frac{\text{W}}{\text{cm}^2 \text{K}^4}$  determined above, the surface area amounts to 5.3  $\text{m}^2$ . This corresponds to a volume of 4  $\text{cm}^3$  or a mass of 8.3 g. With a sinter thickness of 1 mm the heat exchanger covers a substrate surface of 40  $\text{cm}^2$ . This could be conveniently attached to the lid of the MC, which is in direct contact to the detector array.

The necessary surface area in the concentrated stream of the main heat exchanger for EURECA can be calculated with Niinikoski's theory [134]

$$\sigma = \frac{\dot{Q}}{12.5 S T_m^4}. \quad (5.48)$$

Using solely the ESPI powder requires a surface area of  $67 \text{ m}^2$  with a volume of  $440 \text{ cm}^3$ . For comparison, the CCDR has a heat exchanger volume in the concentrated stream of  $1.3 \text{ cm}^3$ . For a mixture of the standard ESPI and  $1 \text{ }\mu\text{m}$  copper powder,  $1 \text{ m}^2$  of the former is required for the heat exchanger above a temperature of approximately  $20 \text{ mK}$  and  $1.4 \text{ m}^2$  of the  $1 \text{ mm}$  powder below that temperature. This corresponds to a heat exchanger volume of  $6.6 \text{ cm}^3$  of the standard and  $1.1 \text{ cm}^3$  of the fine copper powder.

## 5.4 Conclusions

In this chapter the heat transfer between copper and liquid helium at very low temperatures has been reviewed. To overcome the large thermal resistance, sintered heat exchangers with a large surface to volume ratio are commonly used. Sintering theories were reviewed and found unable to reliably predict the sintering result. The sintering parameters: compact preparation, sintering atmosphere, sintering temperature and sintering duration, and their influence on the sintered structure were discussed. The necessary properties for a sintered sponge were defined and the measurement techniques described to verify those.

The sintering of a fine copper powder with an average particle size of  $1.15 \text{ }\mu\text{m}$  and a green surface to volume ratio of  $29044 \frac{\text{cm}^2}{\text{cm}^3}$  was experimentally studied. The sinter was characterised by its fractional density, its surface area and its bonding to a bulk copper substrate. The optimum sintering parameters were found to be an isothermal sintering time of  $10 \text{ min}$ , at  $750 \text{ }^\circ\text{C}$  in a hydrogen atmosphere. The sinter produced in this way, has a fractional density of  $0.524$  and a surface to volume ratio of  $13293 \frac{\text{cm}^2}{\text{cm}^3}$ , which equals an equivalent surface to volume diameter of  $1.9 \text{ }\mu\text{m}$ . Three samples of this sinter with thicknesses of  $0.1 \text{ mm}$ ,  $0.5 \text{ mm}$  and  $1.0 \text{ mm}$  were tested inside the MC of the CCDR between  $10 \text{ mK}$  and  $70 \text{ mK}$ . The samples were approximately half immersed in a saturated dilute solution of a helium mixture and half in the concentrated  $^3\text{He}$  phase. The measured thermal boundary conductivities of the samples with  $0.5 \text{ mm}$  and  $1.0 \text{ mm}$  depth amounted to  $0.05 \frac{\text{W}}{\text{cm}^2 \text{ K}^4}$  and  $0.20 \frac{\text{W}}{\text{cm}^2 \text{ K}^4}$  below  $25 \text{ mK}$  and  $20 \text{ mK}$ . These values are very high in comparison to previous measurements on copper powder. It is thus recommended to verify these results independently.

The studied  $1 \text{ }\mu\text{m}$  powder would be extremely useful EURECA. It would tremendously facilitate the heat transfer from the detector array to helium in the MC. Conventional copper powder would require a heat exchanger volume of  $1720 \text{ cm}^3$ , requiring a large volume inside MC. The  $1 \text{ }\mu\text{m}$  powder

has a volume of only  $4\text{ cm}^3$  and could be conveniently attached to the lid of the MC. For achieving the cooling power for EURECA, a mixture of the standard ESPI and the 1  $\mu\text{m}$  copper powder should be used, with a volume of  $6.6\text{ cm}^3$  and  $1.1\text{ cm}^3$ , respectively.

The spectacular improvement in the thermal boundary conductance, compared with previous results on pure sintered copper powders, can be possibly understood by the small grain size, similar to that of silver powders where spectacularly good results were obtained already much earlier. The grain size approaches the dominant wavelength of sound in helium and the mean free path of electrons in the copper grains.

Among the sources of gross experimental errors, an underestimate of the surface area is clearly excluded, while the poor attachment of the thermometers and/or heaters could lead to a substantial error in the right sense. This is, however, unlikely, because temperature dependences of the measured conductances cannot be explained by a thermal model describing such a system.

# Chapter 6

## Conclusions and Outlook

The nature and constitution of the galactic Dark Matter is one of the key problems of today in particle physics, astrophysics and cosmology. The work presented here addresses important baseline design issues of the European experiment EURECA for the future direct searches of DM particle interactions in their large detector array to be built in the new deep underground laboratory LSM in Modane.

Based on the design studies conducted in this work, the EURECA collaboration decided to adopt a fast cycling DR as Baseline solution. Simulations of background events induced by the radioactivity and cosmic muon interactions in the rock surrounding the experimental cavern, suggested that the pool design was superior to the submarine design for the ultra pure water shield. This constrained to using only highly radiopure materials in the cryogenic enclosure immediately surrounding the detector array. In this work a design was developed, which shows the feasibility of building a detector array almost exclusively of materials with ultralow activity, such as copper and PMMA.

The EMC design techniques outlined in this work also proved to be extremely successful. For the first time, temperatures below 10 mK were measured by resistance thermometry outside a shielded room. It was possible to perform precise measurements at temperatures as low as 10 mK, only limited by the cooling power and residual heat load of the DR. A minimum temperature of 3.64 mK was recorded in the single-shot operation mode. With the experience gained in this work, the author can only draw the attention to the importance of EMC techniques for EURECA. The electrical setup of EURECA will be incomparably more complicated, and therefore it will be even more essential to apply the EMC principles and techniques described in this work from the very beginning.

Studies of the residual heat load on the CCDR yielded hot molecules as the main heat source. It

was found that the heat load can be significantly reduced by a lower temperature of the innermost heat shield. Stainless steel, used for the MC, was the origin of a large time-dependent heat load with a long time constant, while cooling to the lowest temperatures. For EURECA it is thus suggested to reduce the leakage rate of hot molecules into the isolation vacuum by using metallic gaskets and by using materials with low outgassing. Also, the temperature of the innermost heat shield should be as low as possible, preferably close to 20 mK. The use of stainless steel and other materials with large time constants must be completely avoided in the detector array itself and in the nearby cryogenics of EURECA. An efficient vibration damping system should be used for EURECA, as vibrations were found to give rise to temperature instabilities.

In this work, sintered heat exchangers made of fine copper powder were studied. With the sinter parameters derived in this work, very high thermal boundary conductivities of  $0.05 \text{ W}/(\text{cm}^2 \text{ K}^4)$  and  $0.20 \text{ W}/(\text{cm}^2 \text{ K}^4)$  were found for the samples with 0.5 mm and 1.0 mm depth, below 25 mK and 20 mK, respectively. A heat exchanger made of this powder will reduce the heat exchanger volume for EURECA inside the MC by a factor of 400, compared with conventional copper powder. For the main heat exchanger of EURECA, conventional copper powder should be used at temperatures higher than 20 mK, and the finer powder below. This will reduce the heat exchanger volume by a factor of 50, compared with a main heat exchanger made solely of conventional copper powder.

The extremely good results on the thermal boundary conductivity of the  $1 \mu\text{m}$  powder should be confirmed independently. It is proposed to utilize the powder for additional modules in the main heat exchanger of the CCDR. This should increase the cooling power significantly and quantifiably as predicted by inserting our measured surface area and thermal boundary resistivity of the sintered fine powder in equation(4.1).

# Appendix A

## Measurements of the Thermal Boundary Resistance

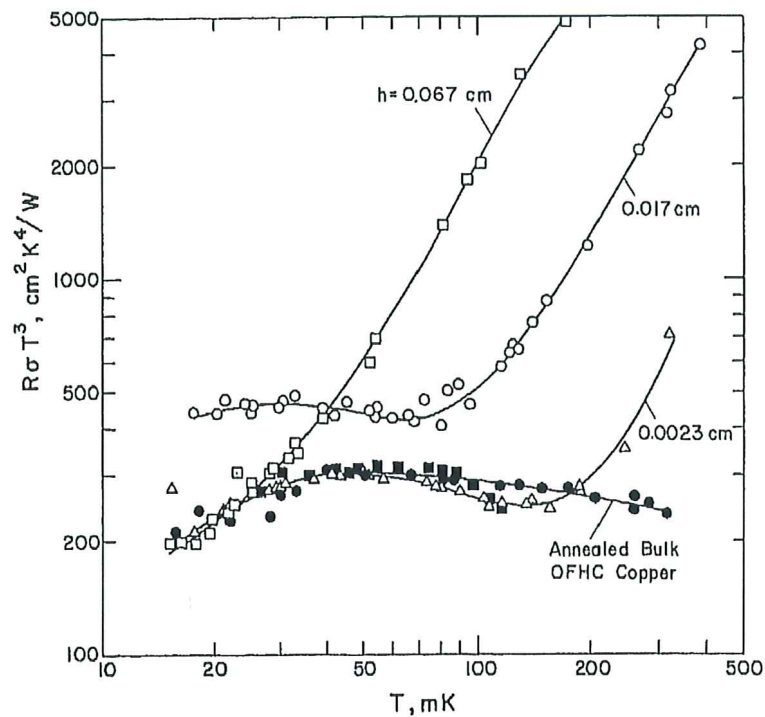


**Figure A.1:** The measured thermal boundary resistance to dilute  $^3\text{He}$  in  $^4\text{He}$  of bulk copper (solid circles) and several copper powder samples. The solid squares are for 16  $\mu\text{m}$  diameter powder and the rest of the data are for 1.8  $\mu\text{m}$  powder of different depths [122].

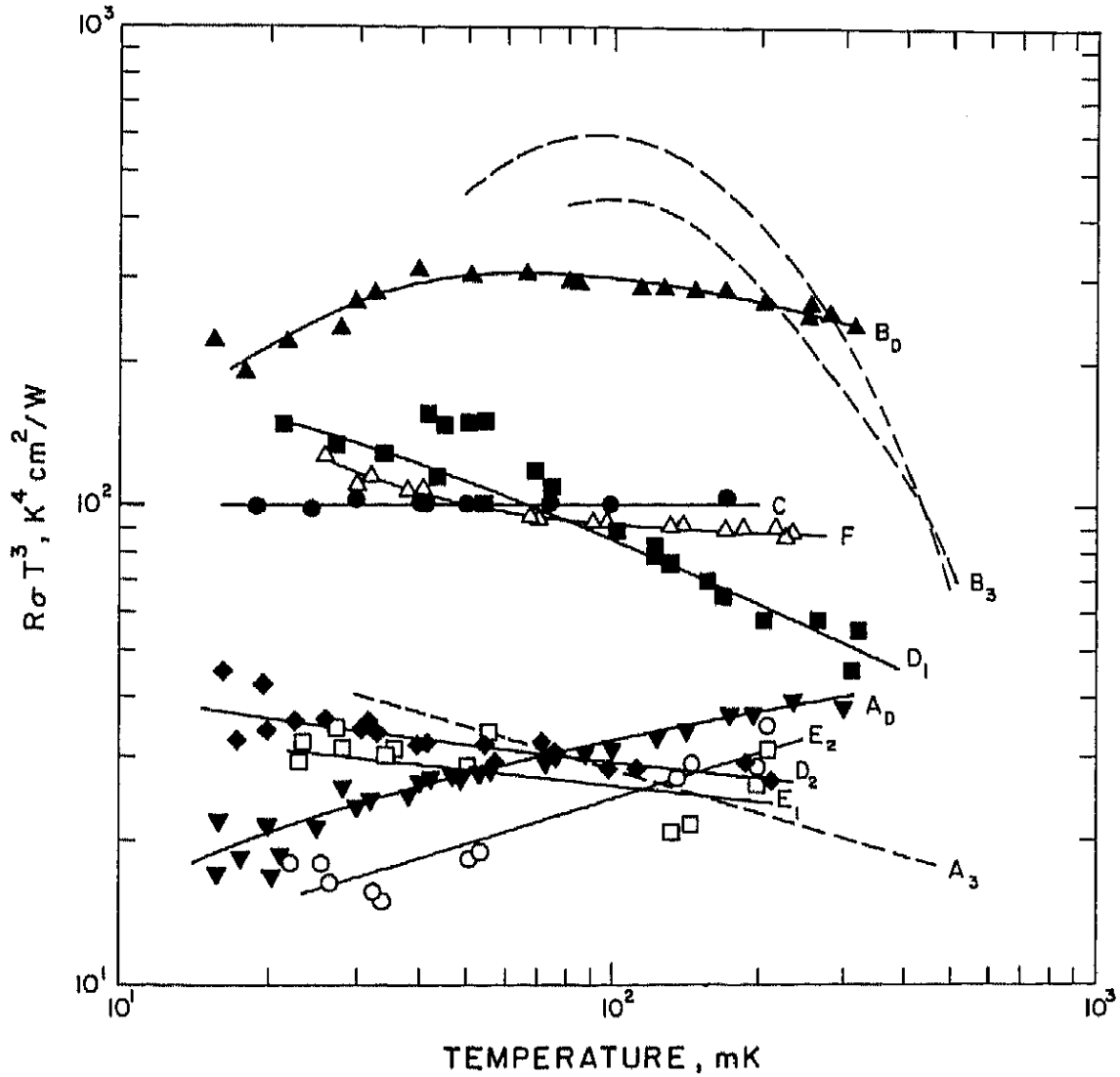


**Figure A.2:** Kapitza resistance of copper and copper alloy cells to the dilute  $^3\text{He}$  stream in a dilution refrigerator. Curves  $A_3$  and  $B_3$  are the Kapitza resistance between work-hardened and annealed copper and pure  $^3\text{He}$  liquid [127]. Curve  $B_D$  shows the measured Kapitza resistance between annealed OFHC copper and dilute  $^3\text{He}$ . The curves  $A_D$ ,  $D_1$ ,  $D_2$ ,  $E_1$  and  $E_2$  are the Kapitza resistance between dilute  $^3\text{He}$  and Cu(Cr) processed with different heat treatments in a hydrogen or an oxygen atmosphere. The curves  $C$  and  $F$  are the Kapitza resistance between dilute solution and Cu-30% Ni and Cu(Zr).

# Bibliography

- [1] W. R. Abel, A. C. Anderson, W. C. Black, and J. C. Wheatley. Low-temperature heat capacity of liquid  $^3\text{He}$ . *Phys. Rev.*, 147(1):111–119, Jul 1966.
- [2] W. R. Abel, R. T. Johnson, J. C. Wheatley, and W. Zimmermann. Thermal conductivity of pure  $^3\text{He}$  and of dilute solutions of  $^3\text{He}$  in  $^4\text{He}$  at low temperatures. *Phys. Rev. Lett.*, 18(18):737–740, May 1967.
- [3] M. Aivazov and I. Domashnev. Influence of porosity on the conductivity of hot-pressed titanium-nitride specimens. *Poroshkovaya Metallurgiya*, 8(9):51–54, 1968.
- [4] U. ALDEMIR and M. BAKIOGLU. Active structural control based on the prediction and degree of stability. *Journal of Sound and Vibration*, 247(4):561 – 576, 2001.
- [5] S. Ali, D. Weile, and T. Clupper. Effect of near field radiators on the radiation leakage through perforated shields. *Electromagnetic Compatibility, IEEE Transactions on*, 47(2):367–373, May 2005.
- [6] S. W. Allen, R. W. Schmidt, and A. C. Fabian. Cosmological constraints from the x-ray gas mass fraction in relaxed lensing clusters observed with chandra. *Astrophysics and Space Science*, 334:L11, 2002.
- [7] A. C. Anderson and et al. Thermal and magnetic properties of dilute solutions of  $^3\text{He}$  in  $^4\text{He}$  at low temperatures. *Phys. Rev. Lett.*, 17(7):367–372, Aug 1966.
- [8] A. C. Anderson and R. E. Peterson. The thermal resistance between electrons and phonons in copper. *Physics Letters A*, 38(7):519 – 520, 1972.
- [9] R. Andrievski. Compaction and sintering of ultrafine powders. *International journal of powder metallurgy*, 30(1):59–66, 1994.
- [10] G. Angloher and et al. Limits on wimp dark matter using scintillating  $\text{CaWO}_4$  cryogenic detectors with active background suppression. *Astroparticle Physics*, 23(3):325 – 339, 2005.
- [11] G. Angloher and et al. Commissioning run of the CRESST-ii dark matter search. *Astroparticle Physics*, 31(4):270 – 276, 2009.
- [12] K. Armstrong. Design techniques for EMC. *The Institution of Electrical Engineers (IEE)*, 63, march 2006.

- [13] J.-P. Bacher and et al. Thermal desorption study of selected austenitic stainless steels. *Journal of Vacuum Science & Technology A: Vacuum, Surfaces, and Films*, 21(1):167–174, 2003.
- [14] H. Baer and et al. Indirect, direct and collider detection of neutralino dark matter in the minimal supergravity model. *Journal of Cosmology and Astroparticle Physics*, 2004(08):005, 2004.
- [15] H. Barthels. Druckverlust in Kugelschüttungen. *Brennst.-Wärme-Kraft*, 24(6):233–236, 1972.
- [16] I. Bat'ko and et al. Design of RuO<sub>2</sub>-based thermometers for the millikelvin temperature range. *Cryogenics*, 35(2):105 – 108, 1995.
- [17] L. Baudis. New opportunities at cern. Talk, May 2009.
- [18] M. Bauer. EURECA and the muons. Talk at the EURECA meeting in Oxford, September 2008. Considerations to be made when building a new experiment.
- [19] M. Bauer. Muons love steel tanks (and that's why we probably should avoid them). Talk at the EURECA meeting in Oxford, September 2008. Monte Carlo studies of muon-induced background for different possible EURECA hall designs.
- [20] G. Baym and C. Ebner. Phonon-quasiparticle interactions in dilute solutions of <sup>3</sup>He in superfluid <sup>4</sup>He: I. phonon thermal conductivity and ultrasonic attenuation. *Phys. Rev.*, 164(1):235–244, Dec 1967.
- [21] P. Bedregal and et al. Robustness in naa evaluated by the youden and steiner test. *Journal of Radioanalytical and Nuclear Chemistry*, 278(3):801–806, 2008.
- [22] K. G. Begeman, A. H. Broeils, and R. H. Sanders. Extended rotation curves of spiral galaxies - Dark haloes and modified dynamics. *mnras*, 249:523–537, Apr. 1991.
- [23] J. D. Bekenstein. Relativistic gravitation theory for the modified newtonian dynamics paradigm. *Phys. Rev. D*, 70(8):083509, Oct 2004.
- [24] L. Bergstrom. Non-baryonic dark matter - observational evidence and detection methods. *REPT.PROG.PHYS.*, 63:793, 2000.
- [25] M. Bertinat, D. Brewer, and G. Butterworth. Observations on the use of sintered copper heat exchangers in experiments with superfluid helium. *Cryogenics*, 13(1):48–49, January 1973.
- [26] K. Blattenberger. Skin depth formula and material properties. WEB.
- [27] G. Bockstiegel. On the rate of sintering. *Trans. TMS-AIME*, 206:580–585, 1956.
- [28] V. Brakel, J. Modry, and M. Svata. Mercury porosimetry:state of the art. *Powder Technology*, 29:1 – 12, 1981.
- [29] J. Brett and L. Seigle. Shrinkage of voids in copper. *Acta Met.*, 11:467 – 474, 1963.
- [30] J. R. Brownstein and J. W. Moffat. Galaxy rotation curves without non-baryonic dark matter, 2006.

- [31] D. Clowe and et al. A direct empirical proof of the existence of dark matter, 2006.
- [32] R. Coble. Initial sintering of alumina and hematite. *Journal of the American Ceramic Society*, 41(2):55–62, February 1958.
- [33] R. Coble and T. Gupta. Intermediate stage sintering. In *Sintering and related phenomena*, ed. G. C. Kuczinski, pages 423–441, New York, 1967.
- [34] R. Corruccini. Gaseous heat conduction at low pressures and temperatures. *Vacuum*, 7-8:19 – 29, 1959.
- [35] S. Cryogenics. [www.statebourne.com](http://www.statebourne.com). WEB.
- [36] F. A. Danevich and et al. Scintillation properties of pure and Ca-doped ZnWo crystals. *physica status solidi (a)*, 205(2):335–339, 2008.
- [37] M. D. Daybell, W. P. Pratt, and W. A. Steyert. Specific heat of dilute Cu(Fe) alloys far below the kondo temperature. *Phys. Rev. Lett.*, 21(6):353–356, Aug 1968.
- [38] A. de Waard, L. Gottardi, and G. Frossati. Minigrail progress report 2001: the first cooldown. *Classical and Quantum Gravity*, 19(7):1935–1941, 2002.
- [39] R. DeHoff and et al. The role of interparticle contacts in sintering. *Powder Metallurgy*, W. Leszynski (ed.), Interscience, New York, pages 31–50, 1961.
- [40] W. Diehl. Accessories for high temperature sintering. *Metal Powder Rep.*, 48(6):54–57, 1993.
- [41] J. Ellis and et al. Update on the direct detection of supersymmetric dark matter. *Phys. Rev. D*, 71(9):095007, May 2005.
- [42] J. Ellis, K. A. Olive, and P. Sandick. Update on the direct detection of dark matter in mssm models with non-universal higgs masses. *New Journal of Physics*, 11(10):105015 (31pp), 2009.
- [43] Eureka Collaboration. Endorsement of recommendations from december technical board meeting. Minutes of the technical board meeting 10.October.2008, October 2008.
- [44] L. Evans. The large hadron collider. *New Journal of Physics*, 9(9):335, 2007.
- [45] A. Evenson, D. F. Brewer, and A. L. Thomson. *Proceedings of the Eleventh International Conference on Low Temperature Physics*, 1:125, 1968.
- [46] H. Exner. Principles of single phase sintering. *Rev. on Powder Metallurgy and Physical Ceramics*, 1(1-4):7–251, 1979.
- [47] H. Fischmeister, E. Artz, and L. Olsson. Particle deformation and sliding during compaction of spherical powders: a study by quantitative metallography. *Powder Metallurgy*, 21(4):179–187, 1978.
- [48] G. Frossati. Grail: A 10 mK, 100 ton spherical gravitational wave antenna. *Journal of Low Temperature Physics*, 101(1-2):81–94, October 1995.

- [49] Y. Fukuda and et al. Measurement of the flux and zenith-angle distribution of upward through-going muons by super-kamiokande. *Phys. Rev. Lett.*, 82(13):2644–2648, Mar 1999.
- [50] S. R. Furtado and O. D. Aguiar. Fast cooling techniques for gravitational wave antennas. *Classical and Quantum Gravity*, 19(7):1973–1978, 2002.
- [51] GEL/210/12. Bs iec 61000-5-2:1997; electromagnetic compati-bility (emc) - part 5: Installation and mitigation guidelines - section 2: Earthing and cabling. Technical report, IEC-International Electrotechnical Commission, 1998.
- [52] G. Gerbier. EURECA: towards  $10^{-10}$  pb. Talk at the EURECA open meeting - September 22nd IAP 2006, September 2006. CEA Saclay, DAPNIA, France.
- [53] G. Gerbier. The proposal of ulisse cavity at LSM, why this proposal, does it fit EURECA needs? Talk at the EURECA Coll. meeting, Garching, October 2007. Gilles Gerbier CEA DAPNIA.
- [54] G. Gerbier and E. Yakushev. Monitoring of neutron flux at EDELWEISS environment. Talk at the EURECA Coll. meeting, Garching, October 2007.
- [55] R. German. *Liquid Phase Sintering*. New York, NY : Plenum, 1985.
- [56] R. German. Sintering densification for powder mixtures of varying distribution widths. *Acta Metallurgica et Materialia*, 40(9):2085 – 2089, 1992.
- [57] R. German. *Sintering Theory and Practice*. Wiley, John & Sons, Inc., 1996.
- [58] R. German. *Particle Packing Characteristics*. Metall Powder Industries Ferderation, Princeton, N.J. (1989).
- [59] R. German and Z. Munir. Surface area reduction during isothermal sintering. *Journal of the American Ceramic Society*, 59(9-10):379–383, 1976.
- [60] P. Gondolo and G. Gelmini. Cosmic abundances of stable particles: Improved analysis. *Nuclear Physics B*, 360(1):145 – 179, 1991.
- [61] M. Goodman and T. Lasserre. Double chooz, a search for the neutrino mixing angle theta-13, 2006.
- [62] A. Green. Dark matter detection. Talk - Cosmology on the Beach, Los Cabos, Mexico, January 2009.
- [63] D. S. Greywall.  $^3\text{He}$  specific heat and thermometry at millikelvin temperatures. *Phys. Rev. B*, 33(11):7520–7538, Jun 1986.
- [64] J. Haasbroek. *Thermal conductivity at very low temperatures*. PhD thesis, Rijksuniversiteit te Leiden, The Netherlands, 1971.
- [65] C. Hagmann and P. L. Richards. Specific heat of stainless steel below  $T = 1$  K. *Cryogenics*, 35(5):345 – 345, 1995.

- [66] H. E. e. b. C. G. K. Hall, S. G. Lipson, and M. R. N. Y. Wiley). *The Physics of Liquid and Solid Helium*, page 375, 1974.
- [67] J. Harrison. Review paper: Heat transfer between liquid helium and solids below 100 mK. *Journal of Low Temperature Physics*, 37(5-6):467–565, December 1979.
- [68] F. Haug. Refrigeration infrastructure for EURECA. Talk at the EURECA meeting in Oxford, September 2008.
- [69] R. Haynes. The mechanical behavior of sintered metals. *Rev. Deform. Behav. Mater.*, 3:1–101, 1981.
- [70] C. Herring. Effect of change of scale on sintering phenomena. *J. Appl. Phys.*, 21:301–303, 1950.
- [71] P. Higgins and Z. Munir. Application of the surface oxide model the sintering of matallic particles. *Powder Metallurgy International*, 14(1):26–29, 1982.
- [72] J. C. Ho, H. R. O’Neal, and N. E. Phillips. Low temperature heat capacities of constantan and manganin. *Review of Scientific Instruments*, 34(7):782–783, 1963.
- [73] R. Hoff and J. P. Gillard. Relationship between microstructure and mechanical properties in sintered coppers. *Modern Developments in Powder Metallurgy*, 4:281–290, 1971.
- [74] M. Horn. *Simulations of the muon-induced neutron background of the EDELWEISS-II experiment for Dark Matter search*. PhD thesis, University Karlsruhe, December 2007.
- [75] J. Jacks. *Canadian Lounal Chem. Engeneering*, 49:699–701, 1971.
- [76] R. Jeschar. *Arch. Eisenhuettenwes.*, 35:91–108, 1964.
- [77] A. Jillavenkatesa, S. Dapkunas, and L. Lum. Particle size characterisation: Practice guide. *National Institute of Standards and Technology*, Special Publication 960-1, Washington DC, 2001.
- [78] J. Jochum. CRESST direct dark matter search with cryogenic detectors. *Progress in Particle and Nuclear Physics*, 57(1):357 – 365, 2006. International Workshop of Nuclear Physics 27th course - Neutrinos in Cosmology, in Astro, Particle and Nuclear Physics.
- [79] G. Jungman, M. Kamionkowski, and K. Griest. Supersymmetric dark matter. *Physics Reports*, 267:195, 1996.
- [80] P. L. Kapitza. Heat transfer and superfluidity of helium II. *Phys. Rev.*, 60(4):354–355, Aug 1941.
- [81] E. H. Kennard. *Kinetic Theory of Gases, With an Introduction to Statistical Mechanics*. New York: McGraw-Hill Book Co, 1938.
- [82] W. Kingery and M. Berg. Study of the initial stages of sintering solids by viscous flow, evaporation-condensation, and self-diffusion. *Journal of Applied Physics*, 26(10):1205–1212, 1955.

- [83] C. S. Kochanek and et al. Clusters of galaxies in the local universe. *The Astrophysical Journal*, 585(1):161–181, 2003.
- [84] J. Koh and G. Fortini. Prediction of thermal conductivity and electrical resistivity of porous metallic materials. *Int. J. Heat Mass Transfer*, 16:2013–2021, 1973.
- [85] D. Kolar, G. Kuczynski, and S. Chiang. On the mechanism of pore coarsening. *Sintering and Heterogeneous Catalysis*, pages 81–88, 1984.
- [86] H. Kraus and et al. EURECA – the european future of cryogenic dark matter searches. *Journal of Physics: Conference Series*, 39:139–141, 2006.
- [87] H. Kraus and et al. EURECA – the european future of dark matter searches with cryogenic detectors. *Nuclear Physics B - Proceedings Supplements*, 173:168 – 171, 2007. Proceedings of the 7th UCLA Symposium on Sources and Detection of Dark Matter and Dark Energy in the Universe, Proceedings of the 7th UCLA Symposium on Sources and Detection of Dark Matter and Dark Energy in the Universe.
- [88] O. Krischer. Vorgänge der Stoffbewegung durch Haufwerke und porige Güter bei Diffusion, Molekularbewegung sowie laminarer und turbulenzartiger Strömung. *Chemie Ingenieur Technik - CIT*, 34(3):154–162, 1962.
- [89] M. Krusius, D. Paulson, and J. Wheatley. Properties of sintered copper powders and their application in a nuclear refrigerator with precise temperature control. *Cryogenics*, 18(12):649 – 655, 1978.
- [90] G. Kuczynski and M. AIME. Self-diffusion in sintering of metallic particles - discussion. *Metals Trans.*, 185:169–178, 1949.
- [91] V. Kudryavtsev. EURECA related work in sheffield. Talk at the EURECA Coll. meeting, Garching, October 2007.
- [92] V. Kudryavtsev. Background studies for EURECA. Talk at the EURECA meeting in Oxford, September 2008. simulations by Vitaly A. Kudryavtsev<sup>1</sup>, Vito Tomasello<sup>1,2</sup>, Matt Robinson<sup>1</sup>, Pia Loaiza<sup>3</sup>, Michael Bauer<sup>2</sup>, 1: University of Sheffield, 2: University of Tuebingen, 3: Laboratoire Souterrain de Modane.
- [93] V. Kudryavtsev. Low radioactivity materials for EURECA. Talk, EURECA annual meeting, Oxford, September 2008.
- [94] V. Kudryavtsev. Simulation of background for EURECA and ULISSE. Talk at the EURECA meeting in Oxford, September 2008. simulations by Vitaly A. Kudryavtsev<sup>1</sup>, Vito Tomasello<sup>1,2</sup>, Matt Robinson<sup>1</sup>.
- [95] F. W. L. and et al. Final Results from the Hubble Space Telescope Key Project to Measure the Hubble Constant. *THE ASTROPHYSICAL JOURNAL*, 553:47–72, May 2001.
- [96] Z. E. L. D. Landau. *Soviet Phys.-JETP* 5, page 101, 1957.
- [97] F. Lenel, G. Ansell, and R. Morris. Sintering of loose spherical copper powder aggregates using silica as marker. *Met Trans.*, 1:2351, 1970.

- [98] Q. Li and et al. Thick film chip resistors for use as low temperature thermometers. *Cryogenics*, 26(8):467 – 470, 1986.
- [99] M. A. Lim and et al. The second measurement of anisotropy in the cosmic microwave background radiation at  $10^5$  scales near the star mu pegasi, 1996.
- [100] W. Little. The transport of heat between dissimilar solids at low temperatures. *Canadian Journal of Physics*, 37(3):–349, 1959.
- [101] O. V. Lounsamaa. *Experimental Principles & Methods below 1 K*. Academic Press, 1974.
- [102] K. I. M. *An Introduction to the Theory of Superfluidity*, volume Chapter 23. Benjamin, New York, 1965.
- [103] C. Martin, D. Bouvard, and S. Shima. Study of particle rearrangement during powder compaction by the discrete element method. *Journal of the Mechanics and Physics of Solids*, 51(4):667 – 693, 2003.
- [104] V. Mikhailik and et al. Temperature dependence of  $\text{CaMoO}_4$  scintillation properties. *Nuclear Instruments and Methods in Physics Research Section A: Accelerators, Spectrometers, Detectors and Associated Equipment*, 583(2-3):350 – 355, 2007.
- [105] V. B. Mikhailik and H. Kraus. Cryogenic scintillators in searches for extremely rare events. *Journal of Physics D: Applied Physics*, 39(6):1181–1191, 2006.
- [106] M. Milgrom. A modification of the newtonian dynamics as a possible alternative to the hidden mass hypothesis. *apj*, 270:365–370, july 1983.
- [107] O. Molerus. *hem.-Ing.-Techn.*, 49:516–577, 1977.
- [108] J. Monroe and P. Fisher. Neutrino backgrounds to dark matter searches. *Physical Review D*, 76:033007, 2007.
- [109] C. Morgan. Material transport by dislocation motion in sintering. *Phys. Sinter.*, 5:31–40, 1973.
- [110] B. Neppert and P. Esquinazi. Temperature and magnetic field dependence of thick-film resistor thermometers (dale type rc550). *Cryogenics*, 36(4):231 – 234, 1996.
- [111] T. Niinikoski. Construction of sintered copper heat exchangers. *Cryogenics*, 11(3):232 – 233, 1971.
- [112] Y. Oda, G. Fujii, and H. Nagano. Thermal resistance in speer carbon resistors below 1 K. *Cryogenics*, 14(2):84 – 87, 1974.
- [113] K. A. Olive. TASI lectures on Dark Matter, 2003.
- [114] B. Patterson and L. Benson. The effect of powder size distribution on sintering. *Prog. Powder Met.*, 39:215–230, 1983.
- [115] F. Pobell. *Matter and Methods at Low Temperatures*. Springer Verlag, 1995.

- [116] M. L. Pool. Radioactivity in silver induced by fast neutrons. *Phys. Rev.*, 53(2):116–123, Jan 1938.
- [117] F. Porcheron, P. Monson, and M. Thommes. Molecular modeling of mercury porosimetry. *Journal Adsorption*, 11(1):325–329, July, 2005.
- [118] S. Prochazka and R. Coble. *Physics of Sintering*, 1:1, 1970.
- [119] S. Prochazka and R. Coble. Surface diffusion in the initial sintering of alumina, part 1. model considerations. *Physics of Sintering*, 2:1–18, 1970.
- [120] R. Radebaugh. *Thermodynamic properties of  $^3\text{He}$ - $^4\text{He}$  solutions with applications to the  $^3\text{He}$ - $^4\text{He}$  dilution refrigerator*. NBS Technical Note. US. Dept. Commerce, Washington, DC, 1967.
- [121] R. Radebaugh and J. Siegwarth. Anomalous thermal resistance between sintered copper powder and dilute  $^3\text{He}$ - $^4\text{He}$  solutions. *Phys. Rev. Lett.*, 27(12):796–799, Sep 1971.
- [122] R. Radebaugh and J. Siegwarth. Heat transfer between fine copper powders and dilute  $^3\text{He}$  in superfluid  $^4\text{He}$ . *Low Temperature Physics—LT 13: Proceedings*, LT 13(Unknown):401 – 405, 1974.
- [123] L. Roszkowski. Simple way of calculating the cosmological relic density. *Phys. Rev. D*, 50(8):4842–4845, Oct 1994.
- [124] H. Rumpf. *Chem.-Ing. Techn.*, 43:367–375, 1971.
- [125] V. Sanglard. EDELWEISS-II: Status and future. *Nuclear Physics B - Proceedings Supplements*, 173:99 – 103, 2007. Proceedings of the 7th UCLA Symposium on Sources and Detection of Dark Matter and Dark Energy in the Universe, Proceedings of the 7th UCLA Symposium on Sources and Detection of Dark Matter and Dark Energy in the Universe.
- [126] V. Sanglard and et al. Final results of the EDELWEISS-I dark matter search with cryogenic heat-and-ionization Ge detectors. *Phys. Rev. D*, 71(12):122002, Jun 2005.
- [127] J. Siegwarth and R. ARadebaugh. The kapitza resistance between cu(cr) and  $^4\text{He}$ ( $^3\text{He}$ ) solutions and applications to heat exchangers. *Conference: 13. international conference on low temperature physics, Boulder, Colorado, USA; Low temperature physics: LT 13.*, 13(1):398–400, Aug 1972.
- [128] D. N. Spergel and et al. First-year Wilkinson Microwave Anisotropy Probe (WMAP) observations: Determination of cosmological parameters. *The Astrophysical Journal Supplement Series*, 148(1):175–194, 2003.
- [129] M. Suomi, A. Anderson, and B. Holmström. Heat transfer below 0.2 K. *Physica*, 38(1):67 – 80, 1968.
- [130] F. Swinkels and M. Ashby. Role of surface redistribution in sintering by grain boundary transport. *Powder Met.*, 23:1–7, 1980.
- [131] M. D. Symans and M. C. Constantinou. Semi-active control systems for seismic protection of structures: a state-of-the-art review. *Engineering Structures*, 21(6):469 – 487, 1999.

- [132] M. Takahashi and et al. Active response control of buildings for large earthquakes - seismic response control system with variable structural characteristics. *Smart Materials and Structures*, 7(4):522–529, 1998.
- [133] J.-M. Ting and R. Lin. Effect of particle-size distribution on sintering. *Journal of Materials Science*, 29(7):1867–1872, January, 1994.
- [134] N. T.O. Dilution refrigeration: new concepts. *Proc. 6th Int. Cryogenic Engineering Con., Grenoble (Guildford: IPC Science and Technology)*, 4:102–111, 1976.
- [135] A. Tortento. EMI control. to be published, 2009.
- [136] VDI-Waermeatlas. *5.Auflage*. VDI-Verlag, Düsseldorf, 1988.
- [137] G. Vermeulen and G. Frossati. Powerful dilution refrigerator for use in the study of polarized liquid  $^3\text{He}$  and nuclear cooling. *Cryogenics*, 27(3):139 – 147, 1987.
- [138] D. Vortmeyer. *Strahlung technischer Oberflaechen*. In *VDI Waermeatlas, 5th edition*. VDI-Verlag, Duesseldorf, 1988.
- [139] M. Watanabe, M. Morishita, and Y. Ootuka. Magnetoresistance of  $\text{RuO}_2$ -based resistance thermometers below 0.3 K. *Cryogenics*, 41(3):143 – 148, 2001.
- [140] J. Wheatley. Liquid  $^3\text{He}$ , liquid mixtures of and  $^3\text{He}$ , and dilution refrigeration. *Journal de Physique Colloques*, 31(C3):C3–109–C3–118, 1970.
- [141] J. C. Wheatley, O. E. Vilches, and W. R. Abel. *Physics*, 4(1), 1968.
- [142] P. Wikus and T. Niinikoski. *Dilution Refrigeration of Multi-Ton Cold Masses*. PhD thesis, Wien TU, Vienna, 2007. Presented on 13 Jun 2007.
- [143] R. Willekers and et al. Thick film thermometers with predictable R-T characteristics and very low magnetoresistance below 1 K. *Cryogenics*, 30(4):351 – 355, 1990.
- [144] J. Zheng and P. Johnson. Evolution of topology during simulated sintering of powder compacts. *Journal of the American Ceramic Society*, 76(11):2760–2768, 1993.



# List of Figures

1.1	The rotation curve of the spiral galaxy DGC 6503 . . . . .	3
1.2	Interaction of galaxy clusters . . . . .	4
1.3	The differential rate for various target materials . . . . .	8
1.4	Exclusion plot showing the targeted sensitivity of EURECA. . . . .	10
1.5	The experimental data of a CRESST prototype detector . . . . .	12
1.6	Direct detection of Wimps . . . . .	13
1.7	Layout of the CDDR system. . . . .	15
2.1	Comparison of detector arrangements. . . . .	25
2.2	7 independent dilution refrigerators . . . . .	26
2.3	Implementation of the cryogenics in the “Submarine” design of EURECA. . . . .	32
2.4	Implementation of the cryogenics in the “Pool” design of EURECA. . . . .	34
2.5	Design load lock . . . . .	38
2.6	Exchanging procedure of a part of the detector material . . . . .	39
2.7	Unloading mechanism . . . . .	40
2.8	Baseline Design of the EURECA cooling and cryogenic system . . . . .	44
2.9	The EURECA cryostat layout. . . . .	45
2.10	Dilution refrigerator unit . . . . .	46
2.11	The vacuum vessel inside the “Pool” . . . . .	47
2.12	The Mixing chamber . . . . .	48
2.13	Access cryoline. . . . .	51
2.14	Layout of the proximity cryogenics . . . . .	53
3.1	The electronic racks . . . . .	59
3.2	Metallic box for connecting the cable shield . . . . .	68
3.3	Segregation and grounding of power and signal cables . . . . .	70
3.4	The patch panel of the not shielded electronic rack. . . . .	71
3.5	Details of the calibration of the temperature sensors inside the MC . . . . .	76
3.6	Analog control circuit for the automatic helium transfer. . . . .	78

3.7	Motor He-transfer. . . . .	79
3.8	Design of the 1 K pot control hardware . . . . .	80
3.9	Two-point control strategy of the 1 K pot pressure . . . . .	81
3.10	Experimental data from the 1 K pot pressure control . . . . .	82
4.1	Comparison of the time constants . . . . .	88
4.2	Fitting of the cooling power measurements . . . . .	91
4.3	Cooling power curves . . . . .	93
4.4	Optimum flow points . . . . .	94
4.5	Time development of the residual heat load . . . . .	95
4.6	Thermal conductivity of stainless steel . . . . .	101
4.7	Vibrations of the top-flange of the CCDR . . . . .	102
4.8	Influence of vibrations on the temperature of the CCDR . . . . .	103
4.9	Measurement hot molecules . . . . .	107
5.1	The neck size ratio. . . . .	118
5.2	Sintering due to surface diffusion and volume mass transport . . . . .	120
5.3	A mould for sintering cylinders and a support . . . . .	126
5.4	SEM image of the green FERRO copper powder . . . . .	133
5.5	Fractional density of the 1 $\mu\text{m}$ copper powder . . . . .	136
5.6	Electroscopical image of the sintered Cu-powder . . . . .	138
5.7	Samples of the fine powder . . . . .	139
5.8	The sintered samples of the ESPI copper powder. . . . .	140
5.9	Mounting of the sensors. . . . .	141
5.10	Samples of the FERRO copper powder. . . . .	142
5.11	The copper support of the 1 $\mu\text{m}$ powder . . . . .	142
5.12	Three samples with the FERRO powder, mounted in the mixing chamber . . . . .	143
5.13	The measured thermal conductance $S$ of 44 $\mu\text{m}$ powder to dilute $^3\text{He}$ in $^4\text{He}$ . . . . .	145
5.14	The measured thermal conductance $S$ of 1 $\mu\text{m}$ powder to dilute $^3\text{He}$ in $^4\text{He}$ . . . . .	147
5.15	Experimental boundary resistivity of the 23 $\mu\text{m}$ copper powder . . . . .	148
5.16	Experimental boundary resistivity of the 1 $\mu\text{m}$ copper powder . . . . .	149
A.1	Thermal boundary resistance to dilute $^3\text{He}$ in $^4\text{He}$ of bulk copper and copper powder . . . . .	155
A.2	Kapitza resistance of copper and copper alloy cells to the dilute $^3\text{He}$ stream . . . . .	156

# List of Tables

1.1	Improvement in sensitivity of a factor of 100 for EURECA. . . . .	11
1.2	Typical examples of sintered heat exchangers . . . . .	21
2.1	Cryogenic requirements for the EURECA experiment. . . . .	23
2.2	General requirements for the EURECA cryogenic and cooling system. . . . .	24
2.3	Design features of 7 separate dilution refrigerators . . . . .	27
2.4	Conversion from the specific activity, in Bq/kg to the atomic fraction in ppb. . . . .	27
2.5	Characteristics of naturally occurring isotopes. . . . .	28
2.6	Radioactive contaminations in Stainless Steel (SS), copper and acrylics. . . . .	29
2.7	Aimed reduction in the background of EURECA . . . . .	30
2.8	Requirements load lock . . . . .	37
2.9	Properties vacuum pendulum valve. . . . .	37
2.10	Precooling simulation . . . . .	43
2.11	Typical properties of cold boxes . . . . .	53
2.12	Examples of average compressor figures . . . . .	54
3.1	Devices in the shielded electronic rack . . . . .	60
3.2	The devices of the unshielded electronic racks. . . . .	61
3.3	The power dissipation of the components located in the electronic racks. . . . .	63
3.4	Attenuation of the patch panel of the shielded electronic rack. . . . .	64
3.5	The EMC connectors . . . . .	69
3.6	The attenuation of the cryostat filters . . . . .	72
3.7	Chebyshev coefficients of the calibration curve for the Lakeshore thermometer. . . . .	73
3.8	Temperature sensors inside the mixing chamber. . . . .	74
3.9	Fitted coefficients of the thermometers in the mixing chamber. . . . .	75
3.10	Components for the automatic level control of the helium bath . . . . .	77
3.11	The components of the 1 K pot control system. . . . .	79
4.1	Coefficient $A$ and $B$ of the cooling power fitting function. . . . .	90
4.2	Points of optimal $^3\text{He}$ flow rate $\text{opt}\{\dot{n}\}$ of the CCDR . . . . .	92

4.3	Measured residual heat load . . . . .	98
4.4	Summary of the residual heat sources . . . . .	109
4.5	Summary of the time-independent heat loads . . . . .	110
4.6	Summary of the time-dependent residual heat loads . . . . .	111
5.1	Properties of pure liquid $^3\text{He}$ , and of $^3\text{He}/^4\text{He}$ mixtures . . . . .	113
5.2	Initial-stage sintering parameters . . . . .	123
5.3	Measurement techniques for sintering parameters . . . . .	129
5.4	The properties of the studied copper powders. . . . .	134
5.5	Maximal absolute errors of the gas permeability measurements . . . . .	137
5.6	Results of the measurement of the surface area $\sigma$ by gas permeability . . . . .	137
5.7	Properties of the sintered samples tested at lowest temperature . . . . .	140



# Nomenclature

## Symbols in Equations

Symbol	Name	Unit
$A$	Number of Nucleons	[1]
$a$	Speed of Sound	m/s
$B$	Field Strength	T
$C$	Integral Thermal Conductivity	W/K
$c$	Viscous Damping Constant	Ns/m
$c_p$	Specific Heat	J/(kgK)
$E$	Energy	J
	or Young's Modulus	N/m <sup>2</sup>
$f$	Frequency	Hz
$H$	Enthalpy	J/mol
	or Hubble Parameter	s <sup>-1</sup>
$L$	Mean Free Path	m
Kn	Knudsen Number	[1]
$k$	Spring Constant	N/m
$M$	Thermal Mass	J/K
	or Molecular Mass	kg/mol
	or Spectral Specific Radiated Energy	W/(m <sup>2</sup> Hz)
$m$	Mass	kg
$\dot{m}$	Mass Flow Rate	kg/s
$\mu_0$	Permeability of free space	H/m
$\mu_R$	Relative Permeability	[1]

Symbol	Name	Unit
$N$	Number of Particles	[1]
$\dot{n}$	Flow Rate	mol/s
Nu	Nusselt Number	[1]
Pr	Prandtl Number	[1]
$p$	Pressure	Pa
	or Perimeter	m
$Q$	Heat (Energy)	J
$\dot{Q}$	Heat Load	W
$\bar{Q}$	Quality Factor	[1]
$\dot{q}$	Specific Heat Flux	W/m <sup>2</sup>
$R$	Electrical Resistance	$\Omega$
Re	Reynolds Number	[1]
$S$	Kapitza Conductance	W/(m <sup>2</sup> K <sup>4</sup> )
$T$	Temperature	K
	Half Life	s
$V$	Volume	m <sup>3</sup>
	or Molar Volume	m <sup>3</sup> /mol
$\dot{V}$	Volumetric Flow Rate	m <sup>3</sup> /mol
$x$	Concentration	[1]
	or Displacement	m
$Z$	Flow Impedance	m <sup>-3</sup>
	or Number of Protons	[1]
$\alpha$	or Absorptivity	[1]
	or Heat Transfer Coefficient	W/(m <sup>2</sup> K)
	or Van der Waals Constant	Jm <sup>3</sup> /mol <sup>2</sup>
	or Accomodation Coefficient	[1]
$\gamma$	Heat Transfer Parameter	W/m
$\Gamma$	Interaction Rate	[1]

<b>Symbol</b>	<b>Name</b>	<b>Unit</b>
$\delta$	Skin Depth	mm
$\varepsilon$	Emissivity/Efficiency	[1]
	<i>or</i> Strain	[1]
$\eta$	Dynamic Viscosity	Pas
$\Theta$	Debye Temperature	K
$\vartheta$	Damping Ratio	[1]
$\lambda$	Thermal Conductivity	W/(m <sup>2</sup> K)
	<i>or</i> Wavelength	m
$\nu$	Kinematic Viscosity	m <sup>2</sup> /s
	<i>or</i> Poisson's Ratio	[1]
$\xi$	Molecular Diameter	m
	<i>or</i> Friction Factor	[1]
	<i>or</i> Thermal Penetration Depth	m
$\sigma$	Surface Area	m <sup>2</sup>
	<i>or</i> Cross Section	m <sup>2</sup>
$\rho$	Density	kg/m <sup>3</sup>
	<i>or</i> Specific Resistance	$\Omega$ m
$\sigma_S$	Stress	N/m <sup>2</sup>
$\tau$	Relaxation Time	s
	<i>or</i> Time Constant	s
$\varphi$	Phase Shift	[1]
$\Omega$	Solid Angle	sr
	<i>or</i> Relative Energy Density	[1]
$\omega$	Angular Frequency	s <sup>-1</sup>

## Physical Constants

Symbol	Name	Value	Unit
$c$	Vacuum Speed of Light	299 792 458	m/s
$E_0$	Permittivity of Free Space	$8.854187817 \cdot 10^{-12}$	F/m
$e$	Euler's Number	2.71828	[1]
$G$	Newton's Constant	$6.67310 \cdot 10^{-11}$	$\text{m}^3/(\text{kgs}^2)$
$H_0$	Hubble Constant	$3.2 \cdot 10^{-18} \text{h}$	$\text{s}^{-1}$
$h$	Planck Constant	$6.62606876 \cdot 10^{-34}$	Js
$\hbar$	Reduced Planck Constant	$1.054571596 \cdot 10^{-34}$	Js
$k_B$	Boltzmann Constant	$1.3806503 \cdot 10^{-23}$	$\text{JK}^{-1}$
$L_0$	Lorentz Number	$2.44301 \cdot 10^{-8}$	$\text{W}\Omega/\text{K}^2$
$R$	Ideal Gas Constant	8.314472	$\text{J}/(\text{molK})$
$\sigma$	Stefan-Boltzmann Constant	$5.6704 \cdot 10^{-8}$	$\text{W}/(\text{m}^2\text{K}^4)$

## Subscripts and Superscripts

Symbol	Name	Symbol	Name
$A$	Adsorption	$M$	Matter
$b$	Bulk	$m$	Mixture
	or Baryonic	$n$	Natural / Normal
$c$	Concentrated Stream / Critical	$o$	Outer
$DM$	Dark Matter	$r$	Radiation
$d$	Dilute Stream	$s$	Surface / Still / Sphere
$e$	Electron	$turb$	Turbulent
$f$	Flow/Force / Fermi	$tot$	Total
$g$	Gas	$sat$	Saturation
$i$	Inlet / Inner	$W$	Wall
$L$	Condensation	$X$	Displacement
$l$	Linear	3	${}^3\text{He}$
$lam$	Laminar	4	${}^4\text{He}$
$liq$	Liquid	$\lambda$	Vacuum Energy
$MC$	Mixing Chamber	$\chi$	Neutralino

## Abbreviations

BBC	Big Bang Cosmology
BET	Brunauer Emmett and Teller
CCDR	CERN Cryolab Dilution Refrigerator
CDM	Cold Dark Matter
CERN	European Organisation for Nuclear Research
CM	Common Mode
CRESST	Cryogenic Rare Event Search with Superconducting Thermometers
DM	Dark Matter
DR	Dilution Refrigerator
EDELWEISS	Expérience pour DEtecter Les WIMPs an Site Souterrain
EMC	ElectroMagnetic Compatibility
EMI	ElectroMagnetic Interference
EURECA	European Underground RarE Calorimeter Array
FB	Film Burner
FEM	Finite Element Method
GPIB	General Purpose Interface Bus
GRAIL	GRavitational wave Antenna In Leiden
HDM	Hot Dark Matter
IVC	Inner Vacuum Chamber
LSM	Laboratoire Souterrain de Modane
NTD	Neutron Transmutation Doping
PMMA	Poly Methyl MethAcrylate
PSD	Particle Size Distribution
RF	Radio Frequency
RRR	Residual Resistivity Ratio
SE	Shielding Efficiency
SF	Spontaneous Fission
SI	Signal Integrity
SUSY	SUperSYmmetry
TES	Transition Edge Sensor
WIMP	Weakly Interacting Massive Particle

---

Dipl.-Ing. Gerhard Burghart  
20, Rue des Deux-Ponts  
1205 Geneva  
Switzerland

phone (office). +41 (0)22 76 71378  
phone (private). +41 (0)76 30 74 528  
E-Mail: [gerhard.burghart@cern.ch](mailto:gerhard.burghart@cern.ch)



### Personal Details

Born: 23.06.1977 in Vienna  
Marital Status: married  
Nationality: Austria

---

## Curriculum Vitae

### Employment

08/2009 – present **CERN - Fellowship,**

03/2006 – 02/2009 **CERN - European Organization for Nuclear Research,**  
Geneva, Switzerland; Doctoral thesis in low temperature physics:  
Cryogenic Layout of the EURECA Dilution Refrigerator

- Baseline design of a dilution refrigerator for a 1-Ton Dark Matter Detector
- Development, design and construction of the electrical setup of the CERN Cryolab Cryostat
- Experimental Study of Residual Heat Loads
- Experimental Study of the Performance of 1  $\mu\text{m}$  Cu powder for heat exchangers

01/2004 – 01/2005 **Delphi Automotive Systems Vienna GmbH,** Vienna, Austria

- Design of machine parts for manufacturing machines
  - Coordination of internal and external partners
- 

### Employment during studies

06/2003 – 08/2003 **KTM-Sportmotorcycle AG,** Mattighofen, Austria  
Test of the effect of alternative fuel on a petrol combustion engine:

- Test of tolerance of the single components
- Mechanical preparation of the engine
- Long term test on the engine test bench

09/2001 **BMW Motoren GmbH Steyr,** Austria – analysis of the regeneration cycles of particle filters for diesel engines

01/2001 – 01/2004 **Sozial Global** – take care of elderly people on weekends

## Education

05/1997 – 05/2004 **Master's Degree in Mechanical Engineering**, Technical University of Vienna, Austria

10/1999 – 05/2004 **Lectures of Commercial Science**, Vienna University of Economics and Business Administration, Austria

10/1995 – 04/1997 **Architecture**, Technical University of Vienna, Austria

09/1987 – 06/1995: **Matura**, Siegmund Freud Gymnasium Vienna, Austria

---

## Army

01/1998 - 08/1998 Karls-Kaserne, Vienna, Austria

---

## Additional Skills

Languages:           **German** - mother tongue  
                          **English** – excellent written and spoken  
                          **French** – good basic knowledge  
                          **Italian** – basic knowledge

Software:            2D- and 3D-CAD-programs: Catia V5, AutoCAD,  
                          Labview, Mathematica, Matlab, Latex, MS Office

---

## Interests

Sport:                Football, swimming, fitness, inline skating  
Others:              Veteran cars, building models, motorsport